X-RAY AND NEUTRON DIFFRACTION ANALYSIS AND FEM MODELLING OF STRESS AND TEXTURE EVOLUTION IN CUBIC POLYCRYSTALS

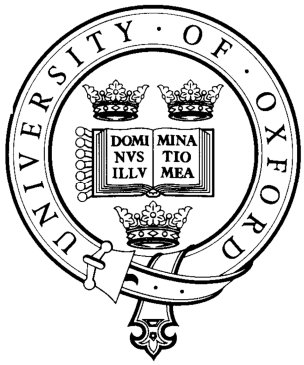

Mengyin Xie

Wolfson College

University of Oxford

A thesis submitted for the degree of

Doctor of Philosophy

Hilary Term 2014

X-ray and neutron diffraction analysis and FEM modelling of stress and texture evolution in cubic polycrystals

Mengyin Xie, Wolfson College, University of Oxford

ABSTRACT

The thesis reports improvements in the characterization techniques for stress and texture in crystalline materials by x-ray and neutron powder diffraction. Furthermore, advances are made in texture evolution modelling and validation against experimental observations.

In the beginning, the fundamental assumption of diffraction strain analysis is numerically examined and verified, namely, that the lattice parameter value determined from fitting the diffraction pattern is equal to the average lattice parameter within the gauge volume.

Next, the task of shear strain determination from powder diffraction measurements is addressed. A method is developed and implemented for the complete 2D strain tensor determination from the multi-directional energy-dispersive x-ray diffraction patterns. The method not only offers a way to evaluate the shear strain, but also provides a better overall strain averaging approach.

Rotation and translation of sample and/or detectors in powder diffraction mode can effectively increase the pole figure coverage and thus the accuracy of texture determination. However, the movements also introduce uncertainties and aberrations into data analysis due to the changes in the diffraction volume and transmitted intensity. In order to overcome these problems, accurate **single exposure** texture characterization techniques are proposed based on several different powder diffraction setups. Numerical analyses are carried out to prove that ***any*** simple texture in cubic polycrystals can be effectively determined using single exposure Debye-Scherrer diffraction pattern analysis. Several experiments are reported on collecting Debye-Scherrer diffraction patterns, multi-directional energy-dispersive x-ray diffraction patterns and multi-directional TOF neutron setup. Efficient data processing procedures of the diffraction patterns for ODF determination are presented.

Crystal plasticity finite element models are developed to model the texture evolution in polycrystalline engineering samples during manufacturing. In the present thesis, quantitative measures extracted from orientation distribution function are employed to make precise comparison between the model and experiment. Unlike the simple uni-axial compression and tension considered in the literature, in the present thesis the complex texture evolution during linear friction welding is modelled as a sequence of different shear deformations.

ACKNOWLEDGEMENTS

I must admit that it has been the most challenging experience for me to complete all the research projects and write this thesis. I also must admit that without the help and support of a few people the completion of this thesis is not possible to reach. Here, I would like to acknowledge these people.

First of all, my greatest gratitude goes to my supervisor, Professor Alexander M. Korsunsky. He gave me the opportunity to join his team and work on some great projects with some of the cleverest people I ever met. He, not only, gave me support to go through difficult moments, but also, guided me to grow from a student with little knowledge in solid mechanics to a researcher in this field. He would be always a model in my life.

A special thank goes to Dr Xu Song who help me a lot on the integration within the team and generously shared his knowledge on the finite element modelling and X-ray diffraction, and to Dr Winfried Kockelmann who help me a lot on the understanding of TOF neutron diffraction and offered a great opportunity to work with GEM diffractometer.

I also wish to thank all the people in the team who I met every day in the office and became my friends: Dr Xu Song, Dr Terry Jun, Dr Jonathan Belnoue, Dr Felix Hofmann, Dr Brian Abbey, Dr Wencai Liu, Nikolaos Baimpas, Tan Sui, Taehoon Kim, Alexander Holovenko, Alexander Lunt, Ricky Ying.

I am very grateful to Rolls-Royce plc. for funding 3 years of my studies through Dorothy Hodgkin Postgraduate Award and to the Engineering Science Department and Wolfson College for the conference and travel bursaries.

Thank you to all my friends I met in Oxford: Jiayao Ma, Jiewen Deng, Tao Zhao, Kun Liang, Jianan Hu, Boon Chia Weng, Xueyuan Jiang, Luying Chen and many many…

Last but not least, I would like to express my deepest gratitude to my parents and my dear wife Wanquan. Without the love, support and understanding I would surely not have accomplished my studies.

PREFACE

This thesis is a collection of the research work carried out by the author in the Department of Engineering Science, University of Oxford, between October 2009 and February 2014, under the supervision of Professor Alexander M. Korsunsky.

I state that the research described herein is original, even though the work of others has drawn upon freely with due acknowledgment in the text. No part of it has previously been submitted for a degree at this or other University.

Some of the work described in this thesis has been published in the following papers:

1. Xie, M. Y., N. Baimpas, et al. (2013). "Texture analysis in cubic phase polycrystals by single exposure synchrotron X-ray diffraction." Journal of Applied Physics **114**(16).

2. Xie, M. Y., T. S. Jun, et al. (2013). "Analysis of Preferred Orientations in Linear Friction Welded (LFW) Aluminium Alloy Specimens using "One-shot" Multi-element Energy Dispersive Synchrotron X-ray Diffraction." Powder Diffraction **28**: S327-S332.

3. Song, X., M. Xie, et al. (2013). "Residual stresses in Linear Friction Welding of aluminium alloys." Materials & Design **50**: 360-369.

4. Baimpas, N., M. Xie, et al. (2013). "The application of geometry corrections for Diffraction Strain Tomography (DST) analysis of a Ni-base superalloy blade." Powder Diffraction **28**: S436-S447.

5. Abbey, B., S. Y. Zhang, et al. (2012). "Neutron strain tomography using Bragg-edge transmission." International Journal of Materials Research **103**(2): 234-241.

6. Korsunsky, A. M., N. Baimpas, et al. (2011). "Strain tomography of polycrystalline zirconia dental prostheses by synchrotron X-ray diffraction." Acta Materialia **59**(6): 2501-2513.

7. Korsunsky, A. M., X. Song, et al. (2010). "Polycrystal deformation analysis by high energy synchrotron X-ray diffraction on the 112 JEEP beamline at Diamond Light Source." Materials Letters **64**(15): 1724-1727.

8. Xie, M. Y., Kockelmann, W., et al. (in revision). “Texture analysis of time-of-flight neutron diffraction data using the MTEX toolkit” Nuclear Inst. and Methods in Physics Research, A

9. Xie, M. Y., Baimpas, N., et al (COMPLAS 2013). “Numerical simulation and experimental validation of texture in extruded wires of a bcc metal” IX Inter-national Conference on Computational Plasticity, Barcelona, Spain.

10. Korsunsky, A. M., Xie, M.Y., et al (IMECS 2012). “X-ray texture analysis and imaging of engineering materials at Oxford HEX-lab” Proceedings of the International MultiConference of Engineers and Computer Scientists 2012 Vol II, IMECS 2012, March 14 - 16, 2012, Hong Kong

TABLE OF CONTENTS

LIST OF FIGURES

LIST OF TABLES

NOMENCLARTURE

d	Lattice plane spacing
a	Lattice spacing
θ	Diffraction angle
h	Plank constant
$\mathbf{C}$	Elastic stiffness matrix
$\boldsymbol{\varepsilon}$	Strain (tensor)
$\boldsymbol{\sigma}$	(Cauchy) stress (tensor)
$\boldsymbol{\psi}$	(Kirchhoff) stress (tensor)
f	Volume fraction of orientation distribution function
E	Young’s modulus
υ	Poisson's ratio
$\mathbf{R}$	Rotation matrix
$\mathbf{F}$	Deformation gradient
$\mathbf{L}$	Velocity gradient
$\mathbf{s}$	Slip direction vector
$\mathbf{n}$	Slip plane normal vector
$\mathbf{D}$	Stretch tensor
$\boldsymbol{\Omega}$	Spin tensor
γ	Shear strain
τ	Schmid stress

Chapter 1 Introduction

1.1 Background and aims of the thesis

Internal stresses distribution within polycrystalline engineering components can affect significantly their mechanical performance and structural integrity, e.g. crack propagation direction and rate, and hence the fatigue life. Depending on whether the component is subjected to external load, the stress can be divided into “live” and residual stresses. Stress analysis often focuses on the live stress distribution. However, the residual stresses caused by the manufacturing history must not be ignored because they frequently make the difference between component integrity and failure under load. Residual stress is also sometimes introduced into a component intentionally to improve its mechanical properties. Compressive residual stresses are known to retard or arrest crack propagation. This phenomenon has been employed to protect the glass screen covers of modern smartphones. The outer layer of the screen is made of toughened glass containing compressive residual stresses. Consequently, even in the presence of scratches and dents from coins and keys in someone’s pocket, the screen remains intact.

Residual and “live” stresses in (poly)crystalline materials are often classified according to the length scale of their action, from macroscopic (Type I) to microscopic inter-granular (meso-scale or Type II) to microscopic intra-granular (micro-scale or Type III). As the length scale of consideration gets smaller, the grain level deformation behaviour and microstructure play progressively important roles in determining the stress state. In particular, the anisotropy of the mechanical (elastic, plastic, thermal) properties of crystallites affects the relationship between the remotely applied load or constraint and the local strain experienced at the grain level, as well as the conversion from this local strain value to stress via Hooke’s law. It is important to note that the anisotropy of the elastic and plastic properties has a strong

influence over the formation of residual stresses during material processing. Therefore, in order to understand the formation of residual stress at the meso- and micro-scales, the statistics of grain morphology and orientation has to be carefully studied.

Crystallographic texture is the term used to refer to the statistics of grain orientation within a (poly)crystalline material. Large plastic deformation and growth processes that take place during manufacturing represent the principal mechanisms for the formation of texture in a component. Texture may cause significant anisotropy within components that affect the mechanical and functional properties. Fig. 1.1 illustrates the influence of texture on the manufacturing of a cup-shaped component by deep drawing. The aluminium sheet used for making the cups has very weak texture (Fig. 1.1.a), resulting in an approximately level edge. In contrast, the sheet used for the cup in Fig. 1.1.b that was characterised by a strong “cube” texture forms an edge that displays a prominent “ear” profile. This provides an example of the significant influence that texture can have on the outcome of manufacturing processes.

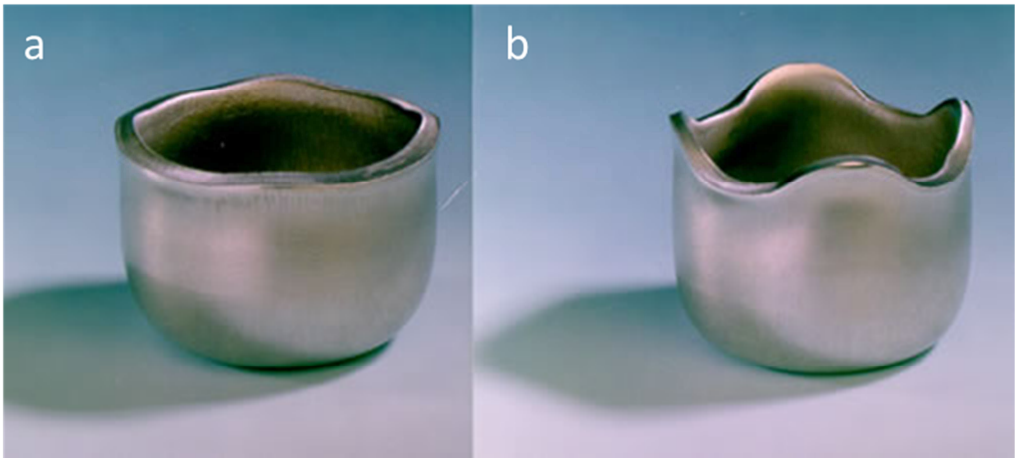

Fig. 1.1 Cups made of aluminium sheet (a) with weak texture and (b) with strong “cube” texture [1].

In order to establish an understanding of how the plastic deformation during the manufacturing process affects the distribution of residual stress and texture within engineering components, and thus to be able to exercise control over them, it is crucial to

characterize the distributions in an accurate way. For (poly)crystalline materials, both elastic strain and texture can be simultaneously characterized by diffraction techniques. The experimental setup and data collection procedures are very similar, although the data analysis procedures are different. The principle of diffraction measurement of elastic strain and texture in crystalline materials relies on the sensitivity of the scattered intensity to the orientation distribution (texture measurement) and of the scattering angle to the crystal lattice spacing. The measured lattice spacing can be used to compute the lattice strain and then stress via Hooke's law. The past few decades have witnessed increased use of synchrotron X-ray and neutron beams to measure stress and texture in crystalline materials. The main advantages of using these methods are the high flux (leading to fast measurement), high penetration ability and non-destructive nature, high spatial resolution and accuracy being afforded, etc…

The present thesis focuses on the use of powder diffraction techniques using advanced radiation sources to study stress and texture. The thesis aims to improve the currently established stress and texture characterization techniques by proposing and using several novel powder diffraction setups and interpretation procedures. It is well known that shear strain cannot be directly measured by diffraction techniques, since to the first approximation it does not cause a change in the lattice interplanar spacing. In order to overcome this limitation a new method is proposed to determine the complete 2D strain tensor from multi-directional energy-dispersive diffraction patterns.

When powder diffraction is used to study texture, sample rotation is commonly carried out in order to increase the pole figure coverage. However, sample rotation also gives rise to a series of problems, such as diffraction volume change, difficulty in performing *in situ* deformation experiments, long experimental time and complicated data processing procedures. In this thesis the theoretical basis is developed and presented for the single

exposure texture characterization (without sample rotation). Several practical experimental results are presented that demonstrate the application of this approach in conjunction with using synchrotron X-ray and TOF neutrons.

The thesis also aims to address some outstanding fundamental challenges in the texture analysis field. The results of modelling and experiments are often compared qualitatively “by eye” in literature, so that the following conclusions are made largely based on the observer’s experience. For the purpose of making better comparison, quantitative measures are proposed of the correlation between the results obtained from modelling and by experimentation. Furthermore, most of the reported results of texture modelling are limited to the consideration of texture evolution during monotonic deformation, e.g. uniaxial tension, compression and simple shear. Here the results are presented of modelling the texture evolution during the complex process of linear friction welding (LFW).

1.2 Structure of the thesis

The thesis is divided into two parts: background literature review and overview of the methods (chapter 2-4), and the reports on original research outcomes (chapter 5-8).

Chapter 2 presents a review of the literature on diffraction techniques. Basic facts on X-ray diffraction are given briefly, e.g. Bragg’s law and the Miller index convention in cubic crystals. Several typical experimental steps are introduced. Attention is focused on powder diffraction and pattern analysis rather than single crystal diffraction.

Chapter 3 presents several methods to extract stress and texture information from powder diffraction patterns. The linear elastic stress-strain relationship (Hooke’s law) for solid materials is presented first. The strains measured at different length scales are discussed, and the focus is put on the discussion of strain averaging at the meso-scale, which corresponds to the length scale of lattice strains measured by powder diffraction techniques.

The principle of determining 2D strain tensor from a Debye-Scherrer diffraction pattern is presented. Switching attention to texture, some basic concepts in texture analysis are introduced first. Texture measurement by diffraction techniques is then introduced, mainly focusing on pole figure measurement by powder diffraction. Several methods of treating the experimental data into pole figures and ultimately into full quantitative texture information (orientation distribution function, ODF) are described.

Chapter 4 present the methodology of the crystal plasticity finite element method (CP-FEM). The concept of crystal plasticity is outlined and explained first. The comparison between crystal plasticity finite element method and other types of crystal plasticity modelling techniques is made. The incremental stepping scheme for crystal plasticity finite element simulation used in this thesis for texture evolution analysis is presented.

Chapter 5 presents two studies devoted to experimental strain analysis. First, an important fundamental question in strain measurement by powder diffraction is addressed: "Is the interplanar lattice spacing determined from a powder diffraction line profile via peak fitting and Bragg's law ***equal*** to the average interplanar lattice spacing within the gauge volume?" Second, the approach is introduced to processing the data obtained from multi-directional energy-dispersive X-ray diffraction detector (or from an area detector used in the monochromatic mode) in order to determine the complete 2D strain tensor within the gauge volume. The approach is then applied to obtain 2D principal strain mapping in linear friction welded samples of Al alloys.

Chapter 6 presents a systematic investigation using MTEX package of the limits and accuracy of full texture information extraction from single exposure Debye-Scherrer diffraction patterns recorded using area detectors. A suite of numerical simulations is described first that provides the fundamental basis for the application of this approach. The

outcomes of two experiments are then presented in order to illustrate the data processing steps involved, and the extraction of the orientation distribution function. The results are compared with those of multi-exposure analyses.

Chapter 7 presents texture analyses using two different types of energy-dispersive detectors with large pole figure coverage from single exposure. The first part focuses on the data processing of a multi-element energy-dispersive X-ray detector used on the high energy synchrotron beamline I12 at Diamond Light Source. The second part focuses on processing the data from GEM time-of-flight neutron diffractometer at ISIS neutron spallation source in Oxford. Several difficulties and challenges associated with the data processing are discussed.

Chapter 8 presents texture evolution modelling by crystal plasticity finite element method (CP-FEM) for cubic polycrystals under three types of deformation: wire extrusion (bi-axial compression), uniaxial compression and linear friction welding (sequential shear). Some possible error sources are identified and their influence on texture modelling validation is discussed. Two approaches are presented to quantitative comparison of models and experimental results in terms of the orientation distribution function.

Chapter 9 presents a critical review of the thesis and discusses the directions for possible future work.

Chapter 2 Literature review

2.1 Diffraction basics

2.1.1 Bragg's law

Diffraction of visible light from objects with structural dimensions similar to the light's wavelength has been observed in many classical optical diffraction experiments, for example, the Young's interference experiment. Since then the exploitation of powerfully penetrating radiation such as x-ray and neutrons to probe the crystal lattice structure has become widely used. The diffraction condition exploited in these experiments can be described in its simplest form by Bragg's law:

$$2d_{hkl}\sin\theta = n\lambda \qquad \text{(Eq. 2.1)}$$

where d_{hkl} is the inter-planar distance between planes defined by Miller indices [2] (section 2.1.2), θ is half of the scattering angle, n is the order of the diffraction (often set to unity, as the first order diffraction has the strongest intensity) and λ is the wavelength of radiation. The geometric relationship between the incident and scattered beams and two (*hkl*) lattice planes is shown in Fig. 2.1.

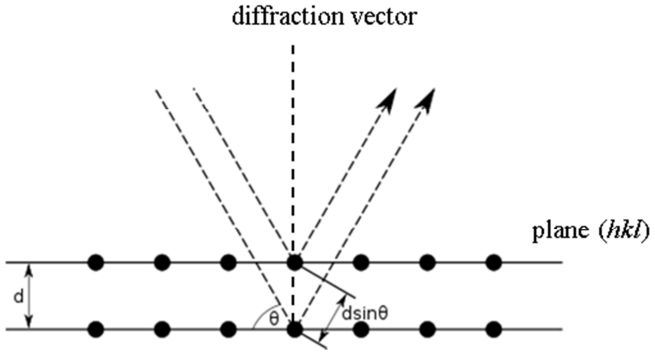

Fig. 2.1 Bragg reflection

2.1.2 Cubic crystal structure and Miller index convention

Miller indices are widely used in crystallography to represent both the crystal direction and the crystal plane. Since cubic crystals are the principal interest of this thesis, the following explanation of the Miller index is only suitable for cubic crystal systems.

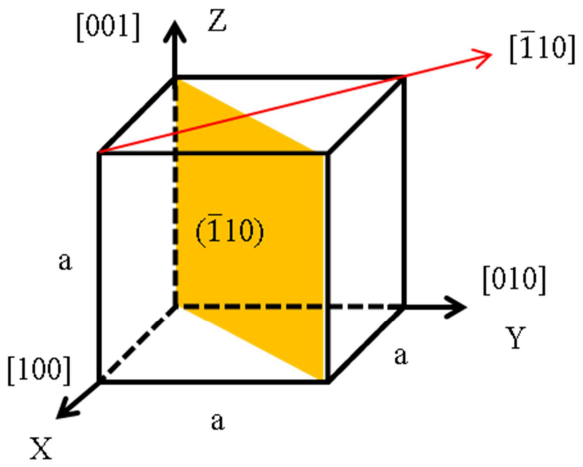

Fig. 2.2 Illustration of crystal direction and plane with Miller index notation in a cubic unit cell.

A simple cubic unit cell is plotted in Fig. 2.2. The twelve edges have an equal length *a* corresponding to lattice parameter in a cubic crystal system. As shown in the picture, a system of Cartesian coordinates is assigned to the cube. The crystal coordinates have three basis vectors: $\vec{a}_1$, $\vec{a}_2$ and $\vec{a}_3$ (referring to X, Y and Z direction in the picture). The length of these basis vectors is the lattice parameter *a*. A crystal direction $\overrightarrow{g_{hkl}}$ is written as [*hkl*] under Miller index notation and its mathematical form is given by,

$$\overrightarrow{g_{hkl}} = h\vec{a}_1 + k\vec{a}_2 + l\vec{a}_3 \qquad \text{(Eq. 2.2)}$$

For instance, crystal directions [100], [010] and [001] are equivalent to $\vec{a}_1$, $\vec{a}_2$ and $\vec{a}_3$ respectively. A crystal plane is written as (*hkl*), and in cubic crystals the corresponding [*hkl*]

direction is perpendicular to the plane. In Fig. 2.2, the shaded plane is written as $(\bar{1}11)$, whose plane normal is the face diagonal indicated by the red arrow $[\bar{1}11]$.

There are many equivalent crystal directions and planes due to symmetrical constraints of the crystal. A family of equivalent crystal directions is written as <hkl>. For example, crystal directions: [100], [010] and [001] are equivalent and <100> is used to represent them all. Brace notation, in the form of {*hkl*}, is used to represent equivalent crystal planes. Crystal plane (100) has two other equivalent planes: (010) and (001). This family of planes is written as {100}.

The distance between two neighbouring (*hkl*) planes is written as d_{hkl}. According to geometric relationship in cubic crystal systems d_{hkl} is given by,

$$d_{hkl} = \frac{a}{\sqrt{h^2 + k^2 + l^2}} \qquad \text{(Eq. 2.3)}$$

Due to the crystal symmetry of the cubic phase, some of the diffractions are forbidden and thus cannot be observed. The forbidden reflections of the cubic phase crystals are listed in Table 2.1.

Table 2.1 Forbidden rules in cubic phase crystals

Bravais lattice	Example materials	Allowed reflections	Forbidden rule
Simple cubic	Po	Any *h, k , l*	None
Body-centred cubic (BCC)	W	*h + k + l=even*	*h + k + l=odd*
Face-centred cubic (FCC)	Cu, Al, Ni,	*h, k , l are all even or all odd*	*h, k , l are mixed even and odd*

2.2 Radiations

2.2.1 Laboratory and synchrotron X-ray sources

X-ray beams can be readily obtained from laboratory sources. These typically consist of a heated filament (cathode) from which electrons are emitted due to high voltage electric field applied between it and a heavy metal target (anode). X-rays are emitted when electrons collide with the heavy target. Most of the energy in the collision process is lost in the form of heat and the x-ray beam only takes a small portion of energy, therefore the energy conversion efficiency of these x-ray sources can be very low.

The mechanisms of x-ray production are generally categorised into two different modes. In the first approach an x-ray photon is emitted when an electron changes its direction of propagation. The energy of the photon is equal to the kinetic energy lost by the electron minus the heat produced. The photon's direction is along a tangent to the electron's path. This process is called the Bremsstrahlung effect (braking radiation) [3], and its schematic is shown in Fig. 2.3.a. In the collision process, most electrons are stopped by the target. This means that the tangential direction becomes arbitrarily defined and x-rays are produced in every direction; therefore these x-rays are always divergent.

The second approach for producing x-rays is by fluorescence effect. In this process some of inner orbit electrons of the target's atoms are knocked out of place by the high energy electrons from the cathode. This causes electrons in the higher energy orbits to fall into the vacant orbit. An x-ray photon is released in the process, such that the photon's energy is equal to the energy difference between the two orbits (the process is schematically shown in Fig. 2.3.b). The X-ray beam produced in this way is called 'characteristic radiation' as the wavelength of the beam is closely related to the type of atom. The beam produced by this process is typically much stronger than the Bremsstrahlung x-ray beam. However, in most

diffraction experiments, characteristic radiation results in the production of peaks on the recorded spectrum.

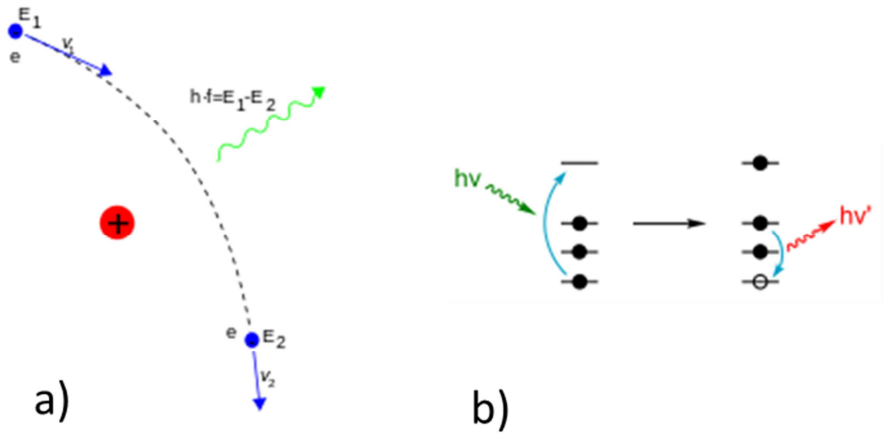

Fig. 2.3 Two different x-ray photon production process: (a) Bremsstrahlung effect [4] and (b) x-ray fluorescence [5].

Synchrotron x-ray was firstly discovered in the 1940s as a by-product of operating a charged particle accelerator [6]. Later, it was recognized to have many advantages over lab x-rays, such as high flux, low divergence and high parallelism. These characteristics served as motivation for the construction of specialized synchrotron light sources and today the third generation of synchrotron x-ray sources are in service. The schematic of a typical modern synchrotron centre is shown in Fig. 2.4.

To obtain synchrotron radiation, a group of electrons are injected from an electron gun into a linear accelerator (Linac), in which a high voltage linear electric field initially accelerates the electrons. In the second step, the electrons enter into a small ring known as a booster synchrotron in which the electrons are accelerated to their final speed (for instance, 3 GeV in Diamond Light Source, UK). In the third step, these high speed electrons are injected into a larger storage ring in which they are continually accelerated to maintain their original

speed. A strong magnetic field is used to repeatedly reorient the direction of the electron beam such that it follows a polygonal path. Due to the Bremsstrahlung effect shown in Fig. 2.3.a, synchrotron radiation (mainly x-rays) is emitted at a tangent to the storage ring. Since no collision occurs, the energy conversion efficiency of a synchrotron x-ray source is much higher than those associated with lab based sources. The x-rays are then optically guided into beamlines where researchers can perform experiments.

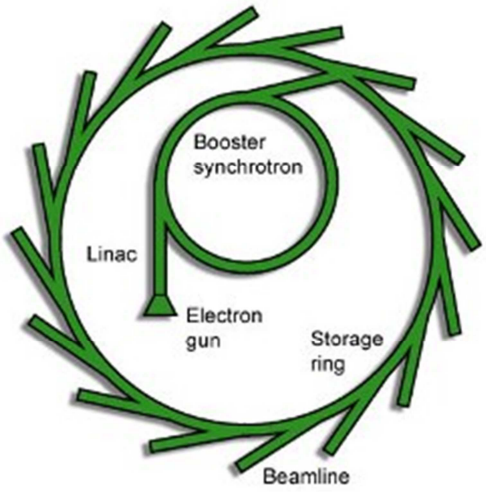

Fig. 2.4 Schematic of a typical synchrotron layout [7].

2.2.2 Neutron beam and the Time-Of-Flight (TOF) technique

The existence of neutron was firstly confirmed in the 1930s by Chadwick. In his experiments Chadwick used α-particles to bombard light atoms such as beryllium and lithium to produce neutrons. Modern neutron sources are categorized into two different types depending on the mechanism used to produce neutron beam. The first type of neutron source employs a nuclear fission chain reaction. For instance, in the Institut Laue–Langevin (ILL) in France, compact uranium alloy plates (that mainly consist of ^{235}U isotope [8]) are used as fission source. Neutrons with a wide spectrum of energies are emitted when ^{235}U isotope

decays to other types of nuclei. The reaction has to be carefully controlled to maintain a steady state.

The second type of source is known as a spallation neutron source and an example is the ISIS pulsed neutron source, UK (the schematic diagram of which is shown in Fig. 2.5). Pulses of H^+ ions (protons) pass through a linear accelerator before being injected into a synchrotron ring for further acceleration. Next, the proton beam is guided into one of the two straight tunnels before being directed at a heavy metal target at the end of the tunnel. The target's nuclei reach higher energy excited states and become unstable before dropping to lower energy (more stable) states. Part of the energy of this exchange is released in the form of neutrons.

In ISIS, energy-dispersive neutron beam diffraction experiments can be carried out using Time-Of-Flight (TOF) neutron scattering technique, which is illustrated in Fig. 2.6. Neutrons produced by pulsed protons have different initial speed when they emerge from the target. A moderator is used to "thermalize" (slow down) the neutrons. Since the spalled neutrons have different speeds, they need different times of flight (TOF's) to arrive at the detector. By the recording the TOF taken for the neutrons to reach the detector and dividing this by the total flight length, the de Broglie wavelength can be worked out as follows:

$$\lambda = \frac{h}{m\nu} = \frac{h}{mL}\mathrm{TOF} \qquad \text{(Eq. 2.4)}$$

Where λ is the wavelength of a neutron; h is Planck's constant (6.582×10^{16} eV·s), m is the neutron rest mass (939.565 MeV/c^2), L is its total flight length and ν is the speed of the neutron.

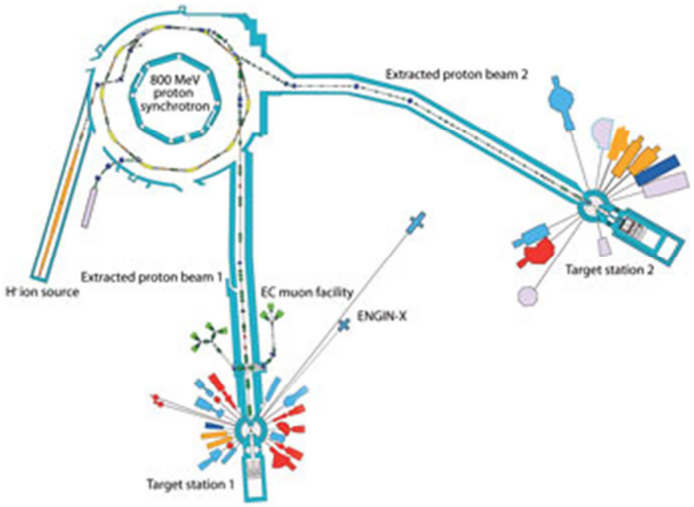

Fig. 2.5 The layout of ISIS and its target stations [9].

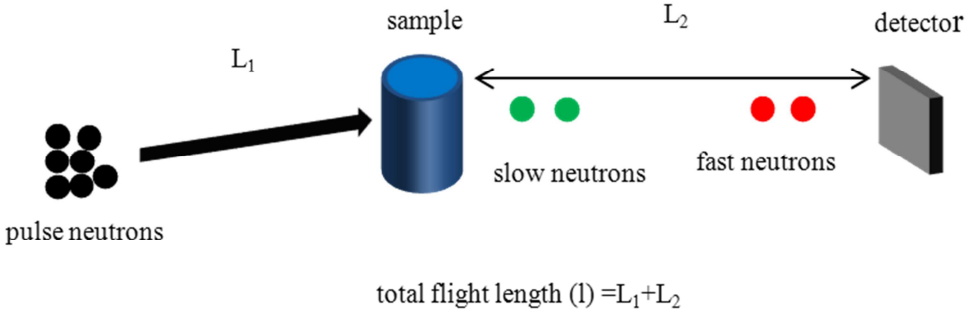

Fig. 2.6 Schematic of TOF neutrons scattering detection.

Both neutrons and x-rays obey Bragg's law when they are diffracted by crystalline materials. However, the differences in their production mechanisms and interaction with materials mean that their applications are very different. Firstly, the flux of synchrotron radiation is much higher and the beam divergence is much smaller than that of neutron beam. This means that synchrotron x-ray diffraction usually only needs very short exposure times (e.g. down to a few milliseconds in beamline I12, Diamond Light Source) and a tiny diffraction volume (e.g. down to sub-micron in beamline B16, Diamond Light Source) to accumulate enough diffracted photons. In comparison, neutron diffraction usually requires much longer exposure times (typically more than 5 minutes e.g. on the GEM instrument, ISIS) and much larger diffraction volumes (typical minimum of 3 × 3 ×3 mm^3 e.g. at GEM, ISIS)

to accumulate data with adequate signal-to-noise ratio. For reasons of speed and efficiency of data collection, if a sample in question can be probed by synchrotron or neutron diffraction, then synchrotron X-ray might be the preferred option.

Another difference between these two diffraction techniques is the variation in the behaviour of neutrons during scattering from atomic nuclei which depends irregularly on the atomic number (Z) of the atom under investigation. In contrast, the strength of interaction between an x-ray beam and the electron cloud of a given atom is proportional to Z^2. Therefore, only weak scattering is observed when attempting to study light elements using an x-ray beam, and also x-ray penetration becomes a limiting issue when studying heavy elements. Neutron sources therefore offer advantages when studying materials consisting of elements that fall into either of these categories.

2.3 Diffraction modes

A diffraction experiment is characterized by the type of beam (electron, x-ray, neutron, etc..), the beam's wavelength (monochromatic or polychromatic), the number of grains in the sample (single crystal or powder), detector dimensionality (point, 1D, 2D and 3D) and the diffraction geometry (reflection or transmission). Many different setups and techniques have been developed in recent years and a comprehensive overview can be found in [10].

The principal interest of this thesis is the use of powder diffraction to study strain and texture in polycrystalline samples. Single crystal diffraction has also been used as a validation tool in texture studies. The difference between single crystal and powder diffraction arises depending on how many grains are present inside the diffraction gauge volume. The single crystal diffraction condition is satisfied when the size of diffraction volume is equal to or smaller than the size of single grain. For this reason, focused beams are often used for single crystal diffraction (as typical material grain sizes are smaller than the size of a collimated

beam). Measuring single crystal diffraction in a transmission arrangement requires very thin samples to ensure that only a few grains are illuminated, and for this reason reflection geometry is often preferred. In powder diffraction, a large number (more than 1,000) of grains need to be illuminated by the beam. Beam size is usually defined by a collimation system and focusing is not required. Depending on the region of interest, powder diffraction can be implemented in either a reflection or transmission geometry. Table 2.2 lists some commonly used diffraction modes and their characteristics.

A more detailed introduction to the techniques used in the thesis will be outlined below including,

1) Electron backscattering diffraction (EBSD) (Section 2.2.1)
2) Monochromatic x-ray powder diffraction in transmission (Debye-Scherrer) (Section 2.2.2)
3) Energy-dispersive beam with multi-detector (Section 2.2.3)

Table 2.2 Characteristics of some common used diffraction techniques.

Beam	Modes	Wavelength	Geometry	Sample	Detector	Instrument/beamline
Electron	Electron Backscattering	Monochromatic	reflection	Single crystal	2D	OIM XM 4 Hikari EBSD System
Synchrotron x-ray	Laue diffraction	Polychromatic	Reflection or transmission	Single crystal	2D	B16, Diamond Light Source
Synchrotron x-ray	Debye-Scherrer	Monochromatic	Transmission	Polycrystals	2D	I12, DLS, UK
Synchrotron x-ray		Polychromatic	Transmission	Polycrystals	Multi-point	I12, DLS, UK
TOF neutron		Polychromatic	Transmission	Polycrystals	Multi-panel	HIPPO,LANSCE ,USA GEM, ISIS, UK

2.3.1 Electron backscattering diffraction (EBSD)

A typical EBSD setup is shown in Fig. 2.7. In this arrangement a polycrystalline sample is titled such that the angle between the plane normal and the incident beam is 70^{o}. The diffraction pattern is recorded in a reflection mode and the diffraction gauge volume is less than ≈100 nm from the surface. The beam is focused to a sub-micron spot on the sample's exterior that needs to be flat and free from contamination. The back scattering diffraction signals are record by a 2D CCD camera and appear as "Kikuchi patterns" [11].

The mechanism of Kikuchi pattern formation is illustrated in Fig. 2.8. Electron diffraction also obeys Braggs' law and the wavelength of an electron is given by:

$$\lambda = \frac{h}{p} = \frac{h}{m_0 v} = \frac{h}{\sqrt{2 m_0 e U}} \qquad \text{(Eq. 2.5)}$$

where h is Plank's constant, p is electron's momentum, m_0 is rest mass, e is elementary charge, U is voltage and v is electron's speed.

The electron beam is monochromatic (with fixed voltage) in an EBSD machine. The accelerating voltage of the beam is usually between 10 and 30 KV which corresponds to a wavelength between 0.122 and 0.070 Å. This wavelength is so short that two very shallow diffraction cones (with solid angles close to 2π) are formed when electrons are diffracted by a particular set of $\{uvw\}$ crystal planes. The two cones intersect the phosphor screen to form a band on the CCD camera. Since the cones are very shallow, the edges of the bands appear to be straight rather than curved (the curvature of the band is exaggerated in Fig. 2.8 in order to demonstrate the cone like behaviour). The central axes of both of the two diffraction cones are coincident with a particular zone axis $[hkl]$ which is parallel to all the $\{uvw\}$ crystal planes. Therefore, a zone axis is always perpendicular to any plane normal $<uvw>$ of a set of zone planes, and this relation is described by the zone law:

$$uh + vk + wl = 0 \qquad \text{(Eq. 2.6)}$$

In Fig. 2.8, the grey plane (*hkl*) is perpendicular to the zone axis [*hkl*]. Extension of this plane would result in an line of intersection on the phosphor screen in the middle of the Kikuchi bands. Therefore, a Kikuchi band is related to a particular (*hkl*) crystal plane and this relationship is key to interpreting an Electron Backscattering Pattern (EBSP).

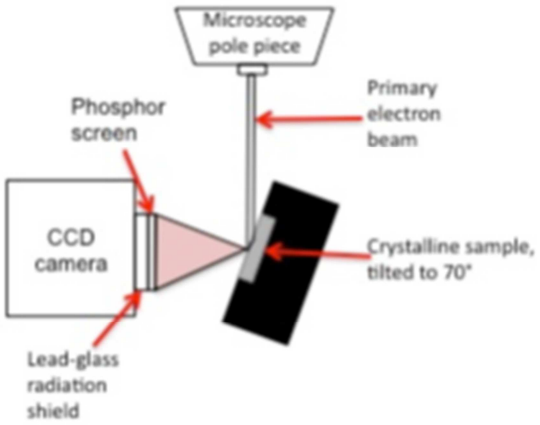

Fig. 2.7 Schematic of a typical EBSD setup.

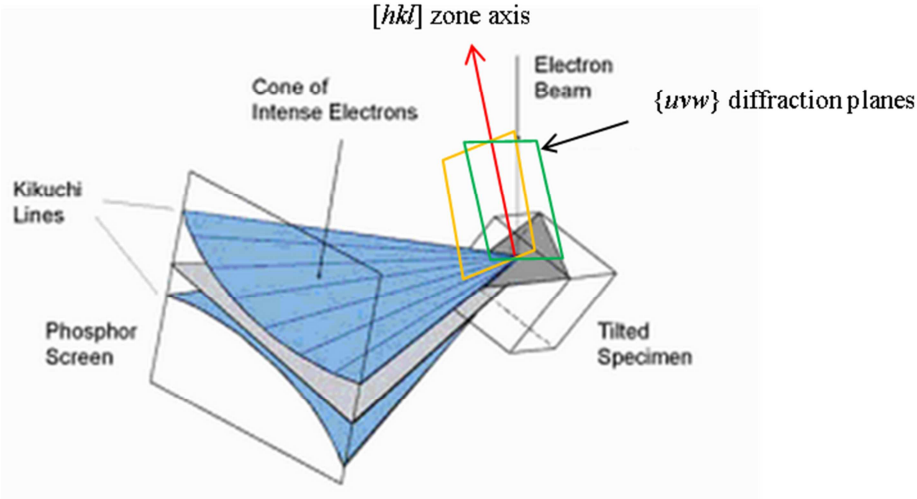

Fig. 2.8 Schematic of the formation of Kikuchi pattern [11].

2.3.2 Monochromatic powder diffraction (Debye-Scherrer diffraction)

Monochromatic X-ray beam diffraction is a classical powder diffraction method in which the sample is placed in a transmission mode and the diffraction pattern is collected by a downstream area detector. This technique is based on the Debye-Scherrer method and a typical setup is shown in Fig. 2.9. One pixel on the detector is equivalent to a traditional monochromatic X-ray point detector. Therefore, the area detector can record a large amount of diffracted information in a single exposure. This characteristic offers particular advantages in texture analysis and this will be discussed further in section **3.3**.

The formation of diffraction patterns is shown in Fig. 2.9. A diffraction cone (for which a cross-section through its central axis is shown) is formed when the beam is diffracted by the polycrystalline sample. The central axis of the cone is along the direction of incident beam and the opening angle (4θ) of the cone is twice the diffraction angle (2θ). It should be noted here that the central axis of a powder diffraction cone is different from that of the cones formed in EBSD setup (section 2.2.1). The area detector is mounted perpendicular to the incident beam so that a circle (Debye-Scherrer ring) is formed by the intersection between the detector and a diffraction cone. If the grains inside gauge volume are randomly orientated, the diffracted intensity on this ring is homogeneous (equal magnitude at all azimuthal angles). In contrast, when preferred orientations exist inside the gauge volume, an intensity inhomogeneity is observed on the Debye-Scherrer ring (see the diffraction pattern in Fig. 2.9).

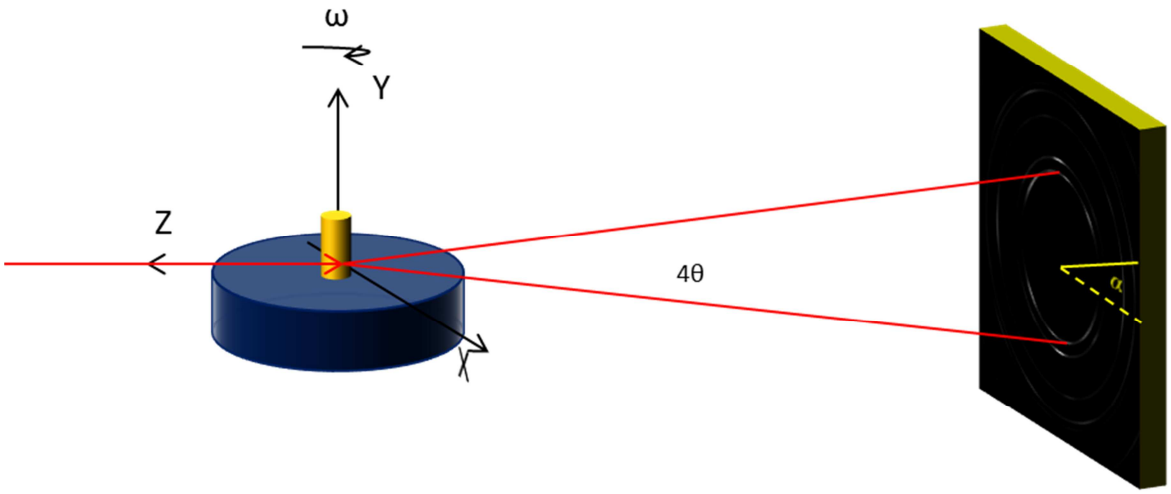

Fig. 2.9 Schematic of Debye-Scherrer diffraction setup.

2.3.3 Multi-direction energy dispersive diffraction

The monochromatic synchrotron x-ray radiation previously mentioned can be produced from the polychromatic storage ring X-rays using filters known as monochromators. This process results in a decrease in transmitted flux and therefore, in order to take full advantage of the synchrotron beam, polychromatic beams can be directly used in diffraction experiments. In order to measure the diffraction produced during these experiments, energy-dispersive X-ray point detectors are often utilized.

Similar to the advantage offered by the use of area detectors in the Debye-Scherrer method, Multi-element (multi-point) energy-dispersive x-ray detectors deliver an improvement in the amount of diffraction information that can be collected in a single exposure. In Fig. 2.10, a 10-element detector [12] from beamline X17B2 at the National Synchrotron Light Source (Brookhaven National Laboratory, USA) is shown as an example of this type of detector. In this setup, ten energy-dispersive point detectors are arranged on a circle in the detector module. The detector records the circular cross section of a single diffraction cone with a fixed opening angle of 4θ. The wide range of input wavelengths and the nature of the energy dispersive detector mean that the diffraction patterns from one

detector can be treated equivalently to an azimuthally binned portion of a Debye-Scherrer diffraction pattern in the same radial direction.

It should be noted that energy-dispersive x-ray multi-element detectors are generally placed downstream of the sample. The reason for this placement is that most of high energy x-rays diffract into the small solid angle from the incident beam. In comparison, low energy x-rays are diffracted in any directions and can therefore be recorded in positions both upstream and downstream of the sample.

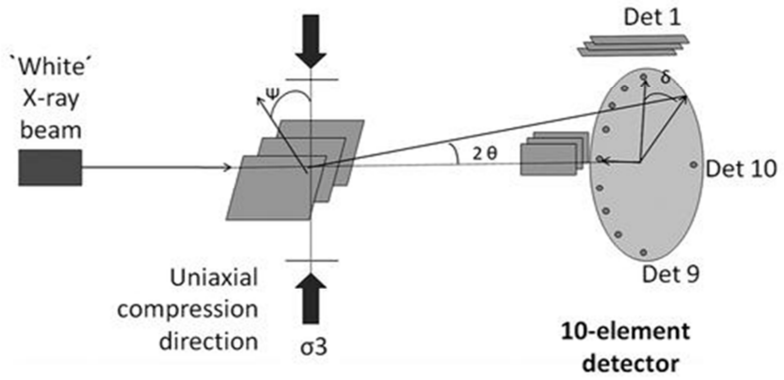

Fig. 2.10 Schematic setup of X-ray energy-dispersive diffraction using a 10-element detector

TOF neutron scattering can also be thought of as a type of energy-dispersive diffraction method (section 2.1.2) in which TOF neutron multi-detectors can be used to collect large amounts of scattering data in a single exposure and sample orientation. Similar to low energy X-ray scattering, neutron diffraction occurs in every direction and therefore TOF neutron multi-detectors have been designed to cover a wide range of solid angles relative to the gauge volume. One such example of a TOF neutron multi-detector is the High-Pressure-Preferred Orientation (HIPPO) diffractometer [13] at LANSCE in the USA (shown in Fig. 2.11). It consists of 5 detector panels, each housing many individual detectors (containing ^{3}He) to resolve the energy of scattered TOF neutrons. The 10° panel is a forward

scattering panel and its function can be regarded as equivalent to the Debye-Scherrer setup (Fig. 2.9) or the energy-dispersive x-ray 10-element detector setup (Fig. 2.10).

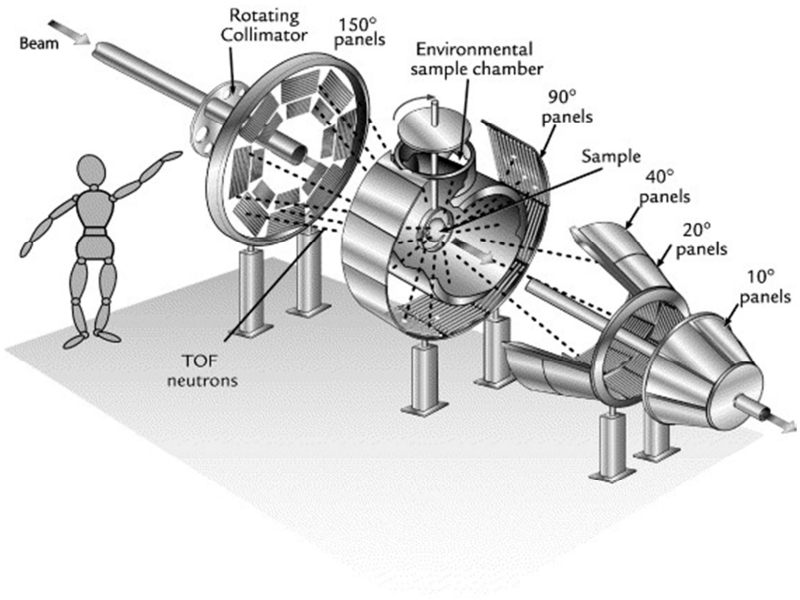

Fig. 2.11 Schematic of TOF neutron HIPPO diffractometer setup.

2.4 Powder diffraction patterns: line profile fitting

2.4.1 Diffraction pattern line profile

A line profile is a function of diffracted intensity against energy or diffraction angle which can be produced using a range of different diffraction based techniques. By fitting this profile, quantitative information about the sample, such as lattice strain and texture can be obtained. In the following example the line profile produced from a Debye-Scherrer diffraction pattern has been used to illustrate the data processing technique which is standardly implemented.

An example Debye-Scherrer pattern is shown Fig. 2.12.a in which the centre of the rings has been identified and marked with a white cross. Azimuthal integration of this pattern has been performed with an angular width of 5° in order to form a spectrum with 72 rows (in which each corresponds to a different azimuthal angle, as shown in Fig. 2.12.b) using Fit2D

[14]. One row from Fig. 2.12.b has been extracted and shown in Fig. 2.12.c, this is known as an angle-dispersive diffraction pattern line profile. It should be noted here that the horizontal axis of the line profile is diffraction angle 2θ, which is converted from pixels positions (r) via a geometric relationship (see Fig. 2.9). The conversion is given by,

$$2\theta = \arctan\frac{r}{D} \qquad \text{(Eq. 2.7)}$$

where 2θ is the diffraction angle, r is the distance from a pixel to the origins of Debye-Scherrer rings and D is the sample to detector distance.

Similar to angle-dispersive diffraction pattern line profiles, an energy-dispersive point detector records the relationship between diffraction intensity and beam energy. This diffraction pattern is called **energy-dispersive diffraction pattern line profile**. The only difference between these two types of line profile is the units of the horizontal axis and therefore the fitting strategies are more or less similar. Below we present the fitting methods used to analyse an angle-dispersive diffraction line profile.

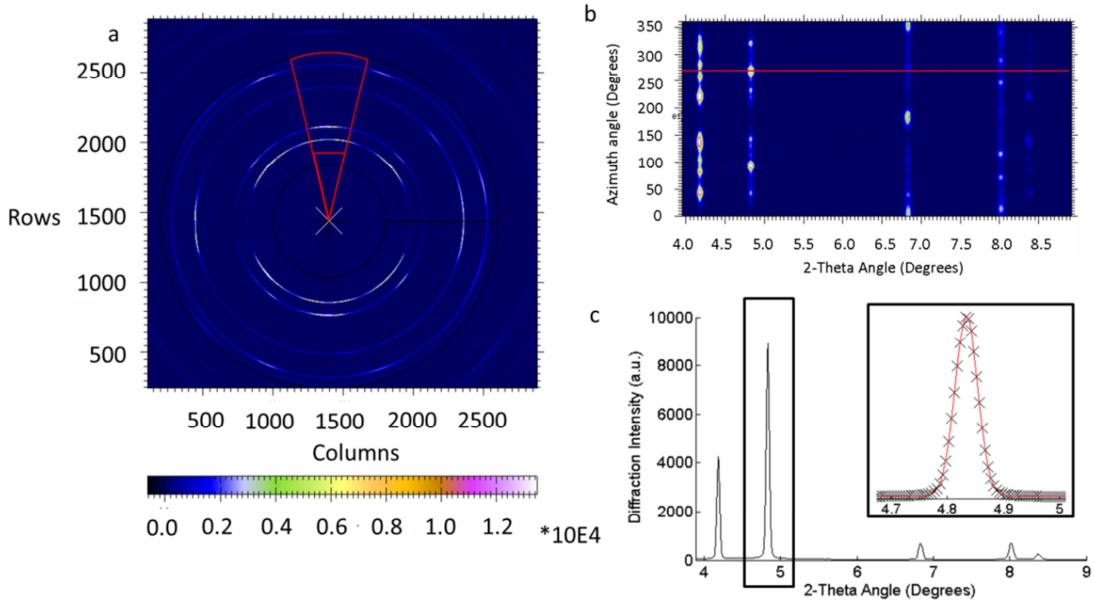

Fig. 2.12 a) A raw Debye-Scherrer diffraction pattern, b) the "caked" diffraction pattern re-plotted as a function of two angular coordinates, c) Single peak fitting applied to the equivalent 1D profile extracted along the red line shown in (b)

2.4.2 Single peak fitting

Several diffraction peaks are seen on the line profile in Fig. 2.12.c. Depending on the exact peak shape, they can be approximated by either symmetric peak functions, for example a Gaussian function, or non-symmetric peak function, for example split-Gaussian function. Here we use a Gaussian function to fit one of the peaks in Fig. 2.12.c.

A Gaussian function for angle-dispersive diffraction peak is given by,

$$I(2\theta) = I_0 + I_{\max} \exp\left(\frac{-(2\theta - 2\theta_0)^2}{2\sigma^2}\right) \qquad \text{(Eq. 2.8)}$$

where $I(2\theta)$ is diffraction intensity at a particular diffraction angle 2θ, I_0 is the average background intensity, $I_{\max}$ is the maximum diffraction intensity of a peak, $2\theta_0$ is the peak centre corresponding to the maximum diffraction intensity $I_{\max}$ and σ is full-width-at-half-maximum (FWHM) of a peak. The integrated intensity (I_{tot}) for such a function is given by,

$$I_{tot} = \int_{-\infty}^{\infty} I_{\max} \exp\left(\frac{-(2\theta - 2\theta_0)^2}{2\sigma^2}\right) d2\theta = I_{\max}\sigma\sqrt{2\pi} \qquad \text{(Eq. 2.9)}$$

The peak centre ($2\theta_0$) and integrated intensity (I_{tot}) can be used to compute engineering strain and quantitative texture information, respectively. A least square fitting method is used to optimize the parameters in Eq. 2.8 by reducing the error between the experimental data and the Gaussian profile predicted.

A line profile is a complicated convolution of many diffraction factors such as, lattice constant (rather than several "independent" *d*-spacings), atomic positions and temperature factors. Full pattern analysis in which all the peaks in a spectrum are simultaneously fitted is often a better approach than single peak fitting (in order to retrieve more information).

2.4.3 Full pattern analysis

Rietveld refinement [15], the first example of this type of approach, considers all possible parameters affecting diffraction intensity in a line profile. For example the Rietveld refinement package MAUD [16] considers angle-dispersive diffraction intensity's mathematical function as,

$$I_i^{calc} = S_F \sum_k L_k \left|F_k\right|^2 S(2\theta_i - 2\theta_k) P_k A + I_i^b \qquad \text{(Eq. 2.10)}$$

where I_i^{calc} is the predicted intensity at a space position *i*, S_F is a scale factor, L_k is Lorentz polarization factor, $S(2\theta_i - 2\theta_k)$ is the peak profile function (for instance a Gaussian function or Voigot function), P_k is a preferred orientation function, *A* is the absorption factor and I_i^b is the background scattering at the space position.

A least squares method can be used to optimize the parameters in Eq. 2.10. However, the number of parameters involved in the optimisation means that this process is much more complex than that of single peak fitting. Therefore, advanced optimization methods, for example, modified least squares, maximum entropy and Monte Carlo methods, are often used in order to achieve convergence more quickly and accurately. Despite the presence of all these advanced tools, time and user experience are still the most important factors to achieve a good match using Rietveld refinement. Furthermore, the fitting strongly relies on manual adjustment and therefore it is impossible to do batch-processing using this approach.

If a more approximate fitting solution is required, for example, the evaluation of the lattice parameter, Pawley refinement [17], can be used as a "weak version" of Rietveld refinement. This approach is recommended when dealing with large amounts of data in batch-processing regime. The main difference between Pawley and Rietveld refinement is that Pawley refinement allows peak intensity to vary freely, whereas peak intensity is strictly dictated by certain parameters in Rietveld refinement. For example, in Pawley refinement,

angle-dispersive powder diffraction profiles could be fitted with only the following parameters: Intensity of each reflection with indices *hkl* - $I(hkl)$, unit-cell metric tensor parameters - *A,B,C,D,E,F*, instrumental zero error - $2\theta_{zero}$ and peak-width parameters - *U,V,W*. Fig. 2.13 shows an example of Pawley refinement for a nickel alloy by GSAS [18] software.

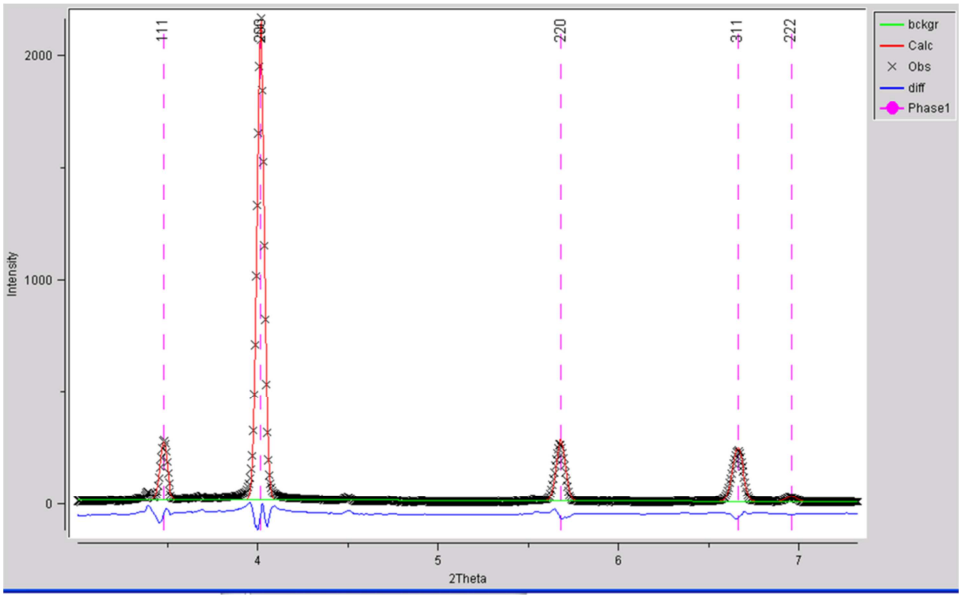

Fig. 2.13 A Pawley fitting to nickel alloy angle-dispersive line profile.

The motivation to use full pattern analysis in the thesis includes: 1) direct fits to the lattice parameter rather than *d*-spacing, giving a better averaging approach to lattice strain determination (this offers special advantages for engineering strain analysis and will be further explained in section **3.4.1**); 2) direct extraction of texture information from Rietveld refinement (detailed discussion given in section **3.9.2**).

Chapter 3 Powder diffraction in stress and texture analysis

This chapter introduces the applications of diffraction techniques (chapter 2) to study stress and texture in polycrystalline materials. The applications of these techniques to tackling several practical problems are presented in the parts of this thesis (**chapters 5 to 7**) devoted to the experimental results. The structure of this chapter is:

1) S**ection 3.1 to 3.5:** Powder diffraction in stress analysis.
2) S**ection 3.6 to 3.9:** Powder diffraction in texture analysis.

3.1 Advantages of diffraction stress measurements

The advantages of using (powder) diffraction techniques to study stress within crystalline materials in comparison to other measurement techniques are:

1) They are truly non-destructive. This feature makes diffraction techniques suitable for *in situ* stress characterization whereas destructive methods are only confined to *residual* stress characterization. Destructive methods rely on removing materials from a test piece, and then the difference between the deformation before and after material removal are quantified in order to deduce residual stress. These types of methods include [19]: sectioning, hole drilling, slitting, layer removal, contour method, etc…
2) They can be used to study stress from the surface to the bulk of an engineering component depending on the length scale of interest, size of the beam used, and whether transmission or reflection geometry is used. Strain gauging and optical microscopy methods [20] are also non-destructive stress measurement methods, but can only be used to analyse the stress at the surface of a sample.

3) They measure elastic strain which can be directly used to compute stress. Recently, Digital Volume Correlation (DVC) [21] and Digital Image Correlation (DIC) methods have been developed to extract strain information from 3D tomographic datasets and 2D radiographic images respectively. They are also based on non-destructive techniques and can measure bulk strain. However, the strains calculated by these techniques are the sum of elastic and plastic strains, and these total strains cannot be directly used for stress calculation.

The direct outputs of all the above mentioned methods are strain rather than stress which cannot be directly measured. Stress is computed from elastic strain through Hooke's law (linear stress-strain relationship).

3.2 Stress-strain relationship (Hooke's law)

A complete description of the stress state at a certain point can be given by a second order tensor σ_{ij}, with i,j ranging from 1 to 3. The tensor's graphical description in 3D Cartesian space is shown in Fig. 3.1.

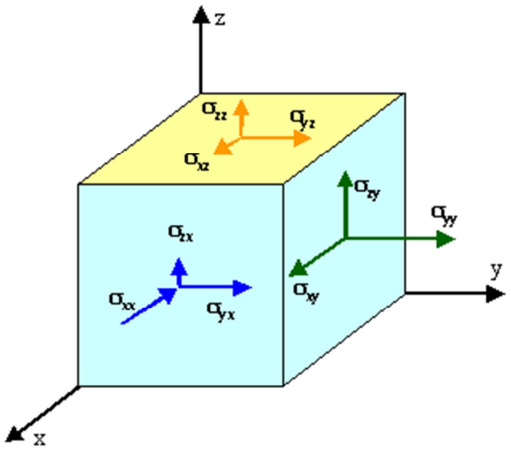

Fig. 3.1 Stress tensor in 3D space.

This tensor is symmetric:

$$\sigma_{ij} = \sigma_{ji} \qquad \text{(Eq. 3.1)}$$

Hence, there are only six independent elements in a stress tensor: three diagonal ones and three non-diagonal ones. The elastic strain state at a certain point can be defined in a similar way as to the stress state a second order tensor ε_{ij}^{e}. This tensor also has diagonal symmetry (Eq. 3.1). **Hooke's law** states that each stress element is given by a linear combination of every elastic strain element, and this relationship is written as,

$$\sigma_{ij} = C_{ijkl}\varepsilon_{kl}^{e} \qquad \text{(Eq. 3.2)}$$

Here the linear coefficients (C_{ijkl}) form a fourth order tensor, the so-called stiffness tensor. Eq. 3.2 can also be expressed in terms of elastic compliance tensor (**S**),

$$\varepsilon_{ij} = C_{ijkl}^{-1}\sigma_{kl} = S_{ijkl}\sigma_{kl} \qquad \text{(Eq. 3.3)}$$

According to diagonal symmetries of stress and strain tensors, both the stiffness and compliance tensors have the following symmetry,

$$A_{ijkl} = A_{jikl} = A_{ijlk} \qquad \text{(Eq. 3.4)}$$

Here tensor **A** can be either the stiffness tensor (**C**) or compliance tensor (**S**).

Next, Voigt notation is used to rewrite Hooke's law for simplicity. The second order (stress and strain) tensors are represented by a vector. For example, the stress vector is written as,

$$\boldsymbol{\sigma} = \begin{bmatrix} \sigma_{11} & \sigma_{22} & \sigma_{33} & \sigma_{23} & \sigma_{13} & \sigma_{12} \end{bmatrix}^{T} \qquad \text{(Eq. 3.5)}$$

The vector of strain tensor can be written in the similar way. Under Voigt notation a stiffness four order tensor can be reduced to a 6×6 matrix, and Hooke's law is then given by,

$$\begin{bmatrix}\sigma_{11}\\ \sigma_{22}\\ \sigma_{33}\\ \sigma_{23}\\ \sigma_{13}\\ \sigma_{12}\end{bmatrix}=\begin{bmatrix}C_{11} & C_{12} & C_{13} & C_{14} & C_{15} & C_{16}\\ C_{21} & C_{22} & C_{23} & C_{24} & C_{25} & C_{26}\\ C_{31} & C_{32} & C_{33} & C_{34} & C_{35} & C_{36}\\ C_{41} & C_{42} & C_{43} & C_{44} & C_{45} & C_{45}\\ C_{51} & C_{52} & C_{53} & C_{54} & C_{55} & C_{56}\\ C_{61} & C_{62} & C_{63} & C_{64} & C_{65} & C_{66}\end{bmatrix}=\begin{bmatrix}\varepsilon_{11}\\ \varepsilon_{22}\\ \varepsilon_{33}\\ \varepsilon_{23}\\ \varepsilon_{13}\\ \varepsilon_{12}\end{bmatrix} \quad \text{(Eq. 3.6)}$$

Here a stiffness matrix element C_{mn} (m, n ranging from 1 to 6) is converted from a corresponding stiffness tensor element C_{ijkl} (i, j, k, l ranging from 1 to 3) by following such a rule: ij or $kl \rightarrow m$ or n. For example, 11→1, 22→2, 33→3, 23→4, 13→5, 12→6. A detailed analysis of this transformation is given in [22]. The number of unknown elements in stiffness matrix C_{mn} can be reduced and some widely used reduction considerations are presented below.

3.2.1 Three-dimensional isotropic Hooke's law

The stress-strain relationship for an isotropic and linearly elastic solid is written as [23],

$$\begin{bmatrix}\sigma_{11}\\ \sigma_{22}\\ \sigma_{33}\\ \sigma_{12}\\ \sigma_{13}\\ \sigma_{23}\end{bmatrix}=\frac{E}{(1+\nu)(1-2\nu)}\begin{bmatrix}1-\nu & \nu & \nu & 0 & 0 & 0\\ \nu & 1-\nu & \nu & 0 & 0 & 0\\ \nu & \nu & 1-\nu & 0 & 0 & 0\\ 0 & 0 & 0 & 1-2\nu & 0 & 0\\ 0 & 0 & 0 & 0 & 1-2\nu & 0\\ 0 & 0 & 0 & 0 & 0 & 1-2\nu\end{bmatrix}=\begin{bmatrix}\varepsilon_{11}\\ \varepsilon_{22}\\ \varepsilon_{33}\\ \varepsilon_{12}\\ \varepsilon_{13}\\ \varepsilon_{23}\end{bmatrix} \quad \text{(Eq. 3.7)}$$

Here all the elements in the stiffness matrix are formed by two independent parameters: isotropic Young's modulus (E) and Poisson's ratio (ν). Table 3.1 lists E and ν of some commonly used non-textured materials.

Table 3.1 Isotropic Young's modulus and Poisson's ratio for some commonly used materials.

Material	Young's Modulus (GPa)	Poisson's ratio (ν)
Tungsten	410	0.30
Alumina	390	0.25
Nickel	215	0.31
Stainless steel	190-200	0.30
Copper	124	0.34
Titanium	116	0.30

3.2.2 Two-dimensional isotropic Hooke's law

If a deformation can be approximated to occur on a 2D plane, the stiffness matrix for an isotropic and linearly elastic solid is much simpler than the one shown in Eq. 3.7. There are two assumptions regarding to plane deformation: 1) Plane strain deformation; 2) Plane stress deformation.

Plane strain deformation referring to the fact that strain components out of *x*-*y* plane are zero,

$$\varepsilon_{13} = \varepsilon_{23} = \varepsilon_{33} = 0 \qquad \text{(Eq. 3.8)}$$

In reality Plane strain deformation is an approximation of such a situation: an object's *z* dimension is much bigger than its *x* and *y* dimensions so that the strain components related to *z* direction can be neglected. Substitute Eq. 3.8 into Eq. 3.7, the Hooke's law for plane strain deformation becomes,

$$\begin{bmatrix}\sigma_{11}\\ \sigma_{22}\\ \sigma_{12}\end{bmatrix}=\frac{E}{(1+\nu)(1-2\nu)}\begin{bmatrix}1-\nu & \nu & 0\\ \nu & 1-\nu & 0\\ 0 & 0 & 1-2\nu\end{bmatrix}\begin{bmatrix}\varepsilon_{11}\\ \varepsilon_{22}\\ \varepsilon_{12}\end{bmatrix} \quad \text{(Eq. 3.9)}$$

$$\sigma_{33}=\frac{E\nu}{(1-2\nu)(1+\nu)}(\varepsilon_{11}+\varepsilon_{22})$$

$$\sigma_{13}=\sigma_{23}=0$$

The second assumption called **plane stress deformation** is made to approximate such a situation: a deformed object has very small *z* dimension compared with the other two (*x* and *y*) dimensions. Under this assumption the stress components out of *x*-*y* plane are zero,

$$\sigma_{33}=\sigma_{13}=\sigma_{23}=0 \quad \text{(Eq. 3.10)}$$

Accordingly the stress-strain relationship is given by,

$$\begin{bmatrix}\sigma_{11}\\ \sigma_{22}\\ \sigma_{12}\end{bmatrix}=\frac{E}{(1-\nu^2)}\begin{bmatrix}1 & \nu & 0\\ \nu & 1 & 0\\ 0 & 0 & 1-\nu\end{bmatrix}\begin{bmatrix}\varepsilon_{11}\\ \varepsilon_{22}\\ \varepsilon_{12}\end{bmatrix} \quad \text{(Eq. 3.11)}$$

$$\varepsilon_{33}=-\frac{\nu}{E}(\sigma_{11}+\sigma_{22})$$

$$\varepsilon_{13}=\varepsilon_{23}=0$$

3.2.3 Three-dimensional Hooke's law in a single crystal

Due to the crystal symmetry many elements in the stiffness matrix of a single crystal must vanish and `some non-zero elements are dependent on other elements. The detailed analysis of how a crystal symmetry affects its stiffness matrix elements is given in [24]. Below the stiffness matrices for cubic and hexagonal crystals are listed, and Table 3.2 and Table 3.3 show the elastic constants for some cubic and hexagonal phase polycrystalline materials that have been studied in the present thesis.

Hooke's law for a cubic crystal:

$$\mathbf{C} = \begin{bmatrix} C_{11} & C_{12} & C_{12} & 0 & 0 & 0 \\ C_{12} & C_{11} & C_{12} & 0 & 0 & 0 \\ C_{12} & C_{12} & C_{11} & 0 & 0 & 0 \\ 0 & 0 & 0 & C_{44} & 0 & 0 \\ 0 & 0 & 0 & 0 & C_{44} & 0 \\ 0 & 0 & 0 & 0 & 0 & C_{44} \end{bmatrix} \quad \text{(Eq. 3.12)}$$

Hooke's law for a hexagonal crystal:

$$\mathbf{C} = \begin{bmatrix} C_{11} & C_{12} & C_{13} & 0 & 0 & 0 \\ C_{12} & C_{11} & C_{13} & 0 & 0 & 0 \\ C_{13} & C_{13} & C_{33} & 0 & 0 & 0 \\ 0 & 0 & 0 & C_{44} & 0 & 0 \\ 0 & 0 & 0 & 0 & C_{44} & 0 \\ 0 & 0 & 0 & 0 & 0 & (C_{11} - C_{12})/2 \end{bmatrix} \quad \text{(Eq. 3.13)}$$

Table 3.2 Elastic constants of some cubic phase metals

Materials	C_{11} (10^{11}N/m^2)	C_{12} (10^{11}N/m^2)	C_{44} (10^{11}N/m^2)	Zener ratio
Aluminium	1.0675	0.6041	0.2834	1.2231
Copper	1.683	1.221	0.757	3.2771
Gold	1.9244	1.6298	0.4200	2.8513
Iron	2.26	1.40	1.16	2.6977
Tungsten	5.2239	2.0437	1.6083	1.0114
Nickel	2.481	1.549	1.242	2.6652

Table 3.3 Elastic constants of some hexagonal phase metals.

Materials	C_{11} (10^{11}N/m^2)	C_{12} (10^{11}N/m^2)	C_{13} (10^{11}N/m^2)	C_{33} (10^{11}N/m^2)	C_{44} (10^{11}N/m^2)
Magnesium	0.5950	0.2612	0.2180	0.6155	0.1635
Titanium	1.6240	0.9200	0.6900	1.8070	0.4670

It should be noted here that the stiffness matrix of a single crystal is orientation dependent. All the matrices and elastic constants showing above are based on the fact that the crystal's coordinates are the same as the lab coordinates. If the orientation of a crystal is known, its stiffness matrix can be calculated by applying a rotation transformation to the stiffness matrix in lab coordinates.

A so called Zener anisotropy factor [25] (the last columns in Table 3.2) is defined for cubic crystal to quantify the degree of elastic anisotropy,

$$A = \frac{2C_{44}}{C_{11} - C_{12}} \qquad \text{(Eq. 3.14)}$$

The stiffness matrix in Eq. 3.12 is equivalent to that in Eq. 3.7 when A is equal to unity. Thus the more A differs from unity, the more elastically anisotropic the material is. For instance, aluminium and tungsten are very close to elastically isotropic as their Zener anisotropy factors are 1.2231 and 1.0114 in Table 3.2.

3.2.4 Three-dimensional Hooke's law in textured materials

A textured polycrystalline aggregate consists of many grains which are characterised by a certain orientation distribution (**section 3.7**) in orientation space. Therefore, the stiffness matrix for a textured polycrystals aggregate should be obtained as an average of the single crystal stiffness matrix over orientation distribution. Here we present three rough but very popular assumptions [22] (Voigt, Reuss and Hill) for the averaging methods.

Voigt assumes that the total strain is uniform within a polycrystal aggregate. Then the overall stiffness matrix is given by,

$$\mathbf{C}^V = \left\langle \mathbf{C}^c \right\rangle \qquad \text{(Eq. 3.15)}$$

Here the superscript *V* is used to denote Voigt uniform strain assumption, the superscript *c* denotes single crystal and the bracket (<>) stands for averaging over grain orientation distribution. The compliance tensor is given by,

$$\mathbf{S}^V = \left\langle \mathbf{S}^{c^{-1}} \right\rangle^{-1} \quad \text{(Eq. 3.16)}$$

The stiffness tensor calculated this way corresponds to **upper bound** average.

Reuss assumes that the total stress instead of strain is uniform in an aggregate. This is for the calculation of **lower bound** average moduli tensor. The stiffness and compliance tensors are given by,

$$\mathbf{S}^R = \left\langle \mathbf{S}^c \right\rangle \quad \text{(Eq. 3.17)}$$

$$\mathbf{C}^R = \left\langle \mathbf{C}^{c^{-1}} \right\rangle^{-1} \quad \text{(Eq. 3.18)}$$

Hill [26] suggests using the arithmetic mean of Voigt and Reuss elastic tensor as a more reasonable estimate of a real case,

$$\mathbf{C}^H = \frac{1}{2}[\left\langle \mathbf{C}^c \right\rangle + \left\langle \mathbf{C}^{c^{-1}} \right\rangle^{-1}] \quad \text{(Eq. 3.19)}$$

$$\mathbf{S}^H = \frac{1}{2}[\left\langle \mathbf{S}^c \right\rangle + \left\langle \mathbf{S}^{c^{-1}} \right\rangle^{-1}] \quad \text{(Eq. 3.20)}$$

3.3 Strain at different length scales

Depending on the length scale of interest, stress and strain in polycrystals materials are often divided into three types [27]:

1) Macro level (illustrated in Fig. 3.2.a): The measured dimension for strain calculation is often larger than millimetres. For instance, the strain measured by conventional strain gauge is a type of macro strain.

2) Meso level (illustrated in Fig. 3.2.b and c): The measured dimension for strain calculation is of the order of hundreds of microns. The measured region often covers thousands of grains, satisfying powder diffraction condition.

3) Micro level (illustrated in Fig. 3.2.c): The measured dimension for strain calculation is smaller than a single grain's dimension (~microns). Strain at this level is often measured by single crystal diffraction.

We use Fig. 3.2 to explain the difference between the three types of strains as well as their measurement techniques below.

3.3.1 Macro level strain

In Fig. 3.2.a a strain gauge is attached to the dog-bone sample's surface to measure its strain due to the applied tensile stress. The strain gauge covers a length of a few millimetres, so that the measured strain corresponds to the average over the gauge length.

3.3.2 Meso level strain

In Fig. 3.2.b a diffraction gauge volume the dog-bone sample is schematically illustrated. Debye-Scherrer diffraction setup (section 2.3) is used to measure the strain that arises in response to the external load within the volume from which the scattering signal is collected (by analogy, this is called the "gauge volume"). When X-ray beam cross-sections vary between 10-1000 μm, the measured strain is a type of meso level strain. Since strain is a directional property, it is important to illustrate (see below) how to determine the magnitude and the direction of this meso level strain.

The formation of Debye-Scherrer pattern from X-ray scattering in the gauge volume is illustrated schematically in Fig. 3.2.b. For the scattered beam direction identified by the solid (red) arrow, the collected diffraction signals come only from the red highlighted grains

(solid sphere markers) that correspond to less than 10 % of the entire gauge volume. A diffraction peak can be extracted from the pixel intensity data using the processing method shown in section 2.4.1. **Single peak fitting** (section 2.4.2) is then used to determine precisely the peak's diffraction angle ($2\theta_0$). It is commonly believed that $2\theta_0$ is related to the average lattice spacing of the corresponding lattice planes {*hkl*} through Bragg's law. This average effect is used as a key postulate in the strain tomography method [28]. A numerical analysis will be presented in **section 5.1** to confirm this postulate. The magnitude of strain related to the average lattice spacing of the solid grains is given by,

$$\varepsilon_{hkl} = \frac{d_{hkl} - d^0_{hkl}}{d^0_{hkl}} \qquad \text{(Eq. 3.21)}$$

where ε_{hkl} is the lattice strain related to the {*hkl*} planes of the solid grains, d^0_{hkl} and d_{hkl} are the unreformed and deformed lattice spacing calculated via Bragg's law from the diffraction peaks of the solid grains.

In order to illustrate the direction of the lattice strain, the geometry of Bragg diffraction for a single solid grain is shown in Fig. 3.2.c. The calculated lattice spacing is the distance between the grain's {*hkl*} planes, whose normal (***n***) has angle θ against the loading direction (Y axis). If high energy (>50 KeV) X-ray beam is used in this measurement, the diffraction angle (2θ) will be very small (<10°). Consequently, the scattering vector has less than 5° angle against the loading direction and the measured solid grain's lattice spacing can be thought of approximately as corresponding to the loading direction.

However, the average lattice strain of the solid grains is not representative enough to the average strain of the whole diffraction volume because of two reasons: 1) the solid grains only occupy 10% of volume of the gauge volume; 2) stress and strain inhomogeneity usually

exists in a polycrystals gauge volume. If only the lattice strain calculated from a single diffraction peak based on single peak fitting were used, this would result in erroneous evaluation of the strain for polycrystal aggregate (meso level strain). In order to get better strain accuracy at this level, one can include more grains (for example, the blue and green grains in Fig. 3.2.b) into strain averaging. The corresponding average methods are introduced in section 3.4.

3.3.3 Micro level strain

In previous section, it is concluded that the calculated strain using single diffraction peak information is an average effect of all the solid grains. In order to resolve the strain distribution within a single grain or a polycrystal aggregate, smaller beam size *i.e.* single crystal diffraction methods have to be used. For example EBSD [29], Laue diffraction [30] and Transmission Electron Microscopy (TEM) [31], are often seen in the literature as suitable to study strain at micro level.

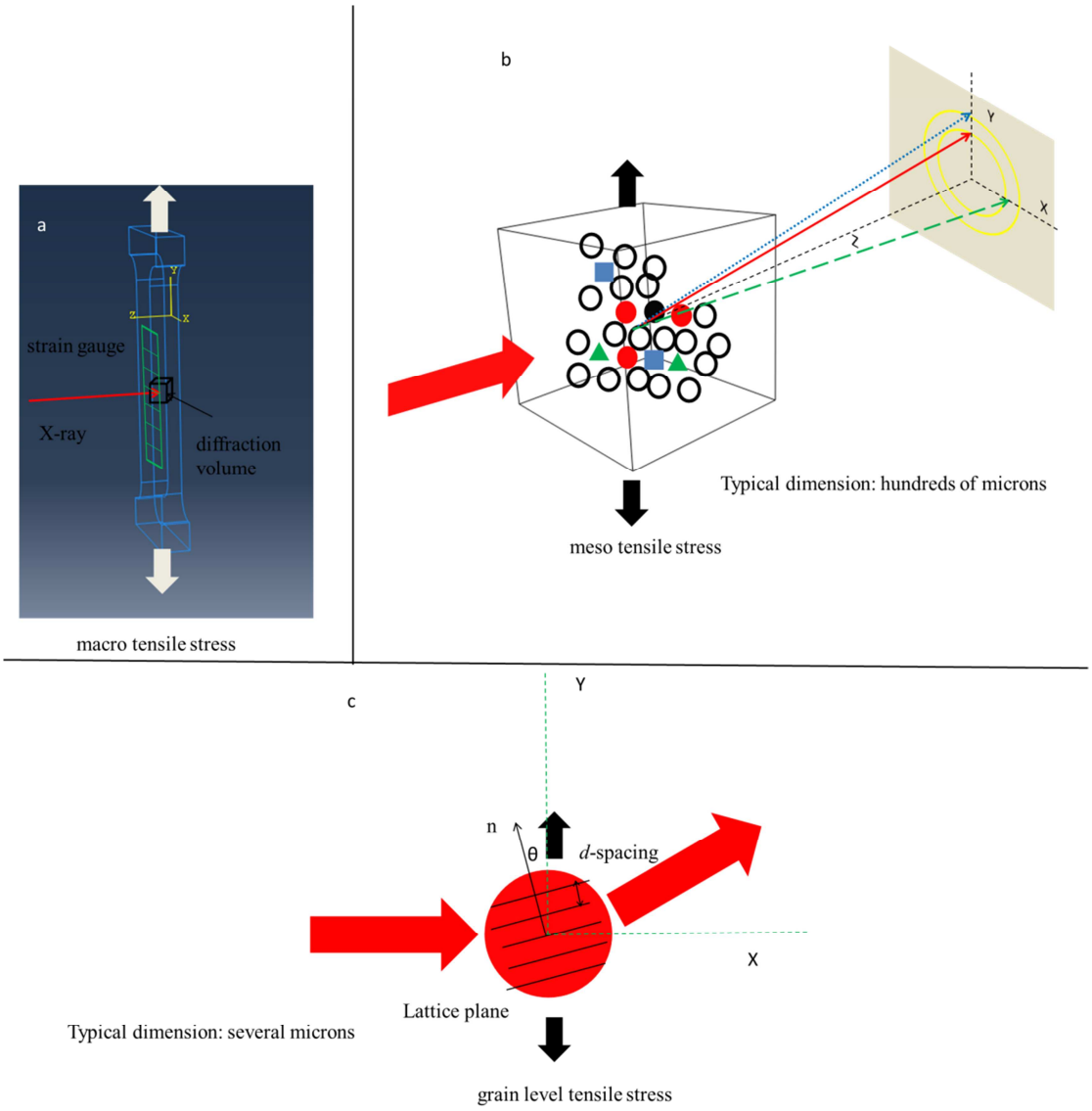

Fig. 3.2 Strain in macro level (a); meso level (b); micro level (c).

3.4 Strain averaging in powder diffraction

3.4.1 Strain average on a line profile

One strain averaging approach in powder diffraction is to consider a line profile rather than a single *hkl* peak (section 3.3.2). For instance, the line profile caked along Y direction in Fig. 3.2.b is used for strain calculation in this section. This line profile contains two diffraction peaks, referring to solid sphere (red) and solid squared (blue) grains. **Full pattern analysis** (section 2.3.3) is performed to the line profile to determine the lattice constant (*a*) of

the cubic polycrystals rather than a d_{hkl} for a particular peak by single peak fitting. By this way the contributions in strain from both red and blue grains are considered. The more diffraction peaks within a diffraction line profile are considered in full pattern analysis, the better the average becomes. The averaged strain out of full pattern analysis is given by,

$$\varepsilon_a = \frac{a - a_0}{a_0} \qquad \text{(Eq. 3.22)}$$

where ε_a is the lattice strain related to lattice constant a, a_0 is the unreformed lattice spacing and a is the deformed lattice spacing.

In **section 5.2**, full pattern analysis will be used to fit energy-dispersive diffraction pattern line profiles for strain measurement. The fitting procedure mainly relies on Pawley refinement (section 2.4.3) implemented into GSAS software. A Matlab code [32] was written to automate the batch-processing for dealing with large amounts of data. Based on this work Zhang [33] developed peak width analysis in order to cope with plastic deformation effect. The method developed by Zhang is used exclusively in the thesis to analyse energy-dispersive diffraction data.

3.4.2 Strain average over a 2D Debye-Scherrer diffraction pattern

In this section, a more advanced method for strain averaging is presented by including more radial line profiles rather a single line profile on a Debye-Scherrer diffraction patterns into strain computation. In Fig. 3.2.b the green grain which also diffracts the beam onto the detector. However, its strain is not considered in section 3.4.1 because its signal is collected by some pixels at X axis on the detector. If the line profile along X axis, for example including the triangular (green) grain, and other radial line profiles are considered in strain calculation, it is surely that a much better average over the gauge will be achieved than only

considering a single line profile. Below we present such a method based on strain tensor transformation.

The relationship between strain tensors in two different coordinates is given by,

$$\varepsilon_{ij}^{'} = \mathbb{R}_{im}\mathbb{R}_{jn}\varepsilon_{mn} \qquad \text{(Eq. 3.23)}$$

where ε_{ij} is strain components in a reference coordinate, $\varepsilon_{mn}^{'}$ is the strain components in a local coordinate and $\mathbb{R}$ is a rotation matrix.

Each diffraction line profile refers to a lattice strain along the radial direction at a specific azimuthal angle, and this strain can be written as $\varepsilon_{\alpha\alpha}$ (α stands for the azimuthal angle of a line profile). For the radial strains measured by a Deybe-Scherrer setup, the transformation between strain tensors is a 2D problem. Thus we only consider four elements on X-Y plane in a strain tensor,

$$\boldsymbol{\varepsilon} = \begin{bmatrix} \varepsilon_{\alpha\alpha} & \varepsilon_{\alpha t} \\ \varepsilon_{t\alpha} & \varepsilon_{tt} \end{bmatrix} \qquad \text{(Eq. 3.24)}$$

where ε_{tt} is the normal strain perpendicular to $\varepsilon_{\alpha\alpha}$, $\varepsilon_{\alpha t}$ and $\varepsilon_{t\alpha}$ are the shear components.

The 2D rotation matrix is written as,

$$\mathbf{R} = \begin{bmatrix} \cos\alpha & -\sin\alpha \\ \sin\alpha & \cos\alpha \end{bmatrix} \qquad \text{(Eq. 3.25)}$$

where α stands for the azimuthal angle of the line profile.

Using Eq. 3.23, the relationship between any radial strains and the principal strains on X-Y plane can be written as,

$$\varepsilon_{\alpha\alpha} = \cos^2(\alpha - \alpha_0) \times \varepsilon_1 + \sin^2(\alpha - \alpha_0) \times \varepsilon_2 \qquad \text{(Eq. 3.26)}$$

Here ε_1 and ε_2 are two principal radial strains on the X-Y plane, and they refers to a specific situation that no shear strains exists at a particular angle α_0.

The unknown three parameters (ε_1, ε_2 and α_0) in Eq. 3.26 can be determined from many measured radial strains $\varepsilon_{\alpha\alpha}$ by using least square fitting. Thus the equation suggests a way to correlate all the azimuthally binned line profiles. This also sheds light on how to measure principal strains within a 2D plane. Korsunsky et al [34] used this technique to evaluate 2D strain state from synchrotron x-ray Debye-Scherrer diffraction data. In section 5.2, this technique is applied to analyse multi-element energy-dispersive x-ray diffraction data for principal strain determination.

3.5 Elastic and plastic strains in powder diffraction

The red grain is under a tensile deformation in Fig. 3.2.c, and its lattice expands in response to the load before the lattice reaches its elastic limit. Once the lattice reaches elastic limit, its lattice spacing cannot be changed anymore even the load is still increased. Therefore, lattice strain measured through Bragg's law only represents the elastic response to the load *i.e.* **elastic strain**, which can be readily used to compute stress. This is often regarded as a major advantage for strain measurement by diffraction techniques.

However, it does not mean that powder diffraction technique cannot be used for plastic strain determination. Once a polycrystals aggregate starts to be deformed plastically, some of the grains would reach their elastic limit and some remain elastic since there is always a stress inhomogeneity inside the aggregate. Dislocations and voids are moved to the grains which have reached their elastic limit in order to accommodate the plastic shape

change for the aggregate. At the same time part of the load on the yield grains is transferred onto those elastically deformed grains [35]. The dislocations and voids inside an aggregate cause powder diffraction peaks broad and asymmetric. A few functions [36, 37] have been proposed to quantify these broadening and asymmetry affects in order to compute plastic strain. In the present thesis the effect of plastic strain is not discussed in later chapters.

3.6 Introduction of texture analysis by diffraction methods

Crystallographic texture [38] is defined as the *lattice preferred orientation* in a polycrystals aggregate. Another type of texture, *shape preferred orientation*, also exists in crystalline materials. For instance, the fibre shape in fibre-reinforced materials is one of the *shape preferred orientations*. Optical methods have been used to determine both types of preferred orientations [39]. The methods mainly rely on advanced light microscopies to capture images on the surface of a sample, and then computer-aid image analysis are used to quantitatively determine those preferred orientations.

Today diffraction techniques are mainly used to determine crystallographic preferred orientation, exclusively referred to as **texture** in the thesis. Similar to the usage of diffraction techniques in strain measurement, there are also two distinct methods for texture studies depending on the relationship between a gauge volume's size and grain's size: single crystal diffraction and powder diffraction. These two methods' applications are introduced in sections 3.8.1 and 3.8.2 respectively.

3.7 Basic concepts in texture study

3.7.1 Orientation

The unit cell is the simplest repeatable unit in a crystal (grain). Here a grain's orientation is treated as its unit cell's orientation. Fig. 3.3 shows a cubic unit cell with an orientation under lab coordinates. A rotation matrix can be used to transform reference coordinates (lab coordinates) to a specific orientation (crystal coordinates),

$$\mathbf{x}_j^{'} = \mathbb{R}_{ji}\mathbf{x}_i \qquad \text{(Eq. 3.27)}$$

where $\mathbf{x}_i$ is a basis vector of lab coordinates, $\mathbf{x}_j^{'}$ is a basis vector of crystal coordinates and $\mathbb{R}_{ji}$ is an element of a rotation matrix. In this thesis an orientation always refers a particular rotation matrix $\mathbb{R}$.

A rotation matrix has only three independent components that are often referred as three Euler angles. Depending on the chosen rotation axis, rotation matrices for a particular rotation angle (θ) are written as,

$$R_x(\theta) = \begin{bmatrix} 1 & 0 & 0 \\ 0 & \cos\theta & -\sin\theta \\ 0 & \sin\theta & \cos\theta \end{bmatrix} \qquad \text{(Eq. 3.28)}$$

$$R_y(\theta) = \begin{bmatrix} \cos\theta & 0 & \sin\theta \\ 0 & 1 & 0 \\ -\sin\theta & 0 & \cos\theta \end{bmatrix} \qquad \text{(Eq. 3.29)}$$

$$R_z(\theta) = \begin{bmatrix} \cos\theta & -\sin\theta & 0 \\ \sin\theta & \cos\theta & 0 \\ 0 & 0 & 1 \end{bmatrix} \qquad \text{(Eq. 3.30)}$$

Here *x*, *y* and *z* are the rotation axe of Euler rotations and θ is the rotation angle.

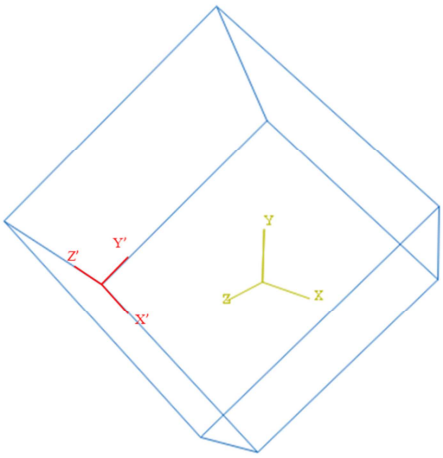

Fig. 3.3 Unit cell with an orientation under lab coordinates.

Any orientation can be constructed by three Euler angles, and its rotation matrix is the dot product of three rotation matrices given by Eqs. 3.28-3.30. Several Euler angle conventions are widely used in texture study, and they are listed in Table 3.4. For instance, a rotation matrix of Bunge convention is constructed by,

$$R_{bunge}(\varphi_1, \Phi, \varphi_2) = R_z(\varphi_1) \bullet R_x(\Phi) \bullet R_z(\varphi_2) \qquad \text{(Eq. 3.31)}$$

Table 3.4 Euler angle conventions.

Euler convention	1st angle (Z axis)	2nd angle	3rd angle (Z axis)	The rotation axis for the 2nd angle
Kocks(symmetric)	Ψ	Θ	φ	Y
Bunge	φ_1-π/2	Φ	π/2- φ_2	X
Matthies	α	β	π-γ	Y
Roe	Ψ	Θ	π- Φ	Y

Orientation of a crystal is a 3D concept and is difficult to visualize. Instead, the relationship between several directions under the crystal's coordinates and a lab coordinates

are studied. Those relationships are projected onto a 2D plane for visualization purpose. The projections are divided as **pole figure** (section 3.7.2) and **inverse pole figure (3.7.3)** depending on whether the reference coordinates is lab coordinates or crystal coordinates, respectively.

3.7.2 Visualization of crystal directions (pole figure)

In this section an example (see Fig. 3.4) is used to illustrate the formation of *100* and *111* pole figures for a particular orientation ($\varphi_1, \Phi, \varphi_2$) of a cubic crystal. Some commonly used notations in texture studies are used here: Rolling direction (RD), Transverse direction (TD) and Normal direction (ND) of sample coordinates refer to X, Y and Z directions in lab coordinates respectively.

An *hkl* pole figure is constructed by projecting plane normal <*hkl*> of a unit cell onto a 2D plane constructed by two perpendicular lab basis vectors (TD and RD in Fig. 3.4). Crystal planes normal <*100*> and <*111*> under lab coordinates of are written as,

$$Pole_{100} = R_{bunge}(\varphi_1, \Phi, \varphi_2) \bullet Miller(1,0,0) \qquad \text{(Eq. 3.32)}$$
$$Pole_{111} = R_{bunge}(\varphi_1, \Phi, \varphi_2) \bullet Miller(1,1,1)$$

Here $Pole_{100}$ and $Pole_{111}$ are vectors under lab coordinates referring to crystal planes normal <100> and <111> respectively. It should be noted here that a crystal direction under lab cooridnates is called a **pole**. $R_{bunge}(\varphi_1, \Phi, \varphi_2)$ is a rotation matrix in Bunge convention, and $Miller(1,0,0)$ and $Miller(1,1,1)$ are crystal planes normal <100> and <111> under crystals coordinates respectively.

Crystal planes normals <100> and <111> are axes with 3-fold and 4-fold symmetry respectively so that there are 3 and 4 *100* and *111*'s poles for a cubic crystal (3 and 4 red lines shown in Fig. 3.4.*a* and *c*) respectively. A unit sphere with the origin coinciding with the centre of the unit cell is drawn. The *100* and *111*'s poles (red lines) intersect the sphere's

surface to form 3 and 4 points on one half of the sphere's surface, respectively. Grey lines are drawn to connect the South Pole (negative ND) and the points on the upper (North) hemisphere. Those grey lines intersect the equator plane (consisting of RD and TD) to form 3 and 4 yellow points for *100* and *111*'s poles (see Fig. 3.4.*b* and *d*) respectively. Fig. 3.4.*b* and *d* are the *100* and *111* **pole figures** for this particular orientation of cubic crystal respectively. The above projection procedure is a so called **stereographic projection** by which a pole in a space is converted into a point on a plane.

3.7.2.1 Stereographic projection

The mathematical relationship between a pole under 3D Cartesian coordinates and its projection under polar coordinates (azimuthal angle α and polar distance ρ) is introduced in this section. The notations of polar coordinates are: 1) RD is defined as 0^o azimuthal angle, and an azimuthal angle increases as it rotates counterclockwise around ND. 2) The unit of polar distance is defined to be degree (°), and its boundary is defined to be 90^o.

The projections are divided into two steps: 1) convert a pole from Cartesian coordinates to spherical coordinates; 2) project the pole from spherical coordinates into polar coordinates.

In the first step a *hkl* pole is transformed from 3D Cartesian coordinates $Pole_{hkl}(x, y, z)$ into 3D spherical coordinates $Pole_{hkl}(\alpha, \varphi, r)$. The following spherical coordinate's notations are defined: α is the same azimuthal angle as in 2D polar coordinates, φ is the inclination angle between a pole and Y axis (TD) and r (r is unity for a unit sphere) is the length of the pole. The relationship between $Pole_{hkl}(x, y, z)$ and $Pole_{hkl}(\alpha, \varphi, r)$ is given by,

$$Pole_{hkl}(\alpha) = \arctan\frac{y}{x}$$
$$Pole_{hkl}(\varphi) = \arccos\frac{z}{r}$$
$$Pole_{hkl}(r) = 1 \qquad \text{(Eq. 3.33)}$$

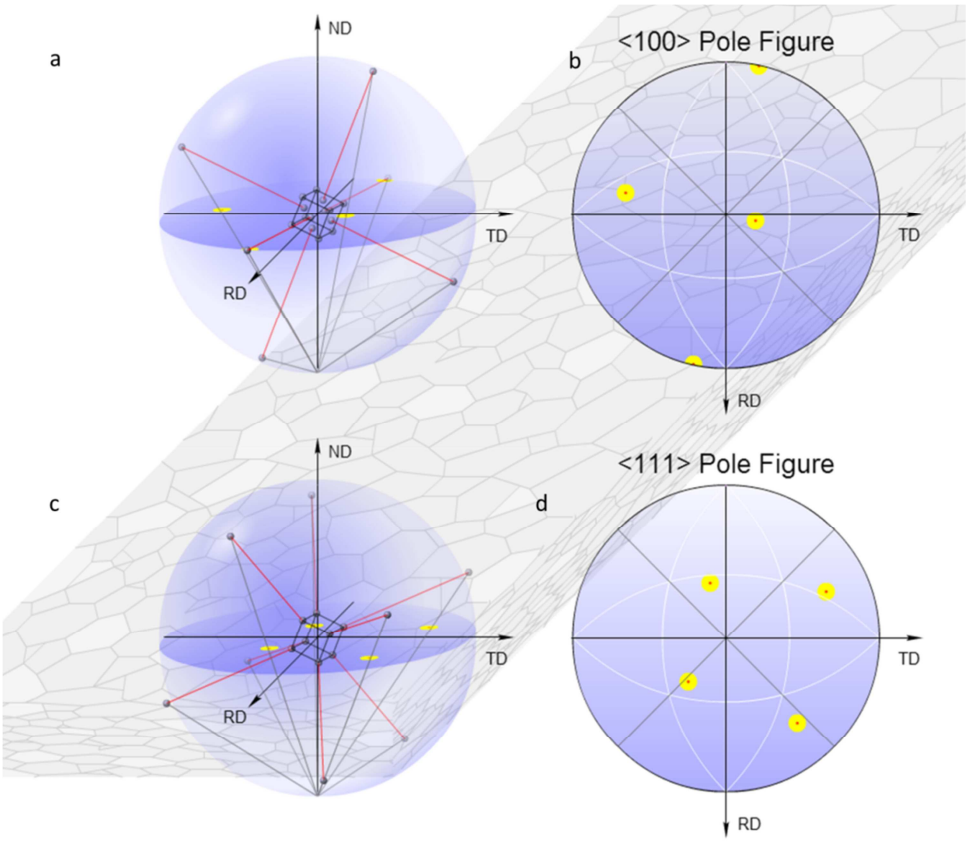

Fig. 3.4 (a) plane normal <100> and unit sphere, (b) *100* pole figure, (c) plane normal <111> and unit sphere and (d) *111* pole figure.

In the second step the pole's polar coordinates is converted from its spherical coordinates. As shown in Fig. 3.4 the azimuthal angle of a pole is not changed before and after projection:

$$\alpha_{polar} = \alpha_{sphere} \qquad \text{(Eq. 3.34)}$$

The geometric relationship between polar distance ρ in polar coordinates and inclination angle φ in spherical coordinates is shown in Fig. 3.5.a. Here, the projection plane (not shown in Fig. 3.5) is a plane tangent to the North Pole containing a circle radius of 2.

This plane is parallel to the equator plane with circle of radius unity shown in Fig. 3.4. A pole is shown by the green arrow, and its projection length is 2tan(φ/2). A pole has its maximum projection length when φ is equal to 90^o (the pole is pointing to the boundary of North hemisphere), and the corresponding projection length is 2. Since the boundary of a polar distance is defined as 90^o, the normalized polar distance for an angle φ is given by,

$$\rho_{stereo} = \frac{2\tan(\varphi/2)}{2} \times \frac{\pi}{2} = \tan(\varphi/2) \times \frac{\pi}{2} \qquad \text{(Eq. 3.35)}$$

3.7.2.2 Equal area projection

Another commonly used projection method in orientation study is called **equal area projection**. The only difference between it and stereographic projection, in terms of geometric relationship to angle φ, is shown in Fig. 3.5.b. The length of the projection (red arrow) of a pole (green arrow) is equal to the length of the green dash line which is 2sin(φ/2). The maximum of the projection's length is $\sqrt{2}$ when angle φ is equal to 90^o. Thus the normalized polar distance is given by,

$$\rho_{equal} = \frac{2\sin(\varphi/2)}{\sqrt{2}} \times \frac{\pi}{2} = \sin(\varphi/2) \times \frac{\sqrt{2}\pi}{2} \qquad \text{(Eq. 3.36)}$$

The main differences between the two projection methods are [22]: 1) angular relationship of any two lines on a spherical surface is preserved in stereographic projection; 2) The size ratio of two areas is preserved in the equal area projection. These differences give rise to the difference of their usages in orientation or texture study. Stereographic projection is usually used to present angular relationships between grains, and the orientations of individual grains can only be measured by single crystal diffraction methods. Therefore, stereographic projection is often used in presenting results measured by single crystal diffraction methods. For instance, in order to understand the twinning relationship between two grains by using EBSD, the rotation matrix (angular relationship) between the two grains

is the key parameter to be identified. In order to preserve this angular relationship, stereographic projection should be used.

In contrast, equal area projection is preferred in powder diffraction texture analysis. The concept of texture is related to the statistical characteristics of preferred orientations in a polycrystal aggregate. Pole figures allow identifying the preferred directions by correspondence with the regions of highest densities on probability maps in orientation space. Therefore, when it is important to keep the pole density information consistent before and after projection, equal area projection should be used. If stereographic projection is used, pole density around the North Pole will be increased, and respectively decreased after the projection. This will result in erroneous identification of preferred directions from pole figures.

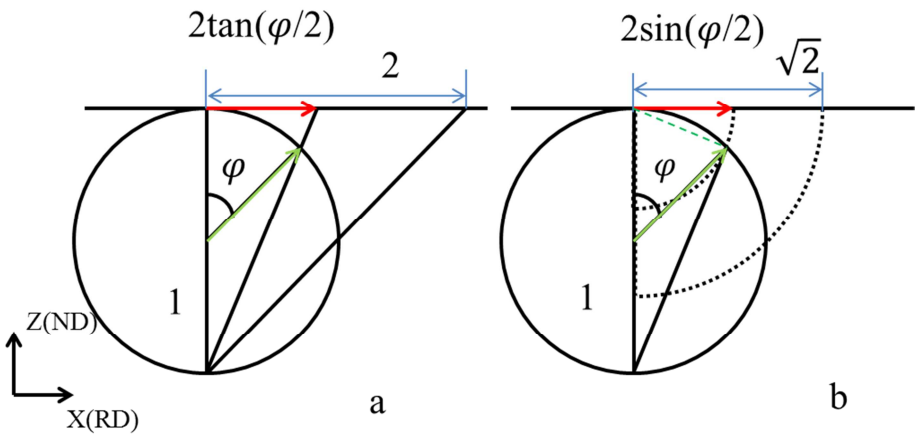

Fig. 3.5 Stereographic projection; (b) equal area projection.

3.7.3 Visualization of lab directions (inverse pole figure)

For constructing an **inverse pole figure** the reference coordinates are crystal coordinates, and a particular direction (usually RD, TD and ND) in lab coordinates is projected onto a plane formed by two crystal directions. The projection methods used in inverse pole figures are the same as in section 3.7.2.1-3.7.2.2 (stereographic and equal area projection). However, the size of the circular 2D projection plane in inverse pole figures is

different as in pole figure. In principle a perfect circular region like the ones in Fig. 3.4.*b* and *d* is needed to represent all possible directions in space. Due to **crystal symmetry**, a single crystal direction [hkl] has many equivalent directions in space. For instance, crystal direction [111] in a cubic crystal has 3 other equivalent directions. Therefore, a smaller region is sufficient to represent all the possible crystal directions in a crystal. For example, the size of a so-called "standard triangle" is shown in Fig. 3.6, which covers all possible crystal directions in a cubic crystal. The higher symmetry a crystal has, the smaller the size of its inverse pole figure is. Similar to this size reduction in inverse pole figure, "**sample symmetry**" also affects the size of a pole figure. For instance, only one quarter of a circular region is needed to present all the directions in space for a sample with orthorhombic symmetry of its texture. However, one should not assume any sample symmetry in any texture characterization experiments in order not to miss any texture information. Sample symmetry is not discussed in all the experimental parts of the thesis.

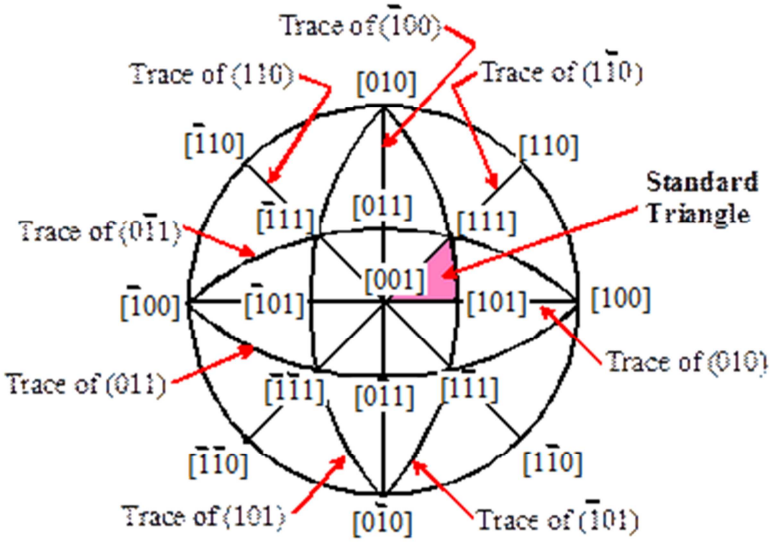

Fig. 3.6 Standard stereographic projection of cubic phase crystal [40].

3.7.4 Visualizations of orientation distribution

Using the pole figure and inverse pole figure constructions are introduced in previous sections. One can only identify *some* preferred crystal orientation directions and *some*

prominent lab directions from ether pole figure or inverse pole figure. However, one direction does not define the orientation of a crystal fully. Thus, for the full description of texture state, the orientation distribution (OD) rather than direction distribution within a polycrystal aggregate is required. In this section several commonly used visualisation methods of ODs are presented.

An orientation space with three Euler angle as ordered basis vectors is often defined to discuss OD became an orientation is fully represented by three Euler angles Fig. 3.7.a shows an OD of a cubic polycrystals aggregate in an orientation space, in which Bunge Euler angle convention is used. It is easier to visualize an OD by its 2D sections (see Fig. 3.7.b), in which an Euler space is sliced along φ_1 directions. The OD's *111* pole figure and x direction of lab coordinates inverse pole figure are shown in Fig. 3.7.c and d, respectively. The mathematical relationship between an OD and its pole figures are mathematically discussed in section 3.9.1.

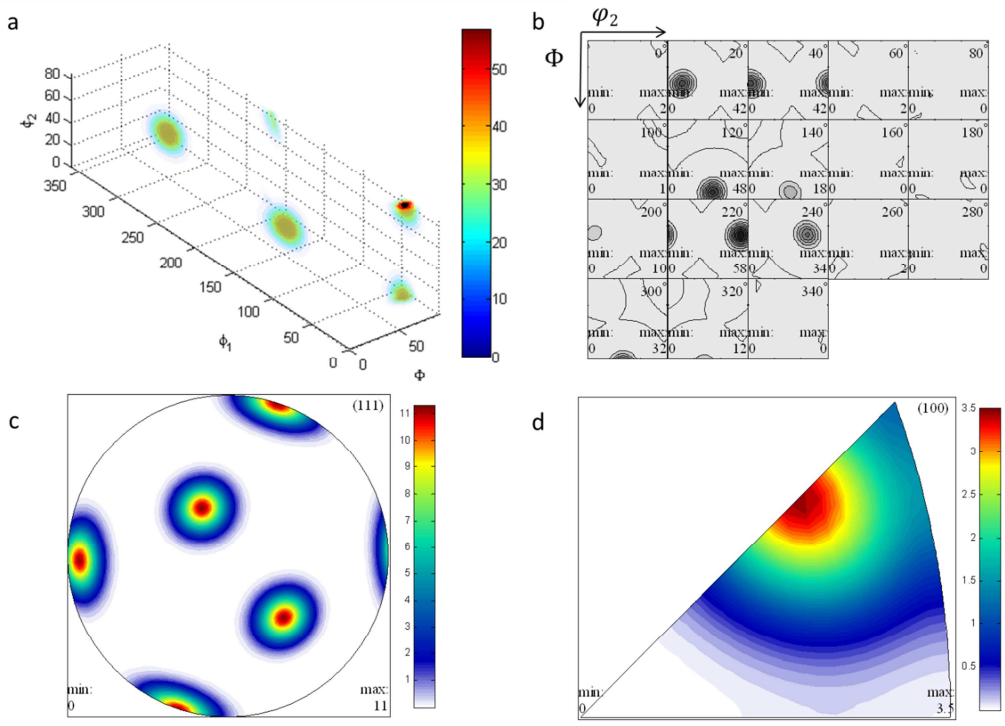

Fig. 3.7 (a) An OD in Euler space; (b) φ_2-Φ sections of the OD; (c) 111 pole figure of the OD; (d) x direction of lab coordinate inverse pole figure of the OD.

3.8 Texture measurement

3.8.1 Orientation determination by single crystal diffraction

Single crystal diffraction techniques, for instance TEM [41], EBSD [42] and x-ray Laue diffraction [43], have been employed to study the orientation of individual grains. As discussed in section 2.3.1, Kikuchi bands are related to certain crystal zone axes in an EBSD study. Crystal zone axis is the key concept in the interpretation of single crystal diffraction patterns. The orientation (three Euler angles) can be directly determined by indexing the zone axes from any (2D) single diffraction pattern. Commercial EBSD and TEM machines usually have powerful Kikuchi patterns indexing software, which can automate orientation determination for a large scanning area. X-MAS (X-Ray Microdiffraction Analysis Software) [44] is often used to index Laue x-ray diffraction patterns for identifying the orientation of the crystal.

3.8.2 Pole figure measurement by powder diffraction

The direct outputs of powder diffraction for texture study are **pole figures** rather than orientations in single crystal diffraction. Advanced algorithms (section 3.9.1) are needed to evaluate the Orientation Distribution Function (ODF), the mathematical function that describes the OD, from the measured pole figures. In this section we introduce several commonly used pole figure measurement methods.

Here we introduce the definition of **pole figure coverage,** a very important concept in powder diffraction texture analysis. It is defined as the coverage of the measured directions in a pole figure (the circular region in Fig. 3.4.*b* and *d*) in a powder diffraction measurement. For a particular measurement, its pole figure coverage does not necessarily need to cover the whole circular region in a pole figure because the unmeasured area in a pole figure can be

reconstructed from the measured area by the advanced ODF conversion algorithms presented in section 3.9. However, the accuracy of the reconstruction of unmeasured area in pole figures and ODF is dictated by the size of the **pole figure coverage**. Therefore, users always try to get the best pole figure coverage in a measurement in order to ensure a good accuracy of the calculated ODF.

3.8.2.1 X-ray pole figure goniometer

X-ray pole figure goniometer was firstly introduced by Schulz et al. [45] for pole figure measurements. It has become a standard piece of equipment for laboratory texture study. A typical setup is shown in Fig. 3.8. Monochromatic x-ray beam is used in this setup. A point detector first performs a 2θ scan to locate the reflection of a set of certain crystal plane {*hkl*}. Then the detector is fixed at that 2θ position. The sample sits on a goniometer which has two rotation axes. One of the rotation axes is the sample's plane normal and the corresponding rotation angle is defined as φ. The other rotation angle is Ψ, which is rotated about the paper surface normal. Diffraction intensity of the certain crystal planes {*hkl*} is collected by a point detector and it can be written as a function of diffraction angle and two rotation angles, $I(2\theta,\varphi,\Psi)$. This intensity is proportional to the possibility of finding the plane normal [*hkl*] (its Miller index is accurately determined from the wavelength of the beam and 2θ via Bragg's law) at a particular direction defined by both angles φ and Ψ. This intensity function is projected to a point in pole figure by either stereographic or equal area projections (section 3.7.2.1 and 3.7.2.2) and the conversion procedure can be written as,

$$I(2\theta,\varphi,\Psi) \xrightarrow{indexing} I_{hkl}(2\theta,\varphi,\Psi) \xrightarrow{projection} I_{hkl}(\alpha,\rho) \qquad \text{(Eq. 3.37)}$$

where *hkl* stands for a family of {*hkl*} plane, α,ρ are the azimuthal angle and polar distance on pole figure, respectively. Equal area projection (section 2.5.1.1) is used in the projection step.

Data collection using the X-ray pole figure goniometer is a rather time-consuming procedure, as the pole figure coverage in a single exposure is only a single dot in a pole figure. Therefore, numerous sample rotations (exposures) have to be conducted in order to achieve satisfactory pole figure coverage to ensure the accuracy of the ODF calculation.

We have introduced in sections 2.3.2 and 2.3.3 several powder diffraction setups in which large area detectors collect a large part of the scattering solid angle in a single exposure. The major advantage of these detectors in texture studies is that they can significantly reduce the data collection time while still achieving the same pole figure coverage as in a pole figure goniometer setup. In order to know how many exposures (sample rotations) are needed to achieve certain pole figure coverage by using these detectors, it is important to know their pole figure coverage in a single exposure (single sample orientation). In addition to that, a particular *hkl* experimental pole figure is easy to construct by filling (integrated) diffraction intensity of the *hkl* peak into its corresponding cells in its pole figure coverage. In next two sections (3.8.2.2 and 2.8.2.3) the pole figure coverage of several detectors in a single exposure are introduced.

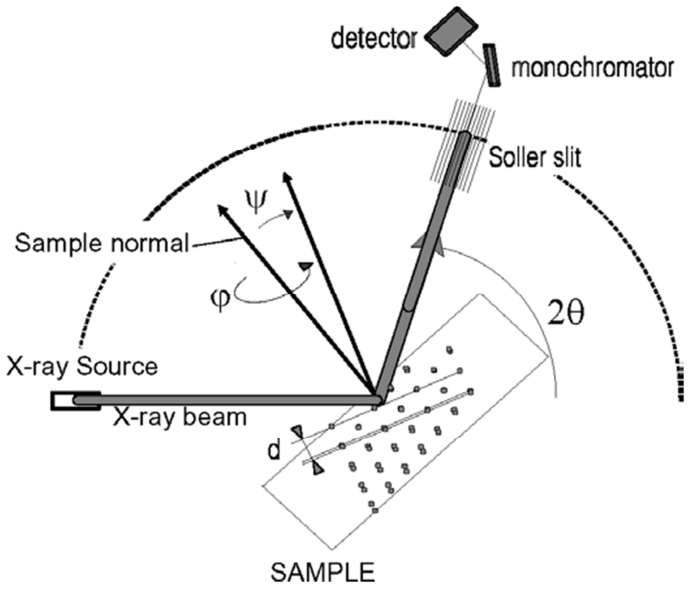

Fig. 3.8 Schematic of a pole figure goniometer setup [38].

3.8.2.2 Pole figure coverage of area detector (Debye-Scherrer diffraction)

Synchrotron x-ray is superior over lab x-ray in terms of higher flux and lower divergence, and it is often used in combination with an area detector in texture studies. An experimental setup of Debye-Schereer diffraction is shown in Fig. 2.9 (section 2.3.2). There are many works in the literature using this setup to study texture. Heidelbach et al. [46] successfully studied fiber texture in metallic wires using single exposure diffraction data of the setup. In this work no sample rotation is needed due to the fact a fibre texture has axial-symmetry. The possibility of studying texture with lower symmetries using single exposure diffraction data of this setup was discussed by Wenk et al [47]. The setup is also often used in *in situ* texture characterization experiment. Margulies et al. [48] studied *in situ* texture change of polycrystalline samples under tensile load and sample rotations were employed to increase pole figure coverage. The setup is also used to study *in situ* texture evolution during high pressure compression [49] and high temperature heating [50].

Here we present the pole figure coverage in a single exposure of an area detector in a Debye-Scherrer diffraction setup and how to increase its pole figure coverage by more sample rotations in Fig. 3.9. The dash ring in Fig. 3.9.a, knowing as an *hkl* pole ring on the unit sphere surface, refers to a particular *hkl* Debye-Scherrer ring with diffraction angle 2θ on area detector is plotted. This dash ring is formed by the intersection between a series of scattering vectors (crystal plane normal {*hkl*} with θ angle against X-Y plane) and the unit sphere. This *hkl* pole ring is projected onto a circular region on X-Y equator plane by using equal area projection (section 3.7.2.2). The projected ring is shown in in Fig. 3.9.b as a red dash ring, which is pole figure coverage of the area detector in a single exposure. This single ring is apparently too sparse to cover a whole pole figure area so that sample rotations about Y axis (sample rotation about X axis will block the x-ray beam and about Z axis will not

change the pole figure coverage) are usually applied to increase pole figure coverage. In Fig. 3.9.b a black dash incomplete ring is shown, referring to a sample with 10^{o} rotation angle about Y axis. It is clear that the more sample rotations around Y axis are applied, the better pole figure coverage the setup can achieve. It should be noted here that the pole ring in Fig. 3.9.a cannot reach North and South Poles owing to the existence of an angle θ. In order to collect more information around North and South Poles, high energy x-ray beam is often used in an experiment to make diffraction angles 2θ smaller.

In chapter 5 we will present a thorough analysis using single exposure data of this setup to study any texture in cubic polycrystals.

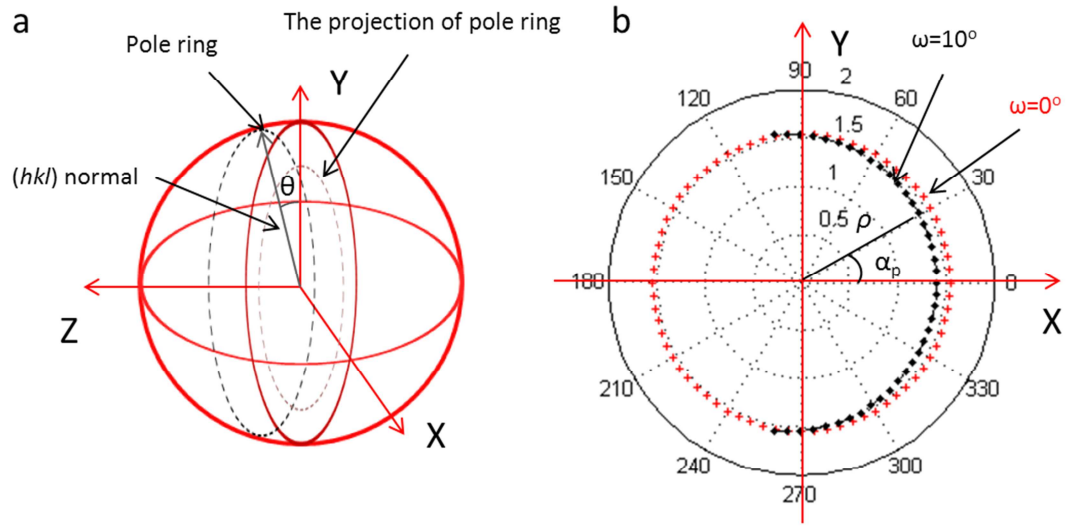

Fig. 3.9 A pole ring in unit sphere referring to a Debye-Scherrer ring and (b) the ring's projection. The pole figure boundary is not shown in *b*.

3.8.2.3 Pole figure coverage of multi-element detector in energy-dispersive diffractions

Texture study by TOF neutron multi-detector was firstly introduced by using NSHR diffractometer installing 7 detectors at different diffraction angles in the same plane [51] at beamline IBR-2 in Dubna, Russia. HIPPO TOF neutron diffractometer (section 2.2.3) is another famous example. It has been widely used for *in situ* texture change observation. For

instance, *In situ* texture changes in the HCP to BCC to HCP phase transformation of zirconium under heating was studied by using HIPPO [52]. It has been proved that the angular resolution of texture results measured by HIPPO can go down to 25^{o} in the orientation space by a detailed quantitative texture analysis [53]. Recently, a mature Rietveld refinement procedure [54] has been established to analyse HIPPO diffraction data making its texture study more user-friendly.

Similar to TOF neutron multi-detector, energy-dispersive x-ray multi-element detector has also been used for texture studies. Bollinger et al. [12] used a ten-element energy-dispersive x-ray multi-detector (shown in Fig. 2.10) to study *in situ* texture change under high pressure. The texture results are reported to be consistent with *ex situ* EBSD measurements.

In multi-direction energy-dispersive powder diffraction (section 2.3.3) diffraction angles are fixed, allowing one not need to consider diffraction angle's contribution in pole figure coverage as in Fig. 3.9. Here, the pole figure coverage of a single sample orientation of HIPPO TOF neutron diffractometer is shown in Fig. 3.10.a as an example of this type of diffraction. It single sample orientation pole figure coverage of is also very sparse so that eight sample rotations (see Fig. 3.10.b) are applied in a measurement to increase the pole figure coverage.

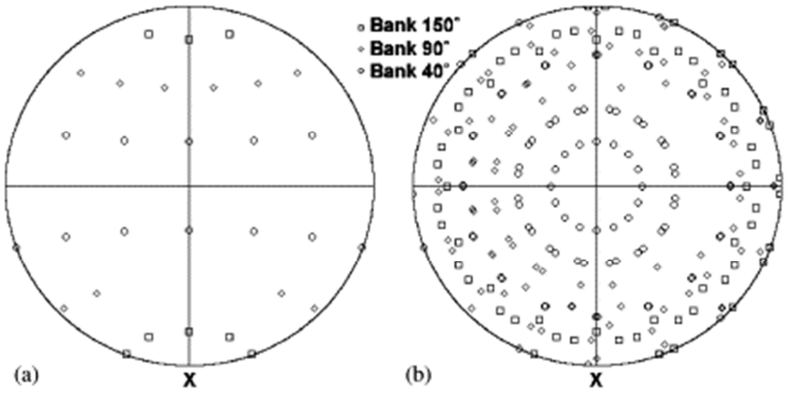

Fig. 3.10 (a) single sample orientation and (b) eight 22.5° sample rotations of pole figure coverage of HIPPO diffractometer [13]

3.9 Texture analysis using powder diffraction pattern data

3.9.1 Pole figure to ODF conversion

Orientation distribution is treated as a continuous mathematical function (ODF) in orientation space. The relationship between pole figure and ODF is given by,

$$P_{hkl}(\alpha,\rho)=\frac{1}{2\pi}\int_0^{2\pi} f(\varphi_1,\Phi,\varphi_2)d\Gamma \qquad \text{(Eq. 3.38)}$$

where $P_{hkl}(\alpha,\rho)$ is pole intensity of a *hkl* pole figure at location (α,ρ), $f(\varphi_1,\Phi,\varphi_2)$ is the volume fraction of an orientation $(\varphi_1,\Phi,\varphi_2)$ in Euler space and Γ is a projection route related to a specific plane normal [*hkl*].

It is easy to compute any pole figure from a given ODF as it is a simple integral of ODF via a certain route in Eq. 3.38. The central problem in texture analysis is the inverse of this equation: given experimental pole figure P, which are even incomplete pole figure from most of measurements, to compute f. In order to determine ODF from experimental pole figures many computational algorithms have been developed. These algorithms fall into two distinct categories [22]:

1) Harmonics method in which computation is performed in Fourier space (section 3.9.1.1 and 3.9.1.2).

2) Direct or discrete method in which computation is directly performed in orientation space (section 3.9.1.3).

3.9.1.1 General harmonics method

Pole intensity functions (here denotes the function on the unit spherical surface, not its projection on 2D plane) are assumed to be expanded into a series of orthogonal spherical harmonic functions,

$$P(a,b) = \sum_{l=0}^{\infty} \sum_{m=-l}^{l} Q_{lm} P_l^m(\cos(a)) \exp(im(b)) \quad \text{(Eq. 3.39)}$$

Here *a* and *b* are two angular spherical coordinates in a pole figure (unit sphere suface).

Owing to the orthogonal properties of spherical harmonics their coefficients (Q_{lm}) can be determined from the experimental data P by integration,

$$Q_{lm} = \int_0^{\pi} \int_0^{2\pi} P(\alpha,\beta) P_l^m(\cos(a)) \exp(-im(b)) \sin(a) dbda \quad \text{(Eq. 3.40)}$$

ODF can also be expanded as,

$$f(\Psi,\Theta,\Phi) = \sum_{l=0}^{\infty} \sum_{m=-l}^{l} \sum_{n=-l}^{l} W_{lmn} Z_{lmn}(\cos\Theta) e^{im\Psi} e^{in\Phi} \quad \text{(Eq. 3.41)}$$

The relationship between their (pole figure and ODF) coefficients Q_{lm} and W_{lmn} is,

$$Q_{lm} = \sum_{n=-l}^{l} W_{lmn} P_l^n(\cos\xi) e^{-in\eta} \quad \text{(Eq. 3.42)}$$

Eq. 2.42 suggests that ODF coefficients W_{lmn} can be calculated through a set of linear simultaneous equations once several pole figures are measured. However, this equation cannot be directly used to calculate ODF from incomplete pole figures. In order to deal with this situation, one solution[55] is suggested by using a third-order polynomial to extrapolate the known of incomplete pole figures to the missing parts.

The main advantage of harmonics method is that it describes texture in Fourier space, and the usage of Fourier coefficients (either Q_{lm} or W_{lmn}) is a compact quantitative representation of texture. Those coefficients makes the identification of texture changes simpler during phase transformation [56]. However, there is also a major disadvantage related

to the usage of harmonics functions knowing as “ghost problem” [57]. The problem is from fact that any pole distribution on a unit sphere surface has an inversion centre. This requires that a spherical harmonic function is symmetric when l is even, but is antisymmetric when l is odd. As a consequence of the antisymmetry, Q_{lm} is always zero when l is odd so that the W_{lmn} calculated from Eq. 3.42 has also to be zero. This is however not true for any realistic texture existed in nature. The ODF information of the l-odd part is called “ghost” and is lost in this harmonics approach.

3.9.1.2 A special harmonics method: MTEX [58] algorithm

A Matlab toolbox MTEX [58] has recently been developed for texture analysis. MTEX assumes that any ODF is a linear combination of non-negative, radially symmetric and “bell-shaped” (unimodal) functions with certain coefficients in 3D Euler space. Similar to a 1D single peak function (e.g. Gaussian or Poisson function) characterized by a peak centre and a half-width, a “bell-shaped” function can also be characterized by an orientation centre (peak centre in Gaussian function) and angular broadening (half-width of Gaussian function) in 3D Euler space. It [58] has been proved that Eq. 3.38 represents a geodesic Radon transform [59] of an ODF. Thus a pole figure can be written as $\mathrm{R}_{hkl} f(g)$, here R stands for Radon transform. The Radon transform (a pole figure) of an ODF are represented as a linear combinations of harmonic functions. Therefore, the algorithm used in MTEX to calculate ODF is categorized as one type of harmonics method.

However, MTEX does not have the same intrinsic problems of harmonics algorithms. The “ghost” problem is minimized by separating an ODF into a random part and a preferred orientation part in MTEX’s iteration. It has been asserted [58] that the “ghost” effect is particularly strong for samples with weak texture. The separation in MTEX ensures that the preferred orientation part of an ODF is artificially made stronger, so that the “ghost” effect is

largely reduced. Besides, since non-negative functions are used to construct an ODF, the ODF intensity always remains positive. It also deals with incomplete pole figure easily, and no special extrapolation as in general harmonics method is used.

As a Matlab toolbox, MTEX is easy to implement in a Matlab routine to automate batch-processing of ODF estimations from many pole figures. This batch-processing capability is the main motivation of using MTEX to study texture in the thesis.

In order to determine the coefficients for a particular "bell-shaped" function, MTEX seeks to minimise a squared error estimator,

$$error = \sum_{\rho} \sum_{\alpha} \left\{ [v_{\alpha}(f)\, \mathrm{R}_{\rho,\alpha}\, f(\mathbf{g}) - I_{\rho,\alpha}]^2 / I_{\rho,\alpha} \right\} \qquad \text{(Eq. 3.43)}$$

Here $v_{\alpha}(f)$ is a normalization factor, $\mathrm{R}_{\rho,\alpha} f(\mathbf{g})$ is the Radon transform of an ODF ($f(\mathbf{g})$) at a position (ρ,α) on pole figur and $I_{\rho,\alpha}$ is the experimental pole figure intensity at position (ρ,α).

The key issue in any optimisation method is to ensure that the solution is stable and not unduly strongly dependent on the initial guess. In order to achieve convergence precisely, MTEX defines a normalization factor v_{α} as:

$$v_{\alpha}(f) = \frac{\sum_{\rho} I_{\rho,\alpha}}{\sum_{\rho} \mathrm{R}_{\rho,\alpha} f(\mathbf{g})} \qquad \text{(Eq. 3.44)}$$

MTEX has gained popularity in literature dedicating for texture studies. Meredith et al. [60] used MTEX to processing raw pole figures measured by lab x-ray pole figure goniometer setup aiming for texture evolution in equal channel angular pressing. Carpenter et

al[61] applied MTEX to analyse the diffraction data measured by HIPPO TOF neutron diffractometer for texture evolution study. It can also be used to estimate ODF from discrete orientations data measured by single crystal diffraction techniques, for instance EBSD [62]. MTEX is not only utilized for crystallographic orientation analysis, but also has been employed to evaluate shape preferred orientation function from tomographic data [63].

3.9.1.3 Discrete method (WIMV method)

The first direct, iterative algorithm for OD determination was proposed by Williams [64]. In this type of method, both ODF and pole figure are considered as consisting of 5^o spacing grid cells in 3D orientation space and 2D direction plane respectively. Therefore, ODF and pole figure are not treated a continuous mathematical functions but some discrete cells. Then the pole figure is not integration but a summation of ODF along a certain route and Eq. 3.38 is rewritten as,

$$P_h(\mathbf{y}) = \frac{1}{N}\sum_{i=1}^{N} f(\mathbf{y} \Leftarrow \mathbf{g}_i) \qquad \text{(Eq. 3.45)}$$

Here, $\mathbf{g}$ represents a crystal orientation (*i.e.* the centre of a 5°×5°×5° orientation cell) and $\mathbf{y}$ represents a point (*i.e.* the centre of a 5°×5° pole cell) on the pole figure of a crystal direction h. The relationship in the bracket ($\mathbf{y} \Leftarrow \mathbf{g}_i$) means that N orientations ($\mathbf{g}_i$) corresponds for a same point ($\mathbf{y}$) on a pole figure.

The WIMV (Williams-Imhof-Matthies-Vinel) algorithm [57] is the most popular discrete method in ODF analysis. Most of popular texture analysis software packages, such as Beartex [65], utilize WIMV algorithm. This algorithm makes an initial guess of ODF ($f_{n=0}$) by placing in each OD cell the geometric mean of the values in the associated experimental pole figure cells,

$$f_0(\mathbf{g}_i) = N_0 \prod_{j=1}^{I} \prod_{m_i=1}^{M_i} p_{h_j}^{\exp}(\mathbf{g}_i \Leftarrow \mathbf{y}_{m_i})^{\frac{1}{IM_i}} \qquad \text{(Eq. 3.46)}$$

Here, I is the number of measured pole figures, m_i is the multiplicity of the $i\,th$ pole, N_0 is a normalization factor and "exp" stands for experimental.

The *(n+1)*st estimate and *n*th estimate are related by the correction factor,

$$f_{n+1}(\mathbf{g}_i) = N_n f_n(\mathbf{g}_i) \frac{f_0(\mathbf{g}_i)}{\prod_{j=1}^{I} \prod_{m_i=1}^{M_i} p_{h_i}{}^{n}(\mathbf{y}_{m_i})^{\frac{1}{IM_i}}} \qquad \text{(Eq. 3.47)}$$

If the initial guess (f_0) is uniform in Eq.3.47, the ODF after the first iteration will have the same format as Eq. 3.46. Through iterations, a pole figure ($f_{n+1}(\mathbf{g}_i)$) are refined till the correction factor diminishes to be less than a pre-set small number or the number of interaction reaches pre-set maximum number of iterations.

3.9.2 Direct texture fitting by Rietveld refinement

Rietveld refinement has been widely used in ODF determination from powder diffraction patterns. It regards a diffraction intensity function in any direction fully described by Eq. 2.10 (section 2.4.3), in which P_k is pole intensity function that is equivalent to the experimental pole figure in section 3.8. The refinement is aiming to minimize the difference between experimental diffraction patterns and the predicted Rietveld profiles. In contrast the difference between experimental pole figure and its prediction are minimized in conventional ODF conversion. The accuracy of ODF determination in both approaches are dictated by the difference between the input data and it predictions.

Rietveld refinement software packages usually have a texture refinement module in which harmonics method or direct algorithm is used to refine the pole intensity function P_k. For example, GSAS [18] only uses harmonics method and MAUD [16] allows users to choose any algorithms among harmonics method, WIMV and Extended-WIMV algorithms.

MAUD has been widely used for texture data analysis in literature. Lutterotti el al [66]used MAUD to study texture from multi angle-dispersive diffraction data measured by x-ray pole figure goniometer. In this work both texture and residual stress in a thin film were evaluated simultaneously, since residual stress is also considered in Rietveld refinement. Lonardelli et al [67] studied dinosaur tendon's texture by using MAUD software to perform Rietveld analysis to the Debye-Scherrer diffraction patterns. MAUD is also able to analyse diffraction data collected from HIPPO TOF neutron diffractometer [68].

When performing texture analysis in MAUD, it is necessary to ensure good quality fitting for the background, scale factor, temperature factor and peak profile functions, etc…, before switching on the texture refinement module. This step is necessary and takes considerable time, even though these parameters are not related to the texture information. One of minor imperfections of this MAUD (or Rietveld) analysis is that it is sometimes difficult to achieve a decent fitting as too many parameters have to be accurately determined. In addition to that, most of time it needs manual adjustment thus it is not easy to automate the process in order to batch-process a large amount of data. Therefore, MAUD is used as a reference tool to validate the texture results given by MTEX in the thesis.

Chapter 4 Texture modelling methods

4.1 Single crystal plasticity theory

The concept of crystal plasticity dates back to the early qualitative observation of lattice slip in aluminium single crystal by Taylor et al [69] and Schmid et al [70]. The principal postulate of the crystal plasticity theory is that the total deformation of a grain consists of the superposition of the elastic deformation of crystal lattice and the permanent (plastic) deformation caused by dislocation slip or lattice twinning. The difference between two plastic deformation modes (dislocation slip and lattice twinning) is shown in Fig. 4.1, in which a FCC single crystal subjected to tensile deformation is illustrated. After dislocation slip, the FCC crystal lattice retains its orientation, whereas the twinned lattice clearly shows a different orientation to the undeformed lattice.

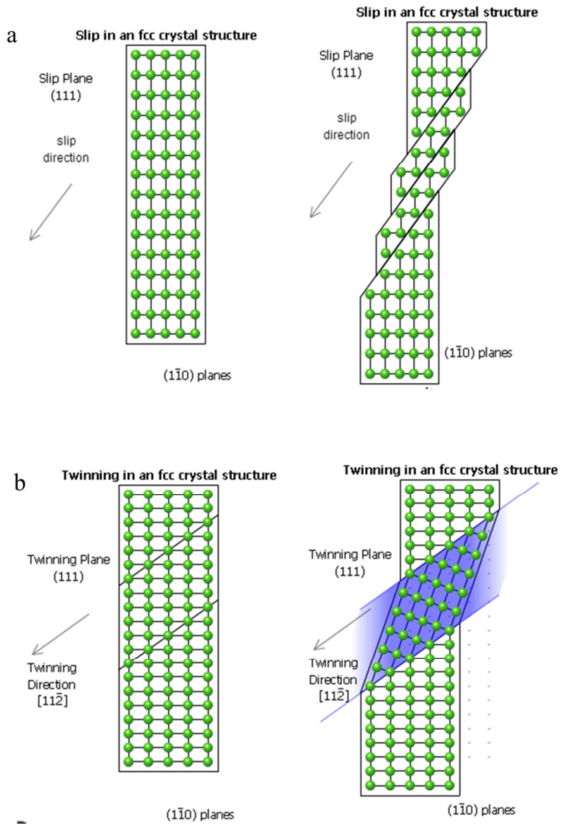

Fig. 4.1 Schematic of lattice slip (a) and twinning (b) [71].

Dislocation slip is the dominant plastic deformation mechanism in cubic phase crystal. In contrast, deformation twinning is more prevalent in crystals with lower symmetry than cubic symmetry [72]. Some exceptions for cubic crystals are known when twinning becomes the more facile mode of plastic deformation. For instance, in twinning induced plasticity (TWIP) steels [73], deformation twinning is intentionally introduced by manganese doping in order to encourage easy plastic deformation and thus allow large strains to failure to be reached. In the present thesis, the motivation for using crystal plasticity is to model texture evolution due to dislocation slip in cubic phase metals (since lattice twinning is rare in these systems).

4.1.1 Lattice reorientation in plastic deformation

Dislocations will glide in a particular slip direction on a particular lattice plane if the resolved shear stress on this particular slip system (defined by the plane and direction) exceeds a critical value known as slip resistance, or also as the critical resolved shear stress (CRSS). Purely plastic deformation of crystal lattice is illustrated in Fig. 4.2.a for a crystal under applied shear stress. It can be seen in the picture that the crystal coordinates basis vectors ($\mathbf{x_1}$ and $\mathbf{x_2}$) remain unchanged before and after dislocation slip. In contrast, under purely elastic deformation the crystal's vertical basis vector ($\mathbf{x_2}$) is changed to ($\mathbf{x'_2}$), as illustrated in Fig. 4.2.b. Apart from the elastic deformation within a single grain, rigid body rotation of grains also contributes to the reorientation of the crystal lattice. Both these effects must be taken into account when we consider a polycrystalline aggregate subjected to large deformation. In the introduction to the kinematics of crystal plasticity given below (section 4.1.2), the rigid body rotation of a material point is treated as part of elastic deformation of that point for the purposes of simplicity.

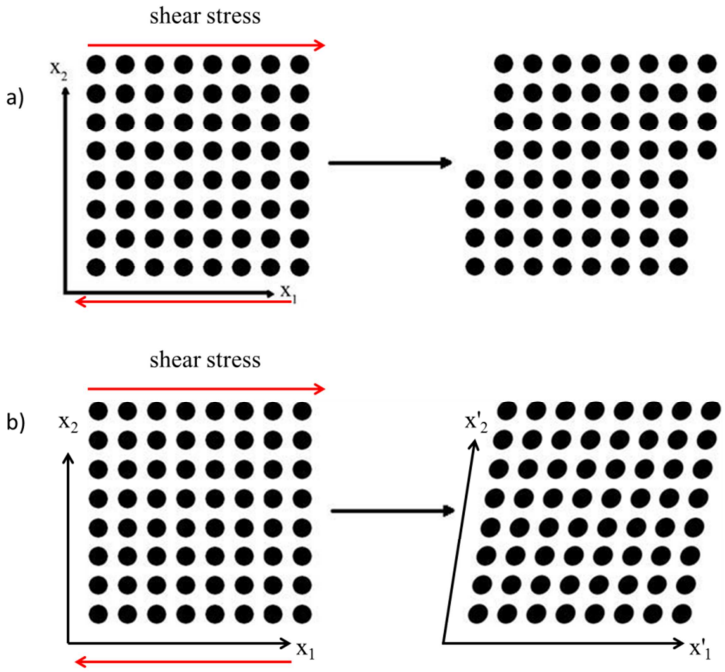

Fig. 4.2 Crystal lattice under the application of a shear stress: (a) purely plastic deformation; (b) purely elastic deformation.

4.1.2 Kinematics of single crystal plasticity

The foundations of the kinematical theory of the mechanics of crystals were laid down by Taylor [74], and the mathematical description was later completed by Hill [75], Rice [76] and Hill and Rice [77]. This section gives a short summary of the theory, and is mainly based on the formulations given by Asaro and Rice [78] and Asaro [79].

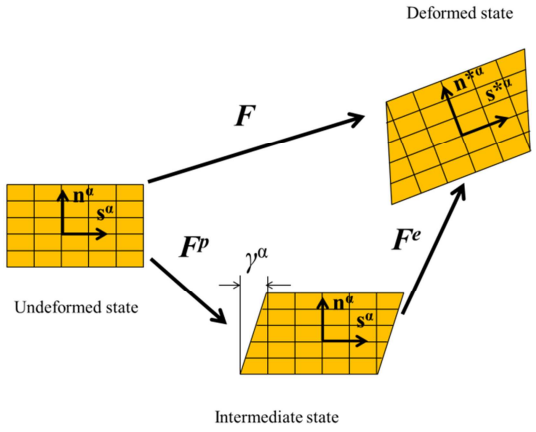

Fig. 4.3 Schematic of the transformation from an undeformed lattice to a deformed lattice by the application of a deformation gradient.

We use x_i (i=1,2,3) coordinates to represent the position of a material particle in the undeformed single crystal in Fig. 4.3. If a crystal is subjected to a displacement field $u_i(x_i)$, a point inside this crystal moves to a new position y_i. The relationship between x_i and y_i is written as,

$$y_i = x_i + u_i \qquad \text{(Eq. 4.1)}$$

The deformation gradient associated with this point is defined as,

$$F_{ij} = \delta_{ij} + \frac{\partial u_i}{\partial x_i} \qquad \text{(Eq. 4.2)}$$

The Jacobian defined as $\det(\mathbf{F})$ will also be useful in later derivation. The total deformation gradient F in Eq. 4.2 can be decomposed into the product of the elastic (including rigid body rotation) and plastic parts (shown in Fig. 4.3),

$$F_{ij} = F^e_{ij} \bullet F^p_{ij} \qquad \text{(Eq. 4.3)}$$

Here the superscripts *e* and *p* stand for elastic and plastic, respectively.

The velocity gradient L of this point is given by,

$$L_{ij} = \frac{\partial \dot{u}_i}{\partial y_j} = \frac{\partial \dot{u}_i}{\partial x_k}\frac{\partial x_k}{\partial y_j} = \dot{F}_{ik} F^{-1}_{kj} \qquad \text{(Eq. 4.4)}$$

Substituting Eq. 4.3 into Eq. 4.4, the velocity gradient can be rewritten as,

$$L_{ij} = \dot{F}_{ik} F^{-1}_{kj} = \left(\dot{F}^e_{ik} F^p_{kl} + F^e_{ik} \dot{F}^p_{kl} \right)\left(F^{p-1}_{lm} F^{e-1}_{mj} \right) = \dot{F}^e_{ik} F^{e-1}_{kj} + F^e_{ik} \dot{F}^p_{kl} F^{p-1}_{lm} F^{e-1}_{mj} \qquad \text{(Eq. 4.5)}$$

The velocity gradient is decomposed into an elastic part $\mathbf{L}^e$ and a plastic part $\mathbf{L}^p$,

$$L_{ij} = L_{ij}^{e} + L_{ij}^{p} \qquad \text{(Eq. 4.6)}$$
$$L_{ij}^{e} = \dot{F}_{ik}^{e} F_{kj}^{e-1}$$
$$L_{ij}^{p} = F_{ik}^{e} \dot{F}_{kl}^{p} F_{lm}^{p-1} F_{mj}^{e-1}$$

Plastic flow in a crystal occurs only by shearing over a few slip systems (see the intermediate state in Fig. 4.3). As indicated above, a slip system is characterized by two unit vectors: the slip direction $\mathbf{s}^{\alpha}$ and the slip plane normal $\mathbf{n}^{\alpha}$ in reference to the undeformed solid. The velocity gradient due to the shearing caused by slip activity is written as,

$$\dot{F}_{ik}^{p} F_{kj}^{p-1} = \sum_{\alpha} \dot{\gamma}^{\alpha} s_i^{\alpha} n_j^{\alpha} \qquad \text{(Eq. 4.7)}$$

Here $\dot{\gamma}^{\alpha}$ is plastic shear strain rate on the αth slip system.

As shown in Fig. 4.3, the slip direction $\mathbf{s}^{\alpha}$ and slip plane normal $\mathbf{n}^{\alpha}$ in the undeformed state remain unchanged after the application of the plastic deformation gradient $\mathbf{F}^{p}$. Hence, these vectors are only changed by the action of the elastic deformation gradient $\mathbf{F}^{e}$. The slip direction $\mathbf{s}^{*\alpha}$ and the slip plane normal $\mathbf{n}^{*\alpha}$ in the deformed crystal can be written as,

$$s_i^{*\alpha} = F_{ik} s_k^{\alpha} = F_{ik}^{e} s_k^{\alpha} \qquad \text{(Eq. 4.8)}$$
$$n_i^{*\alpha} = F_{ik} n_k^{\alpha} = F_{ik}^{e} n_k^{\alpha}$$

Here the star symbol (*) stands for deformed state,

Substituting Eqs. 4.7-4.8 into Eq. 4.6, the plastic velocity gradient $\mathbf{L}^{p}$ can be written as,

$$L_{ij}^{p} = F_{ik}^{e} \dot{F}_{kl}^{p} F_{lm}^{p-1} F_{mj}^{e-1} = F_{ik}^{e} \left(\sum_{\alpha} \dot{\gamma}^{\alpha} s_i^{\alpha} n_j^{\alpha}\right) F_{mj}^{e-1} = \sum_{\alpha} \dot{\gamma}^{\alpha} s_i^{*\alpha} n_j^{*\alpha} \qquad \text{(Eq. 4.9)}$$

The velocity gradient $\mathbf{L}$ can also be decomposed into a pure stretch part (D) and a pure skew part (Ω)),

$$D_{ij} = (L_{ij} + L_{ji})/2 \qquad \text{(Eq. 4.10)}$$
$$\Omega_{ij} = (L_{ij} - L_{ji})/2$$

Both $\mathbf{D}$ and $\mathbf{\Omega}$ are decomposed into elastic and plastic part,

$$D_{ij} = D_{ij}^{e} + D_{ij}^{p} \qquad \text{(Eq. 4.11)}$$
$$\Omega_{ij} = \Omega_{ij}^{e} + \Omega_{ij}^{p}$$

The elastic and plastic parts of stretch tensor ($\mathbf{D}^e$ and $\mathbf{D}^p$) and spin tensor (Ω^e and Ω^p) can be expressed as,

$$D_{ij}^{e} = (L_{ij}^{e} + L_{ji}^{e})/2 = (\dot{F}_{ik}^{e} F_{kj}^{e-1} + \dot{F}_{jk}^{e} F_{ki}^{e-1})/2 \qquad \text{(Eq. 4.12)}$$
$$D_{ij}^{p} = (L_{ij}^{p} + L_{ji}^{p})/2 = (\sum_{\alpha} \dot{\gamma}^{\alpha} s_i^{*\alpha} n_j^{*\alpha} + \sum_{\alpha} \dot{\gamma}^{\alpha} s_j^{*\alpha} n_i^{*\alpha})/2$$
$$\Omega_{ij}^{e} = (L_{ij}^{e} - L_{ji}^{e})/2 = (\dot{F}_{ik}^{e} F_{kj}^{e-1} - \dot{F}_{jk}^{e} F_{ki}^{e-1})/2$$
$$\Omega_{ij}^{p} = (L_{ij}^{p} - L_{ji}^{p})/2 = (\sum_{\alpha} \dot{\gamma}^{\alpha} s_i^{*\alpha} n_j^{*\alpha} - \sum_{\alpha} \dot{\gamma}^{\alpha} s_j^{*\alpha} n_i^{*\alpha})/2$$

4.1.3 Constitutive law

A simple introduction of stress-strain relationship for a single crystal has been given in section 3.2.3. However, this simple formulation of the stress-strain relationship was given with respect to static global coordinates and becomes invalid if the local system of coordinates of a crystal (i.e. related to the crystal axes) is rotated during crystal deformation. The rate form (constitutive law) of the stress-strain relationship in the rotated crystal coordinates is presented below.

The Jaumann rate ($\overset{\nabla^e}{\boldsymbol{\psi}}$) of Kirchhoff stress ($\boldsymbol{\psi}$) at a material point is related to the point's elastic stretch tensor by a fourth order elastic stiffness tensor $\mathbb{C}$ [79],

$$\overset{\nabla^e}{\boldsymbol{\psi}}_{ij} = \mathbb{C}_{ijkl} : D^e_{kl} \qquad \text{(Eq. 4.13)}$$

This Jaumann rate $\overset{\nabla^e}{\boldsymbol{\psi}}$ is also the corotational rate of Kirchhoff stress on the axis that rotates with the crystal lattice,

$$\overset{\nabla^e}{\psi}_{ij} = \dot{\psi}_{ij} - \Omega^e_{ik}\psi_{kl} + \psi_{ik}\Omega^e_{kl} \qquad \text{(Eq. 4.14)}$$

Later in section 4.3 we present a time-integration scheme using crystal plasticity theory implemented in a UMAT subroutine of ABAUQS [80] finite element software. In UMAT, stresses are defined in terms of the Cauchy stress ($\boldsymbol{\sigma}$) rather than Kirchoff stress ($\boldsymbol{\psi}$). The relationship between the two stress tensors is:

$$\psi_{ij} = \det(\mathbf{F})\sigma_{ij} \qquad \text{(Eq. 4.15)}$$

The change rate of the Jacobian ($\det(\mathbf{F})$) is given [81] by,

$$\dot{\det}(\mathbf{F}) = \frac{d\det(\mathbf{F})}{dt} = \det(\mathbf{F})D_{kk} = \det(\mathbf{F})D^e_{kk} \qquad \text{(Eq. 4.16)}$$

The logarithm of the Jacobian is given [82] by,

$$\ln(\det(\mathbf{F})) = \Delta\varepsilon_{kk} \qquad \text{(Eq. 4.17)}$$

Here, $\Delta\boldsymbol{\varepsilon}$ is strain increment that could be assumed to be small. The Taylor expansion for Eq. 4.17 is then written as,

$$\ln(\det(\mathbf{F})) = \det(\mathbf{F}) - 1 - \frac{1}{2}(\det(\mathbf{F}) - 1)^2 + \ldots \cong \det(\mathbf{F}) - 1$$

Thus,

$$\det(\mathbf{F}) = 1 + \Delta\varepsilon_{kk} \cong 1 \qquad \text{(Eq. 4.18)}$$

Similar to Eq. 4.14, the corotational rate of Cauchy stress on the axis that rotates with crystal lattice is written as,

$$\overset{\nabla^e}{\sigma}_{ij} = \dot{\sigma}_{ij} - \Omega^e_{ik}\sigma_{kl} + \sigma_{ik}\Omega^e_{kl} \quad \text{(Eq. 4.19)}$$

Using Eqs. 4.13-4.19, the Jaumann rate ($\overset{\nabla^e}{\boldsymbol{\sigma}}$) of Cauchy stress is finally written as,

$$\overset{\nabla^e}{\sigma}_{ij} + \sigma_{ij}D^e_{mm} = \mathbb{C}_{ijkl} : D^e_{kl} \quad \text{(Eq. 4.20)}$$

4.1.4 Rate dependent plasticity and hardening laws

Either Kirchoff stress ($\boldsymbol{\psi}$) or Cauchy stress ($\boldsymbol{\sigma}$) can be projected onto the αth slip system to obtain the Schmid stress (the resolved shear stress) τ^α [82],

$$\tau^\alpha = \frac{1}{2}(s_i^\alpha \psi_{ij} n_j^\alpha + n_i^\alpha \psi_{ij} s_j^\alpha) = \psi_{ij} : [\frac{1}{2}(s_i^\alpha n_j^\alpha + n_i^\alpha s_j^\alpha)] \quad \text{(Eq. 4.21)}$$
$$= \det(\mathbf{F})\sigma_{ij} : [\frac{1}{2}(s_i^\alpha n_j^\alpha + n_i^\alpha s_j^\alpha)]$$

Schmid law states dislocations begin to glide on the αth slip system when the Schmid stress τ^α on this system becomes larger than the critical resolved shear stress g^α (also called the initial shear resistance). The shear (gliding) strain rate for this slip system is approximated by the power law [83],

$$\dot{\gamma}^\alpha = \dot{\gamma}_0 \text{sign}(\tau^\alpha)\left(\frac{|\tau^\alpha|}{g^\alpha}\right)^{1/m} \quad \dot{\gamma}^\alpha = \dot{\gamma}_0\, sign(\tau^\alpha)\left(\frac{|\tau^\alpha|}{g^\alpha}\right)^{\frac{1}{m}} \quad \text{(Eq. 4.22)}$$

where $\dot{\gamma}^\alpha$ is the shear rate on the α slip system; $\dot{\gamma}_0$ is the initial shear rate; τ^α is the resolved shear (Schmid) stress; g^α is the initial slip resistance (CRSS); m is the rate sensitivity parameter. This equation gives a rate-independent response to the shear stress when m reaches infinity.

Strain hardening is often observed in plastic deformation, and is modelled by the increase of the initial slip resistance (SRSS) g^{α} through time increments,

$$\dot{g}^{\alpha} = \sum_{\beta} h_{\alpha\beta} \dot{\gamma}^{\beta} \qquad \text{(Eq. 4.23)}$$

Here $h_{\alpha\beta}$ are the so-called hardening moduli suggested by Peirce, Asaro and Needleman [84] and Asaro [85] in the following forms:

$$h_{\alpha\alpha} = h(\gamma) = h_0 \operatorname{sech}^2 \left| \frac{h_0 \gamma}{\tau_s - \tau_0} \right| \qquad \text{(Eq. 4.24)}$$
$$h_{\alpha\beta} = q h(\gamma)$$

where h_0 is initial hardening modulus, τ_0 is yield slip resistance and equals to the initial (time zero) value of slip resistance g^{α}, τ_s is the initial (stage I) critical resolved shear stress (material constant), q is a constant, and γ is Taylor cumulative shear strain (the sum over all slip systems of time integrals of $\dot{\gamma}^{\alpha}$).

4.1.5 Slip systems in cubic crystals

Inside a crystal dislocations are favoured to glide on certain slip planes and along certain directions, and a group of a particular slip plane and particular slip direction is called a **slip system**. The rules of slip system determination in FCC and BCC structure crystal are presented here as only cubic crystals are discussed in the thesis. Each dislocation is characterised by the Burgers vector (deficit in lattice displacement obtained over a loop around the dislocation core) and the dislocation line. The energy associated with a straight dislocation segment is proportional to Gb, where G is the shear modulus, and b is the Burgers vector magnitude. The probability of slip decreases exponentially with the distance by which individual atoms need to jump in order to accomplish an elementary act of dislocation segment displacement in the slip plane. Therefore, favoured slip planes must be the ones with

the shortest interatomic distance *i.e.* the highest planar atoms' density. These planes are often close-packed planes. On a certain slip plane, the favoured slip direction of dislocations should also be the one with the shortest atomic distance *i.e.* the highest linear atoms' density.

In the FCC structure, all close packed planes are of the type {111}, and these are the slip planes in the slip systems in this structure. An example of such slip systems in the FCC structure is shown in Fig. 3.4: crystal plane $(1\bar{1}1)$ and direction [011]. Due to cubic crystal symmetry three other crystal planes are equivalent to crystal plane $(1\bar{1}1)$, and they are (111), $(11\bar{1})$ and $(\bar{1}11)$. Since Miller indices has been introduced in section 3.1, here we use {111} to represent all 4 crystal planes equivalent to crystal plane $(1\bar{1}1)$. Crystal direction [011] on the crystal plane $(1\bar{1}1)$ has two other equivalent directions: [110] and $[10\bar{1}]$. The same type of direction is written as <011>. Therefore, there are 12 (three times four) {111}<011> slip systems in FCC structure.

For a BCC structure, which is not a close-packed structure, one of its slip systems is: crystal plane $(\bar{1}01)$ with the highest planar atomic density and crystal direction $[1\bar{1}1]$ with the highest linear atomic density are also plotted in Fig. 4.4. There are also 12 (six times two) {101}<111> slip systems in BCC crystals.

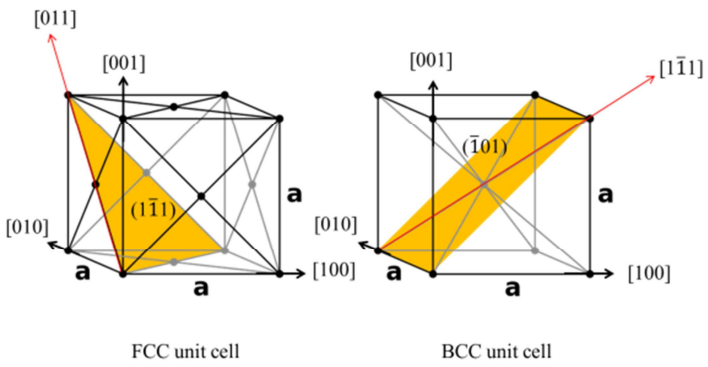

Fig. 4.4 Slip planes and slip directions in the FCC and BCC structure

Slips can also occur on other planes apart from the most favoured planes, especially at elevated temperatures. In the BCC structure the atomic density on the {110} planes (not truly close-packed planes) is only slightly higher than on other planes. Therefore, it is relatively easy to see other slip systems in the BCC structure being activated. For instance, α-Fe has up to 48 slip systems at room temperature. These slip systems are: 12 {101}<1$\bar{1}$1> (common slip systems in BCC structure), 24 {123}<111> and 12 {112}<111>. Although {111}<011> is the dominant slip system in the FCC structure at room temperature, other slip systems may be activated at higher temperatures. In order to illustrate the temperature effect on the activation of slip systems in FCC structures more conveniently, we define two temperatures in FCC metals: T_1 and T_2. Below T_1, slip will exclusively occur on the {111} plane; between T_1 and T_2, slips are seen on both {111} and {110} planes; above T_2, slip is only seen on {110} planes. Table 4.1 [86] lists the two temperatures for several FCC single crystals whose lattice slip behaviour at different temperatures has been observed experimentally.

Table 4.1 temperatures corresponding to {111} slip exclusively (T_1) and {110} slip exclusively (T_2).

Metal	T1(K)	T2(K)
Al	350	540
Ni	700	1225
Au	650	900
Cu	820	>1270
Ag	870	>1185

Some works have discussed the effect of dislocation slips on non-favoured slip system on texture simulation in some simple deformations. Li et al [87] considered that there are 12 {111}<110> and 6 {100}<011> slip systems in an artificial FCC structure crystal. Plane strain deformation was applied to the FCC polycrystals aggregate beginning with random

texture. The results show that a slight difference exists in the final texture between models considering the 18 slip systems and 12 {111}<110> slip systems. Boogaard et al [88] used a visco-plastic self-consistent model to study texture evolution of Al-Mg-Si sheet in a thermo-mechanical forming process. The temperature in the forming was at 250^{o}C. They considered that four types of slip systems {111}<110>, {110}<110>, {100}<110> and {112}<110> are activated owing to the high temperature, and the corresponding CRSS ($_{g^{\alpha}}g^{\alpha}$) ratios for the four types of slip system are 0.9:1:1.1:1 respectively. As a result of this CRSS ratio setting, the slip system {111}<110> remains the most favoured slip system. By comparing the model considering 4 types of slip systems with the model considering only the {111}<110> slip system, it has been concluded that only a slight difference exists between their texture results. Since slip on non-favoured slip systems only has a very minor effect on the texture evolution in cubic polycrystals during deformation, we only consider slips on favoured slip systems.

4.2 Polycrystal plasticity modelling techniques

In section 4.1, a mathematical description of **single crystal** plasticity has been presented. In order to model the plastic deformation of a polycrystal, it is necessary to combine the appropriate numerical implementation of the constitutive equations introduced above with a model that is informed about the polycrystal geometry and enforces at least some of the following conditions: displacement continuity between grains, strain compatibility within each grain, and force equilibrium both locally (at the level of stresses) and globally (at the level of the entire structure or parts of it). The vital step is to use the known deformations (boundary conditions, external load, etc…) applied to the polycrystal aggregate to determine deformation gradients **F** for each constitutive single grain. Three types of modelling techniques have been proposed for dealing with this question in the literature: 1) Taylor type model; 2) self-consistent polycrystal plasticity model; 3) crystal plasticity finite element method.

The first approach was proposed by Taylor [74]. He assumed that each single grain inside a polycrystalline aggregate experiences exactly the same strain as the entire aggregate. This ensures continuity of displacements and compatibility of strains, and also allows easy calculation of stresses from known strains. Taylor's model is an example of a so-called full constraint theory. Another famous full constraint approach was proposed by Sachs [89], who assumed that each grain inside a polycrystal aggregate experiences the same stress as the entire aggregate. Taylor and Sachs' models correspond to the upper bound and lower bound deformation to the single grains respectively. However, these two models have distinct drawbacks: stress equilibrium within a polycrystals aggregate is violated under Taylor's assumption and strain compatibility is violated under Sachs's assumption. Furthermore, grain's interaction within the aggregate is ignored in all the full constraint approaches.

Self-Consistent (SC) framework [90-92] is a more realistic modelling approach compared to Taylor type models. In a SC polycrystals model, a single grain is separated from a polycrystal aggregate and treated as an inclusion. The rest of the grains are treated as an average medium. The key assumption is made that stress equilibrium is satisfied between the inclusion (single grain) and the average medium (the rest of grains) under deformation. By this assumption, a single grain is considered to interact with all the rest of grains in an aggregate. However, in reality a grain should only interact with the neighbouring grains.

Finite element (FE) framework gives a better description of the interaction between grains than SC frameworks. In FE analysis, the realistic grain interactions are achieved through the construction of shape functions (section 4.2.2). In addition to that, stress equilibrium over an entire polycrystals aggregate is realized through a weak form of the principle of virtual work (section 4.2.2). The first introduction of Crystal Plasticity Finite Element (CPFE) modelling was made by Peirce et al. [84], and now it evolves to have very broad applications [93].

4.2.1 CPFE modelling for texture evolution analysis

Kalidindi et al [94] proposed a CPFE model dedicated to polycrystal texture evolution analysis, and this model has been widely accepted as a mature texture analysis tool. Commercial FE analysis software ABAQUS [80] was used in this model, and the single crystal plasticity theory (section 4.1) based on a fully-implicit time-integration scheme was implemented through UMAT subroutine in ABAQUS. Texture evolution was modelled for an isotropic copper sample under simple compression, simple tension, plane strain compression and simple shear deformations [95]. Experimental measurements and Taylor model results were compared to this CPFE model, and it was reported that Taylor model gave a first order estimation to the experimental results but the CPFE model is much more similar to the experimental results.

Below we use this CPFE model as an example to illustrate two distinct characteristics in popular CPFE models: 1) grain-to-IP assignment; 2) the usage of polycrystals representative volume element (RVE).

Firstly, materials properties (orientation, elastic modulus, plasticity parameters, etc…) of a single grain are directly assigned to each Integration Point (IP) of a finite element such that a finite element mesh is associated with a polycrystal aggregate. As a result, a large numbers (more than 1,000) of finite elements are usually needed to model a polycrystal aggregate consisting of thousands of grains. Since the computation time in a FE analysis increases significantly as the number of IPs increases, texture evolution modelling for a large scale polycrystals aggregate will be impossible by using such a grain-to-IP assignment strategy.

The second characteristic and also a solution in order to save computation time is that a cubic polycrystals Representative Volume Element (RVE) is often idealized from a full

scale object and used for CPFE modelling. This RVE has to include hundreds of grains in order to represent a specific location at a polycrystalline object. Consequently, the deformations (boundary conditions) of that specific location are also idealized in order to apply to the RVE. However, it is sometimes impossible to simplify deformations (boundary conditions) for a complicated deformation process. As a consequence, main stream CPFE models are often used to model texture change during monotonic “simple plastic deformation” , such as sheet rolling [96] –plane strain compression; wire drawing –uniaxial tension [97]; torsion – simple shear [98] etc...

4.2.2 Finite element analysis basis [99]

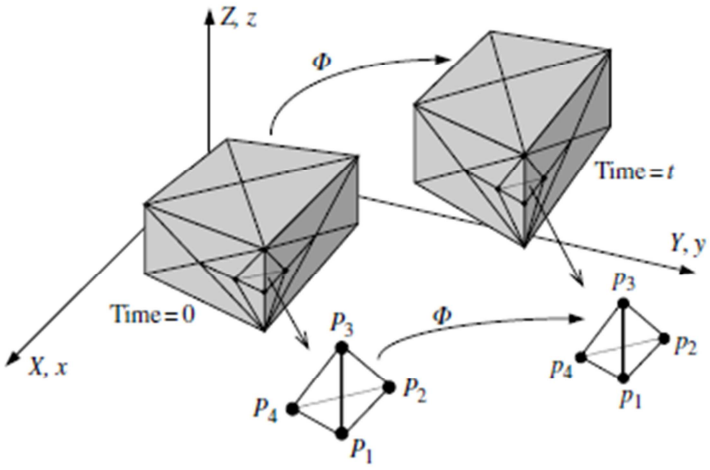

Fig. 4.5 Schematic diagram showing the finite element discretization of a body by 3D tetrahedral elements [99].

In the FE analysis an object is discretized into small elements (an example is shown in Fig. 4.5). A particular tetrahedral element consists of vertices P1, P2, P3 and P4 is shown in the picture. The corresponding deformed element consists of vertices p1, p2, p3 and p4. A tetrahedral element with arbitrary shape representing any element in Fig. 4.5 under reference coordinates is shown Fig. 4.6.a. This arbitrary shape element can be transformed into a regular tetragonal element (Fig. 4.6.b) referred to the local coordinates.

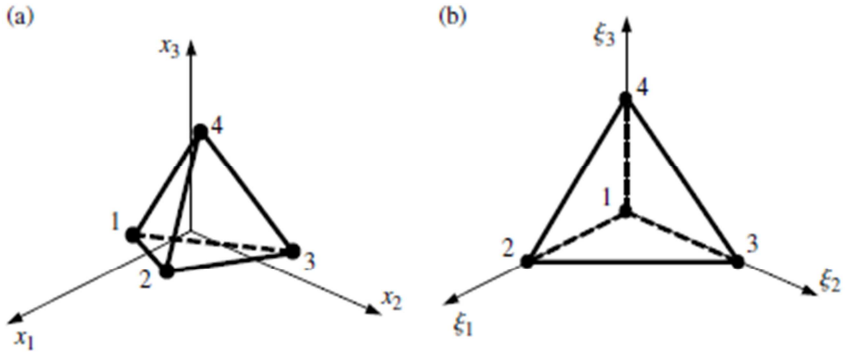

Fig. 4.6 Four-noded tetrahedral element shown with respect to (a) the current configuration and (b) the local element reference frame [99].

A Jacobian matrix (J_P) is used to associate the coordinates of any point P in reference coordinates ($\mathbf{x}_p$) and local coordinates ($\boldsymbol{\xi}_j$), and it is written as a differential format:

$$\mathbf{J}_p = \frac{\partial \mathbf{x}_p}{\partial \boldsymbol{\xi}_p} \qquad \text{(Eq. 4.25)}$$

The key assumption made in FE analysis is that the displacement of any point P inside an element can be interpolated by the displacements of its vertices.

$$\mathbf{u}_p(\xi) = \sum_i^4 N_i \mathbf{u}_i(\xi) \qquad \text{(Eq. 4.26)}$$

where, $\mathbf{u}_p(\boldsymbol{\xi})$ is a 3×1 displacement vector of P under local coordinates; $N_i(\xi)$ is a 3×3 matrix; $\mathbf{u}_i(\xi)$ is a 3×1 displacement vector of the *i*th node (vertex). A more general matrix format of Eq. 4.26 is written as,

$$\mathbf{u}(\xi) = \mathbf{N}\mathbf{u}_I(\xi) \qquad \text{(Eq. 4.27)}$$

Here $\mathbf{u}(\xi)$ is still a 3×1 vector; $\mathbf{u}_I$ becomes a 12×1 vector for tetrahedral elements, as it consist of 3 displacements of 4 vertices; $\mathbf{N}$ is a 3×12 matrix accordingly and is called **shape function**. Displacement compatibility over the element is enforced by the equation.

The strain of any point in the element is the differentiation with respect to the point's displacement:

$$\boldsymbol{\varepsilon}(\xi) = \frac{\partial \mathbf{u}(\xi)}{\partial \xi} = \frac{\partial \mathrm{N}}{\partial \xi}\mathbf{u}_I(\xi) = \mathbf{B}\mathbf{u}_I(\xi) \qquad \text{(Eq. 4.28)}$$

According to Hooke's law, stress at the point is written as,

$$\boldsymbol{\sigma} = \mathbf{C}\boldsymbol{\varepsilon}^e \qquad \text{(Eq. 4.29)}$$

Here Voigt notation is used; $\boldsymbol{\sigma}$ is 6×1 stress vector; $\mathbf{C}$ is 6×6 stiffness matrix; $\boldsymbol{\varepsilon}^e$ is 6×1 elastic strain vector.

The Lagrangian L of the element is defined as,

$$L = T - U + W \qquad \text{(Eq. 4.30)}$$

Here T is the total energy of element; U is the total potential energy; W is the work done by non-conservative force. T, U and W are given by,

$$\begin{aligned} T &= \frac{1}{2}\int_{\Omega} \rho \dot{\mathbf{u}}^T \dot{\mathbf{u}}\, dV \\ U &= \frac{1}{2}\int_{\Omega} \boldsymbol{\varepsilon}^T \boldsymbol{\sigma} dV \\ W &= \int_{\partial\Omega} \mathbf{u}^T \mathbf{t} dV \end{aligned} \qquad \text{(Eq. 4.31)}$$

Here $\mathbf{u}$ and $\dot{\mathbf{u}}$ are the displacement and velocity vector respectively; $\boldsymbol{\varepsilon}$ and $\boldsymbol{\sigma}$ are stain and stress vector respectively; $\mathbf{t}$ is the external stress vector applied on the element; Ω and $\partial\Omega$ represent the volume and the surface of the element respectively.

Substituting Eq. 4.27-4.29 and 4.31 into Eq. 4.30 and it becomes,

$$L = \frac{1}{2}\dot{\mathbf{u}}_I^T\left(\int_{\Omega} \rho \mathbf{N}^T \mathbf{N} dV\right)\dot{\mathbf{u}}_I - \frac{1}{2}\mathbf{u}_I^T\left(\int_{\Omega} \rho \mathbf{B}^T \mathbf{C}\mathbf{B} dV\right)\mathbf{u}_I + \mathbf{u}_I^T \int_{\partial\Omega} \mathbf{N}^T \mathbf{t} dA \qquad \text{(Eq. 4.32)}$$

For simplicity we define,

$$\mathbf{m} = \int_{\Omega} \rho \mathbf{N}^T \mathbf{N} dV \qquad \text{(Eq. 4.33)}$$
$$\mathbf{k} = \int_{\Omega} \rho \mathbf{B}^T \mathbf{C} \mathbf{B} dV$$
$$\mathbf{f} = \int_{\partial\Omega} \mathbf{N}^T \mathbf{t} dA$$

Then the Lagrangian becomes,

$$L = \frac{1}{2} \dot{\mathbf{u}}_I^T \mathbf{m} \dot{\mathbf{u}}_I - \frac{1}{2} \mathbf{u}_I^T \mathbf{k} \mathbf{u}_I + \mathbf{u}_I^T \mathbf{f} \qquad \text{(Eq. 4.34)}$$

The virtual work over a time period between t_1 and t_2 is written as,

$$J = \int_{t_1}^{t_2} L dt = \int_{t_1}^{t_2} (\frac{1}{2} \dot{\mathbf{u}}_I^T \mathbf{m} \dot{\mathbf{u}}_I - \frac{1}{2} \mathbf{u}_I^T \mathbf{k} \mathbf{u}_I + \mathbf{u}_I^T \mathbf{f}) dt \qquad \text{(Eq. 4.35)}$$

The Hamilton principle states that the variation of virtual work in any time period must to be zero:

$$\delta J = \int_{t_1}^{t_2} L dt = \int_{t_1}^{t_2} (\frac{1}{2} \delta(\dot{\mathbf{u}}_I^T \mathbf{m} \dot{\mathbf{u}}_I) - \frac{1}{2} \delta(\mathbf{u}_I^T \mathbf{k} \mathbf{u}_I) + \delta(\mathbf{u}_I^T \mathbf{f})) dt \qquad \text{(Eq. 4.36)}$$
$$= \int_{t_1}^{t_2} \delta \mathbf{u}_I^T (-\mathbf{m} \ddot{\mathbf{u}}_I - \mathbf{k} \mathbf{u}_I + \mathbf{f}) dt = 0$$

Since $\delta \mathbf{u}_I^T$ stands for any possible displacement, Eq. 4.36 requires,

$$-\mathbf{m} \ddot{\mathbf{u}}_I - \mathbf{k} \mathbf{u}_I + \mathbf{f} = 0 \qquad \text{(Eq. 4.37)}$$

Eq. 4.37 is the finite element equilibrium equation. In the absence of inertia force, it becomes,

$$\mathbf{k} \mathbf{u}_I = \mathbf{f} \qquad \text{(Eq. 4.38)}$$

Above gives a simple introduction to achieve displacement (strain) compatibility and stress equilibrium within an element. All the vectors and tensors are in local coordinates (ξ).

In FE analysis an object has N number of such elements, and all the variables should be under reference coordinates (**x**). Therefore, the displacement interpolation (Eq. 4.26) of any point in an object can be rewritten as,

$$\mathbf{u}(\xi) = \sum_{i}^{4N} N_i \mathbf{u}_i(\xi) \qquad \text{(Eq. 4.39)}$$

Here, 4*N* stands for *N* number of tetrahedral element with 4 vertices.

The derivatives of the shape function under reference coordinates can be written as,

$$\nabla_{\mathbf{x}} \mathbf{N}(\xi) = \frac{\partial \mathbf{N}(\xi)}{\partial \mathbf{x}} = \frac{\partial \mathbf{N}(\xi)}{\partial \xi} \frac{\partial \xi}{\partial \mathbf{x}} \qquad \text{(Eq. 4.40)}$$

Apply the Jacobian matrix (Eq. 4.25) and it becomes,

$$\nabla_{\mathbf{x}} \mathbf{N}(\xi) = \frac{\partial \mathbf{N}(\xi)}{\partial \xi} (\mathbf{J})^{-1} \qquad \text{(Eq. 4.41)}$$

Accordingly the strain vector (Eq. 4.28) is written as (It should be noted here that this strain vector is not the one really used in a FE analysis and is an just approximation for illustration purpose),

$$\boldsymbol{\varepsilon}(\mathbf{x}) = \frac{\partial \mathbf{u}(\xi)}{\partial \mathbf{x}} = \left[\nabla_{\mathbf{x}} \mathbf{N}(\xi)\right] \mathbf{u}_I(\xi) \qquad \text{(Eq. 4.42)}$$

The other steps for deducing stress equilibrium equation in an object are similar to that for Eq. 4.37. In summary, the key steps in a general FE analysis are two: 1) The formation of shape function $\mathbf{N}$; 2) using Jocabian matrix (Eq. 4.25) to transform all the variables from local coordinates to reference coordinates. These steps can be automatically achieved in commercial FE analysis software such as ABAQUS.

4.3 An implicit time-integration scheme of single crystal plasticity

In this thesis, single crystal plasticity theory (section 4.1) is implemented into UMAT Fortran subroutine of ABAQUS through an implicit time-integration proposed by Huang [100]. This scheme has been used in many CPFE modelling works for instance, mechanical performance of cardiovascular stent [101], directional dependence of crack growth along a copper/sapphire bicrystal interface [102]. Moreover it also has been used intensively in texture evolution studies of polycryatals aggregates under plastic deformation. For instance, the scheme was modified to incorporate deformation twinning into plastic mechanisms, and used to model both lattice strain and texture evolution in Zircaloy-2 [103]. Texture evolution in a tungsten wire drawing processing was also modelled by a modified version of the scheme [97]. This well established scheme is slightly modified in the present thesis for texture evolution modelling in Chapter 8. Below we present the key equations of the scheme.

This scheme is followed by the tangent modulus method for rate dependent solid developed by Peirce et al [104]. Due to the incremental nature of an implicit FE analysis in ABAQUS, all the variables presented in section 4.1 should be given in incremental format. Below we give their incremental formats starting with incremental shear strain. The increment of shear strain γ^{α} on the αth slip system within time increment Δt is written as,

$$\Delta\gamma^{\alpha} = \gamma^{\alpha}(t+\Delta t) - \gamma^{\alpha}(t) \qquad \text{(Eq. 4.43)}$$

A linear interpolation is used to link the shear strain increment with shear rates:

$$\Delta\gamma^{\alpha} = \Delta t[(1-\theta)\dot{\gamma}^{\alpha}_{t} + \theta\dot{\gamma}^{\alpha}_{t+\Delta t}] \qquad \text{(Eq. 4.44)}$$

Here the parameter θ ranges from 0 to 1, with 0 corresponding to simple Euler time integration scheme. It [104] suggests that θ would be chosen between 0.5 and 1. *Theta* is set to 0.5 exclusively for all the simulations in the thesis.

The Taylor expansion of the shear strain rate (Eq. 4.22) is given by,

$$\dot{\gamma}^{\alpha}_{t+\Delta t} = \dot{\gamma}^{\alpha}_{t} + \frac{\partial \dot{\gamma}^{\alpha}_{t}}{\partial \tau^{\alpha}} \Delta \tau^{\alpha} + \frac{\partial \dot{\gamma}^{\alpha}_{t}}{\partial g^{\alpha}} \Delta g^{\alpha} \qquad \text{(Eq. 4.45)}$$

Where $\Delta \tau^{\alpha}$ and Δg^{α} are the resolved shear (Schmid) stress and current slip resistance increment from *t* to *t*+Δ*t* time period.

Substitute Eq. 4.45 into Eq. 4.44, and it can be rewritten as,

$$\Delta \gamma^{\alpha} = \Delta t[\dot{\gamma}^{\alpha}_{t} + \theta \frac{\partial \dot{\gamma}^{\alpha}_{t}}{\partial \tau^{\alpha}} \Delta \tau^{\alpha} + \theta \frac{\partial \dot{\gamma}^{\alpha}_{t}}{\partial g^{\alpha}} \Delta g^{\alpha}] \qquad \text{(Eq. 4.46)}$$

Recall that the Schmid stress τ^{α} is given by Eq.4.21. In order to express the equation (Eq. 4.21) more concisely, we define two tensors:

$$P^{\alpha}_{ij} = [\frac{1}{2}(s^{\alpha}_{i} n^{\alpha}_{j} + n^{\alpha}_{i} s^{\alpha}_{j})] \qquad \text{(Eq. 4.47)}$$
$$W^{\alpha}_{ij} = [\frac{1}{2}(s^{\alpha}_{i} n^{\alpha}_{j} - n^{\alpha}_{i} s^{\alpha}_{j})]$$

Then Eq. 4.21 can be rewritten as,

$$\tau^{\alpha} = \frac{1}{2}(s^{\alpha}_{i} \psi_{ij} n^{\alpha}_{j} + n^{\alpha}_{i} \psi_{ij} s^{\alpha}_{j}) = \det(\mathbf{F}) \sigma_{ij} P^{\alpha}_{ji} \qquad \text{(Eq. 4.48)}$$

The rate change of τ^{α} is given by [82],

$$\dot{\tau}^{\alpha} = [\mathbb{C}_{ijkl} : P^{\alpha}_{kl} + W^{\alpha}_{ik} \sigma_{jk} + W^{\alpha}_{jk} \sigma_{ik}] : D^{e}_{ij} \qquad \text{(Eq. 4.49)}$$

And in incremental format,

$$\Delta\tau^{\alpha} = [\mathbb{C}_{ijkl} : P_{kl}^{\alpha} + W_{ik}^{\alpha}\sigma_{jk} + W_{jk}^{\alpha}\sigma_{ik}] : [\Delta\varepsilon_{ij} - \sum_{\beta=1}^{N^s} P_{ij}^{\beta}\Delta\gamma^{\beta}] \qquad \text{(Eq. 4.50)}$$

Here $\sum_{\beta=1}^{N^s} P_{ij}^{\beta}\Delta\gamma^{\beta}$ represent the sum of $P_{ij}^{\beta}\Delta\gamma^{\beta}$ over N^s (all) slip systems.

From the general hardening equation of lattice slip (Eq. 4.23), the increments of current hardening function Δg^{α} are given by,

$$\Delta g^{\alpha} = \sum_{\beta} h_{\alpha\beta}\Delta\gamma^{\alpha} \qquad \text{(Eq. 4.51)}$$

Using Eqs. 4.51 and 4.50, $\Delta\gamma^{\alpha}$ (Eq.4.6) for next time increment can be determined.

Here we present the corotational stress increments $\Delta\sigma_{ij}$ related to shear increment ($\Delta\sigma_{ij}$ can be deduced from Eq. 4.20 but the deducing steps [82] are omitted here):

$$\Delta\sigma_{ij} = \mathbb{C}_{ijkl}\Delta\varepsilon_{kl} - \sigma_{ij}\Delta\varepsilon_{kk} - \sum_{\alpha}[\mathbb{C}_{ijkl}P_{kl}^{\alpha} + W_{ik}^{\alpha}\sigma_{jk} + W_{jk}^{\alpha}\sigma_{ik}]\Delta\gamma^{\alpha} \qquad \text{(Eq. 4.52)}$$

So far, most important variables' (shear strain, Schmid stress, hardening functions and Cauchy stress) incremental formats are present. Below we present the increment formal of lattice distortion (slip direction **s**, slip plane normal **n** and rotation matrix of a grain **R**).

By differentiating Eq. 4.8, one gets,

$$\begin{aligned} \dot{s}_i^{*\alpha} &= (D_{ij}^e + \Omega_{ij}^e)s_j^{*\alpha} \\ \dot{n}_i^{*\alpha} &= -n_i^{*\alpha}(D_{ij}^e + \Omega_{ij}^e) \end{aligned} \qquad \text{(Eq. 4.53)}$$

And in incremental format, they are given by,

$$\begin{aligned} \Delta s_i^{*\alpha} &= \{\Delta\varepsilon_{ij} + \Omega_{ij}\Delta t - \sum_{\beta}[P_{ij}^{\beta} + W_{ij}^{\beta}]\Delta\gamma^{\alpha}\}s_j^{*\alpha} \\ \Delta n_i^{*\alpha} &= -n_i^{*\alpha}\{\Delta\varepsilon_{ij} + \Omega_{ij}\Delta t - \sum_{\beta}[P_{ij}^{\beta} + W_{ij}^{\beta}]\Delta\gamma^{\alpha}\} \end{aligned} \qquad \text{(Eq. 4.54)}$$

The rate of rotation matrix (orientation of a single crystal) is obtained by only considering the elastic skew part $\mathbf{\Omega}^e$ (including rigid body rotation) in Eq. 4.53,

$$\dot{\mathbf{R}} = \mathbf{\Omega}^e \bullet \mathbf{R}_{t0} \qquad \text{(Eq. 4.55)}$$

The resulting rotation at time $t0 + \Delta t$ is given by,

$$\mathbf{R}_{t0+\Delta t} = \mathbf{R}_{t0} + \dot{\mathbf{R}}\Delta t = (\mathbf{I} + \mathbf{\Omega}^e \Delta t) \bullet \mathbf{R}_{t0} \qquad \text{(Eq. 4.56)}$$

$$= \left(\delta_{ij} + \Omega_{ij} - \Delta\gamma^{\alpha} \sum_{\beta} W_{ij}^{\beta} \right) R_{ji}$$

In summary, the implicit time-integration scheme for single crystal plasticity presented above can be incorporated into a polycrystal model to represent time-dependent inelastic deformation that leads to grain rotation and the associated texture evolution. The approach to predicting texture evolution in polycrystals that was preferred in the present study involved simulating the deformation of RVE under given loading, by creating a simple model geometry using ABAQUS CAE, and prescribing the boundary conditions and external loading accordingly.

Chapter 5 The interpretation of strain measurement by x-ray powder diffraction

The governing equation of diffraction (Bragg's law) relates the beam energy (or wavelength), diffraction angle and the interplanar spacing of the crystal. Whenever a powder diffraction experiment is carried out for the purpose of lattice parameter determination, this equation is applied to the data collected from a particular gauge volume. If it is assumed that the two of the parameters that enter Bragg's law are known, then the value of the third one (the lattice parameter) can be found. In practice the wavelength (energy) and the scattering angle are in fact known with a degree of uncertainty, which leads to peak broadening once the collected intensity are plotted as a function of the lattice spacing. However, it is important to note that the interplanar spacing itself that is being determined also has a variation within the sampling volume. Sometimes this variation can be ignored, and the value obtained from the application of Bragg's law assigned to the entire sampling volume. In other situations the variation of interplanar spacing is in fact of primary interest to the researcher. So what is actually determined by the application of Bragg's law to a particular diffraction peak? How is the value determined from a diffraction experiment (real or simulated) relate to the distribution (and the average) of the lattice parameter (or interplanar spacing) within the gauge volume?

This question is answered in the first half of this chapter by means of simulated diffraction experiments. The first part of this chapter focuses on the analysis of how the strain distribution within the diffraction volume affects the lattice parameter determination. This provides solid basis for the key postulate that is later used in the strain tomography method (first presented in [105] without proof). Recently this strain tomography method has been applied to reconstruct the strain distribution within a cross-section of a zirconia ceramic

dental bridge that was subjected to *in situ* bending (to simulate chewing) and characterised by powder synchrotron X-ray powder diffraction [28].

In the second part of this chapter (section 5.2), the attention is focused on the variation of the strain measured from a particular gauge volume as a function of the azimuthal (in plane) angle. As illustrated in section 3.4, strain averaging over larger number of grains in a polycrystal volume can effectively improve the accuracy of strain determination at the mesoscopic level. The strain average method using Debye-Scherrer diffraction patterns presented in section 3.4.2 is used to evaluate the 2D residual strain tensor from multi-directional energy-dispersive X-ray diffraction patterns. The measured samples are a non-textured Ti-6Al-4V four-point-bent bar and a strongly textured Aluminium AA2024 alloy linear friction weld, whose diffraction patterns were collected at beamline I12, Diamond Light Source, UK.

5.1 A strain tomography experiment

5.1.1 Background of the experiment

A dental bridge made of Yttria-stabilized-zirconia (YSZ) (shown in the insert picture of Fig. 5.1.a) was subjected to *in situ* three-point bending loading to imitate the loading during mastication. Owing to the loading, a characteristic bending distribution of longitudinal strain is expected to be found in a cross-section perpendicular to the longitudinal direction, as shown in the insert picture of Fig. 5.1.a). Debye-Scherrer diffraction patterns of this sample were collected at beamline ID15B (ESRF, Grenoble, France) in order to characterize the longitudinal strain distribution on the cross-section.

The dental bridge was mounted on a sample stage allowing three axis translation (x, y and z) and φ rotation (around the z axis). The side view of the Debye-Scherrer diffraction setup as well as the sample is illustrated schematically in Fig. 5.1.a. The incident beam was

monochromated to have photon energy of 86.93 keV, and collimated to have a cross-section size of 0.1 × 0.1 mm^2. The beam traversed the entire thickness of the sample, and scattered from the zirconia bridge framework to form Debye-Scherrer patterns recorded by a two-dimensional Pixium detector with pixel matrix of 1920(H) × 2640(V) and pixel size of 154 × 154 μm^2. Sample-to-detector distance (D_0) calibration was made using a CeO_2 stress-free powder sample, and its value was precisely determined to 731.93 mm. The sample was rotated around the vertical axis (z axis) between 0° and 180° in steps of 3.6, *i.e.* through a total of 51 rotation angles. At each rotation angle, the sample was scanned across the beam in steps equal to the beam spot on the sample (0.1 mm).

Diffraction pattern line profiles referring to longitudinal strains were obtained by "caking" the Debye-Scherrer patterns with 10^o azimuthal width along the vertical direction (the caking procedure is seen at section 2.4.1). Due to the high energy (86.93 keV) of the beam and the consequent small diffraction angles, the lattice parameter determined from those line profiles were closely approximated to those along the longitudinal direction.

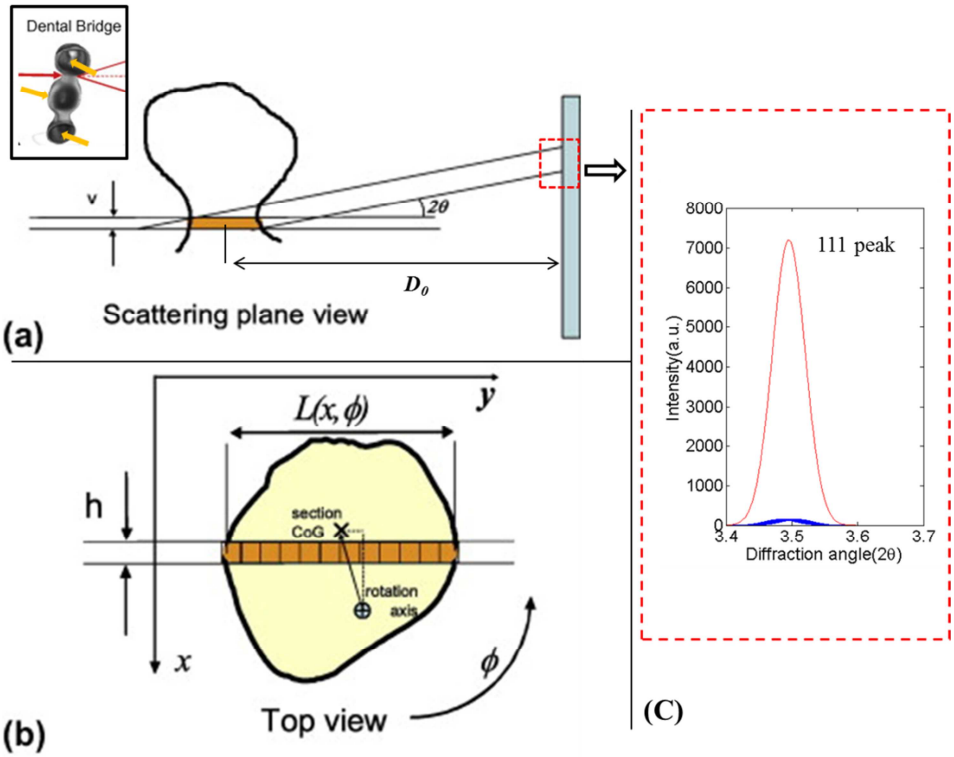

Fig. 5.1 (a) Scattering plane view of the diffraction setup, (insert) schematic of the zirconia dental bridge under 3-point bending, (b) the measured cross-section of the dental bridge and (c) the Gaussian peaks (blue curves) of many cells and their sum (red curve) refereeing to the whole gauge volume.

5.1.2 Average lattice parameter approximation

Owing to the average nature of powder diffraction, the lattice parameter determined from a diffraction pattern via Bragg's law is commonly accepted as the **average** lattice parameter over the gauge volume. This approximation is suitable for instances of characterization when the accuracy of lattice parameter is not required to be very high, e.g. in quantitative phase analysis. However, in strain determination the error of lattice parameter determination has to be less than 0.01% (equivalent to 100 microstrain). When a strong lattice parameter variation is present in a gauge volume, it is conceivable that the lattice parameter measured by powder diffraction may turn out to be very significantly different from the average lattice parameter (e.g. up to 1%, i.e. 10,000 microstrain). It is important to carry out careful error analysis to test this commonly accepted hypothesis by assuming the presence of strain variation within a gauge volume.

Furthermore, this approximation is used as the key postulate in the strain tomography experiment (section 5.1.1). In Fig. 5.1.b, the lattice parameter determined for each *x* scan is assumed to be the averaged lattice parameter of the whole gauge volume. Then the **integral** of lattice parameter along the incident beam direction over the gauge volume is obtained by multiplying the determined (average) lattice parameter with the length of the gauge volume. This integral is analogous to the **integral** of materials density (in conventional tomography) along the x-ray beam path recorded by a pixel on a 2D detector. Once a full *x* and φ scan is performed in Fig. 5.1.b, a lattice parameter sinogram referring to lattice parameter distribution on the cross-section is readily obtained. By using the same reconstruction algorithms as in conventional tomography, this sinogram is converted to the lattice parameter distribution on the cross-section and can be later used for strain analysis.

In order to support the hypothesis of average lattice parameter, a numerical simulation was performed to compute an *hkl* diffraction peak from a gauge volume, by discretising the volume into many small equally sized cells, each with a constant strain inside. Several different types of strain variations between cells were considered to study the extent to which this affects the difference between the average lattice parameter and the “measured” lattice parameter (referring to the centre of the simulated *hkl* diffraction peak).

5.1.2.1 Diffraction peak simulation

Three key postulates are used to carry out the numerical simulation of diffraction peak formation in the dental bridge experiment:

1) The measured sample-to-detector distance (D_0) in the experiment is assumed to correspond to the distance from the centre of the gauge volume to the detector (see Fig. 5.1.a).

2) A particular *hkl* peak identified in the "caked" diffraction pattern line profile is the sum of many **Gaussian** peaks produced by discrete cells within the diffraction volume (see Fig. 5.1.c, where the blue peaks are Gaussian peaks of individual cells and the red peak is the sum total peak). The cells have the same size (see Fig. 5.1.b) and are assumed to produce *hkl* diffraction peaks fully described by Gaussian functions with different peak centres (section 5.1.2.2), but identical peak shape (section 5.1.2.3).

3) The **measured lattice parameter** of a gauge volume is assumed to be computed from the centre of an *hkl* peak (the red peak in Fig. 5.1.c) determined by Gaussian peak fitting (section 2.4.2) via Bragg's law.

For quantitative evaluation of the difference between the **average** (a_0) and **measured** (a_{simu}) lattice parameters, an error measure is defined in the form of relative strain difference between them,

$$e = \left| \frac{a_0 - a_{simu}}{a_0} \right| \qquad \text{(Eq. 5.1)}$$

5.1.2.2 Peak centre of a cell

Based on the second postulate, the gauge volume (the length is about 5.0 mm) shown in Fig. 5.2.b along the incident beam direction is discretised into 0.1 mm equal length cells. There are fifty 0.1 × 0.1 × 0.1 mm^3 cubic cells inside such a gauge volume.

Let a strain variation $\varepsilon(y)$ exist along the incident beam direction within the volume. Let the left end of the diffraction volume in Fig. 5.2.b be defined as zero, and the incident beam direction correspond to the positive y direction. Owing to the strain distribution, a lattice parameter distribution present in the gauge volume is given by:

$$a(y) = (\varepsilon(y) + 1)a_0 \qquad \text{(Eq. 5.2)}$$
$$= (\varepsilon(y) + 1) \times 4.01\text{Å}$$

Here a_0 (4.01Å) is the strain-free lattice parameter of cubic zirconia.

The diffraction angles 2θ of *hkl* peaks of cells are obtained from Eq. 5.2 through Bragg's law:

$$2\theta(y) = 2\arcsin\frac{\lambda_0}{2a(y)}\sqrt{h^2 + k^2 + l^2} \qquad \text{(Eq. 5.3)}$$

On a 1-D diffraction pattern directly "caked" from a Debye-Scherrer pattern, the horizontal axis is the distances between pixels and the centre of the rings (this distance is denoted as r) rather than diffraction angle 2θ. According to Eq. 2.7 (section 2.4.1), the distance r is defined by both sample-detector-distance D and diffraction angle 2θ,

$$r(y) = D(y)\tan 2\theta(y) \qquad \text{(Eq. 5.4)}$$

Based on the first postulate, D_0 (731.93 mm) refers to the centre of the gauge volume (y=2.5 mm). Therefore, the sample-detector-distance D of a cell at position y is given by,

$$D(y) = D_0 + 2.5 - y \qquad \text{(Eq. 5.5)}$$

Substituting Eq.5.5 and Eq. 5.3 into Eq. 5.4, the diffraction peak centre r for a cell at position y is given by,

$$r(y) = (D_0 + 2.5 - y)\tan\left[2\arcsin\frac{\lambda_0}{2a(y)}\sqrt{h^2 + k^2 + l^2}\right] \qquad \text{(Eq. 5.6)}$$

5.1.2.3 Peak shape of a cell

The shape of a Gaussian peak is defined by two parameters: peak width σ and peak height I_{max}. In section 5.1.3.1 it will be shown that the peak width of constitutive cells has very significant impact on the difference between the average and measured lattice parameters.

The rule to determine the peak shape of a single cell is to find the best pair of σ and I_{max}, which give the closest match between simulated (the sum of Gaussian peaks produced by constitutive cells) and experimental *hkl* peak. An experimental 1-D diffraction pattern of zirconia is shown in Fig. 5.2.a, and its *111* peak is shown in Fig. 5.2.b. Three pairs of σ and I_{max} (**for a single cell**) were used to simulate *111*difraction peak (the **sum** of many Gaussian peaks, shown in Fig. 5.2.c). In order to ensure consistency in the three simulated peaks, their integrated intensity are intentionally chosen to be equal (the product of σ and I_{max} is 150). The peak widths of constitutive Gaussian peaks in the three simulated peaks are 0.1, 0.3 and 0.5 for green, blue and black curves respectively. By comparing the three simulated peaks with the experimental peak (Fig. 5.2.b), it is found that the one with σ=0.3 is the most similar one to the experimental observation. Therefore, in the results and discussion section (section 5.1.3), the peak width is used to perform error analysis between average and simulated lattice parameters.

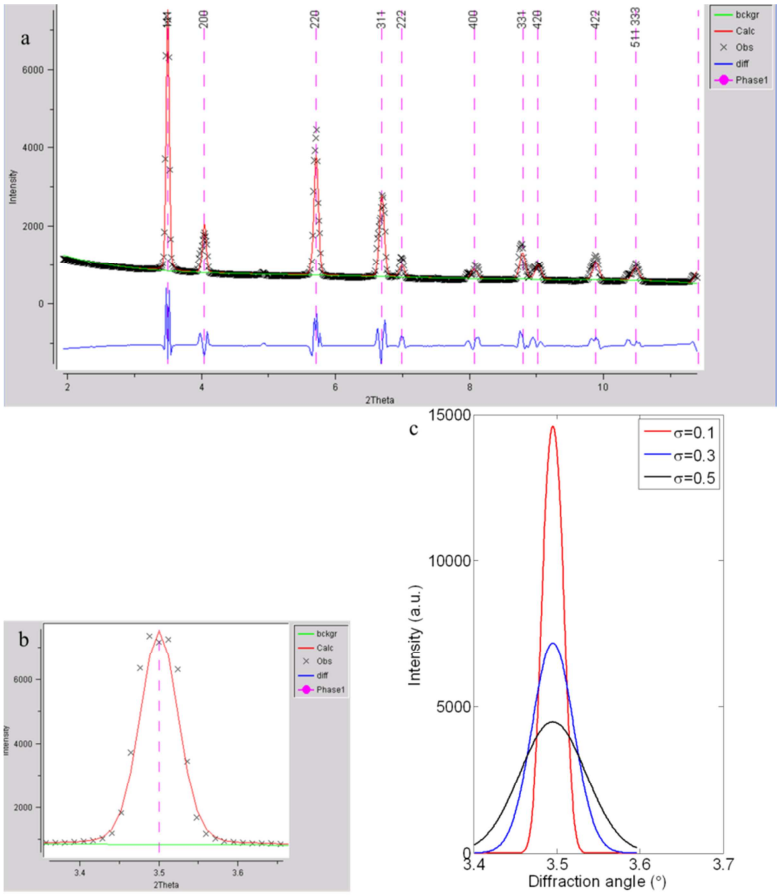

Fig. 5.2 (a) A diffraction pattern line profile of zirconia in vertical (longitudinal) direction at a particular x and ϕ position, (b) 111 diffraction peak of the pattern in a and (c) the simulated 111 peaks corresponding to three peak widths of a cell (red-0.5, blue-0.3 and black 0.1).

5.1.3 Results and discussion

5.1.3.1 Error analysis results

Four different types of strain (lattice parameter) variation (shown in Fig. 5.3) were considered: 1) constant, 2) linear, 3) quadratic and 4) step. The simulation parameters and results of these four types of distribution are present in Table 5.1. The strain range (second column in the table) is defined as the variation of lattice parameter from the average lattice parameter in terms of strain (Eq. 5.1). The elastic strain limit for cubic zirconia is about ± 600

microstrain (units of 10^{-6}) so that the strain range for any lattice parameter distribution is intentionally chosen to correspond to the elastic strain limit.

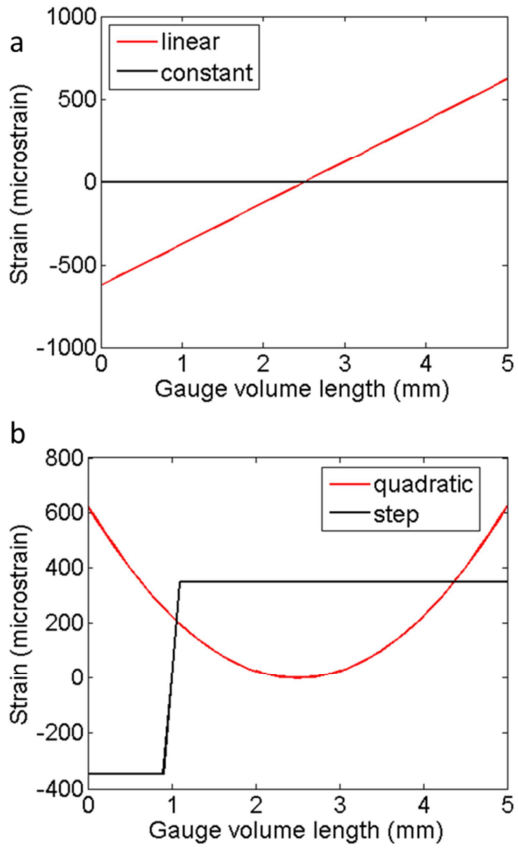

Fig. 5.3 (a) Linear and constant strain variation; (b) quadratic and step strain variation.

Table 5.1 Simulation results.

			Error (microstain)		
Distribution	strain range	range	σ=0.1	σ=0.3	σ=0.5
Constant	[0,0]	0	5.05×10^{-07}	5.81×10^{-08}	2.40×10^{-06}
Linear	[-623.44,623.44]	1246.88	-0.239	-0.7779	-0.8414
Quadratic	[0, 623.4414]	1090.61	-217.94	-26.875	-10.1009
Step	[349.13,349.13]	698.11	123.92	15.12	5.34

The first two distributions (constant and linear) are used to test whether the numerical simulation is reasonable because in principle their errors should be rather small. From Table 5.1, it shows that the errors for both constant and linear strain distributions are negligible (less than 1 microstrain) in strain analysis.

The last two distributions are introduced to imitate some extreme situations, where steep strain gradient is present in a gauge volume and may result in a large error between the average and measured lattice parameters. It is found that for σ=0.3 (the most appropriate peak width for the experimental conditions used) the errors are less than 30 microstrains (-26.875 for quadratic and 15.12 for step), so that these errors are still acceptable for the purposes of strain evaluation (less than 100 microstrain). It should be noted that, for σ=0.1 the absolute errors become larger than 100 microstrains (217.94 for quadratic and 123.92 for step variation). This level of error may not be acceptable in engineering strain analysis. However, as discussed in section 5.1.2.3, the low width (σ=0.1) version of the single cell peak does correspond well to the experimental conditions, so that using that value is not thought to be suitable in this particular simulation.

In summary, based on the simulation results, it is concluded that the lattice parameter determined by single peak fitting to a diffraction peak can be regarded as the average lattice parameter of the entire volume to within acceptable error.

5.1.3.2 Lattice parameter sinogram

An experimental diffraction pattern line profile of zirconia is shown in Fig. 5.2.a. On close examination it is found that most diffraction peaks are split. This peak splitting is caused by many factors such as the strain variation within the gauge volume, geometry of the gauge volume (length) and additional peak broadening due to the beam bandwidth. To our knowledge, it is impossible in all cases, without invoking additional information, to deconvolve precisely the peak splitting to find distinct lattice parameters corresponding to each peak. In the data analysis of the dental bridge experiment, single peak fitting rather than multi-peak fitting was used to extract lattice parameter (d-spacing) from 111 (non-split) diffraction peaks. Translation and rotation scans were performed in the experiment that

spanned the full width of the specimen at every rotation angle, and angular range from 0° to 180°. The lattice parameter sinogram (*i.e*. its variation with the sample rotation angle) is shown in Fig. 5.4. This is the form of data that can be used for strain tomography reconstruction [28].

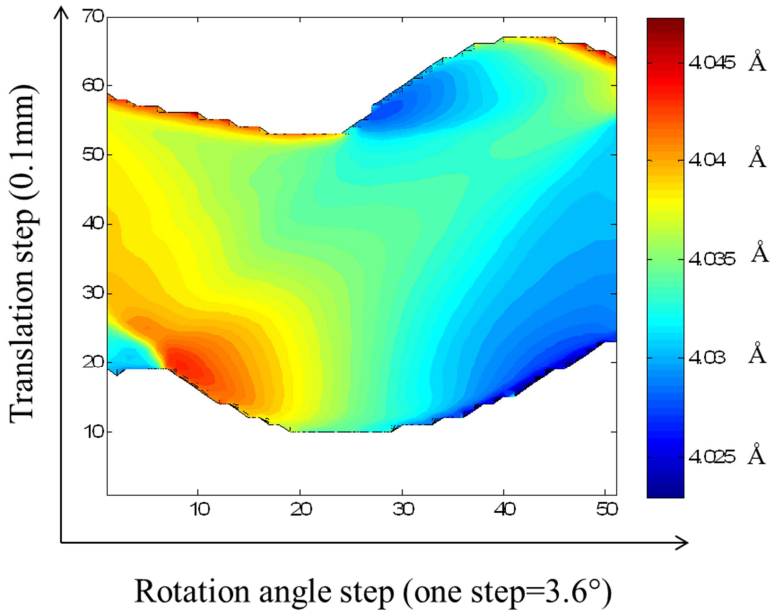

Fig. 5.4 Lattice parameter (determined by single peak fitting) sinogram of the cross-section shown in Fig. 5.1.b

5.2 Measurements of 2D elastic strain tensor

5.2.1 Introduction

The synchrotron x-ray diffraction experiments reported here were carried out at beamline I12, Diamond light source, UK. The multi-element energy-dispersive detector (see Fig. 5.5) (sometimes referred to as the “horseshoe” detector) is installed on this beamline. Its design and data collection procedures allow in principle the investigation 2D elastic strain tensor in test samples. However, until the present study such analysis has not been presented. The principle of the determination of a strain tensor from normal strains at different radial directions on a 2D plane was illustrated in section 3.4.2. Since shear strain cannot be directly

measured by any diffraction techniques, this strain tensor determination technique offers an indirect way to evaluate residual shear strain in samples (within the plane perpendicular to the incident X-ray beam). Diffraction patterns collected by this detector can also be used for quantitative texture analysis using interpretation procedures that will be presented in Chapter 7.

For the first investigation of the 2D strain tensor using the "horseshoe" detector, a non-textured titanium alloy bar sample was selected. The sample was subjected to four-point bending, giving rise to the known principal strain directions. This simplifies the data processing algorithm, and allows ready validation of the interpretation procedures. For the second example, a more challenging problem was selected of mapping the residual strain tensors in several linear friction welds (LFW's) between Al alloy bars. This process is characterised by strong shear strain gradients in the vicinity of bond line, accompanied by significant shortening of the assembly and the associated formation of flash[1], as described below.

Linear Friction welding (LFW) is a relatively novel solid state joining technique offering unique advantages over conventional melting welding techniques. The major stages of deformation that occur in the LFW process can be described as follows: 1) two components are brought into contact and then subjected to reciprocal motion parallel to the interface between them under normal pressure (the linear friction element of the process). The direction of reciprocal movement is shown by the vertical arrow in Fig. 5.6.b. 2) A forging force is applied along the longitudinal direction of the two components (horizontal direction in Fig. 5.6.b). The linear friction generates a large amount of heat, such that the material lying close to the interface is softened. The forging force then causes the expulsion of the softened material from the near-interface zone, and the forging of the two components

[1] materials forced out during the welding

into one. Linear friction welding process is likely to result in strong shear residual strain gradients in the final welded product. It is well known that shear strain cannot be directly measured by diffraction techniques, since the underlying Bragg equation relates the peak shift to the change in the interplanar lattice spacing that does not change under shear. To our knowledge, diffraction measurement of the residual shear strain distribution in linear friction welds has not been reported in the literature. The strain tensor determination method presented below allows the study of the residual shear strain distribution in a LFW weld and other engineering assemblies.

5.2.2 Experimental

5.2.2.1 Multi-directional energy-dispersive x-ray diffraction setup

The multi-directional energy-dispersive x-ray diffraction experimental setup at beamline I12 (Diamond Light Source, Harwell Oxford Campus, UK) is shown in Fig. 5.5.a. The front view of the "horseshoe" detector is shown in Fig. 5.5.b. The multi-element detector consists of 23 elements, or cells. Each detector-element can record an energy-dispersive diffraction line profile. The azimuthal angular difference between two neighbouring detector-elements is 8.18°.

The diffraction geometry of one detector-element is illustrated in Fig. 5.5.c by showing a diffraction plane view. Two slits (S_1 and S_2) are used to collimate the incident beam to define the beam cross-section of the size 0.8μm×0.8μm. Two other slits (S_3 and S_4) are placed downstream of the sample to collimate the diffracted beam to a cross-section typically less than 1.0μm×1.0μm. Owing to the intersection of incident beam and diffracted beam, a diamond-shaped diffraction gauge volume is defined (see Fig. 5.5.c). The diffraction angle for each element-detector is around 5^o, and this angle is precisely determined through a calibration process by using a powder standard with precisely known lattice parameters

(NIST Si or LaB_6). Since the diffraction angle (5^o) is very small, strain measurement direction for each detector element lays only 2.5^o out of the sample plane (that is perpendicular to the incident beam). It is safe to assume that each detector registers the strain along the radial direction defined by the azimuthal position of each detector-element: error analysis demonstrates that the *relative* error that arises from this assumption does not exceed 0.1%.

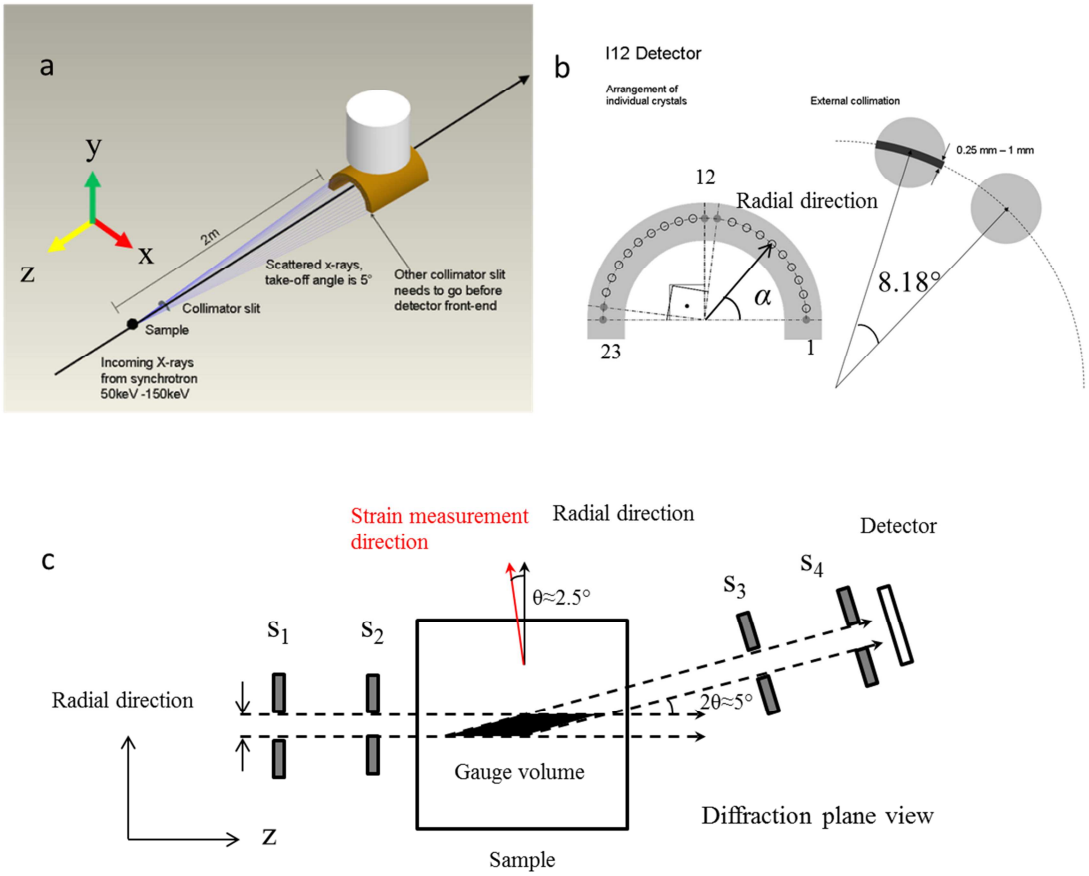

Fig. 5.5 (a) High energy multi-element energy-dispersive x-ray powder diffraction setup, (b) front view of multi-element detector and (c) diffraction geometry for a detector element

5.2.2.2 A Ti−6Al−4V alloy four-point bent beam

A Ti−6Al−4V alloy bar with a size of $1.7 \times 4.5 \times 60$ mm^3 (shown in Fig. 5.6.a) was machined from the middle of a Ti−6Al−4V alloy plate, which was produced by vacuum arc melting above the phase transus temperature followed by cross-rolling and annealing to

minimize the crystallographic texture. The microstructure and texture in this material have been studied before and reported elsewhere [106]. The orientation distributions within both phases (α phase-hexagonal close packed structure and β phase-BCC structure) were found to be close to random.

The sample was plastically deformed in the four-point bending configuration and unloaded prior to diffraction measurement, creating a locked-in residual stress–strain state. In the diffraction experiment, the sample was scanned across the beam with a step of 0.1 mm along the middle line of the four point bend configuration (see Fig. 5.6.a).

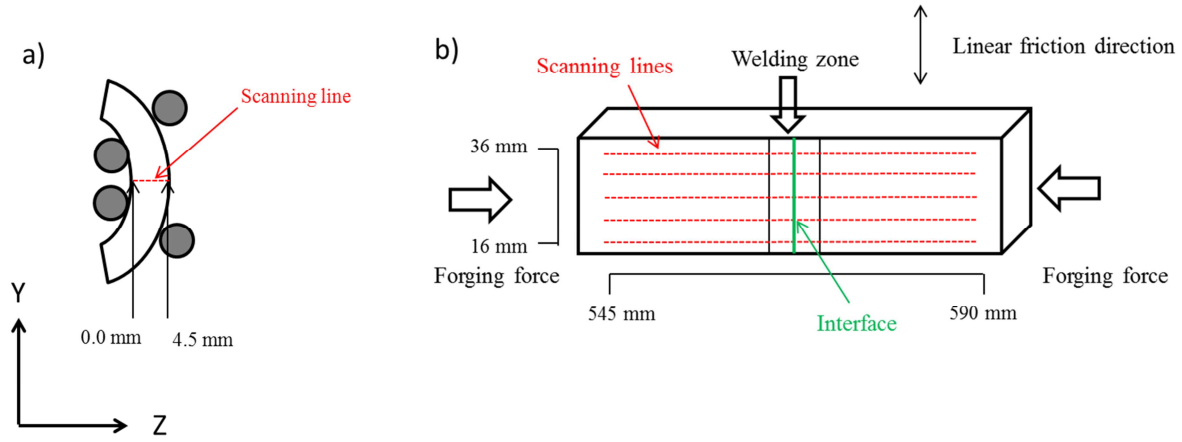

Fig. 5.6 (a) A four-point bent beam and (b) a linear friction welding assembly.

5.2.2.3 Aluminium alloy AA2024 Linear Friction Welding (LFW) assembly

LFW joints were made at TWI (The Welding Institute, Abington, Cambridge, UK) by using different welding parameters bonding together pairs of aluminium alloy AA2024 bars [107] that were manufactured by Hot Isostatic Pressing (HIP) followed by extrusion, which introduced strong textures into the bar material.

At room temperature, the AA2024 alloy has the nominal elastic modulus of 75 GPa and Poisson's ratio of 0.33, and the tensile yield stress of 320 MPa. A welded assembly has

dimensions of ~155×36×15 mm^3 and its geometry is shown in Fig. 5.6.b. Five line scans with the step of 0.333 mm were conducted for each sample, and the scanning lines are illustrated in Fig. 5.6.b. Three LFW samples were measured. The common welding parameters for the three samples were the amplitude and frequency of the reciprocal motion of 2 mm and 50 Hz, respectively. The manufacturing parameters that were different between samples are listed in Table 5.2. The upset in the third column of the table is defined as the total length loss of the two components before and after welding.

Table 5.2 LFW manufacturing parameters.

Sample name	Forging Force (kN)	Upset (mm)
W4	90/90	13.49
W5	77/77	9.51
W7	77/77	12.28

5.2.3 Data processing

5.2.3.1 Pattern fitting and the strain-free lattice parameter

The diffraction patterns from a single detector element and their Pawley fitting by GSAS of the Ti−6Al−4V bent beam and an aluminium LFW sample are shown in Fig. 5.7.a and b respectively. It is clear that α-phase (marked as phase 1 in Fig. 5.7.a) in is the dominant phase in this titanium alloy. The unit cell of the α-phase (hexagonal) titanium has two lattice parameters: *a* and *c*. Since this titanium sample is used as a validation of the strain tensor determination technique, only the strains related to lattice parameter *a* will be discussed below for the reason of simplicity. A detailed discussion [108] about lattice strain in such a Ti−6Al−4V alloy shows that the difference between lattice strains calculated from *a* and *c* are minor, and an average of them would be more representative to the real strain of the gauge volume. There is only one lattice parameter *a* for FCC structure aluminium, and it is used for strain calculation for all the LFW samples.

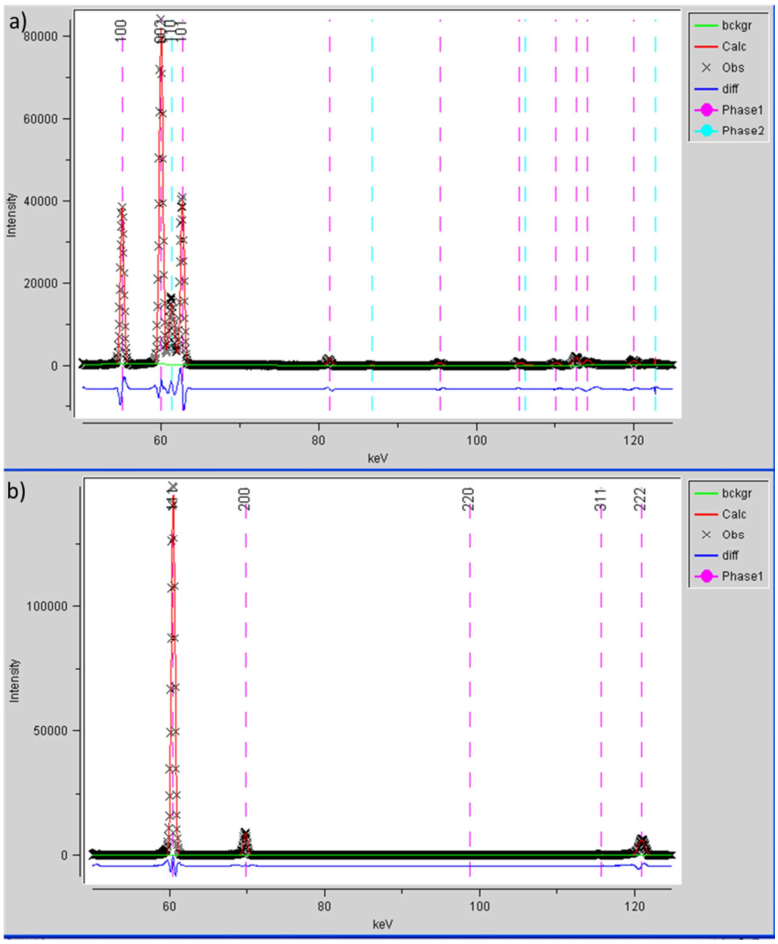

Fig. 5.7 Energy-dispersive X-ray diffraction patterns of the Ti−6Al−4V alloy bent beam (a) and the Aluminium alloy AA2024 LFW sample (b).

It is vital to define a strain-free lattice parameter while using lattice parameters to calculate lattice strains. Two different methods were employed to determine strain-free lattice parameters for the bent beam and LFW samples. The centre of the scanning line of the bent beam is on the neutral axis of the bent beam. Thus, the lattice parameters measured at this point are regarded as a close approximation to the stress (strain) free parameter. For the LFW samples, since the far field (the left or right end) of a sample has experienced the least deformation from the welding processing, it is assumed the measured lattice parameters at the left and right ends of a sample are the strain-free lattice parameters for the left and right half of scanning lines, respectively.

5.2.3.2 Weighted least squared fitting

For all the diffraction pattern line profiles, Pawley refinement, and the outputs were: the lattice parameter *a* and the relative fitting error δ (expressed in units of microstrain and has the same format of Eq. 5.1). Therefore, there were 23 groups of lattice parameters and fitting errors for each particular scanning point.

The radial strain ($\varepsilon_{\alpha\alpha}$) of a scanning point corresponding to each detector-element is written as,

$$\varepsilon_{\alpha\alpha} = \frac{a_\alpha - a_\alpha^0}{a_\alpha^0} \qquad \text{(Eq. 5.7)}$$

Here α is the azimuthal angle of a particular detector-element, a_α and a_α^0 are the lattice parameters measured by this detector-element at the scanning point, and at the strain-free point respectively.

In section 3.4.2 it was shown how the 2D principal strains within a plane are related to the radial strain $\varepsilon_{\alpha\alpha}$ via Eq. 3.26. Considering the fact that the fitting errors of diffraction patterns from different detector-elements can be different, a weighted least square fitting method was used to optimize the fit for the unknown parameters in Eq. 3.26. The purpose of weighting was to ensure that the interpretation favoured the measurements with smaller fitting errors. The error estimator *E* in this weighted least square fitting is defined as,

$$E = \sum_{\alpha=1}^{23} \left(f_\alpha (\varepsilon_{\alpha\alpha}^p - \varepsilon_{\alpha\alpha}) \right)^2 \qquad \text{(Eq. 5.8)}$$

Here f_α is a weighting factor corresponding to the radial strain at azimuthal angle α, $\varepsilon_{\alpha\alpha}^p$ is the radial strain from Eq. 3.26, and $\varepsilon_{\alpha\alpha}$ is the measured radial strain.

We define f_α to have the following form:

$$f_\alpha = \frac{1}{\delta_\alpha^0 \times \delta_\alpha} \qquad \text{(Eq. 5.9)}$$

Here δ_α^0 and δ_α are the fitting errors (uncertainties) of the strain-free and the measured point obtained from the detector-element located at angle α. If the fitting error for a measured point is large (*i.e.* the measured strain has low accuracy), its weighting factor becomes small, so that the measurement contributes less to the weighted fit than other more accurate measurements in the optimization dataset.

In order to judge the goodness of the optimization, a normalized quality function is defined as,

$$R_p = \frac{\sum_{\alpha=1}^{23} (f_\alpha (\delta_\alpha^0 - \delta_\alpha)^2}{\sum_{\alpha=1}^{23} (f_\alpha \delta_\alpha^0)^2} \qquad \text{(Eq. 5.10)}$$

This quality function allows the evaluation of the credibility of the principal strains and directions (the complete strain tensor) determined by the optimization of Eq. 3.26: the bigger the R_p value, the less accurate is the result for the corresponding strain tensor.

5.2.3.3 Strain tensor analysis for the Ti alloy bent beam

Owing to the isotropic diffraction of x-rays from the non-textured bent beam, the diffraction patterns recorded by the 23 detector-elements have very similar intensity and signal-to-noise ratio. The fitting errors for different detector-elements are almost the same, and the weighting factors defined by Eq. 5.8 can be taken to be equal to unity.

A result of fitting Eq. 3.26 to the measured strains of at a scanning point of the bent beam is shown in Fig. 5.8. It is clear that the fitting quality is very good and this suggests that this strain tensor determination method is well suited to this sample.

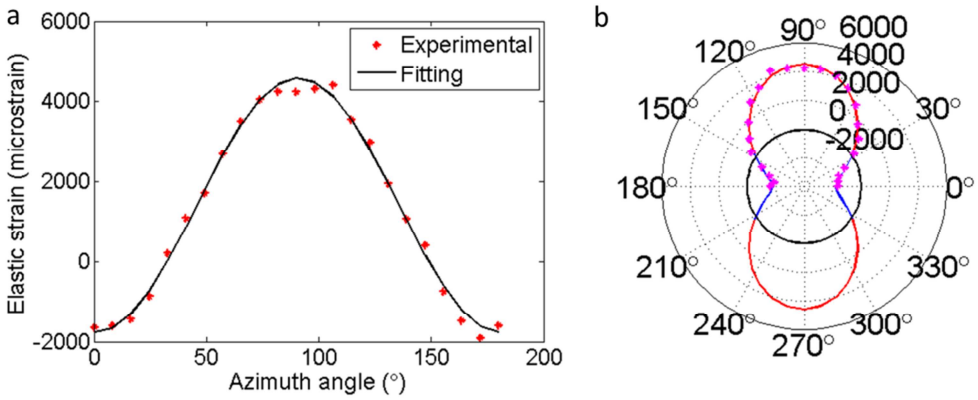

Fig. 5.8 (a) Data fitting to determine a strain tensor and (b) the same data fit for parameter *a* shown in polar coordinates.

5.2.3.4 Strain tensor fitting for linear friction welds

Strong textures are expected to exist in the LFW samples owing to their manufacturing history. The presence of texture in the samples is evident from the diffraction intensity azimuthal inhomogeneity at a single scanning point (see Fig. 5.9). The picture shows that the intensity of any *hkl* diffraction peak (at the same energy) is not uniform along the azimuthal direction. As a result of the diffraction patterns inhomogeneity, the lattice parameters determined from different directional diffraction patterns have different associated fitting errors.

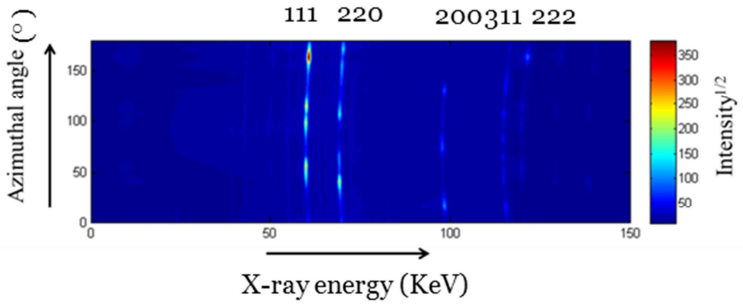

Fig. 5.9 Azimuthal diffraction patterns from a single scanning point on a LFW sample.

Therefore, one should not consider the lattice parameters to contribute equally to the principal strain fitting. The weighted least squares fitting method (section 5.3.2.2) was used

to determine the 2D elastic strain tensors for these samples. Fig. 5.10 shows several weighted fitting examples with different R_p values. The length of red bar in the figure is proportional to the weighting factor defined by Eq. 5.8. It is clear that in the figure the fitting curve (blue line) has a tendency to be closer to the data points with longer bars (bigger weighting factors). Although the fitting quality of this sample is not as good as that of the bent beam (Fig. 5.8), the fitting curves do capture the most accurate measurements.

It should be noticed that in Fig. 5.10.c, a sinusoidal trend among the measurements is captured by the fitting curve even with the R_p value of 80.84%, suggesting that this weighted fitting method helps extract useful information even from very noisy data. In subsequent analysis, any scanning point with R_p value higher than 80% was excluded from the interpretation of strain and stress distribution in order to ensure the accuracy. Most of such points with high R_p values are located within the welding zone of the LFW sample. The reason for the presence of high R_p in the welding zone is due to the strong distortion of the microstructure by high shear during the welding process, causing grain refinement, rotation and alignment [109].

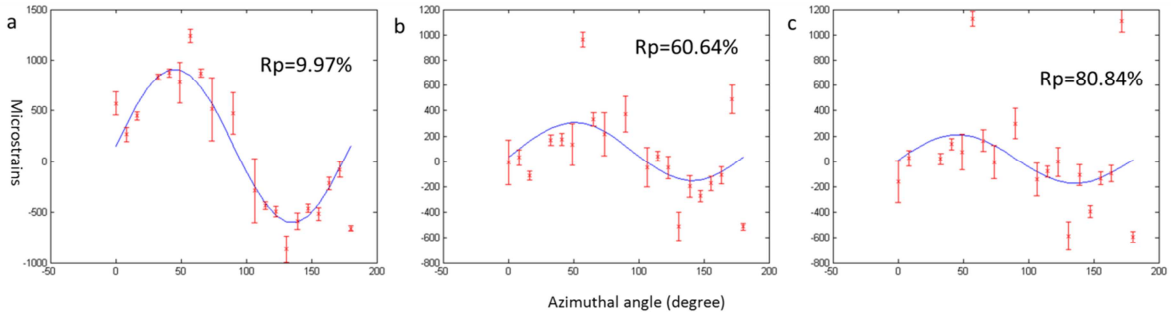

Fig. 5.10 Weighted least squares fitting curves at (a) R_p=9.97%, (b) R_p=60.64% and (c) R_p=80.84%. These three scanning points are from the far field, intermediate and welding zone in section 8.3.1.1 respectively.

5.2.4 Results and discussion

5.2.4.1 Ti-6Al-4V four point bent beam

The measured principal strain direction of the scanning line of the bent beam is shown in Fig. 5.11.a in terms of principal azimuthal angle α_0 defined by Eq. 3.26. It is clear in the figure that α_0 is always close to 90^o, corresponding to the fact that the principle strain directions are along Y and X axes in the laboratory coordinates. This principal direction distribution also agrees with the classical bending theory. Since the scanning line is the middle (symmetry) line of the four-point bend configuration, the bending stress along the longitudinal direction should dominate the principal strain orientation.

We denote the principal strains referring to transverse (X) direction and longitudinal (Y) direction through least square fitting as E11′ , E22′ respectively. Since the principal strain directions are known by Fig. 5.11.a to be along Y and X directions, the strains directly measured by the 12^{th} detector-element (the strain is denoted as E22) (see Fig. 5.5.b) and by 1^{st} and 23^{rd} detector-elements (strains are denoted as E11(0) and E11(180)) correspond to the principal strains E22′ and E11′ respectively. However, it should be noted that the principal strains E22′ and E11′ determined by the optimization are actually the averages through all the radial strains measured by detector-elements, so that they should be more representative (accurate and robust) than the direct measurements E22, E11(0) and E11(180) as discussed in section 3.4.2. Fig. 5.11.b plots the distribution of these five strains (E11(0), E22, E11(180), E11′ and E22′) along the scanning line. Very minor difference between the principal strains and direct measurements is seen.

The strain distribution shown in Fig. 5.11.*a*, *b* and *c* agrees well with the strain distribution on the middle line of a similar four-point bent beam reported by Korsunsky at al [108]. In Fig. 5.11.*d*, the theoretical strain distribution on the line is illustrated before and

after the bending load removed. Using the plane stress deformation assumption and Hooke's law (Eq. 3.11), the elastic strain distribution on the scanning line shown in Fig. 5.11.b are converted into stress distribution shown in Fig. 5.11.c, in which S11 and S22 are the stresses calculated from the direct strain measurements E11(0) and E22, and S11′, S22′ and S12′ refers to the calculation based on the optimized principal strains E11′ and E22′, respectively. It is clear that only one stress component (S22 or S22′) along the Y axis exists on the scanning line, and the remaining stress components are almost zero. This stress distribution again agrees with the fact the scanning line is the symmetry line of the four-point bending configuration, meaning that the principal stress on the middle line can only be associated with the longitudinal (Y) direction.

In summary, the principal strain distribution in the Ti-alloy bent beam sample was successfully identified using the strain tensor determination method, and the results agree with the predictions of the beam bending theory.

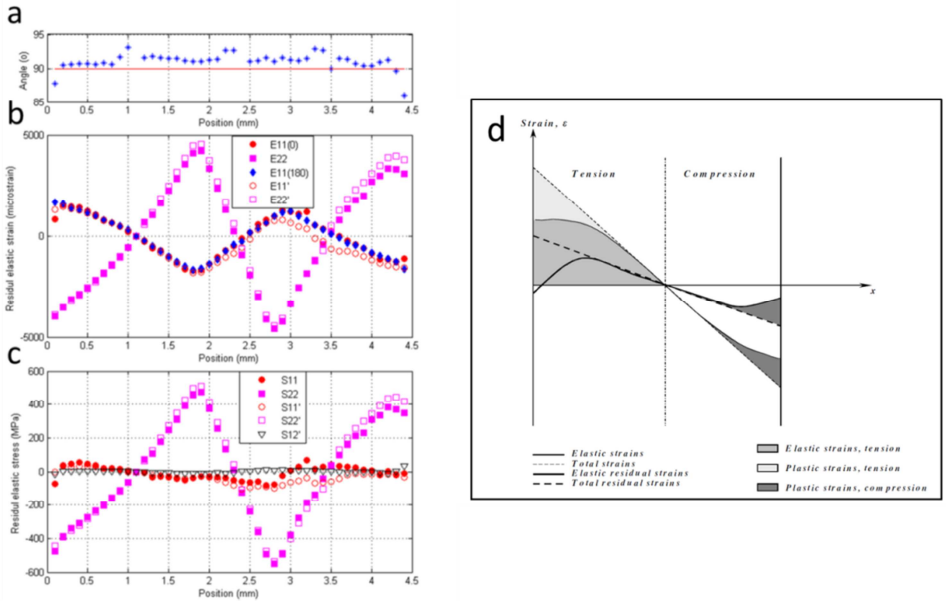

Fig. 5.11 (a) The variation of the principal direction. (b) Comparison of strain values between directly measured (E11(0), E22 and E11(180)) and calculated (E11′ and E22′) strains (c) Comparison of stress values between calculated stresses from directly measured strain (S11 and S22)

and fitting strain (S11′ , S22′ and S12′). (d) The schematic of the (total, plastic and elastic) strain distribution on the scanning line before and after removing the bending load [33].

5.2.4.2 LFW samples

Principal strain mapping

The diffraction patterns of the five scanning lines of all three specimens were processed (i.e. Pawley-refined and sine-wave fitted) to compute their principal strains. The resulting principal strains mappings are plotted in Fig. 5.12. Some conventions are introduced in order to allow the presentation of two principal strains in Fig. 5.12: the green and blue vectors refer to the principal strain ε_1 (within the second and fourth quadrant) and the principal strain ε_2 (within the first and third quadrant), respectively. A strain vector within either the third or fourth quadrant refers to negative (compressive) strains.

Two symmetries are clearly present in the principal strain mapping. The first and second symmetries are with respect to the sample axes along the Y and X directions, respectively. These principal strain symmetries agree with the fact that the deformation that took place during the welding process had the same symmetries: 1) the friction deformation's symmetric line is the central axis along the X direction; 2) the forging deformation symmetric line is the central axis along the Y direction.

It is worth noting that in all three mappings the principal strain magnitude on the central scanning line (Y=26mm) is the smallest and the on the edge (Y=16 and 36 mm) scanning lines, the biggest. However, in conventional diffraction characterization [109] of normal strain of LFW samples, often only scans along the central line in the longitudinal direction (X axis) are reported. The new principal strain mappings reveal the fact that the residual strain magnitude is the smallest on this central line, and that more attention should be paid to other locations on the sample.

It is apparent from visual examination that sample W5 appears to have the greatest strain magnitudes. At first sight, this appears to contradict the fact that sample W5 should have experienced the smallest deformation under the smallest forging force (77KN) and upset (9.51 mm).

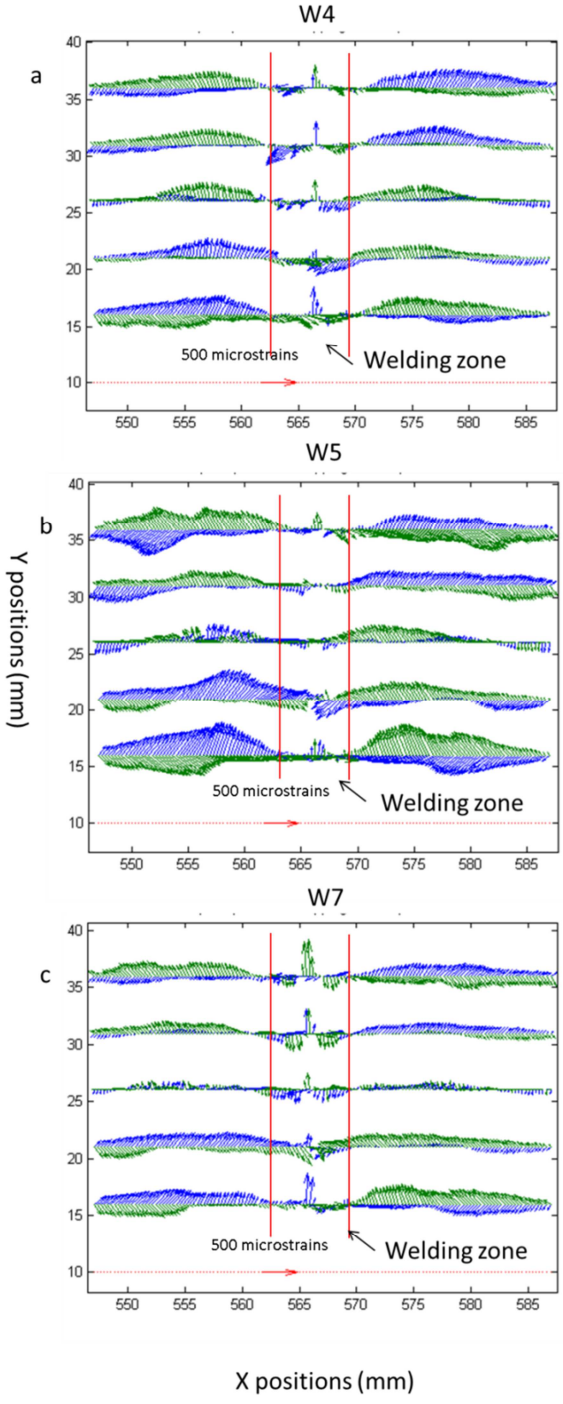

Fig. 5.12 Principal strain mappings samples (a) W4, (b) W5 and (c) W7.

Maps of strain components under lab coordinate (E_{11}, E_{22} and E_{12})

In the welding process, each side of a LFW sample mainly experiences two kinds of mechanical loading: one is compression by the forging force along the longitudinal (X) direction, and the other one is frictional (shear) deformation along the transverse (Y) direction under the friction force acting along the interface. Therefore, it is worth studying the normal strains (E_{11} and E_{22}) along the main deformation directions (X and Y) and the corresponding shear strains (E_{12}) distribution on a sample. The normal strains (E_{11} and E_{22}) are directly computed by Eq. 3.26 from the principal strains (Fig. 5.12) by setting the orientation angle α (relative to the most positive principal strain direction) equal to 0^o and 90^o, respectively. For the calculation of the shear strain (E_{12}), Eq. 3.26 can be rewritten in below format,

$$\varepsilon_{\alpha t} = (\varepsilon_2 - \varepsilon_1) \times \cos(\alpha - \alpha_0) \times \sin(\alpha - \alpha_0) \qquad \text{(Eq. 5.11)}$$

Here $\varepsilon_{\alpha t}$ is the shear strain between a radial direction with azimuthal angle α and its transverse direction, ε_1 and ε_2 are two principal strains, α_0 is the corresponding azimuthal angles for this pair of principal strains. In order to calculate E_{12}, α is set to 0^o.

It is well known that, for a 2D strain tensor the max shear strain ($\frac{\gamma_{\max}}{2}$) can be found when the rotation angle between the chosen coordinate and the principal coordinate ($\alpha - \alpha_0$) equals to $\pm 45^o$. According to Eq. 5.11, $\frac{\gamma_{\max}}{2}$ is given as,

$$\frac{\gamma_{\max}}{2} = \pm \frac{1}{2} \times (\varepsilon_2 - \varepsilon_1) \qquad \text{(Eq. 5.12)}$$

In below analysis, the max shear strain will be compared to the shear strains under lab coordinates (**E_{12}**).

The two normal components under lab coordinates of 2D elastic strain tensor **(E_{11}, E_{22})** and the shear component under lab coordinates **(E_{12})** as well as the max shear strain ($\frac{\gamma_{max}}{2}$) of the five scanning lines of the samples are plotted as contours and shown in Fig. 5.13, Fig. 5.14 and Fig. 5.15 respectively.

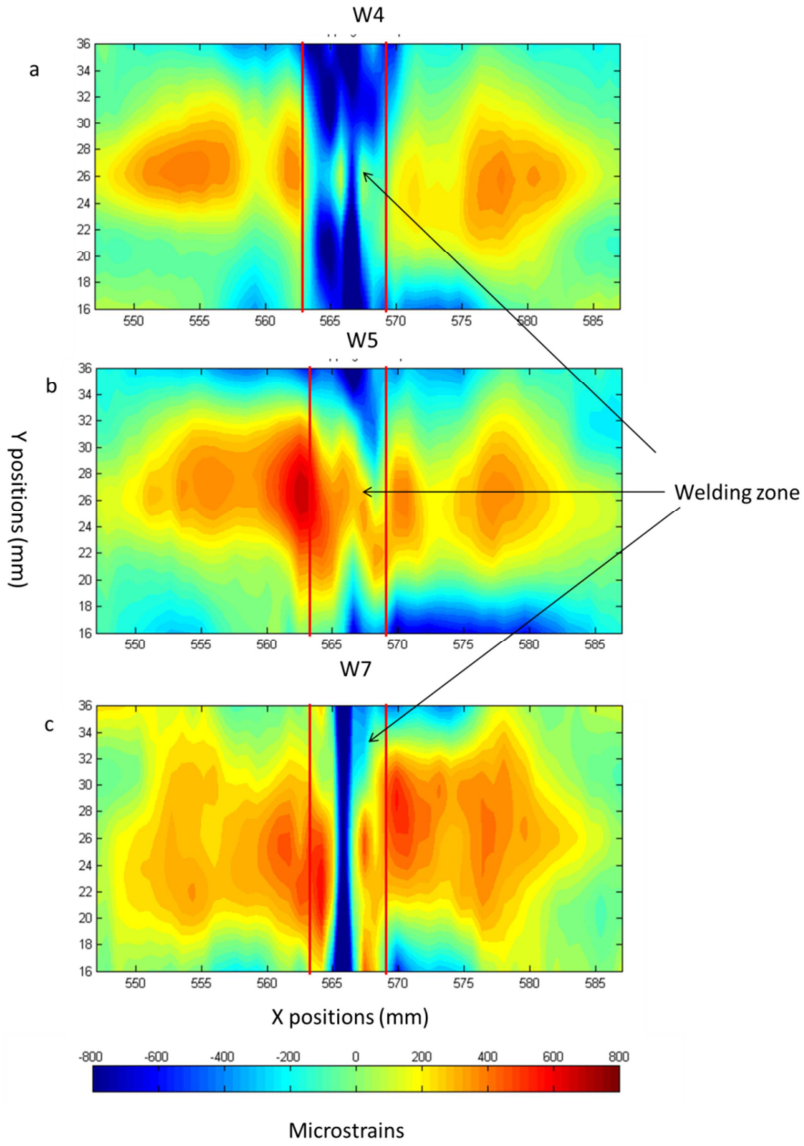

Fig. 5.13 E_{11} strain mappings of LFW samples (a) W4, (b) W5 and (c) W7.

From the E11 strain maps (Fig. 5.13) it is apparent that the E11 strain intensity on the central scanning line (Y=26 mm) along X axis is much higher than the values on the other scanning lines. This observation is different from the principal strain mapping (Fig. 5.12)

where the strain magnitudes on the central scanning line (Y=26 mm) are the smallest. Two tensile residual strains localization zones appear in the left and right sides of all the mappings, and the in terms of sizes of strain localization zones, ranking of the three samples is W7>W5>W4. However, in terms of strain magnitude W5 looks to be the strongest, which is consistent with the observation in the principal strain mappings.

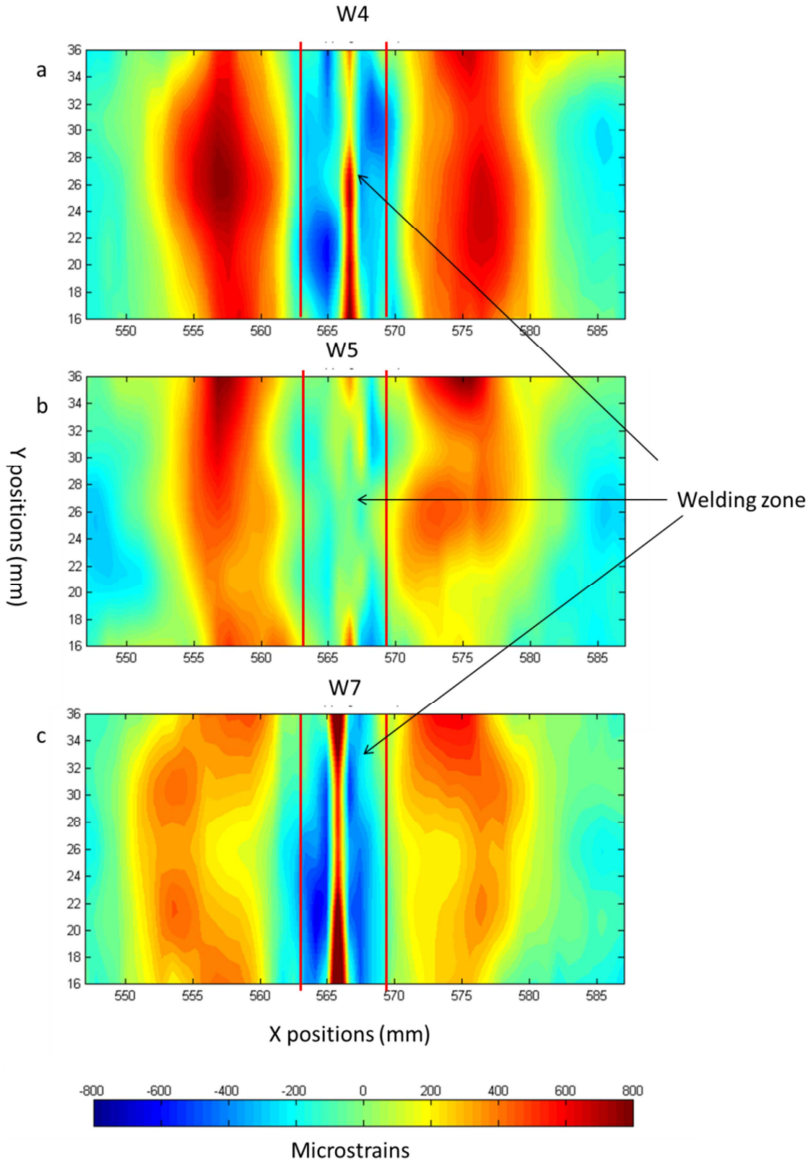

Fig. 5.14 E_{22} strain map of LFW samples (a) W4, (b) W5 and (c) W7.

In Fig. 5.14, two E_{22} strains localization belts exist at the regions from X=553 mm to X=563 mm on the left side and from X=573mm to X=580 mm on the right side. The ranking

of the three samples in terms of the strain magnitude is W4>W5>W7, which is different from the principal strain mapping ranking.

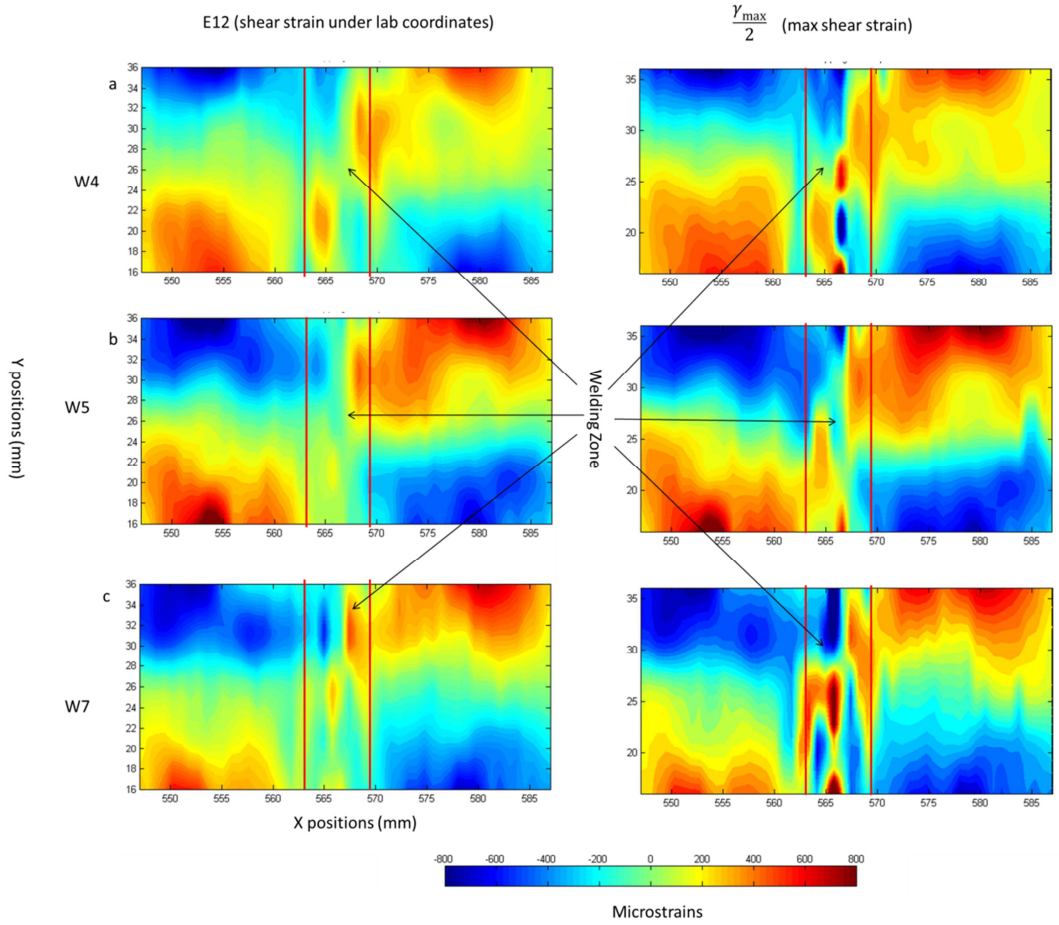

Fig. 5.15 E_{12} (left column) and $\frac{\gamma_{max}}{2}$ (right column) strain mapping of LFW samples.

In Fig. 5.15, the distributions of E_{12} shear strain and max shear strain ($\frac{\gamma_{max}}{2}$) are almost identical. Shear localization zones appear at four corners on the edges at X=554 mm and X=580 mm on each side. This shear strain localization may be related to fact that in the welding process a lot of material was pushed out into the regions next to these corners to form the ear-shaped ‘flash’. It is clear that sample W5 contains much greater shear strain magnitude than both samples W7 and W4.

It should be noted here that there is almost zero shear strain on the central scanning line along the X direction (Y=26 mm). However, the shear strain distribution in LFW samples should not be ignored, since the magnitude of shear can reach 800 microstrains (equivalent to the maximum strain in E_{11} and E_{22} maps) at the localization zones (four corners).

Stress (plane von Mise and Tresca mapping)

Owing to the fact that the Z dimension (16 mm) of all LFW samples is smaller than the other two (X and Y) dimensions, and that the main deformation in the welding process occur along either X or Y directions, we assume that Hooke's law in the plane stress approximation can be used for this particular problem. In addition, the elastic properties of the aluminium alloy can be treated as isotropic. This is due to the fact that its Zener factor is 1.33, which is close to unity (Table 3.2). Therefore, Eq. 3.11 is written as shown below to compute the principal stress from the principal strains,

$$\begin{bmatrix} \sigma_1 \\ \sigma_2 \end{bmatrix} = \frac{E}{(1-\nu^2)} \begin{bmatrix} 1 & \nu \\ \nu & 1 \end{bmatrix} \begin{bmatrix} \varepsilon_1 \\ \varepsilon_2 \end{bmatrix} \quad \text{(Eq. 5.13)}$$

The plane stress *von Mises* stress approximation is computed from the principal stresses by,

$$S_{mise} = \sqrt{\frac{(\sigma_1 - \sigma_2)^2 + \sigma_1^2 + \sigma_2^2}{2}} \quad \text{(Eq. 5.14)}$$

For the *Tresca* stress calculation, we only consider the stress within X-Y plane, and the *Tresca* stress is given as,

$$S_{Tresca} = \left| \frac{\sigma_1 - \sigma_2}{2} \right| \quad \text{(Eq. 5.15)}$$

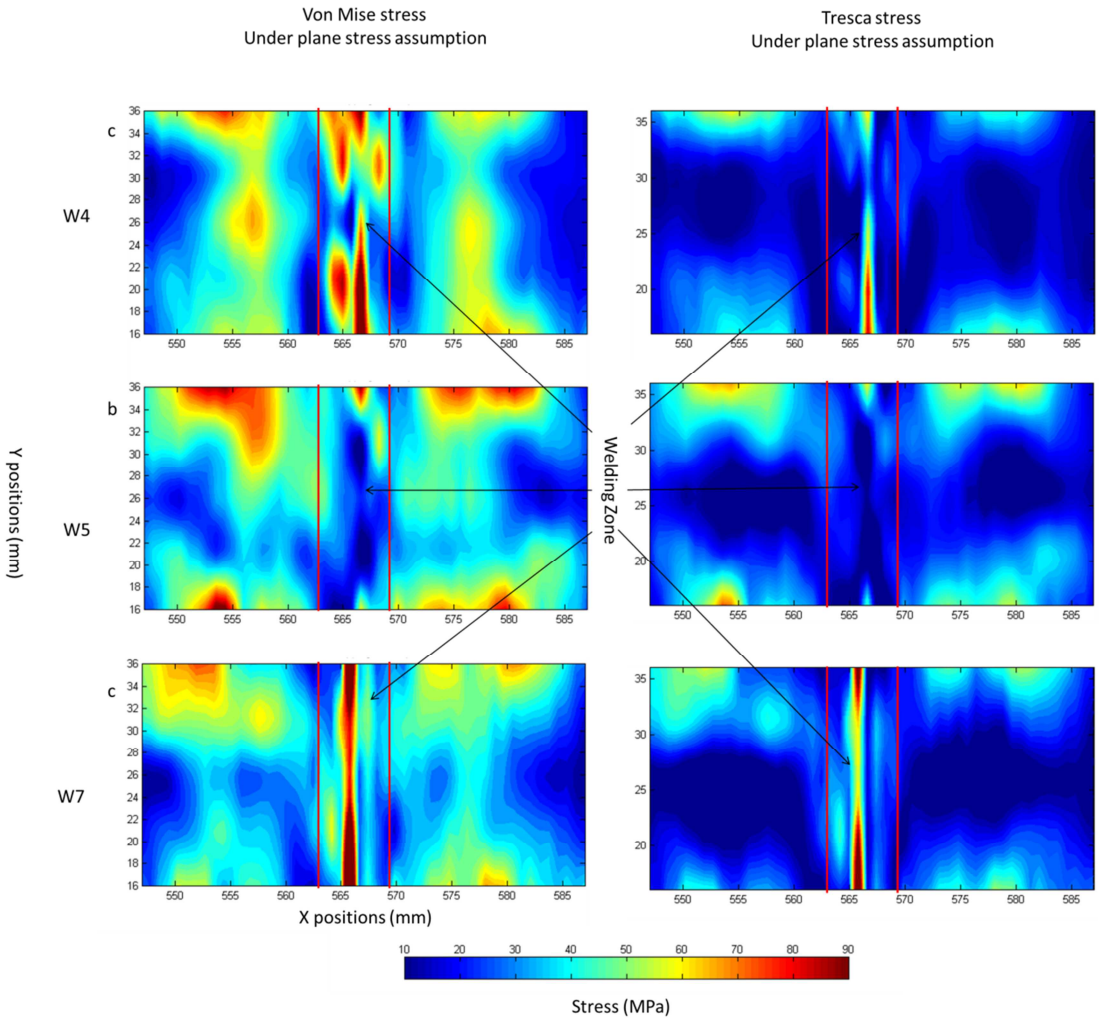

Fig. 5.16 Stress mapping of LFW samples (left column: *von Mise* stress; right column Tresca stress).

The *von Mises* stress and *Tresca* maps for the three samples are shown in Fig. 5.16. It is evident that the distributions of *von Mises* stress and *Tresca* stress are quite similar although the magnitude of *Tresca* stress is smaller than that of *von Mises* stress.

The four corners with largest strain magnitude in the shear strain mappings (Fig. 5.15) also have the highest stress magnitude. The four stress localized corners in sample W5 have the strongest stress magnitude. Since the nominal tensile yield stress for this aluminium alloy is 320 MPa, the proximity of the stress state to plastic due to the presence of residual stress

should be taken into account in any engineering design using these joints in real engineering application.

In summary, the main findings of the 2D elastic strain tensor characterization programme applied to the three LFW samples are:

1) The weighted least square fitting method (section 5.2.3.4) can effectively extract the 2D elastic strain tensor from the multi-element energy-dispersive x-ray diffraction patterns collected from the LFW samples.

2) Sample W5 has the strongest principal strain, E12 shear strain and *von Mise* stresses magnitude, although its forging force and upset are smaller than the other two (W4 and W7) samples. However, the E11 and E22 strain maps show that sample W5 does not have the strongest magnitude. This difference suggests that pure E11 and E22 strain analysis may not be representative enough to show the real residual stress distribution in weld samples, since the E12 shear strain plays a dominant role in determining the principal strain and stress maps.

Chapter 6 Texture interpretation from single exposure monochromatic synchrotron X-ray diffraction

6.1 Introduction

Preferred crystal orientations are almost invariably present in engineering components as a consequence of manufacturing history. In order to characterize the structural anisotropy and the associated anisotropy of mechanical properties, and also to clarify the underlying deformation mechanisms responsible for their formation, it is of particular interest for engineering researchers to analyse the texture distributions and their evolution within the engineering components with high spatial resolution. Geologists, archaeologists, forensic scientists may also gain helpful information from texture characterization to improve their understanding of the history and provenance of the samples. A particular challenge that remains outstanding in the texture characterization field is to develop a fast single-exposure technique to allow efficient texture scanning and mapping, and to streamline the data interpretation.

The key question that often arises in texture studies and that we wish to address here is whether an accurate Orientation Distribution Function (ODF) of a sample can be extracted from a single exposure diffraction pattern obtained with a fixed area detector and without sample tilting. The fundamental significance of single exposure (with fixed sample and detector positions) is the diffraction volume that remains uniquely defined, fixed during measurement. As a consequence, the ultimate spatial resolution achievable by this technique is unaffected by the imprecision of sample positioning in the beam associated with translation and rotation (tilting) stages. In contrast, as the diffraction gauge volume is made smaller by beam focusing or collimation, it becomes inevitably blurred or smeared during sample

rotation and detector scanning. Furthermore, the resulting measurement represents the effect of an aberration over different diffraction volumes. The challenge of using a single exposure X-ray diffraction pattern is associated with the fact that it covers only a small portion of the pole orientation space, putting the accuracy and reliability of the calculated (reconstructed) ODF in question. However, if multiple *hkl* crystal plane reflections are present in the diffraction pattern and are considered together in quantitative texture analysis, the fact that different *hkl* reflections are linked by the ODF may be used to good advantage, so that the effective pole figure coverage is significantly improved. The present investigation focuses on quantitative texture analysis in engineering samples with high crystal symmetries, specifically, cubic phases. The complexity of textural information contained in the ODF of such high symmetry materials is considerably smaller than for samples with low crystal symmetry. It is worth pointing out, however, that low symmetry materials have a larger number of non-redundant diffraction lines that allow probing different portions of their ODFs. Thus the inversion of textures for low symmetry materials may in some cases turn out to be just as well-constrained as in the case of cubic materials.

Recently, experimental procedures for the evaluation of ODF on the basis of single exposure were reported using monochromatic X-rays and Debye-Scherrer 2D diffraction patterns collected using an area detector [110, 111] and energy dispersive X-ray with a multi-element detector [112]. A small number of sample rotations were used on the time-of-flight (TOF) neutron HIPPO diffractometer (LANL, USA) for quantitative texture studies [113] . The key uncertainty is however that, as mentioned in [114], a single Debye-Scherrer diffraction pattern **may be** sufficient to determine an ODF only in some **special** cases. A more systematic approach is needed aimed at validating the texture determination procedures from single exposure.

Due to the large amount of raw diffraction patterns involved, another challenge in texture analysis is the automation and speed of the ODF calculation. In many popular texture software packages, for instance, Beartex [65], MAUD [115] and GSAS [116], the iteration of ODF calculation has to be performed manually, making it is difficult to implement the calculation as an automatic process. Besides, using Rietveld refinement (the core algorithm in those texture software packages) requires users to have considerable experience and demands considerable time and effort to achieve good fit to the patterns. Recently, a Matlab toolbox MTEX [58] has been developed that allows direct estimation of ODF from raw pole figures. The accuracy (quality) of estimated ODF by MTEX is largely dependent on the quality of raw pole figures, because the match is sought directly to the raw pole figures. In contrast, in Rietveld refinement raw diffraction patterns are the fitting objects. MTEX is based on harmonics method (see Section 3.8), but the underlying ODF approximation is by non-negative bell-shaped functions. Hence, the famous inherited “ghost” problem often associated with the harmonics approach is minimised. The Matlab implementation is flexible and can be run repeatedly and algorithmically for many ODF estimations in a relatively short period of time.

The present Chapter introduces a routine that extracts raw pole figures from the single-exposure Debye-Scherrer diffraction pattern and calculates the ODF based on these raw pole figures. Firstly, a numerical simulation is presented to discuss the possibility of ODF estimation from the raw pole figures with single ring pole figure coverage (equivalent to single exposure Debye-Scherrer pattern) for cubic phase polycrytstals. Secondly, we illustrate the entire sequence of steps involved in the novel method, from raw pole figure production to ODF estimation, on the example of two real applications.

The experimental data were collected using a high energy (providing energies up to 150 KeV) monochromatic X-ray powder diffraction setup in transmission geometry at

beamline I12, Diamond Light Source. Debye-Scherrer diffraction patterns were recorded using an area (2D) detector. The main advantages of using high energy X-rays here are the low absorption and very small (less than 10 degrees) diffraction angles, making X-ray path length correction in the raw pole figure production unnecessary. The ODFs derived from the single-exposure pattern are compared with those obtained from multiple exposures with sample rotation. Besides, the comparison of ODF estimation between MTEX and MAUD (Riteveld refinement) from single exposure data is also made. Both MTEX and MAUD can extract ODFs from multiple exposure Debye-Scherrer patterns, but it takes an extremely long time for MAUD to process data (further discussion can be found in section 6.4.2). The comparison of the ODF analysis of multiple exposure diffraction patterns between MTEX and MAUD is not present. The results presented in this chapter provide solid evidence of the validity of ODF estimation from single exposure diffraction pattern. On this basis the approach is introduced to processing large datasets that arise from spatially resolved experiments, *i.e.* texture scanning or mapping.

6.2 Texture simulation

A important concept of the minimal pole figure coverage for determining a single preferred orientation was discussed in Helming's papers [117, 118]. In contrast, the situation addressed in this chapter is such that the pole figure coverage of the single exposure Debye-Scherrer diffraction pattern is fixed by the experimental geometry and monochromatic beam energy. The question becomes modified to the following: With given fixed pole figure coverage, can ***any*** single preferred orientation in the fundamental zone be determined accurately? Furthermore, assuming that the preferred orientation considered is simple enough to be mathematically represented as a linear combination of single preferred orientations, can the linear combination coefficients be determined?

Although the provision of a “pure” mathematical solution to the problem in the form of a theorem or an analytical formula is extremely challenging, alternative routes of obtaining a satisfactory answer to the question exist, and can be pursued. In the present study a set of carefully designed numerical experiments (simulations) was employed to tackle the questions. The simulations were carried out for FCC polycrystals, but they should be applicable to all cubic structure phases, since all cubic phase structures are represented in a similar way in the MTEX algorithm used for ODF.

6.2.1 Probing an arbitrary single preferred orientation

The aim of this section is as follows. By searching through the entire fundamental zone of cubic crystals, single preferred orientations are sought for which the error of ODF reconstruction from the single-exposure Debye-Scherrer diffraction pattern is greatest. To ensure the complete coverage, the fundamental zone of cubic crystals ($0<\varphi_1<360^o$, $0<\Phi<90^o$, $0<\varphi_2<90^o$) is discretised into cubic cells with the dimension $5^o\times 5^o\times 5^o$ in the Euler space (Euler angles are given in the Bunge convention). The entire fundamental zone contains $72\times18\times18=23{,}328$ equally sized cells. A distinct single preferred orientation is associated with each of the cells.

In the Bunge-Euler convention, the three Euler angles (φ_1, Φ, φ_2) refer to the rotations around *Z*, *X* and *Z’* axes associated with the laboratory system of coordinates (see Fig. 6.8). The incident beam direction (*Z* axis) is the central axis of the Debye-Scherrer ring system and is also the rotation axis for Euler angle φ_1. Therefore, any two sample orientations that have different φ_1 but identical other two angles (Φ, φ_2), their experimental pole figures are “identical” but for a rotation around the *Z* axis. The errors of their reconstruction by MTEX are therefore equal. Therefore, for the purpose of answering the question posed above, probing any single (Φ-φ_2) cross-section plane in the orientation space is sufficient to

represent the entire orientation space. This reduces the number of “square” cells needed to provide complete coverage of the entire fundamental zone (and hence the entire orientation space) is given by 18×18= 324 single preferred orientations. This reasoning step reduces the computational expense very significantly, but does not detract from the generality of the result.

The simulation is performed mainly with the help of the MTEX package. In MTEX, a single preferred orientation is defined as a bell-shaped function characterised by the orientation centre (the centre of the cubic cell in Euler space) and a half-width (orientation broadening). In this simulation, “de la Vallee-Poussin” bell-shaped function is used and the half-width is assumed to be either 10^o or 5^o. Some special cases of extremely sharp texture (yet nevertheless polycrystalline!) with orientation broadening smaller than 5^o may exist in nature. However, the techniques for analysing such sharp textures are likely to be more akin to the approach to the study of single crystals. For most samples of common relevance to applications, the 5^o broadening appears to be a good representation of realistic texture half-width. It is worth noting that 5^o is also corresponds to the standard angular width parameter in texture analysis. The simulated ODFs all correspond to FCC crystal structure (space group “m-3m”). No texture symmetry (sample symmetry) was assumed in the simulation. The lattice parameter was set equal to 3.8 Å, *i.e.* the mean value over many cubic phase metals.

The simulated ODFs were “probed” by simulating the high energy X-ray Debye-Scherrer diffraction (the schematic of the setup is shown in Fig. 6.8). Fig. 6.1 illustrates the “numerical experimentation” and the reconstruction procedures for the simulated ODFs. A single preferred orientation with the orientation centre at (φ_1=32.5°, Φ=2.5°, φ_2=5.0°) and 10° orientation broadening is shown in Fig. 6.1.a. Six “numerical-experimental” pole figures of the simulated single preferred orientation referring to single exposure Debye-Scherrer diffraction pattern were extracted from Fig. 6.1.a and plotted in Fig. 6.1.b. Next, these

"numerical-experimental" pole figures were imported into MTEX to reconstruct the ODF (Fig. 6.1.c). As shown in the figure, the difference between a simulated ODF (Fig. 6.1.a) and the reconstructed ODF (Fig. 6.1.c) appear minor to the eye.

In order to quantify the difference between the two ODFs, a normalized square variance sum is (called the "l2 error" in MTEX) was defined as:

$$\varepsilon = \frac{\sum_i (f_1(g_i) - f_2(g_i))^2}{\sum_i f_1(g_i)^2} \qquad \text{(Eq. 6.1)}$$

Here, f_1 and f_2 are the crystallite volume fractions corresponding to a particular orientation g_i of the ODFs. It is evident that the normalized squared variance (called the ODF difference) is proportional to the difference between two ODFs (i.e. the larger ε is, the bigger difference exists between two ODFs), but is normalised with respect to the strength of texture being considered.

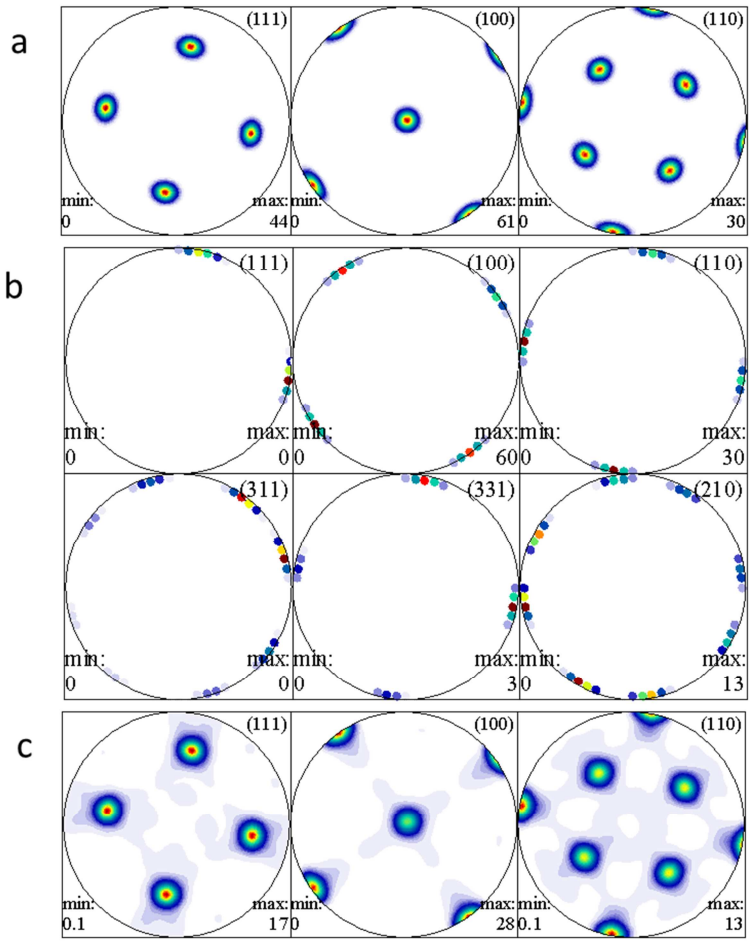

Fig. 6.1 (a) Simulated pole figures referring to single preferred orientation at (φ_1=32.5°, Φ=2.5°, φ_2=5.0°), (b) the corresponding "experimental" pole figures and (c) the reconstructed pole figures.

Fig. 6.2 shows the errors (Eq. 6.1) between the simulated and reconstructed ODFs on two different Φ-φ_2 cross-sections and with two different values of orientation broadening (10^o and 5^o). The two φ_1 angles are randomly chosen to eliminate the effect of periodicity. It is evident that the error contour maps appear to be quite similar at two different φ_1 angles, which conforms with the argument employed for reducing the 3D orientation space to a 2D orientation plane.

It has to be noted that, although the error values in Fig. 6.2.*a* and *b* appears to be much larger than in *c* and *d*, it does not mean that the reconstruction quality of Fig. 6.2.*a* and *b* is worse than that for *c* and *d*. Since different orientation broadening parameters (10^o and 5^o)

were used in the two groups of simulation, comparison of the errors between analyses with different orientation broadening values should be made with care. It might be possible to "normalize" the contour maps with the orientation broadening parameter, but the normalization is not discussed here because the relationship between the error and broadening parameter is not linear. For example, in terms of the above measure the difference between the simulated single preferred orientation ODF with 10^o and 5^o orientation broadening and a uniform (random) ODF are equal to 4.6406 and 13.4479, respectively. These two values may help interpret the error contours for different orientation broadening parameters.

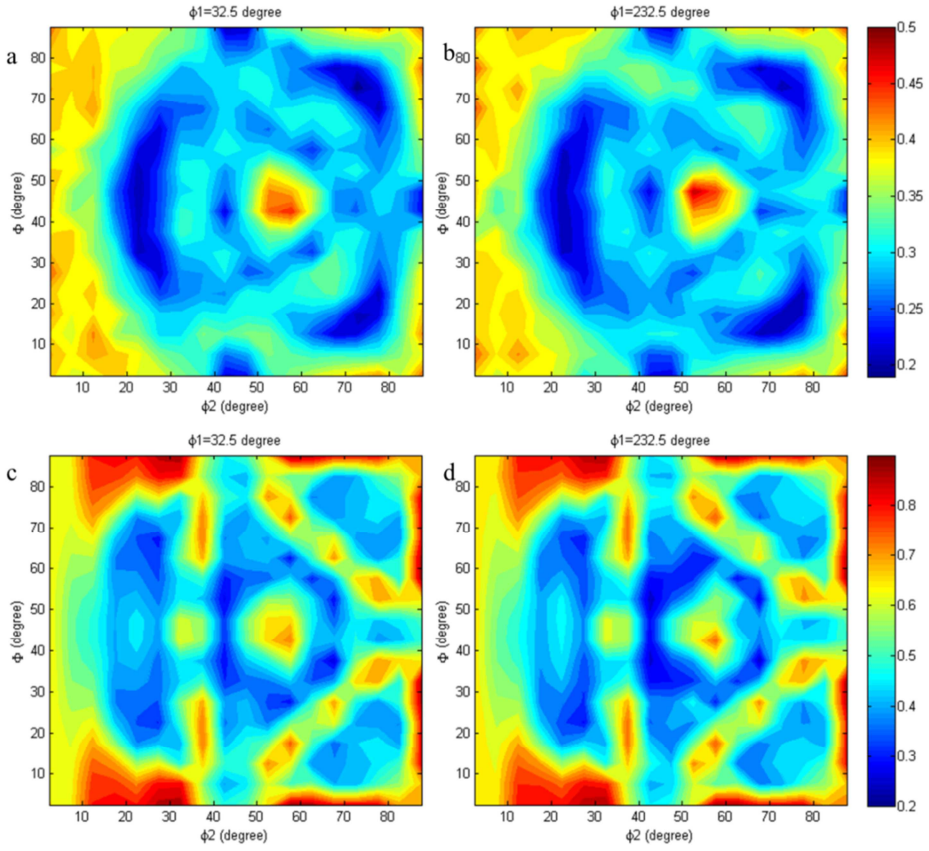

Fig. 6.2 Error maps (*a* and *b*) on Φ- φ_2 cross-section with 10^o orientation broadening of $\varphi_1=32.5^o$ and with $\varphi_1=232.5^o$, respectively; error maps (*c* and *d*) on Φ- φ_2 cross-section with 5^o orientation broadening of $\varphi_1=32.5^o$ and with $\varphi_1=232.5^o$, respectively. The Euler angles are in Bunge conventions, and each Φ- φ_2 cross-section represents one slice of the fundamental zone in orientation space for cubic crystal.

The most meaningful information revealed by Fig. 6.2 is that the maximum error of the ODF reconstruction for 5^o broadening and 10^o broadening are found to be 0.8926 and 0.4854, respectively, and the corresponding orientations were (φ_1=32.5^o, Φ=57.5^o, φ_2=87.5^o) and (φ_1=232.5^o, Φ=52.5^o, φ_2=47.5^o), respectively. It appears that the ODF reconstructions at those two orientations were the least accurate in the entire orientation space. If the ODF reconstruction quality is acceptable for these worst cases, one may conclude that it is safe to probe any single preferred orientation by such a method.

Fig. 6.3 shows the pole figures of the simulated and reconstructed ODFs at these two orientations. It is evident that, for 10^o broadening the difference between the two pole figures is negligible. For the 5^o broadening the reconstructed pole figures show a somehow noticeable difference to the simulated pole figures. Although in Fig. 6.3.d the pole figure maxima (PFM) are captured, in Fig. 6.3.c the PFMs appear somewhat elongated. This may lead to confusion in the texture interpretation in real applications. If a similar simulation were to be performed for the case of smaller orientation broadening (for instance, 2.5^o and 1^o), one may expect the difference between the simulated and reconstructed pole figures with the highest reconstruction error to be even larger than those with the 5^o broadening. Therefore, a conservative recommendation is to restrict the use of the present method to the estimation of ODFs from samples that do not possess very sharp textures, i.e. have orientation broadening less than 5^o.

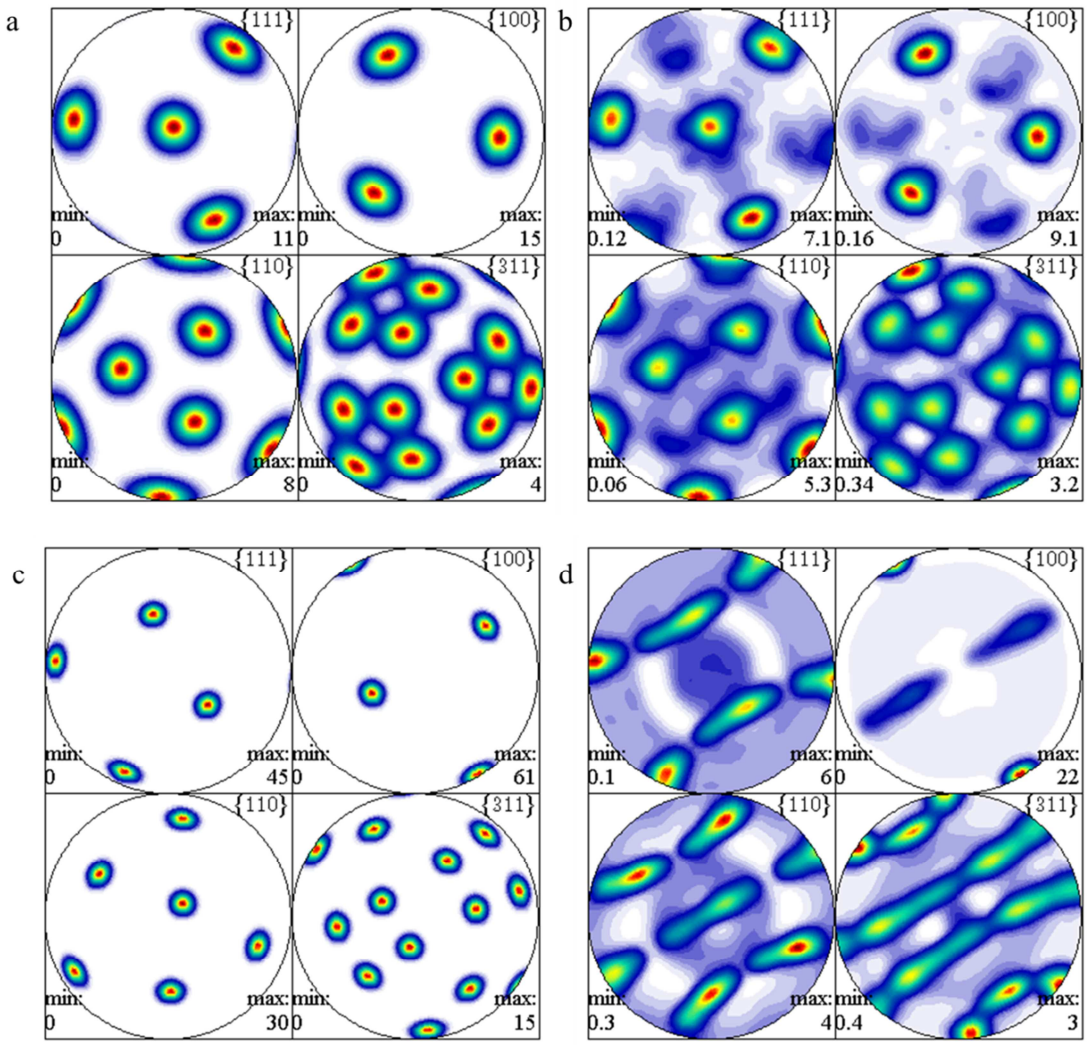

Fig. 6.3 Pole figures (*a* and *b*) of simulated ODF generated by MTEX with orientation centre at (φ_1=32.5°, Φ=57.5°, φ_2=87.5°) and with 10° orientation broadening, and the recalculated ODF by single exposure Debye-Scherrer pole coverage, respectively; Pole figures (*c* and *d*) of simulated ODF generated by MTEX with orientation centre at (φ_1=232.5°, Φ=52.5°, φ_2=47.5°) and with 5° orientation broadening, and the recalculated ODF by single exposure Debye-Scherrer pole coverage, respectively.

Fig. 6.4 shows 111 pole figure coverage of the orientations contained in the two Φ-φ_2 cross-sections considered above. The two instances of pole figure coverage are found to be related by a 200° rotation around the *Z* axis that corresponds to the φ_1 angle difference between them. The markers are densely distributed, since the dimension of the cell was set to only 5°. It appears that the chosen discretisation of the fundamental zone into 5° ×5°×5° cells should lead to a good representation of all possible single textures. Although finer

discretisation is possible, it would only increase the computational expense without improving the accuracy of the result.

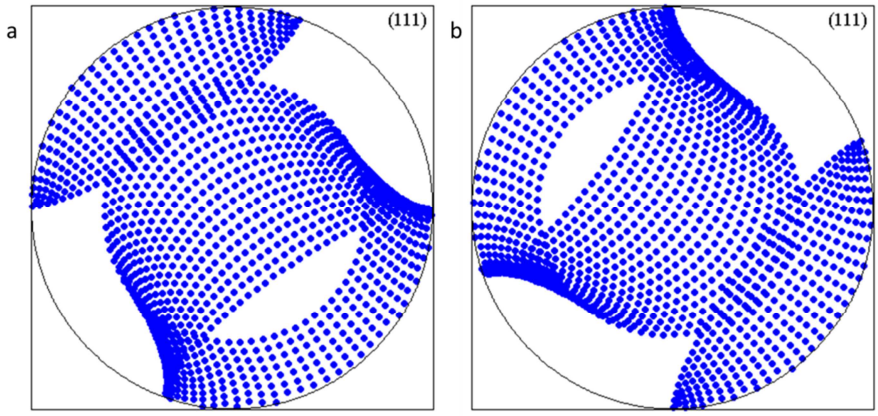

Fig. 6.4 Poles figure coverage (*a* and *b*) of Φ-φ_2 cross-section with $\varphi_1=32.5^o$ and with $\varphi_1=232.5^o$, respectively.

In summary, we conclude that single exposure Debye-Scherrer diffraction dataset can effectively capture all single preferred orientations with orientation broadening larger than 5^o within the fundamental zone of FCC crystals.

6.2.2 Simulated ODF with three preferred orientations combined

We consider that a realistic ODF that may be treated as a linear combination of single orientations. In this section an artificial ODF is created by adding four single preferred orientation ODFs: odf_0 is a uniform function referring to a random texture; the other three ODFs have the same orientation broadening of 10^o, and the orientation centres are ($\varphi_1=10^o$, $\Phi=20^o$, $\varphi_2=100^o$), ($\varphi_1=70^o$, $\Phi=14^o$, $\varphi_2=50^o$) and ($\varphi_1=141^o$, $\Phi=43^o$, $\varphi_2=60^o$) for odf_1, odf_2, and odf_3 respectively. The simulated ODF is mathematically represented by the equation:

$$ODF = 0.2\times odf_0 + 0.3\times odf_1 + 0.2\times odf_2 + 0.3\times odf_3 \qquad \text{(Eq. 6.2)}$$

The pole figures of the 111, 200 and 220 reflections obtained by projecting the simulated ODF are shown in Fig. 6.5.*a*. The three orientation centres (odf_1, odf_2, and *odf3*) are intentionally chosen to place the two PFM spots in the 200 pole figure close to each other, in order to assess the resolution of the ODF reconstruction.

The "ring" pole figures (shown in Fig. 6.5.*b*) similar to those obtained from the six Debye-Scherrer rings (cf. Fig. 6.1.b) were extracted from the simulated ODF. Fig. 6.6 illustrates the ODFs reconstructed from the raw pole figures in two different ways. Firstly, the first **four** reflections (111, 200, 220 and 311) were used to recalculate the ODF. Secondly, the reconstruction was performed using all **six** raw pole figures (111, 200, 220, 311, 331, and 420). This approach offers a means of evaluating the influence of the number of *hkl* reflections on the accuracy of ODF determination. The full sets of pole figures for the two ODF reconstructions are shown in Fig. 6.6. By comparing Fig. 6.6.*a* and *b* with the original pole figures (Fig. 6.5.a), it appears that Fig. 6.6.*b* gives closer similarity to Fig. 6.5.a than Fig. 6.6.*a*. This observation is also confirmed using the error metric of Eq. 6.1: the differences of each of the two reconstructed ODFs from the original ODF are found to be 0.6228 and 0.4159, respectively. Therefore, including more *hkl* reflections into the ODF estimation processes is likely to improve the accuracy of ODF reconstruction significantly.

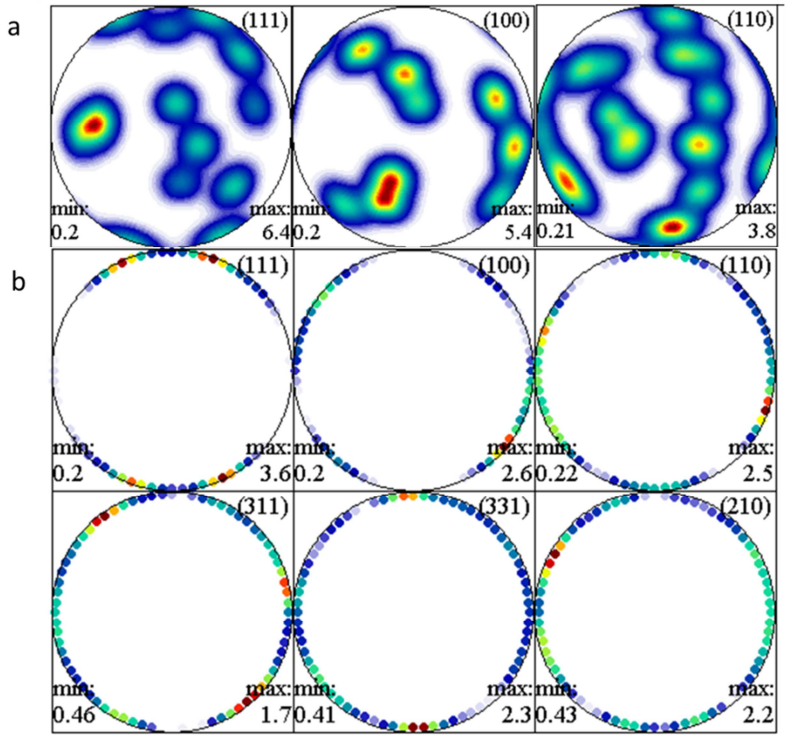

Fig. 6.5 a) Full set of pole figures of the simulated ODF with three preferred orientations; b) six raw pole figures extracted from the full pole figures.

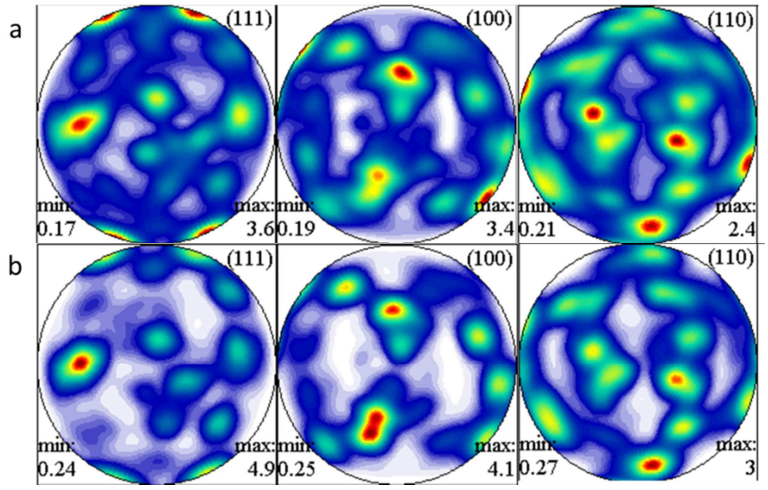

Fig. 6.6 a) Full pole figures projected from the reconstructed ODF using raw pole figures **for four** reflections (111, 200, 220, 311); b) full pole figures projected from the ODF reconstructed using **six** raw pole figures (111,200,220,311,331,420). The corresponding starting pole figures are shown in Fig. 6.5.

6.2.3 Simulated ODF obtained from CP-FEM

The ODF presented in the previous section was merely a linear combination of single preferred orientations. This may not be representative of realistic textures present in practical engineering samples. In order to generate an ODF that is suitably complex and yet realistic, a crystal plasticity finite element model (CP-FEM) [12] was employed to simulate sheet rolling texture formed in FCC materials. [100][101](Huang 1991)In the CP-FEM analysis, a representative volume element (RVE) was given the mechanical properties of copper, *i.e.* the elastic moduli c11=168400MPa, c12=121400MPa, and c44=75400MPa. The plastic deformation at the crystal level was regarded as only being due to crystal slip. The set of 12 octahedral slip systems, {111} <110> was considered active for the FCC phase. There were 512 elements (*i.e.* single orientations) introduced into the RVE in order to represent random sample texture before deformation. The final texture of the RVE is illustrated in Fig. 6.7.a. Thus, the simulated ODF in this section may still be regarded as arising from a linear combination of many single preferred orientations with certain broadening. However, in the CP-FEM simulation this initial ODF undergoes evolution consistent with that experienced by FCC polycrystals during sheet rolling.

The procedures for ODF probing and reconstruction described in the previous section was again employed here. Fig. 6.7.*b* and *c* are the full pole figures of the reconstructed ODFs based on four reflections and six reflections respectively. It is clear that both *b* and *c* capture the key features of *a*, but *c* is much closer to *a*. The errors between the two recalculated ODFs and the original ODF were 0.4418 and 0.2801 for four-reflection and six-reflection reconstructions, respectively. From the present analysis the conclusions is drawn that in order to achieve good accuracy, ODFs should be reconstructed by including the data for as many reflections as possible, and no fewer than four, in any case.

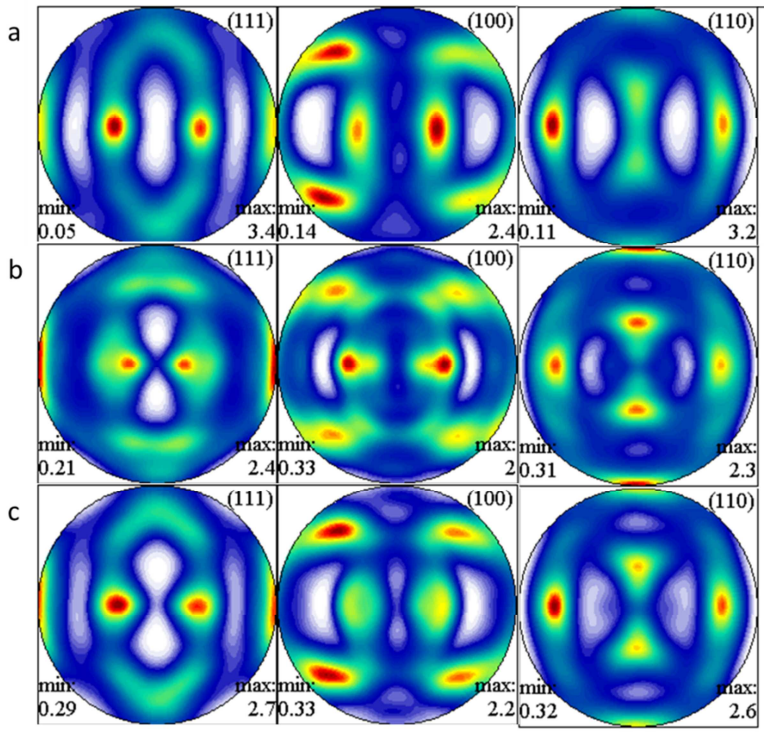

Fig. 6.7 a) Typical pole figures from rolled copper by CPFEM; b) the recalculated pole figures by 111, 200, 220, 311 raw pole figures; c) the recalculated pole figures by on all six (111, 200, 220, 311, 331 and 420) raw pole figures.

6.3 Experimental validation

6.3.1 Samples and experiment setup

Two samples with different deformation histories were chosen to carry out texture analysis. The first sample was an extruded tungsten wire with the diameter of **0.1 mm**. The second sample was a cylinder machined from a cold-rolled copper plate. The diameter of the copper cylinder was **5 mm**. The data collection was performed at beamline I12 (JEEP), Diamond Light Source. The experimental arrangement corresponds to the Debye-Scherrer diffraction setup shown in Fig. 6.8. The sample was mounted on a 5-axis sample stage which allows multiple axis translation and rotation. An area detector (Thales Pixium RF4343) was placed downstream of the sample to collect diffraction patterns. The detector characteristics were: pixel size 148 × 148 μm^2; active area 2880 × 2881 pixels. The beam size was controlled by slits to define a square cross-section (100 × 100 μm^2). For the tungsten wire, the

X-ray beam energy was set at 100 KeV, and the sample to detector distance was 1178.41 mm. For the copper cylinder, the beam energy was 80 KeV, and the sample to detector distance was 1178.40 mm.

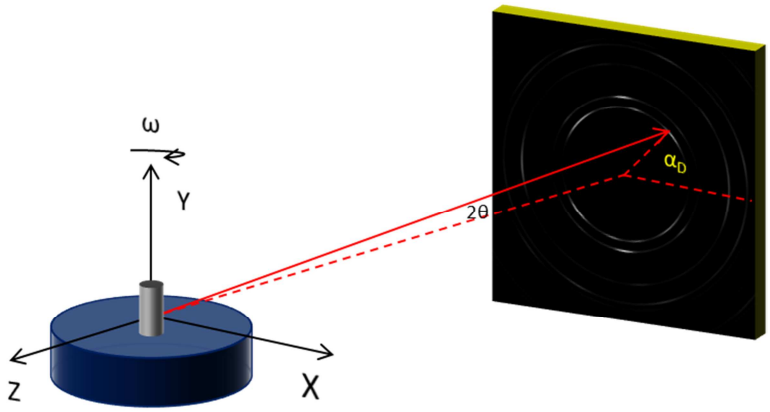

Fig. 6.8 Schematic diagram of the monochromatic X-ray powder diffraction setup (transmission mode).

6.3.2 Raw pole figure production

6.3.2.1 Pole figure coverage at multiple sample orientations

The pole figure coverage for a single exposure (i.e. the sample placed at a particular rotation angle) has been illustrated in Fig. 3.9 of section 3.8.2.2. In order to determine the pole figure coverage for diffraction patterns obtained with multiple sample orientation, the mathematical relationship is derived here between the Debye-Scherrer rings at different sample rotation angles ω, and the raw pole figure. To assist the derivation, Fig. 3.9 is shown again as Fig. 6.9.

In Fig. 6.9.a, a pole ring corresponding to the Debye-Scherrer ring associated with the sample rotation angle $\omega = 0^o$ is plotted on the surface of a unit sphere. The normal vector to the <*hkl*> crystal plane that connects the centre of the unit sphere to the pole ring having the azimuthal angle (α_D) on the area detector (X-Y plane) can be written as,

$$\mathbf{k}(\theta,\alpha_D)=\begin{bmatrix}\cos\theta\cos\alpha_D\\ \cos\theta\sin\alpha_D\\ \sin\theta\end{bmatrix} \qquad \text{(Eq. 6.3)}$$

Here θ is the half of the diffraction angle 2θ.

The sample rotation around Y axis (ω rotation) is introduced in the experiment in order to increase the pole coverage. The matrix for rotation by angle ω is multiplied by the plane normal vector, so that a rotated vector is obtained:

$$\begin{aligned}\mathbf{k}'(\theta,\alpha_D,\omega)&=\mathbf{R}_Y(\omega)\mathbf{k}(\theta,\alpha_D) \qquad \text{(Eq. 6.4)}\\ &=\begin{bmatrix}\cos\omega & 0 & \sin\omega\\ 0 & 1 & 0\\ -\sin\omega & 0 & \cos\omega\end{bmatrix}\begin{bmatrix}\cos\theta\cos\alpha_D\\ \cos\theta\sin\alpha_D\\ \sin\theta\end{bmatrix}\end{aligned}$$

The spherical coordinates of vector $\mathbf{k}'(\theta,\alpha_D,\omega)$ are,

$$\begin{aligned}r&=1 \qquad \text{(Eq. 6.5)}\\ \theta_{inc}&=\frac{\sqrt{k_1'^2+k_2'^2}}{k_3'}\\ \phi_{az,right}&=\frac{k_2'}{k_1'}\end{aligned}$$

Here, the standard notation convention for spherical coordinates is used, as already shown in section 3.7.2: r is the length of the vector; θ_{inc} is the inclination angle with respect to the positive Z axis; $\phi_{az,right}$ is the azimuthal angle on the X-Y plane (when ω equals to zero, this angle equals to α_D).

Finally, the equal area projection method (section 3.7.2.2) is used to project this rotated unit vector onto the X-Y plane:

$$\rho = \sqrt{2} \times \sin(\frac{\theta_{inc}}{2}) \times 90^{o} \qquad \text{(Eq. 6.6)}$$

$$\alpha_p = \phi_{az,right}$$

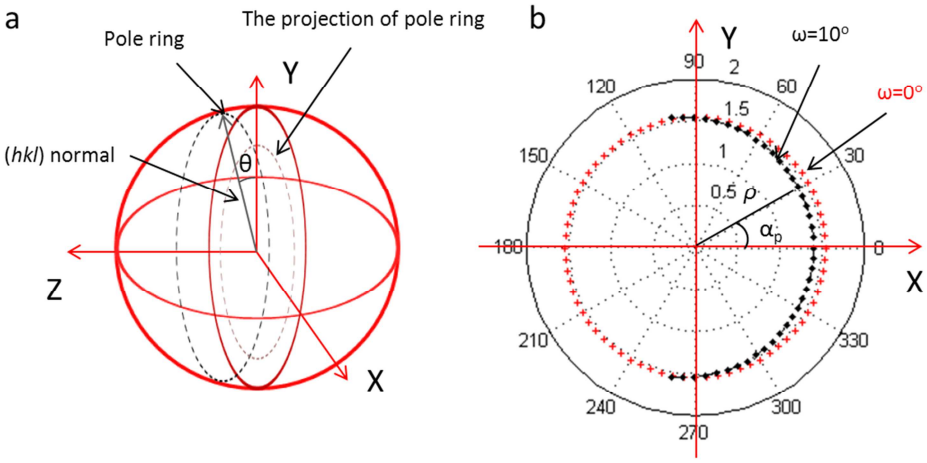

Fig. 6.9 a) The circle mapped out on the unit sphere surface by the points corresponding to a particular Debye-Scherrer ring; b) the equal area projection of rings on the equatorial circle in the X-Y plane.

6.3.2.2 Diffraction intensity correction

The above procedure allows determining the location on the pole figure of the ends of lattice normal vectors that are in the diffraction condition for scattering into points on the Debye-Scherrer rings at different sample rotation angles ω. In order to produce raw pole figures, the diffraction patterns are processed in two steps: 1) Gaussian peak fitting (section 2.4.2) to determine the integrated intensity for each diffraction peak; 2) the integrated intensity is placed into the corresponding cells of the pole figure.

A step of diffraction intensity correction is often needed in the assembly of raw pole figures. This is due to the differential attenuation associated with path length difference for the incident and scattered x-rays. However, for the particular diffraction geometry used in this experiment, the path lengths of the diffracted x-rays are almost identical for all the azimuthal binning portions on a particular Debye-Scherrer ring. The path length ratio

between the longest one and the shortest one is given by $1/\cos(2\theta)$. Since the diffraction angles (2θ) for all the diffraction peaks of interest do not exceed 10^{o}, the length ratio can only vary between 1.015 and 1.0, i.e. can be considered negligible.

6.4 Results and discussion

6.4.1 Texture of extruded tungsten wire

Fig. 6.10.a shows the "raw" pole figures of the tungsten wire based on four reflections: 110, 200, 211 and 310. These reflections have the smallest diffraction angles (so there is no need for diffraction intensity correction) and are the strongest among the visible rings (high signal-to-noise ratio). Although the diffraction angle of the 220 ring is smaller than that of the 310 ring, the 220 ring is ignored in ODF calculation because the texture information contained in it is identical to the 110 ring already used. It was verified that including the 220 reflection made no apparent difference to the calculated ODF.

The raw pole figures were then imported into MTEX and ODF computed by the function "calcODF". There are several key inputs for the function: 1) Sample texture symmetry (see section 3.7.3). For this experiment, no texture symmetry was assumed so as not to miss any texture information in the calculated ODF. 2) Crystal symmetry. Tungsten is a BCC structure material, so that cubic space group "m-3m" is used here. 3) The uni-modal bell-shaped function used to approximate the ODF and to represent its half-width, "de la Vallee-Poussin" function was used and the half-width (orientation broadening) was set to 5^{o}.

The projections of the calculated ODF of tungsten wire are shown in Fig. 6.10.*b*. Due to the fact that the pole densities (Radon transformation of the ODF) in MTEX are approximated by harmonic functions, the pole figures appear smooth in plots. The full pole figures capture all PFMs present in the raw pole figures. It can be concluded that the wire has

a typical “fibre” texture [119]: the normal of the crystal planes {110} is aligned with the extrusion direction of the wire (Y direction in lab coordinates). The normals of other crystal planes appear to be randomly distributed around the extrusion direction. This was evident in the experiment, since the diffraction patterns appear to be identical at any sample rotation angle ω. The fibre texture is well-known to arise commonly in engineering samples manufactured by extrusion. This suggests that the ODF calculation carried out in the current study was successful.

The fibre texture is characterised by the presence of an axis of symmetry, such that the single exposure diffraction pattern of the wire provides the full texture information, even though the pole figure coverage corresponds to only one ring (see Fig. 6.10.a). It should be kept in mind, however, that no sample texture symmetry was assumed in the ODF calculation. This stands in contrast with evidence from the literature, where this symmetry assumption is often used in order to simplify the ODF calculation.

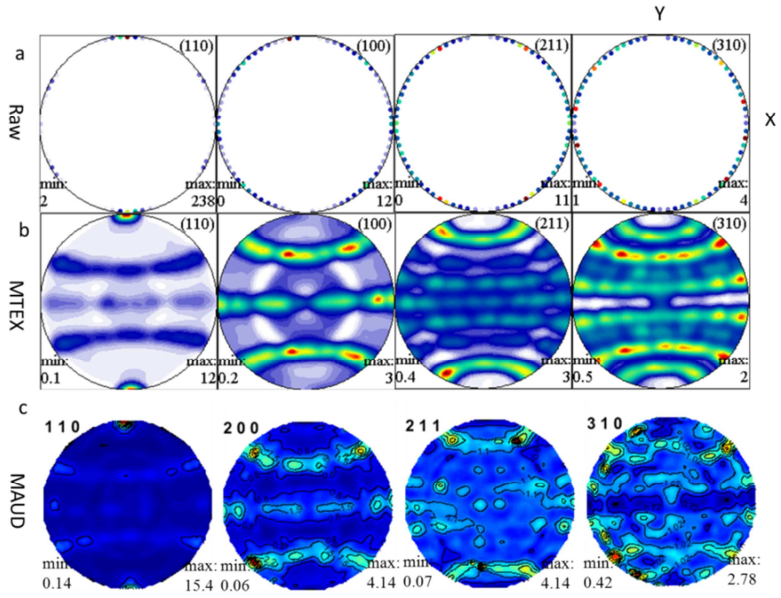

Fig. 6.10 Pole figures of tungsten wire. a) Raw pole figures from a single 2D diffraction pattern; b) the full pole figures calculated by MTEX; c) the full pole figures calculated by MAUD. The maximum intensity in the (110) pole figure in *c* is 15.087, but the maximum limit for colour bar is set to 6 to show more details of the other pole figures.

Fig. 6.10.c shows the full pole figures of the wire calculated by MAUD. No sample texture assumption was made for Rietveld fitting. The pole figures appear very close to those obtained by MTEX, with the pole figure intensity of the PFMs also very similar. Compared with the plots in Fig. 6.10.b, the smoothness of the MAUD pole figures is not as good as of the MTEX ones. This is because the pole figures are not approximated by continuous mathematical functions. There is a general recommendation for the ODFs calculated by MAUD to be smoothed with a Gaussian filter, as this smoothing also helps in removing artefacts from ODF cells. Fig. 6.11 shows the results of Rietveld fitting of the diffraction patterns in MAUD. The fitting is seen to capture the diffraction intensity distribution along the vertical (azimuthal) direction of the raw pattern (apart from the background noise in the lower region), suggesting that the fitting exercise was successful.

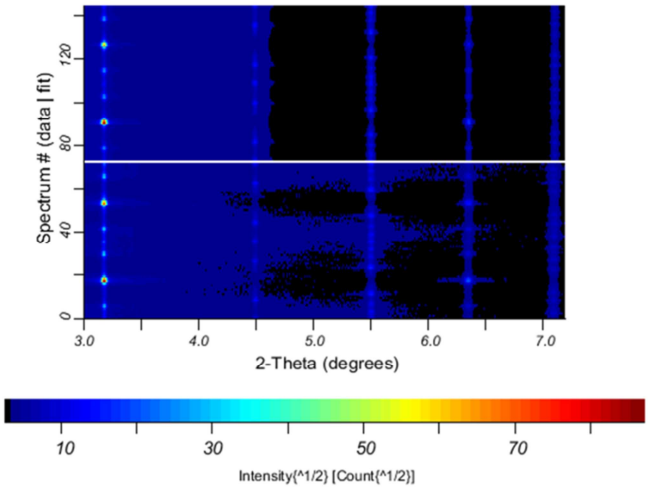

Fig. 6.11 Rietveld fitting of 2D diffraction pattern of tungsten wire by MAUD: lower half of figure: raw diffraction patterns; upper half of figure: fitted patterns.

6.4.2 Texture of copper cylinder machined from a rolled plate

The copper cylinder that was machined from a rolled copper plate so that its axis was aligned with the short transverse direction had possessed texture that displayed no axial symmetry. This case was studied as being representative of the generic texture situation with

a view to compare the accuracy of ODF determination between the techniques based on the analysis of Debye-Scherrer patterns from single exposure and multiple exposures (i.e. involving sample rotation). The cylinder was mounted with its axis aligned parallel to the vertical sample stage rotation axis *Y* that was used to change the sample rotation angle ω in steps of 5^o from 0° to 180^o. Diffraction patterns were collected at each increment of rotation. Four diffraction rings (111, 200, 220, 311) were analysed for ODF evaluation.

Fig. 6.12.a shows the raw pole figures of the single exposure diffraction pattern obtained at ω=0°. Fig. 6.12.b shows the raw pole figures of the diffraction patterns assembled from all ω=0° to 180^o with a step of 5^o (*i.e.* the assembly of 36 diffraction patterns). Fig. 6.12.c shows the pole figures displayed on the standard $5^o \times 5^o$ grid, with the pole intensity of each cell averaged by the correspondent pole intensity in Fig. 6.12.b. The averaging procedures are follows: 1) count how many data points fall into a $5^o \times 5^o$ cell and denote the number as *N*; 2) sum the intensity of the *N* data points and denote the summed intensity as *I*; 3) assign the averaged intensity *I*/*N* to represent this cell. This standard grid averaging is a common data pre-possessing step in the ODF calculation using WIMV algorithm. It should be noted here that both Fig. 6.12.b and 6.12.c have large pole figure coverage (more than 80% of the entire pole figure area), so that they can be used as a comparative reference for evaluating the quality of full pole figure reconstruction by MTEX from the single exposure diffraction pattern. These three groups of raw pole figures were imported into MTEX to calculate ODFs, and the corresponding full pole figures calculated by MTEX are shown in Fig. 6.13.*a*, *b* and *c* respectively.

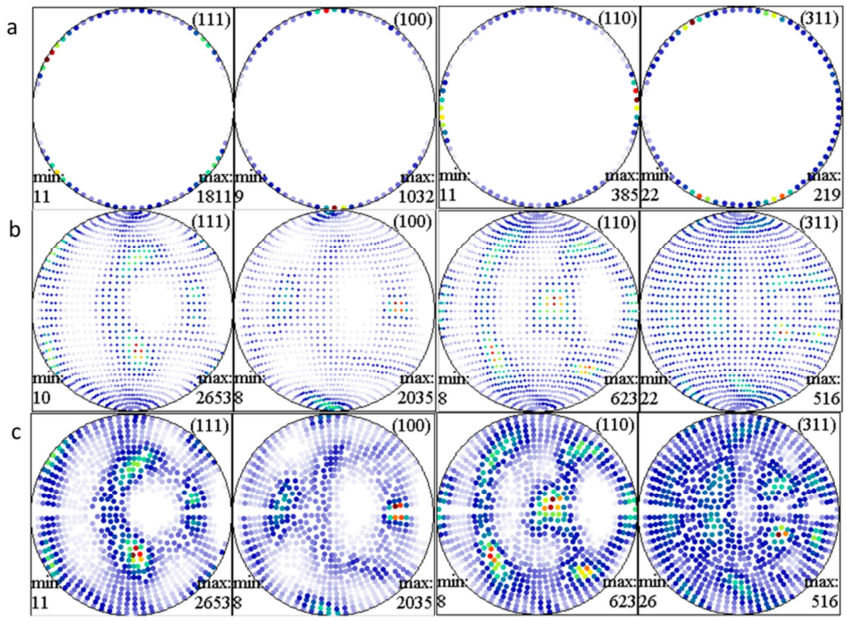

Fig. 6.12 Raw pole figures of the copper cylinder: a) From single exposure diffraction pattern at $\omega=0^{o}$; b) From multiple diffraction patterns and ω coverage from 0^{o} to 180^{o}; c) From multiple diffraction patterns and ω coverage from 0^{o} to 180^{o}, and the intensity averaged within each $5^{o}\times5^{o}$ cell.

By comparing the full pole figures (Fig. 6.13.*a*) of the single exposure diffraction pattern and the raw pole figure (Fig. 6.12.*a*), it is found that all the PFMs in the raw pole figure are captured well by the single-exposure analysis. The raw pole figures with full ω rotations (Fig. 6.12.b and c) and the full pole figures (Fig. 6.13.b and c) also agree well. These agreements confirm that the approach proposed here is able to capture all basic texture information.

The pole intensities in Fig. 6.13.*b* are much higher than in Fig. 6.13.*c*, even though the raw pole figures intensities are almost identical. This means that the texture represented by Fig. 6.13.*b* is sharper than that represented by Fig. 6.13.*c*. The latter raw pole figures are the averages of the former pole figures, so that the "sharpness" of the texture is smoothed by the average operation. The pole intensities of Fig. 6.13.*a* are much smaller than both in Fig. 6.13.*b* and *c*, and the shapes of the PFM regions are slightly different. The PFM regions in Fig. 6.13.*b* and *c* appear to be rotated around the Z axis compared with those in Fig. 6.13.*a*.

These differences may be associated with the reduced precision of single exposure texture analysis compared to the multi-exposure approach. However, another possible explanation must be considered, namely, the fact that the diffraction gauge volume is changing whilst the sample is rotated around the *Z* axis. As illustrated in Fig. 6.14, the texture information probed by the X-ray diffraction setup while rotating the sample refers to different gauge volumes of which only a small portion represents an overlap. In the classical raw pole figure analysis it is assumed implicitly that, despite the change in the gauge volume, all diffraction patterns can be combined into a single pole figure. This assumption remains true only when the texture remains identical (or at least strongly similar) in all those gauge volumes, *i.e.* that the texture gradient in the sample is not very strong. In view of the above argument it is difficult to conclude whether the full pole figure reconstruction from a single exposure (Fig. 6.13.*a*) is more or less reliable than that obtained with much better pole figure coverage, but with changes in the underlying gauge volume (Fig. 6.13.*b* and *c*). The problem of gauge volume change in texture measurement was the main motivation for the author's search for a reliable rotation-free (single exposure) technique for texture measurement.

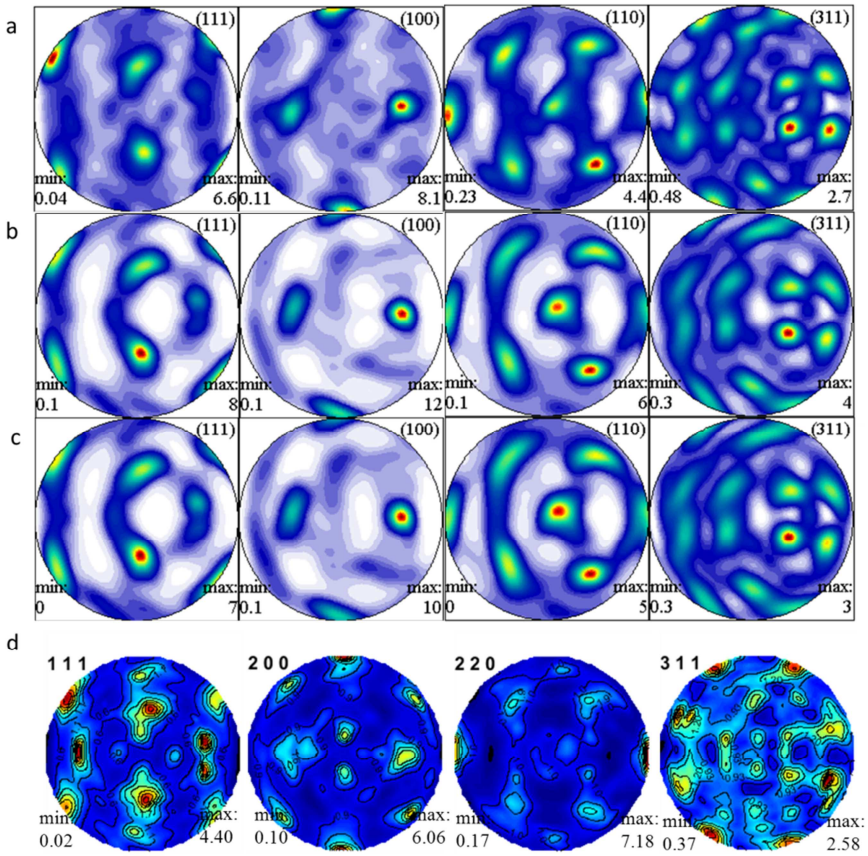

Fig. 6.13 Full pole figures of the copper cylinder. a) Calculated from the $\omega=0^{o}$ set of raw pole figures by MTEX; b) calculated from the $\omega= 0^{o}$ to 180^{o} sets of raw pole figures by MTEX; c) calculated from the $\omega= 0^{o}$ to 180^{o} set of raw pole figures with standard grid by MTEX; d) full pole figures by Rietveld fitting (MAUD) from $\omega=0^{o}$ (single exposure) diffraction pattern.

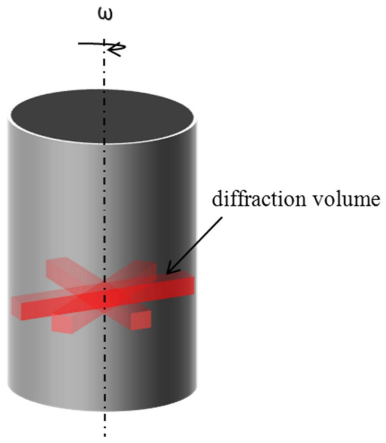

Fig. 6.14 Schematic diagram of the gauge volume change in copper cylinder during sample rotation.

In order to investigate the relationship between the accuracy of ODF determination and the number of sample exposures at different rotation angles, ODF errors were computed according to Eq. 6.1 between the reference ODF and the ODFs reconstructed based on the different number and range of rotation angles. Since the raw pole figures plotted in Fig. 6.12.*b* and *c* have very large pole figure coverage, their calculated ODFs were taken as reference. The errors computed with respect to them were denoted by ε_1 and ε_2, respectively. The plot showing the dependence of the error values as a function of the rotation angle ranges is shown in Fig. 6.15. The two curves show that the errors decrease as more rotation angles are included, suggesting that, as a rule of thumb, the greater number of sample rotations (better pole figure coverage) gives rise to more "accurate" ODF determination.

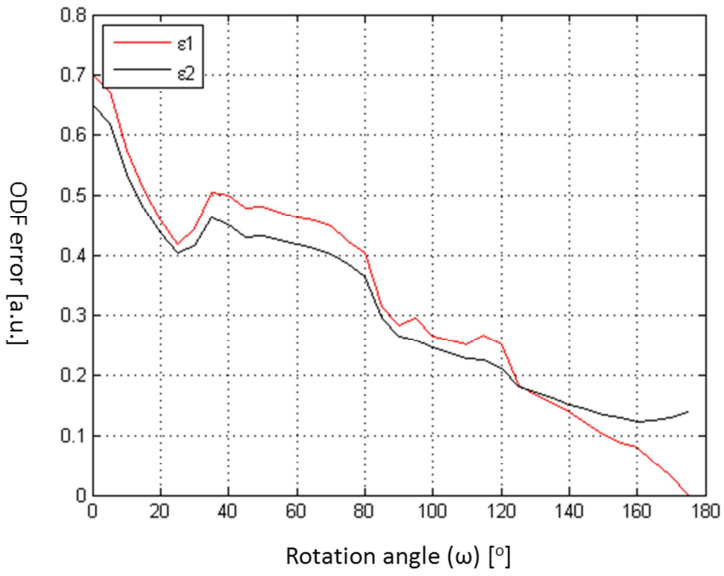

Fig. 6.15 The measure of difference between ODFs with different rotation ranges with respect to the reference ODFs from $\omega=0^o$ to 180^o raw pole figures without grid (upper curve) and $\omega=0^o$ to 180^o raw pole figures with standard 5°×5° grid (lower curve).

It appears that for the copper cylinder the single exposure diffraction pattern is sufficient to extract full preferred orientation information. However, better pole figure coverage improves the accuracy of the ODF analysis. The pole figures in Fig. 6.13 show a typical "cube" texture [119] present in the sample. In Fig. 6.13.*d*, the full pole figures

calculated from MAUD by analysing the $\omega=0^{o}$ diffraction pattern are shown. The PFM regions mostly agree with the ones in the other pole figures in Fig. 6.13, and the minor difference might be associated with the "ghost" (odd) part of harmonic functions or the difference in the ODF representation and calculation algorithms. The Rietveld fitting in MAUD is shown in Fig. 6.16. Similar to the case of tungsten wire, the fitting captures most features of the diffraction patterns, but the match remains imperfect. Diffraction patterns representing multiple rotations were also imported into MAUD, and full pole figures were calculated. The full pole figures are similar to those shown in Fig. 6.13.*d*. The MAUD calculation was found to be time-consuming (approximately one hour on an Intel Core 2 Duo 3.32 GHz CPU and 3.25 GB RAM machine) when 3 rotations ($\omega=0^{o}$ to 10^{o}) were involved. The calculation became practically impossible when a larger number of input patterns was used. In comparison, MTEX only takes 25 seconds (10 seconds for raw pole figure production and 15 seconds for ODF calculation) to run a full ODF estimation process for the same dataset.

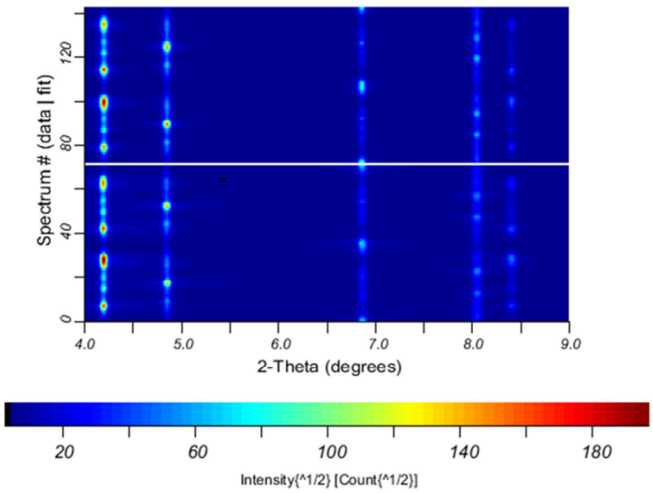

Fig. 6.16 Rietveld fitting of one ($\omega=0$) 2D diffraction of copper cylinder by MAUD: lower part of the figure: raw diffraction patterns; upper part of the figure: fitted patterns.

6.5 Conclusion

A high energy monochromatic X-ray texture measurement setup and the associated data processing routines for pole figure production and ODF estimation using MTEX package have been presented. The ODFs calculated by MTEX agree well with the ones calculated by MAUD. For cubic phase polycrystals and relatively simple textures (those that can be treated as linear combinations of single preferred orientations with more than 5^{o} orientation broadening), the ODFs extracted from single exposure Debye-Scherrer diffraction pattern were found to be largely representative to the full texture. Since this approach does not require any sample rotation and the data conversion is readily performed in Matlab, it is particularly suitable for texture measurements involving with large amount of data, such as texture area mapping and *in situ* texture evolution studies (*i.e.* local analysis with texture change). However, it is also important to note that the accuracy of the "single exposure" approach is directly connected with many factors: for example, the beamline arrangement (beam energy and sample to detector distance, etc.), the crystal symmetry, the sample shape and the texture level (the texture cannot be too sharp).

Chapter 7 The application of texture analysis by single-exposure multi-directional energy-dispersive XRD and TOF neutron diffraction

The previous chapter presented the introduction, discussion and assessment of the use of monochromatic Debye-Scherrer setup for single exposure evaluation of the full texture information. The present chapter is devoted to the application of the single exposure approach to interpret energy dispersive diffraction patterns collected by a multi-directional X-ray detector, and a multi-directional TOF neutron detector.

The first part of this chapter focuses on the texture interpretation of multi-directional X-ray energy-dispersive diffraction patterns of the LFW sample was used for 2D strain analysis in section 5.2. The second part deals with the texture analysis from the neutron diffraction patterns collected by the TOF neutron multi-detector instrument GEM, ISIS spallation neutron source, UK.

7.1 Single exposure texture analysis in a LFW sample using multi-directional X-ray diffraction detector

7.1.1 Experimental

The collection of diffraction patterns of LFW samples was presented in section 5.2. Texure analysis was carried out only the diffraction patterns of the central scanning line of the sample W7. The sample coordinates with respect to the lab coordinates are illustrated in Fig. 7.1.a. Diffraction patterns in the far field (i.e. the right and left end of the sample) display

strong anisotropy along the azimuthal direction (see Fig. 7.1.b) due to the strong texture caused by the manufacturing history.

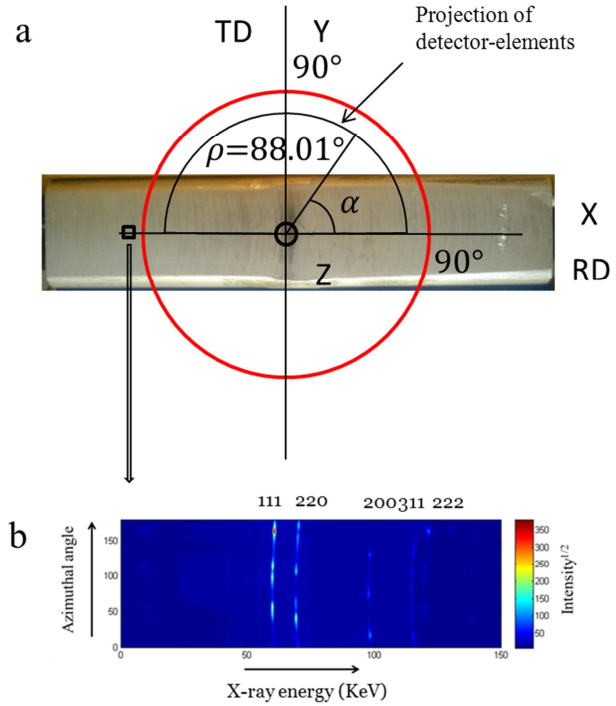

Fig. 7.1 a) Sample coordinates; b) Multi-direcitonal energy-dispersive x-ray diffraction pattern from the location indicated on the sample.

The equal area projection of the pole figure region covered by the “horseshoe” detector is shown in Fig. 7.1.a. The azimuthal angle (within X-Y plane) of each detector element unchanged after the projection. The polar distance ρ of each detector element is calculated by substituting φ=2.5° (half of the scattering angle of 5°) into Eq. 3.36 of section 3.7.2, giving the polar distance of 88° (as shown in Fig. 7.1.a).

Fig. 7.2.a shows the experimental (incomplete) pole figures processed from the single exposure diffraction patterns collected at the centre of the sample (bond line). Fig. 7.2.b shows the full pole figures reconstructed by MTEX. The reconstructed pole figures capture all pole figure maxima (PFM) spots present in the experimental pole figures, although the intensities do not match because of the difference in the normalization (done by MTEX to the

full pole figure). It should be noted that the single exposure pole figure coverage of this "horseshoe" detector is only half that of a Debye-Scherrer ring (see Chapter 6), and the azimuthal resolution is only 8.2° (worse than the binning resolution 5° for the diffraction patterns derived from the Debye-Scherrer rings), so the "horseshoe" detector may be expected to provide less accurate texture information than the monochromatic area detector setup when only single exposure diffraction data is used for texture analysis.

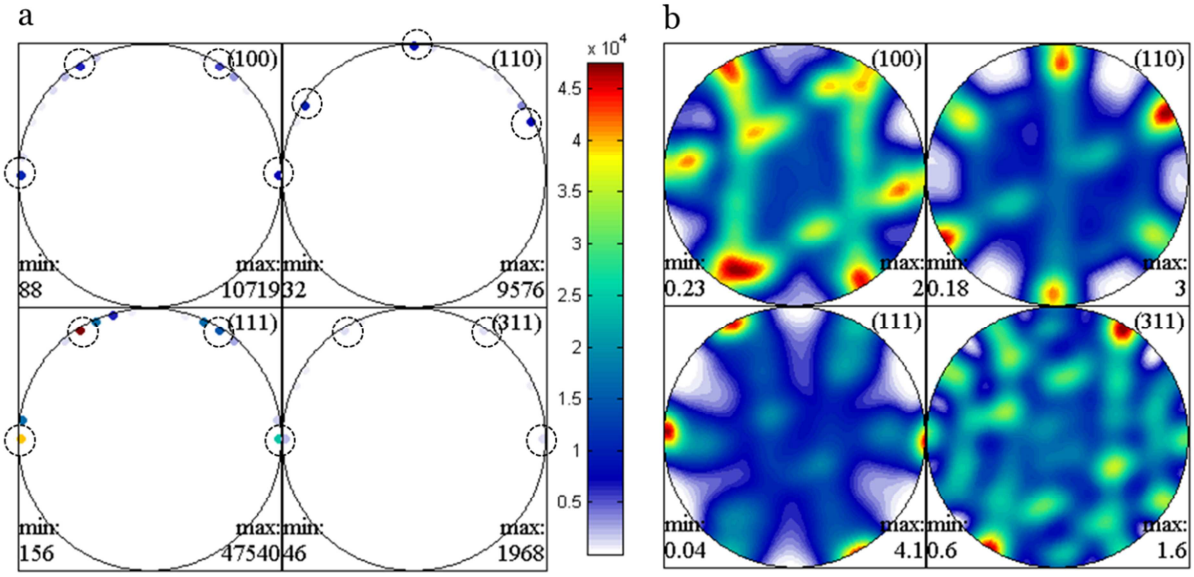

Fig. 7.2 (a) the experimental pole figures at the bond line; (b) full pole figures reconstructed from (a). There are 23 data points in each *hkl* experiental pole figures (a). However, only a few data points are displayed with color becuase the intensity varioation among the data points are huge.

7.1.2 Results and discussion

Fig. 7.3 shows 111 full pole figures for several locations on the scanning line. It is evident that the pole figures are symmetric about the bond line. This texture symmetry is also consistent with the mechanical loading symmetry during the manufacturing process of the LFW joint.

In Fig. 7.3, the pole figures at the far field (distance=-4mm) appear to have features corresponding to rolling deformation and the rolling direction is along the longitudinal direction of the LFW joint. This agrees with the manufacturing history that the two parts of

the LFW joints are manufactured by bar rolling. By comparing the pole figures at positions of -3mm and -2mm, it is evident that a rotation is present between the two about the Z aixs (along the incident beam direction). The pole figures obtained at the location -1mm (close to the bond line) show typical features of extrusion (“fiber”) texture in the longitudinal (X) direction. At the centre of the weldment (position=0mm), the pole figure shows a 6-fold symmetry that is a common feature in 111 pole figures of cubic polycrystals subjected to a simple shear deformation on X-Y plane. The shear texture feature suggests that the main driving force for the texture change at the very centre of LFW joint is the shear deformation during linear friction welding.

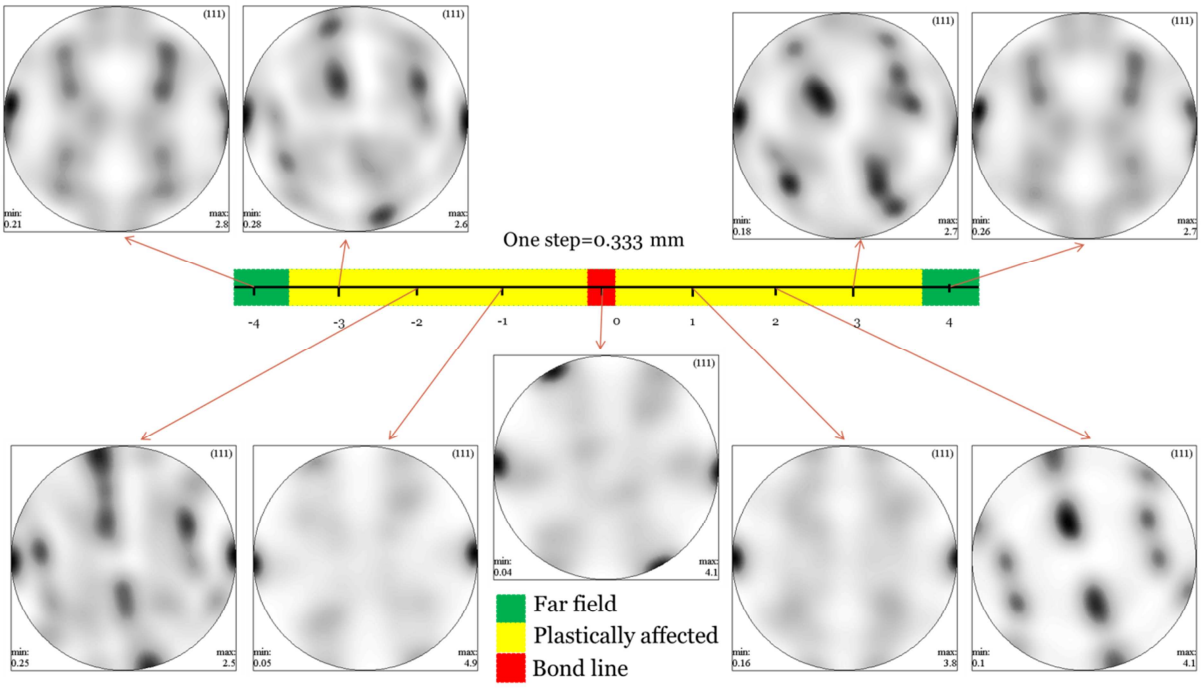

Fig. 7.3 The 111 pole figures at different locations on the scanning line of the sample.

In Fig. 7.3, the appearances (pole intensity distribution) of pole figures change significantly across the welding zone, suggesting that the degree of preferred orientation changes significantly, i.e. a steep texture gradient is present along the longitudinal direction in the sample. In an attempt to quantify this texture variation, we compute the so-called texture index, defined as

$$ti = \int f(g)^2 dg \qquad \text{(Eq. 7.1)}$$

Here g stands for orientation and is expressed in terms of the three Euler angles, and $f(g)$ is the MRD (*i.e.* ODF intensity) at a particular orientation.

This texture index can be used to describe quantitatively the severity of texture. For instance, a random orientation distribution with uniform $f(g)$ corresponds to the texture index of unity. In contrast, the texture index of single orientation can approach to a large number. Therefore, the bigger the texture index of an ODF, the stronger the corresponding texture is. Fig. 7.4 shows the variation of the texture index along the scanning line. Most of the texture index values lie around 2, except for the scanning point at position = 2mm. This point with a much larger texture index is regarded as an outlier: it is expected to be similar to that at position = -2mm owing to the symmetry about the bond line.

Therefore, in terms of the texture index, most points on the scanning line appear "equally severely" textured. The appearance of the pole figures changes significantly, however, suggesting that texture index definition alone does not provide sufficient quantitative and qualitative differentiation between textures at different locations in this particular sample. A further analysis of texture evolution on the central scanning line of this LFW sample will be presented in section 8.3 based on the use of EBSD, Debye-Scherrer diffraction and CPFEM modelling.

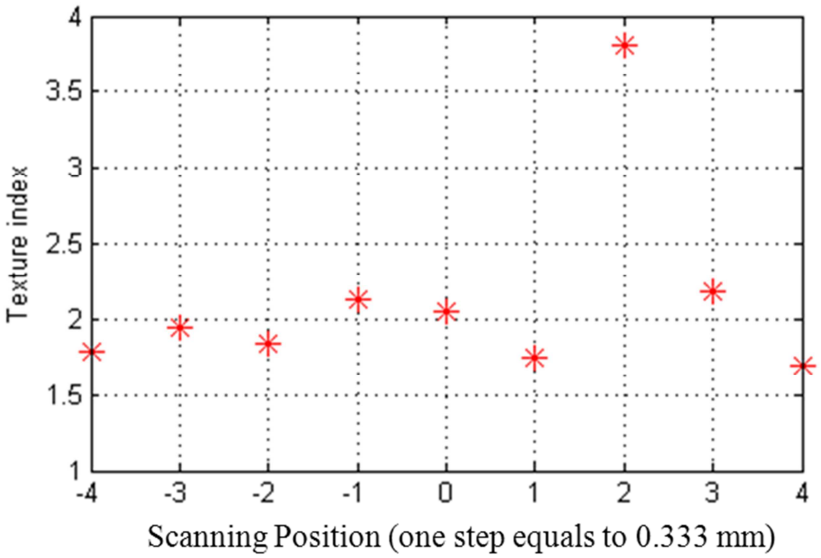

Fig. 7.4 Texture index variation along the scanning line.

7.2 Texture analysis of single exposure TOF neutron powder diffraction patterns

7.2.1 Introduction

Owing to the large solid angle coverage, Morden Time-Of-Flight (TOF) neutron multi-detectors have attracted significant attention in crystallographic texture studies. For instance, the NSHR diffractometer at IBR-2 in Dubna, Russia [51] and HIPPO at LANSCE, USA [13] (section 3.8.2.3) are two pioneering examples of such detectors used for texture studies. The main advantage of using this type of detector in texture measurement is the large pole figure coverage achieved with a single sample orientation (single exposure). This is a manifestation of the same principle as in the Debye-Sherrer (chapter 6) and the white beam "horseshoe" x-ray detector (section 7.1) setups. It is therefore worthwhile considering the feasibility of using the diffraction patterns collected from only a few (or even single) sample orientations for full evaluation of the sample texture.

GEneral Materials (GEM) diffractometer at ISIS spallation neutron source, UK is designed for the total scattering signal collection from both crystalline and non-crystalline

materials. The detector module has a very large solid angle coverage, and the resolution in reciprocal-space is also excellent [120]. The pole figure coverage of this GEM diffractometer under single sample orientation is even greater than for the TOF neutron detectors mentioned above. These characteristics make it ideal for quantitative texture studies. The diffraction data collected under two sample orientations (two exposures) have been used successfully to perform quantitative texture analysis using Rietveld refinement [121]. Besides, the diffractometer also allows high temperature studies, e.g. texture evolution under creep, at temperatures up to 1300^{o}C [122].

This section presents the quantitative texture interpretation (by MTEX) of diffraction patterns collected at GEM diffractometer. The aim of the present study is to provide a novel texture interpretation method to supplement the existing approach based on Rietveld refinement. Unlike the texture interpretation using Rietveld refinement, MTEX requires the input in the form of raw pole figures (rather than raw diffraction patterns). Therefore, in order to ensure the accuracy of texture interpretation by using MTEX, careful attention has to be paid on the conversion from raw diffraction patterns to raw pole figures. As it has been pointed out the chapter 6, the raw pole figure generation consists of two steps: 1) the determination of pole figure coverage and 2) the determination of the integrated intensity of diffraction peaks. The pole figure coverage of GEM detector can be precisely determined, as the position of each detector element is already known. However, it is important to correct the integrated intensity of diffraction peaks because of 1) the attenuation anisotropy caused by the sample geometry, and 2) the difference in the counting efficiency of individual detector channels.

In GEM, the raw diffraction pattern of any sample is often divided (normalized) by the diffraction pattern of a solid vanadium rod. This data operation can effectively eliminate the influence of detector efficiency variation, but sample geometry correction must still be

done. Neutrons interact rather weakly with metallic materials, so that the attenuation difference might not be very strong for the sample geometry that is close to sphere. Nevertheless, it is important to study the influence of sample geometry on the accuracy of ODF determination by MTEX from the diffraction patterns collected at GEM. For this purpose, texture measurement was carried out on a copper cylinder with the length to diameter ratio of 3:1. The reason for choosing this cylindrical shape was that the maximum to the minimum neutron path length ratio is equal to its length to diameter ratio (3:1). Moreover, it is relatively easy to prepare other samples with the same geometry. Thus, it would be very meaningful for the guidance of sample preparation if the geometry of the copper cylinder is found to only have a minor influence on the accuracy of the ODF determination.

The pole figure coverage of the GEM multi-detector (Fig. 7.5.b) is close to the X axis, but large gaps are present in the direction around the Y axis. It may be anticipated therefore that the accuracy of ODF determination may drop if a sample is placed for texture measurement so that the preferred orientations align closely with the Y axis. In order to address this concern, an aluminium alloy bar with strong axial preferred orientation was studied. In addition, samples with weak texture often present problems to ODF determination, for instance, the “ghost” problem may arise. In order to study the influence of weak texture on the accuracy of ODF determination, a nickel turbine blade manufactured by Direct Laser Deposition (DLD) was studied that had already been characterized by X-rays revealing a weak texture.

7.2.2 Experimental

7.2.2.1 The GEM diffractometer and its pole figure coverage

A brief introduction of GEM diffractometer pertaining specifically to texture studies is given here, more details for this instrument can be found in [120]. An overview of the

multi-detector of the GEM diffractometer is shown in Fig. 7.5.a. A vacuum sample chamber is placed at the centre of the diffractometer. Either a four-axis (three translations and one rotation) sample stage or an automatic sample changer can be installed in the chamber for diffraction pattern collection at ambient temperatures. For low and high temperature texture studies various cryostats and furnaces are available to cover the temperature range between 1 and 2000 K. The studies at non-ambient conditions are typically restricted to acquisitions with a single sample orientation only. The detector module can be subdivided into seven banks with the overall number of detector elements installed reaching about 7000. The forward scattering banks (bank 1, 2 and 3) have longer path length, but the d-spacing resolution of these forward banks is much lower than of the 90-degree and back-scattering banks due to the divergence term in the resolution function [120].

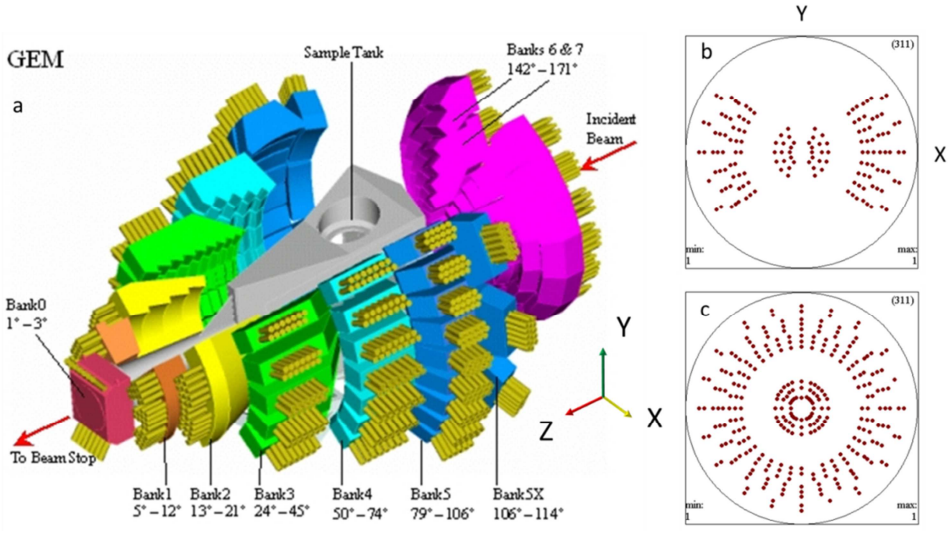

Fig. 7.5 (a) Overview of GEM diffractometer; (b) pole figure coverage of GEM diffraction data for acquisition in a single orientation; (c) pole figure coverage of GEM diffraction data for acquisition in two orientations related through 90^{o} rotation about the Z-axis

As mentioned the introduction, the raw diffraction patterns are normalized by the diffraction patterns of a solid vanadium rod in order to minimize the influence caused by detector elements efficiency variation. The normalized spectra of all 7000 detector elements are binned into 164 groups of diffraction patterns in order to improve the signal-to-noise ratio.

The binning operation forms 164 virtual “detector groups”. The azimuthal angles of the detector elements within the same detector group are the same, but the diffraction angle (2θ) coverage of detector groups varies between 5° to 10°. The pole figure coverage of these detector groups with single sample orientation is shown in Fig. 7.5.b. In order to increase pole figure coverage, the sample can be rotated around the beam direction (Z axis) by 90^o to take another measurement. The pole figure coverage from these two sample orientations (0^o and 90^o) is shown in Fig. 7.5.c. In this way, the accuracy of ODF determination can be significantly improved compared to that for single sample orientation.

7.2.2.2 Split-Gaussian single peak fitting

A diffraction pattern from a single binned detector group is shown in Fig. 7.6. The diffraction peaks are found to be asymmetric. In order to obtain the integrated intensities of the peaks, the so-called split-Gaussian function peak profile is used to fit the peaks. Although many other advanced peak profile functions have been used to describe precisely the asymmetric TOF neutron diffraction peaks, such as those proposed by Von Dreele et al. [123] and Ikeda-Carpenter [124], the simple split Gaussian function ensures rapid convergence of peak fitting and is relatively easy to implement in a batch job. The “split-Gaussian” function can capture effectively the peak shape of diffraction peaks collected at GEM (a fitting is shown in the inset of Fig. 7.6).

The split-Gaussian peak function is given by,

$$f_{left} = A\exp(-\frac{(x-d_0)^2}{2\sigma_1^2}) \qquad \text{if } x < d_0 \qquad \text{(Eq. 7.2)}$$

$$f_{left} = A\exp(-\frac{(x-d_0)^2}{2\sigma_2^2}) \qquad \text{if } x \geq d_0$$

Here A is the peak intensity, d_0 is the d-spacing at maximum intensity; and σ_1 and σ_2 are the peak half-widths for the left and right part of the peak, respectively. The integrated intensity for the split Gaussian function is given by,

$$I_{tot} = \frac{\sqrt{2}}{2} A\pi(\sigma_1 + \sigma_2) \qquad \text{(Eq. 7.3)}$$

This peak function however does not cope well with overlapped peaks, for instance the peaks in the low d-spacing range (d<1.0) in Fig. 7.6. In order to tackle those overlapped peaks, full pattern analysis, such as Pawley method [17] or LeBail method [123, 125] have been suggested, but those fitting methods are more difficult to carry out in a batch processing mode compared to the split-Gaussian method. In the present study, only those individual peaks rather than overlapped peaks are analysed for the experimental pole figure constructions.

Texture analysis by Rietveld refinement of the same diffraction data set was conducted using MAUD to provide a comparison with the MTEX texture analysis approach. A texture analysis wizard feature available in MAUD performs an automatic fit to the diffraction patterns. No further manual adjustment was used in MUAD fitting procedure.

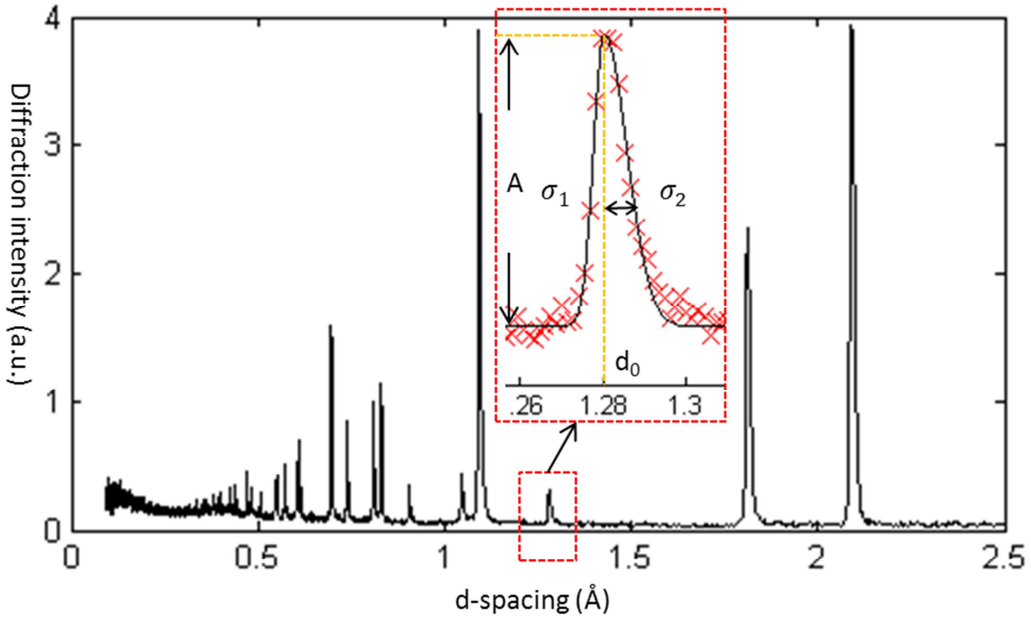

Fig. 7.6 Diffraction pattern from a group of detector elements. (Inset) "split-Gaussian" function single peak fitting for one of the diffraction peaks.

7.2.2.3 Sample details

Three samples (see Fig. 7.7) were measured in order to address the challenges for ODF determination by MTEX of TOF neutron diffraction patterns collected at GEM.

1) A cylinder of 5 mm diameter and 15 mm length was cut from a rolled copper plate (with the cylinder axis in the through-thickness direction) to ensure strong texture. The beam size was set to 15 × 15 mm^2 to envelop the entire sample. A can made of vanadium foil with the same dimension as the copper cylinder was also prepared. The can was filled with copper powder and put into the GEM diffractometer to collect the diffraction patterns, to be used to eliminate the cylindrical shape influence on the ODF determination of the copper cylinder.

2) A rolled aluminium alloy bar characterised by X-ray diffraction with the known fibre texture was also studied. The normals of the {111} crystal plane is preferentially aligned with the rolling direction. The neutron beam size was set to 3 × 3 mm^2.

3) A laser sintering system (EOSINT M 270; EOS GmbH, Krailling, Germany) was used to produce a small nickel turbine blade. The neutron beam size for the nickel DLD blade measurement was set to 10 × 10 mm^2.

The exposure time for each diffraction pattern collection was 1 hour in order to ensure good statistics. In addition, the texture information for all samples was obtained by using monochromatic synchrotron X-ray diffraction with sample rotation at beamline I12 (JEEP), Diamond Light Source, UK [126].

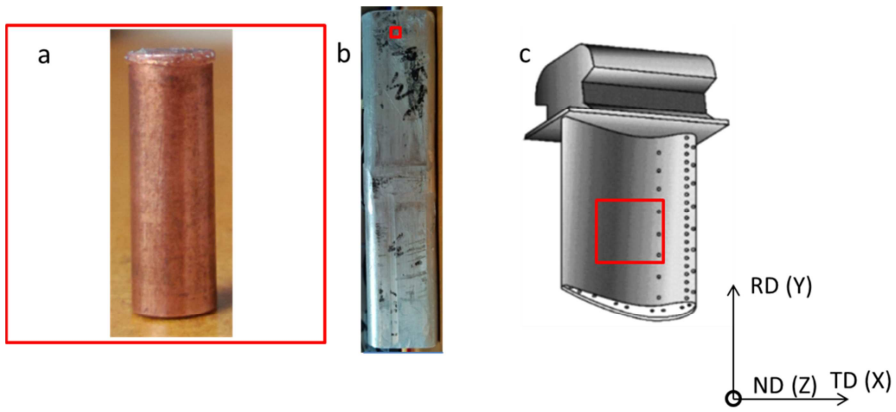

Fig. 7.7 Samples and their orientations with respect to laboratory coordinates. (a) copper cylinder; (b) aluminium rolled bar; (c) nickel DLD blade. The beam sizes are illustrated by the red squared box, and are 15×15 mm^2, 3×3 mm^2 and 10×10 mm^2 for *a*, *b* and *c* respectively.

7.2.3 Results and discussion

7.2.3.1 Copper cylinder

The copper cylinder was measured in two orientations: 1) the **0^o orientation** (as shown in the centre of the 111 pole figure of Fig. 7.8.a) and 2) rotated from the **0^o orientation** around the Z axis by 90^o (called the **90^o orientation**). Four groups of incomplete pole figures with a single orientation of the cylinder are shown in Fig. 7.8, in which *a* corresponds to the raw diffraction pattern of the copper cylinder at 0^o orientation, *b* corresponds to the diffraction patterns of the copper powder-filled vanadium container at 0^o orientation, *c* corresponds to the diffraction patterns of the copper cylinder at 0^o orientation

after shape correction (i.e. calculated as $c=a / b$), and d corresponds to the raw diffraction pattern of the copper cylinder at 90^{o} orientation. It should be noted that for the cylinder filled with copper powder (non-textured) in Fig. 7.8.b, some minor intensity variation still exists (for instance, the ratio between the maximum (0.015) and minimum (0.0088) is found to be about 2 in the 100 pole figure).

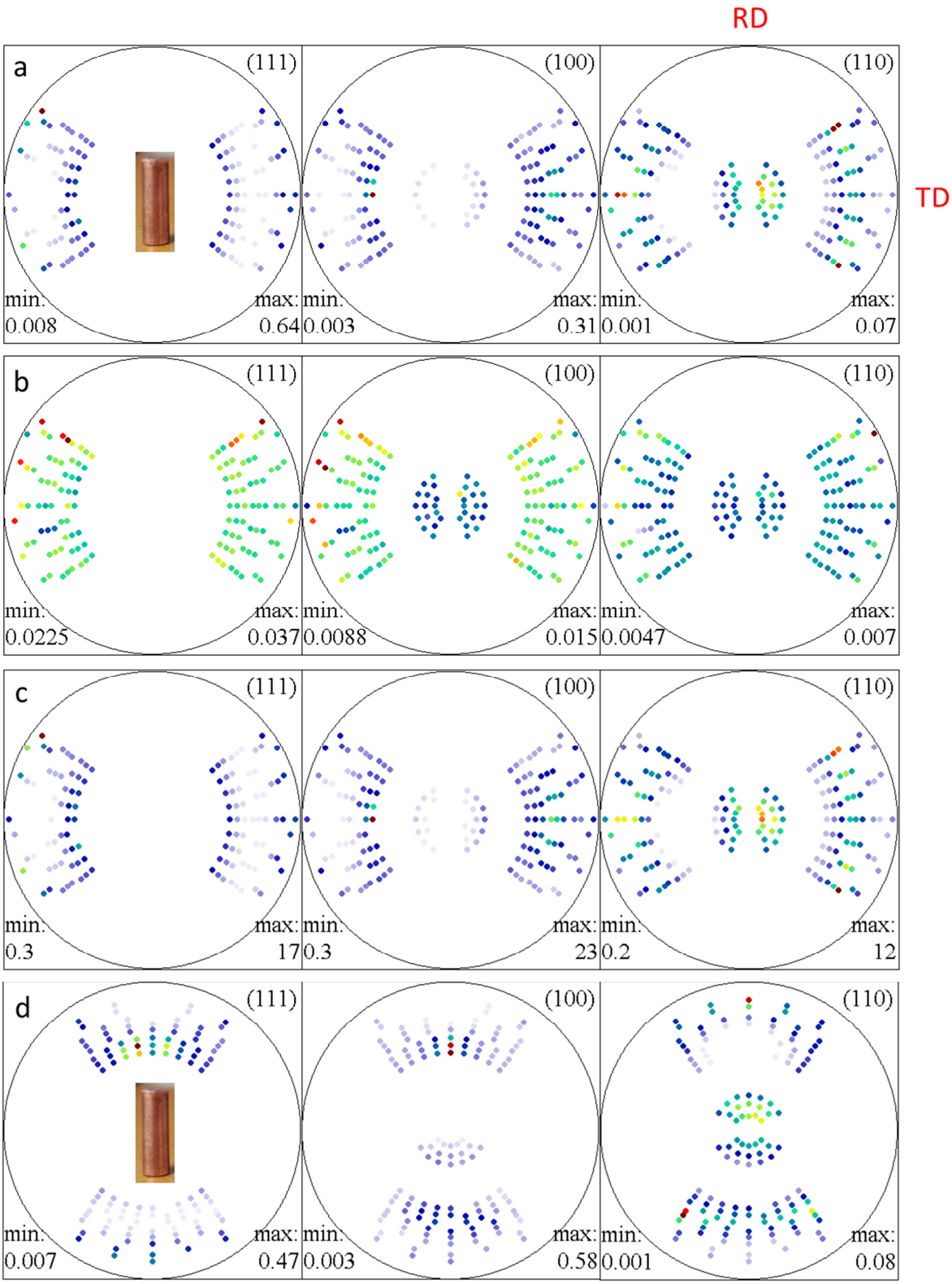

Fig. 7.8 Experimental pole figures (a) of the copper cylinder at 0^o orientation, (b) of the vanadium cylinder can filled by copper at 0^o orientation, (c) of the copper cylinder at 0^o orientation after the cylindrical shape correction, and (d) of the copper cylinder at 90^o orientation. The copper cylinder was drawn in the centre of the pole figures to illustrate the sample orientation with respect to the pole figure coverage.

The full pole figures calculated by MTEX from Fig. 7.8.*a*, *c* and *d* are shown in Fig. 7.9.*a*, *b* and *c* respectively. The full pole figure calculated by MAUD from the same diffraction patterns as used in Fig. 7.9.*a* is shown in Fig. 7.9.*d*. The results of synchrotron X-ray diffraction measurement for the copper cylinder are shown in Fig. 7.9.*e*. All pole figures in Fig. 7.9 appear to be very similar, suggesting that the results of TOF diffraction patterns collected at GEM by MTEX processing are consistent with other standard methods.

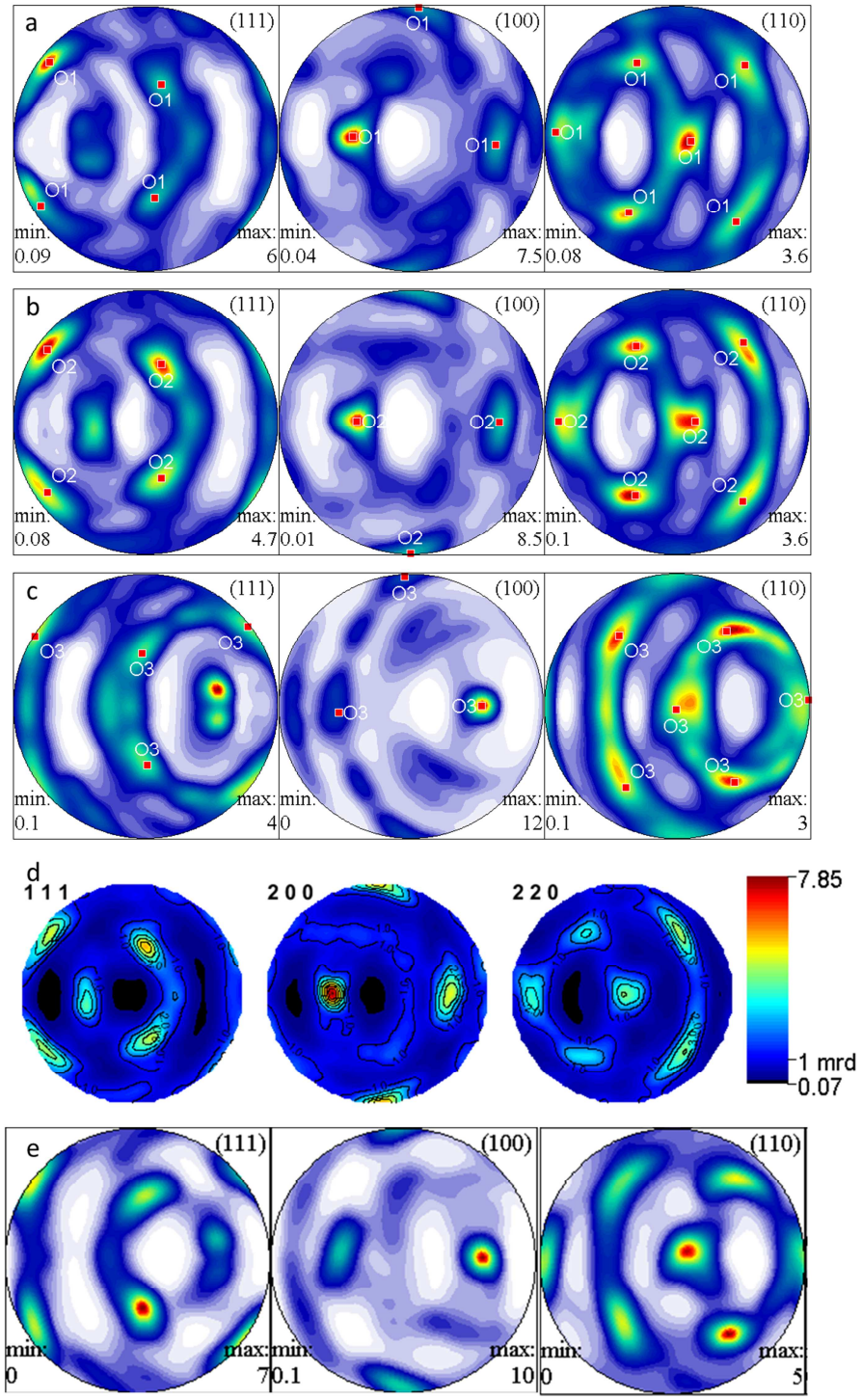

Fig. 7.9 Full pole figures after MTEX calculation of the raw diffraction pattern (a) of the copper cylinder at 0^{o} orientation, (b) of the diffraction pattern of the copper cylinder at 0^{o} orientation after the shape effect correction, and (c) the raw diffraction patterns of the copper cylinder at 90^{o} orientation. The preferred orientations are marked as O1, O2 and O3 in (*a*), (*b*) and (*c*) respectively. Figure (*d*) shows pole figures after MAUD fitting of the raw diffraction pattern of the copper cylinder at 0^{o} orientation, and (*e*) shows the pole figures of the copper cylinder measured by X-ray diffraction.

Some minor differences between pole figures are still detectable in Fig. 7.9. Since Fig. 7.9.*a*, *b* and *c* have been obtained using the same method, it is better to compare the difference between them quantitatively rather than qualitatively. The preferred orientations of the three groups of pole figures are identified by finding the maxima of intensity in the ODFs. Only one single preferred orientation, which is close to the classical "Goss" texture [119], is present in the three groups of pole figures. "Goss" texture is marked as O1, O2 and O3 in Fig. 7.9.*a*, *b* and *c*, respectively. As pointed out in previous chapters, a single preferred orientation can be characterized by an orientation centre (three Euler angles) and an orientation broadening parameter. Since only "Goss" texture is present in all three groups of pole figures, the difference between them can be discussed below in terms of the difference in the orientation centre and orientation broadening.

Table 7.1 lists the orientation centres (column 2-4), the smallest rotation angle between the orientation centres and the O2 orientation (column 5), the volume fraction of the ODF intensity within 20^{o} orientation broadening from the orientation centres (column 6) and the volume fraction compared to that of O2 (column 7). Here, since the diffraction data associated with orientation O2 is free from the cylindrical shape effect, the orientation is used as the reference to show the ODF determination accuracy without diffraction intensity correction. Diffraction data associated with orientation O1 corresponds to a situation in which TOF neutrons were scattered approximately along the radial directions of the cylinder, and the one associated with O3 were scattered approximately around the longitudinal direction of the cylinder. Thus the O1 preferred orientation is likely to be more eweakly affected by the cylindrical shape effect than the O3 orientation. It is found in Table 7.1 that the smallest rotation angle (column 5) between O1 and O2 is less than that between O3 and O2. In terms of orientation broadening, the O1 shows a bigger ODF intensity volume fraction percentage (79.4 %) than the O2 (71.8%). The volume fraction of a particular orientation is defined as

the ratio of the sum of ODF intensity (MRD) within 20 degree neighbourhood from a chosen orientation to the sum (which is unity if an ODF is normalized) of MRD over the entire Euler angle space. These quantitative comparisons reveal that the orientation O1 is closer to the reference orientation O2 than O3, confirming that the diffraction data associated with O1 suffers smaller aberration caused by the cylindrical shape effect. It is evident that these aberrations are likely to affect slightly the quantitative interpretation of texture, but present no problem to the qualitative identification of the texture type as a clear "Goss" texture seen in all pole figures. Therefore, we suggest that it is not necessarily to perform diffraction intensity correction caused by the sample geometry to the diffraction patterns collected at GEM that are intended for general texture analysis. Only when precise quantitative texture information is needed, the shape correction ought to become a concern.

Table 7.1 Details of the characteristics of the three (O1, O2 and O3) preferred orientations: orientation centre, misorienation against O2, volume fraction of the orientation, the percentage of O2.

	Orientation centre in Bunge convention (degree)					
	phi1	Phi	phi2	angle against O2 (degree)	Volume fraction within 20 degree	percentage of O2
O1	267.571	36.1877	88.96	4.0766	0.2331	79.4
O2	268.757	33.6774	91.1278	0	0.2933	100
O3	90.417	44.4821	273.152	12.5365	0.2107	71.8

7.2.3.2 Aluminium rolled bar

The diffraction pattern collection of the aluminium rolled bar was also carried out for two sample orientations (0^o and 90^o). Fig. 7.10.*a*, *b* and *c* show the three sets of full pole figures after the MTEX calculation: sample orientations are 0^o, 90^o and the assembly of the two orientations, respectively. Fig. 7.10.*d* shows the full pole figures derived from X-ray measurements, in which the normal of crystal planes {111} display two strong preferred directions close to the rolling direction (RD).

When the sample is mounted at 0^o orientation, the diffraction patterns of GEM can only cover the texture information around the transverse direction (TD) in Fig. 7.10.d. Thus, the main texture information is not captured, namely, the preferred directions around the rolling direction (RD) in the 111 pole figure of Fig. 7.10.d. In contrast, when the sample is mounted in the 90^o orientation the main texture information is effectively probed by GEM. As expected, the data assembly from both 0^o and 90^o orientations gives a superior coverage. The conclusions are further confirmed by Fig. 7.10. Fig. 7.10.a does not show the normals of crystal planes {111} having preferred directions around the RD, because the diffraction data does not effectively probe that scattering range. Secondly, Fig. 7.10.b clearly shows that the normal of crystal planes {111} preferentially align to the RD and much closer to the reference pole figure (Fig. 7.10.d). Thirdly, Fig. 7.10.c has the closest similarity to Fig. 7.10.d among Fig. 7.10.a b and c, because it has the best pole figure coverage. It should be noted that, owing the poor pole figure coverage at the periphery region, 111 pole figures in netierh Fig. 7.10.a, b and c can resolve the fact that the normal of crystal planes {111} has two preferred orientations next to the RD, but at low resolution may present an average effect (two preferred direction are averaged into one).

It follows that owing to the orientation of the pole figure coverage of GEM multi-detector under a single sample orientation, for samples with strong “fibre” texture it is recommended to obtain the ODF using the diffraction patterns collected from two sample orientations (0° and 90°).

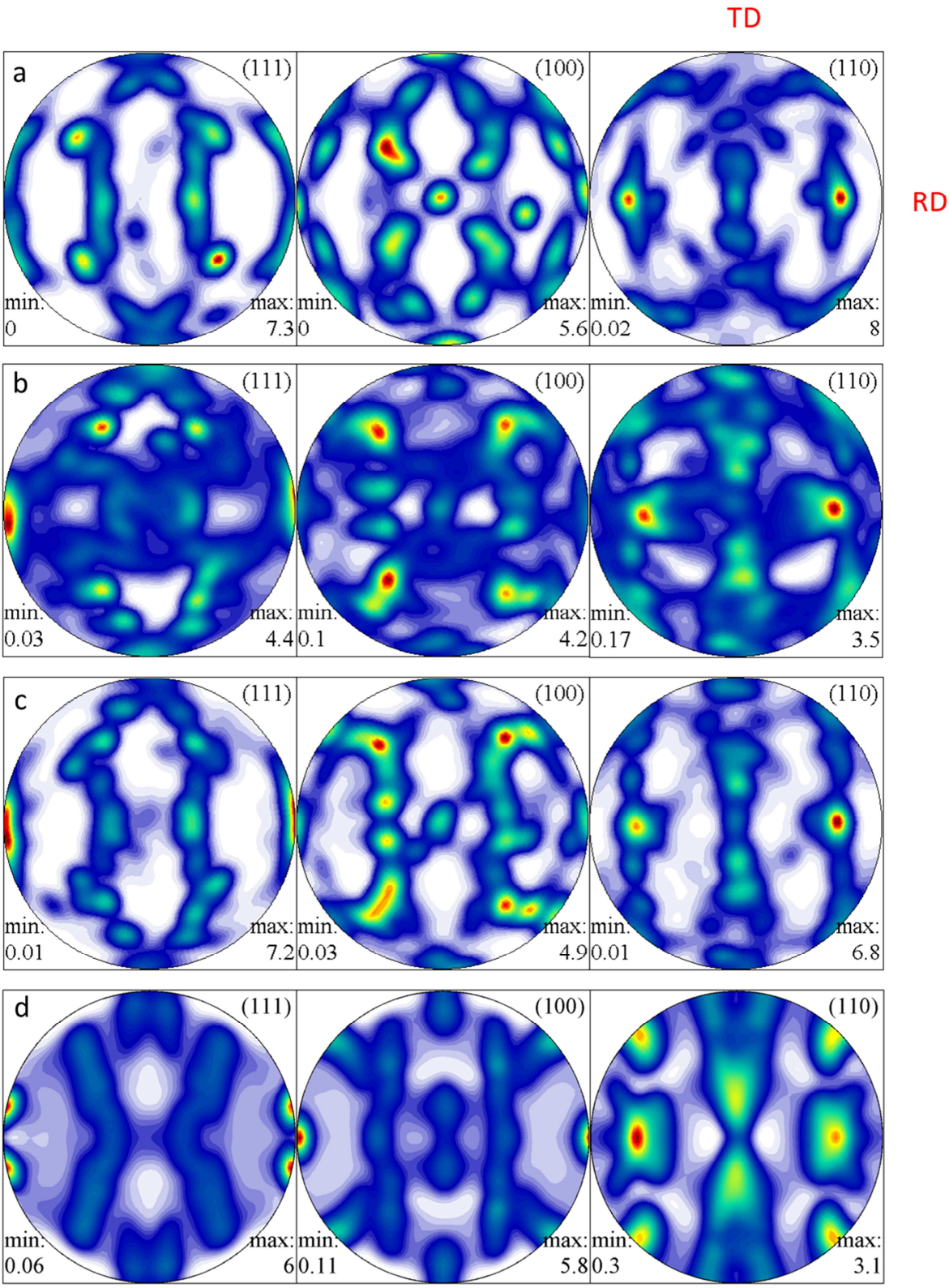

Fig. 7.10 Full pole figures by MTEX of aluminium rolled bar (a) at 0^{o} orientation, (b) at 90^{o} orientation, and (c) the combination of two sample orientations. (d) Full pole figures derived from X-ray measurements of aluminium rolled bar.

7.2.3.3 Nickel DLD blade

Diffraction pattern collection from the Ni alloy blade was conducted only at 0^o orientation (Fig. 7.7.c). During direct laser deposition (DLD) manufacturing the blade was build up along the RD, so that it is reasonable that the preferred direction of a particular type of crystal plane normal should be aligned with the RD. This is confirmed by the X-ray measurements: a weak preferred orientation consists of the normal of the crystal planes {*100*} being aligned with the RD (Fig. 7.11.c). The sample texture is clearly not as strong (sharp) as the previous two samples. Such weak texture may lead to errors in the texture interpretation using harmonics method. Fig. 7.11.a and b show the full pole figures calculated by MTEX (using a harmonics-based approach) and MAUD (a well-established Rietveld approach), respectively. The dominant preferred orientation of the sample as revealed by the X-ray measurements (*100* poles aligned to the RD) is present in both the MTEX and MAUD results. From the author's subjective point of view, the *111* pole figure from MAUD analysis appears more similar to the X-ray results than the MTEX results. However, it is difficult to conclude which result matches the X-ray result better, because 1) the differences and similarities are vague owing to low intensities, and 2) the pole figures are processed and displayed using different methods. Therefore, in order capture all meaningful texture information, especially in samples believed to have weak texture, it is recommended that both ODF determination techniques (MAUD and MTEX) be used to process the diffraction patterns.

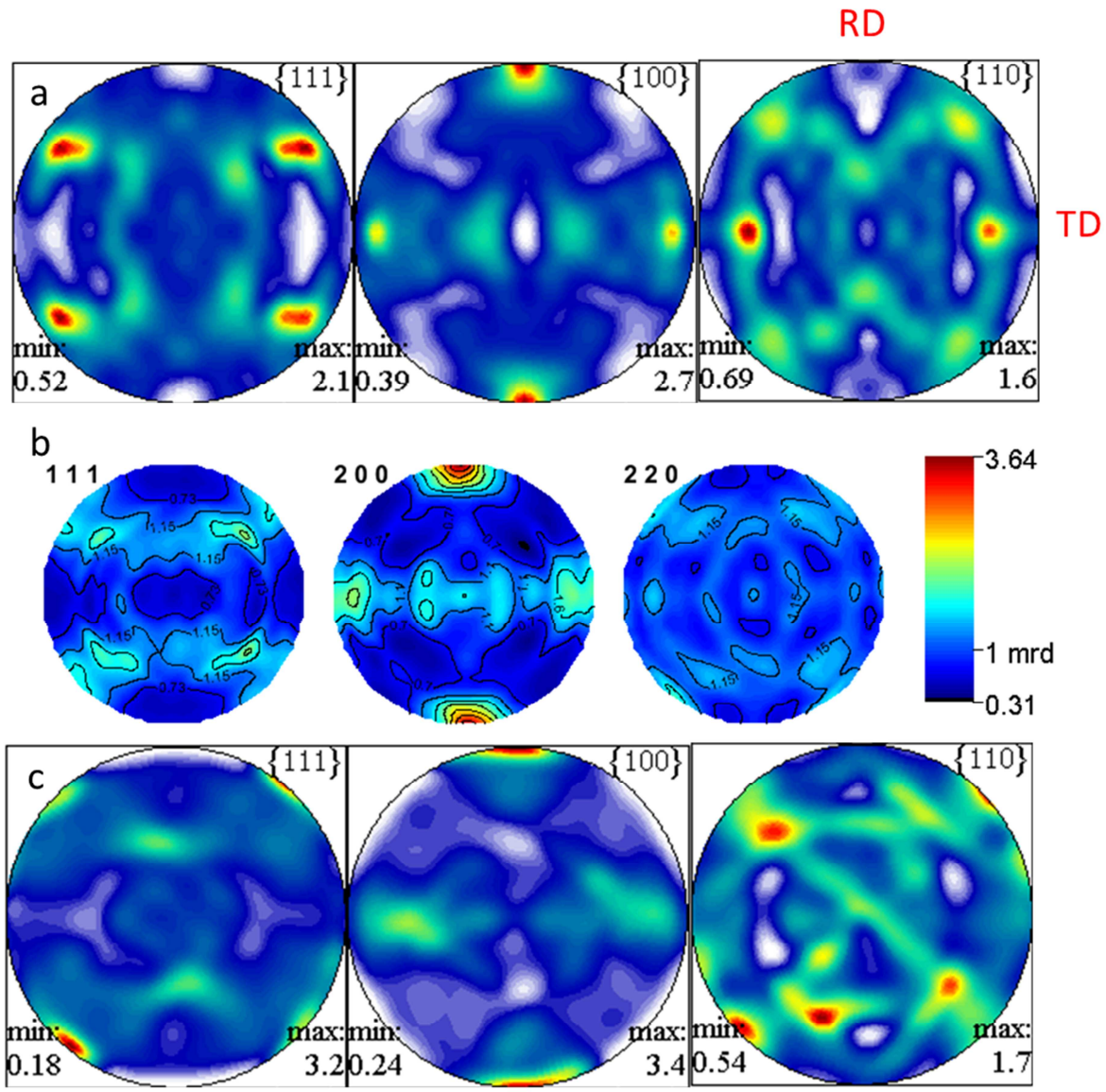

Fig. 7.11 (a) Full pole figures calculated by MTEX of the nickel DLD blade at 0^{o} orientation; (b) full pole figures calculated by MAUD from the nickel DLD blade at 0^{o} orientation, and (c) full pole figures from X-ray measurements of the nickel DLD blade.

7.2.3 Conclusion

MTEX processing for the estimation of ODF from experimental pole figures derived from diffraction patterns collected at GEM diffractometer was presented. The results calculated by MTEX show good agreement with MAUD analysis and X-ray measurements. This approach may be thought to be not as powerful as MAUD, because: 1) it does not have any build-in diffraction intensity correction feature and 2) overlapping diffraction peaks

present a challenge currently. However, the real advantage of this MTEX approach is the batch-processing capability of large datasets.

The main findings of the present study are:

1) After the study of the influence of sample geometry on the accuracy of ODF determination of the copper cylinder, it is found that the cylindrical shape effect gives rise only to very minor aberrations in the quantitative texture information, but does not affect the qualitative identification of the “Goss” texture in the sample.

2) From the study of aluminium alloy bar with strong directional preferred orientation, it is found that when the sample is mounted at a particular orientation (0° orientation) the calculated ODF contains very large errors compared to the reference ODF. These errors arise due to the unsuitable pole figure coverage for a single sample position within GEM diffractometer. It is recommended that for a sample with possible strong directional preferred orientation, diffraction patterns used for ODF calculation be collected at least with two sample orientations (0° and 90°).

3) MTEX approach is capable of reliable interpretation of diffraction patterns collected from samples with weak texture.

Chapter 8 The modelling of texture evolution by the Crystal Plasticity Finite Element Method

In this chapter, the Crystal Plasticity Finite Element (CPFE) framework presented in chapter 4 is used to model the texture evolution in metal forming processes. The principal aims of the chapter are twofold: 1) to find a reliable characteristic of the ODF that would allow making quantitative comparisons between the ODFs obtained from experiments and modelling, and 2) to assess the feasibility of calibrate the parameters of the model (especially the boundary conditions) in order to trace back the deformation history of the sample.

The first task is to model the extrusion of a tungsten wire. Experimental texture interpretation of this material has already been presented in Chapter 6. In the first instance, the ODF normalized error measure defined by Eq. 6.1 can be used for comparison between modelling and experiment. The wire was measured in the as-received condition, so that comparison can only be made between the final stage of the model and the experiment (rather than the processing history).

In another study carried out in addition to the tungsten wire analysis, the evolution of texture within a sample was modelled and determined experimentally. The sample was a copper cylinder subjected to *ex situ* uniaxial compression. The volume fraction of preferred orientations described in section 7.2 was used to relate the experimental results with the model.

One of the most significant practical purposes of modelling texture evolution is trying to understand the deformation history of a sample of unknown provenance by matching the texture prediction from the model to the observed preferred orientation. It is important to note

that texture changes are strongly dependent on the strain path. Therfore it is not possible to understand the texture evolution within a sample with complicated deformation history merely by considering the texture measured in the as-received condition. It is precisely for this reason that most texture modelling studies reported in literature are only applied to proportional loading deformation, e.g. uniaxial or biaxial tension, uniaixal or biaxial compression, and simple shear.

In the third section of the chapter we presented an attempt to determine the strain path experienced by the material within an LFW joint during manufacturing by matching the model to experimentally determined ODF obtained in the as-received condition. The approach is based on the hypothesis that the LFW process may be treated as the combination of cyclic shear deformation (linear friction) with uniaxial compression (forging). Several of texture characterization techniques, namely EBSD, monochromatic Debye-Scherrer diffraction, and TOF neutron diffraction are applied to the sample to ensure the most accurate and detailed texture information is obtained. Then the boundary conditions of the CPFE model are carefully adjusted to match the experimental observations.

8.1 Texture evolution modelling of the extrusion of a tungsten wire extrusion

8.1.1 Boundary conditions and other initial conditions

Fig. 8.1.a illustrates a typical extrusion process: a wire of initial diameter d_1 is pushed through a hard die. The diameter of the wire is reduced to d_0 after extrusion. From the modelling point of view, the extrusion process can be thought equivalent to either uniaxial tension with Z axis being the tensile axis (the strain rate matrix is given in Eq. 8.1), or biaxial compression in X-Y plane (the strain rate matrix is given in Eq.8.2). It is found in the course

of simulation that Eq. 8.2 is more suitable, as significantly larger overall deformation can be achieved than using Eq. 8.1.

$$\dot{E} = \begin{bmatrix} \sqrt{\frac{1}{1+\Delta}} - 1 & 0 & 0 \\ 0 & \sqrt{\frac{1}{1+\Delta}} - 1 & 0 \\ 0 & 0 & +\Delta \end{bmatrix} \quad \text{(Eq. 8.1)}$$

$$\dot{E} = \begin{bmatrix} -\Delta & 0 & 0 \\ 0 & -\Delta & 0 \\ 0 & 0 & \frac{1}{(1-\Delta)^2} - 1 \end{bmatrix} \quad \text{(Eq. 8.2)}$$

Any material point within the wire undergoes approximately uniform deformation during the extrusion process. A cubic Representative Volume Element (RVE) is used in the CPFE model to represent a material point. The RVE consisting of 12×12×12=1728 C3D8R elements (8-noded linear cubic) is created in ABAQUS CAE. As the element has only one Integration Point (IP), enhanced hourglass control has to be used in the model in order to ensure quadratic element behaviour under bending deformation. Elements with more IPs (quadratic elements) can also be used but that increases significantly the computational expense.

The crystal plasticity equations presented in chapter 4 are implemented in a UMAT subroutine within ABAQUS [100]. Before applying deformation to the RVE, each IP is assigned an orientation belonging to a randomOrientation Distribution (OD). The RVE represents a polycrystalline aggregate of 1728 individual grains with initial random texture.

Fig. 8.1.b shows the shape change of the RVE before and after biaxial compression in which the tensile strain along the Z axis ε_{33} equals 1.0.

Tungsten has a BCC structure. The common BCC slip system {110}<111> was used as the vehicle for plastic deformation. Some other parameters used in the model are summarized below:

1) Elastic constants for tungsten are C_{11}= 522390 MPa, C_{12}=204730 MPa, C_{44}=160830 MPa [7].

2) In Eq. 4.22, the initial shear rate ($\dot{\gamma}_0$) was set to 0.001 s^{-1}, and m was given the value of 10.

3) In Eq.4.24, the initial hardening modulus (h_0) was set to 1000 MPa, and saturation stress (τ_s) and the initial critical resolved shear stress were set to 400 MPa and 200 MPa respectively. The constant q was chosen to be equal to 1.4.

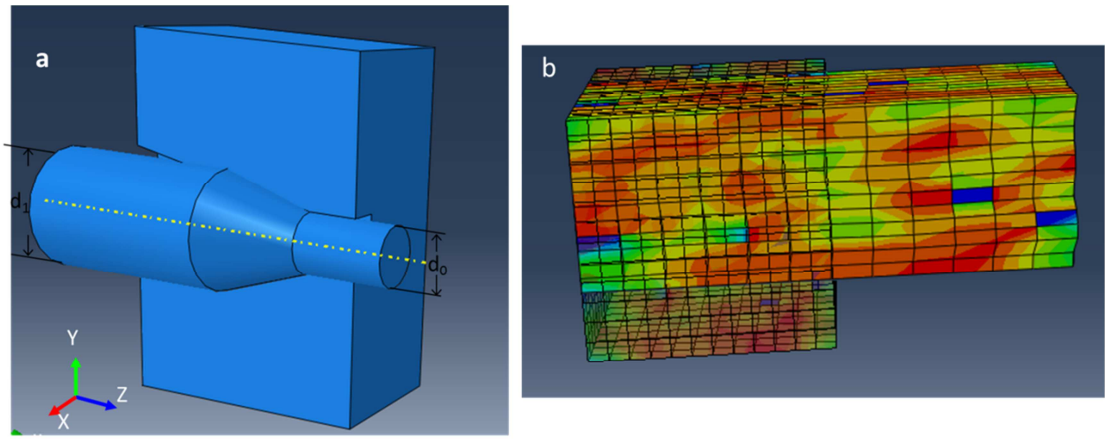

Fig. 8.1 (a) Illustration of wire extrusion and (b) RVE shape change before and after deformation subjected to a extension along Z axis with ε_{33} of unity.

8.1.2 ODF estimation from discrete orientations

The orientations of all the IPs at any deformation stage can be used to form a discrete orientation distribution (OD). The scattering pole figures of the OD corresponding to ε_{33} of

unity are shown in Fig. 8.2.a. Since experimental results are in the form of continuous ODF, discrete ODs extracted from the CPFE model have to be converted into continuous ODFs using MTEX in order to perform quantitative comparison. The same angular parameters (5^o orientation broadening, and 5^o for the ODF resolution) as in the experimental data processing were used as input in MTEX to ensure the consistency. Fig. 8.2.b shows the projections of the calculated continuous ODF from discrete OD referring to Fig. 8.2.a, and it clearly shows that Fig. 8.2.b captures all the PFM present in Fig. 8.2.a.

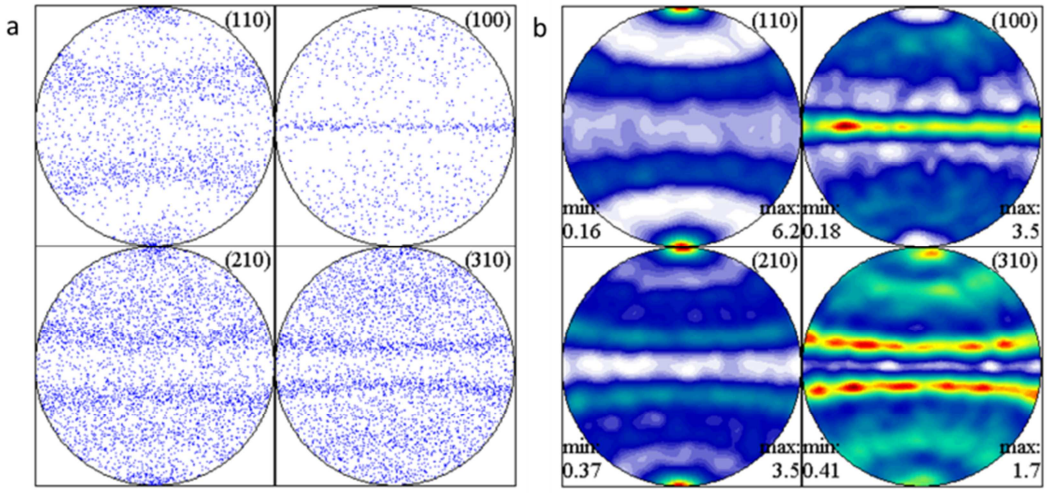

Fig. 8.2 (a) Scatter plots and (b) continuous contour plots of pole figures at $\varepsilon_{33}=1.0$.

8.1.3 Comparison between experiment and modelling

The ODF differences defined by Eq. 6.1 (in chapter 6) are computed between the simulated and experimental ODFs in order to perform quantitative comparison. The comparison is illustrated in Fig. 8.3.

At $\varepsilon_{33} = 0$, the RVE has initial random texture such that the pole figures do not show any PFM. When the tensile strain ε_{33} was increased to 1.8758, the pole figures began to display features corresponding to the typical extrusion characteristics in BCC metals: the normals of the {110} crystal planes are found to become parallel with the extrusion direction.

However, at this strain value it is also worth noting that the normals of the {210} crystal planes also became aligned with the extrusion direction, which is not seen in the experimental data. Tensile strain ε_{33} was further increased to 49 (the convergence limit for the bi-axial compression deformation modelling approach). The simulated pole figures obtained at this strain appear to be more similar to the experimental data, compared to those of $\varepsilon_{33} = 1.8785$. Note that the PFM in the 210 pole figure at $\varepsilon_{33} = 49$ is no longer completely aligned with the extrusion direction, shows the trend towards the 210 pole figure from the experiment.

One may argue that the simulated ODF at $\varepsilon_{33} = 49$ still largely differ from the experimental ODF, as the ODF error (0.5) is far away from zero compared with the ODF error (0.89) at $\varepsilon_{33} = 0$. It should been pointed out that, even for two groups of very similar pole figure the ODF error between them can be considerably "large". For example, the pole figures of Fig. 6.13.b and Fig. 6.13.c (Chapter 6) looks almost identical by eye, the ODF error between them is 0.14 as shown in Fig. 6.15.

The ODF error curve indicates that the mismatch between the experimental and simulated ODFs decreases monotonically as the tensile strain increases. It would be ideal if this curve had a simple shape (e.g. parabolic), so that the minimum ODF error would correspond to the real strain applied to the sample during manufacturing. However, the finite element calculation reaches the convergence limit for this one-step extrusion process simulation.

Further improvement on the CPFE model would be to consider a two-step extrusion process: 1) to deform the RVE to the convergence limit in the first step and 2) assign the deformed ODF into a new cubic RVE to deform it in the second step. Much higher values of tensile strain can be applied to the RVE can then be reached. We note that very high values of tensile strain are expected for the real extrusion process, as indicated by the as-received

sample diameter of 0.1 mm. Moreover, it should be noticed that, huge temperature change (annealing effect) often happens in wire production process and the annealing effect may modify the texture caused by pure extrusion. A better model should consider the temperate effect on texture change.

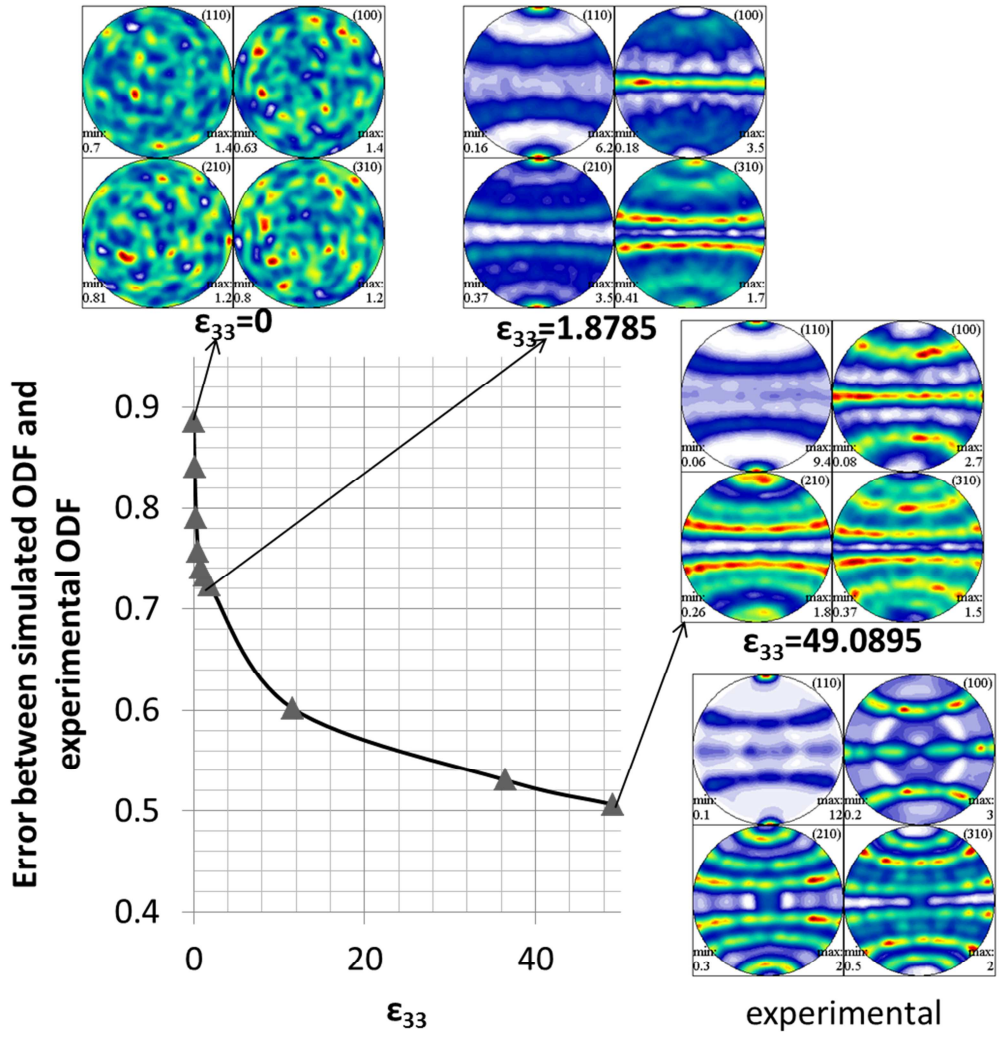

Fig. 8.3 Texture and ODF mismatch evolution with increasing tensile strain.

8.1.4 Conclusion

The results reported represent the attempt to bring together, in a systematic way, the experimental and modelling approaches to texture analysis. It is described how the data obtained from CPFE modelling can be post-processed to derive continuous ODF. Also

introduced is the use of quantitative measure of ODF difference that allows quantitative assessment of the “goodness of fit” between simulation and measurement.

8.2 Texture evolution modelling of an aluminium cylinder subjected to *ex situ* uniaxial compression

8.2.1. Introduction

In this section, *ex situ* texture measurement experiments on an aluminium alloy cylinder under uniaxial compression weer used to validate the texture evolution prediction by a CPFE model. In comparison to the tungsten wire in the previous section, the texture evolution history of the aluminium cylinder during the deformation is obtained experimentally, allowing the model to be validated using many data points rather a single one. Texture characterization after *ex situ* deformation was successfully made using GEM diffractometer. A logical further step would be to conduct *in situ* texture evolution study. Doing this using GEM diffractometer presents a practical challenge. The other aim is to use the volume fraction of preferred orientation, another quantitative measure that is distinct from the ODF difference, to correlate the results obtained from modelling and experiment.

8.2.2. Samples

Five cylinders (6 mm length, 6 mm diameter) were machined from a rolled bar of aluminium alloy HE30 (British specification equivalent to AA6082). The cylindrical axis was aligned with the rolling direction, with the samples having identical “fibre” texture inherited from the bar. Four cylinders were compressed along the rolling direction to different strain values, whilst one cylinder was left undeformed as a reference. The definition of coordinate axes with respect to the five sample studied is shown in Fig. 8.4.a. The deformation details of the samples are listed in Table 8.1.

Texture characterization of the samples was performed at GEM. Diffraction patterns at two sample orientations (0° and 90°) are taken. The texture information was obtained from the diffraction patterns using the method described in chapter 7.

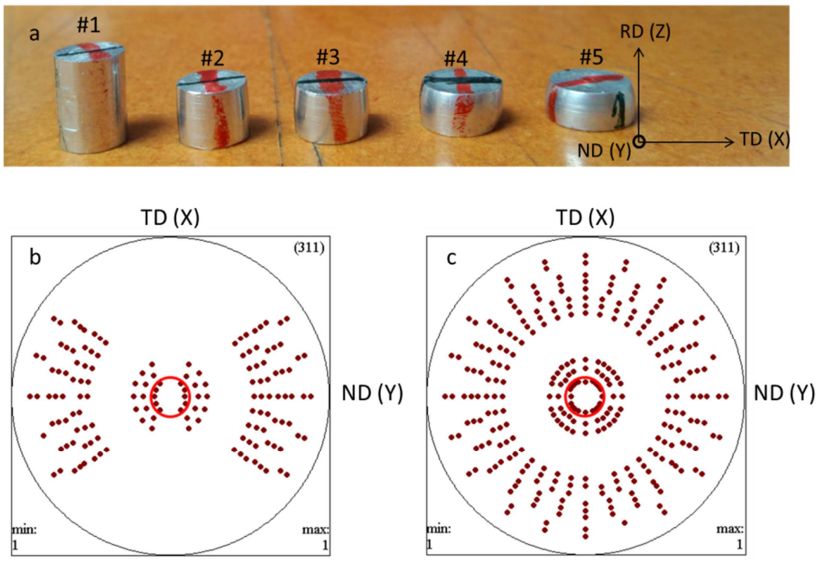

Fig. 8.4 (a) Aluminium alloy HE30 cylinders (No. 1, 2, 3, 4 and 5 from left to right). The lab Cartesian coordinates is also shown on the right. (b) Pole figure coverage of single exposure GEM diffraction data and (c) pole figure coverage of two exposures GEM diffraction data. The projection of the cylinder is drawn as a red circle in both *b* and *c*.

Table 8.1 Details of five aluminium samples. l_0 is the original length of a sample; l is the deformed length of a sample; Δl is length reduction during uniaxial compression; ε_1 is compressive strain using sample 1 as reference; ε_2 is compressive strain using sample 2 as reference.

Sample	l_0 (mm)	l(mm)	Δl (mm)	ε_1	ε_2
1	6	6	0	0	
2	5.94	5.17	-0.77	0.12963	0
3	5.95	4.67	-1.28	0.21513	-0.085
4	5.98	3.95	-2.03	0.33946	-0.21
5	6.08	3.53	-2.55	0.41941	0.29667

8.2.3 Results and discussion

8.2.3.1 Experimental results

The full pole figures obtained from the raw diffraction patterns under two sample orientations (0° and 90°) are shown in Fig. 8.5. The first three groups (sample 1 to 3) of pole

figures clearly show that a strong 111 fibre texture and a weak 100 fibre texture exist along the rolling direction (Z direction). As described in section 7.2, preferred orientation can be characterized by the orientation centre and the volume fraction of the preferred orientation within certain orientation broadening. Here the volume fraction of 111 fibre texture is defined as the sum of the ODF intensity of the orientations with the normal of the crystal plane {111} that has less than 10^o misorientation with respect to the rolling direction (RD). The volume fraction of 100 fibre texture is defined in the same way. The changes of the volume fractions of the fibre textures as a function of compressive strains are shown in Fig. 8.6.

As shown in Fig. 8.6.a, sample 1 (ε=0.0) has a much smaller 111 fibre texture volume fraction compared to sample 2 (ε=-0.13), suggesting that the fibre texture at ε=0.0 is weaker than that at ε=-0.13. However, the pole figures (Fig. 8.5) show that the maximum intensity on the 111 pole figures are almost identical, suggesting the fibre textures of the two samples are equally strong. This is probably because during the measurement the rolling direction of sample 1 was not aligned as well with the Z axis. This misalignment can also be seen from the pole figures of sample 1, in which the maximum intensity of the 111 pole figure is not at the centre (Z direction). It is evident that this misalignment was only present in texture results for sample 1. Because of this anomalous behaviour, sample 1 (strain=0.0) was ignored in the further discussion of texture evolution.

Fig. 8.6.a also shows that the volume fraction of the 111 fibre texture decreases monotonically as the compressive load increases, suggesting that the 111 fibere texture is being supressed by the increasing uniaxial compression. In contrast, the volume fraction of the initially weak 100 fibre texture is seen to increase slightly with increasing load (see Fig. 8.6.b). It is well-known that the 111 fibre texture along RD arises as the result of extrusion. Fig. 8.6 reveals that the effect is reversible, i.e. that uniaxial compression along RD can effectively shift sample texture closer to random.

Fig. 8.7 shows pole figures of samples 1 and 2 calculated from the diffraction patterns collected at sample orientations 0^o, 90^o, and the assembly of the two sample orientations. It is clear that the rolling direction of sample No.1 was not aligned well with the Z axis at 90^o sample orientations, so that the 111 pole figure of the assembly of the two sample orientations displays the same misalignment. It should be noted here that this kind of misalignment may happen during texture characterization, especially when changing the sample's position. This highlights the argument in favour of the single exposure (single sample orientation) texture characterization technique in order to prevent sample misalignment effects. In contrast, the rolling direction of sample 2 was always well-aligned with the Z axis at both sample orientations (0^o and 90^o). Sample 1 was ignored in the subsequent discussion of texture evolution.

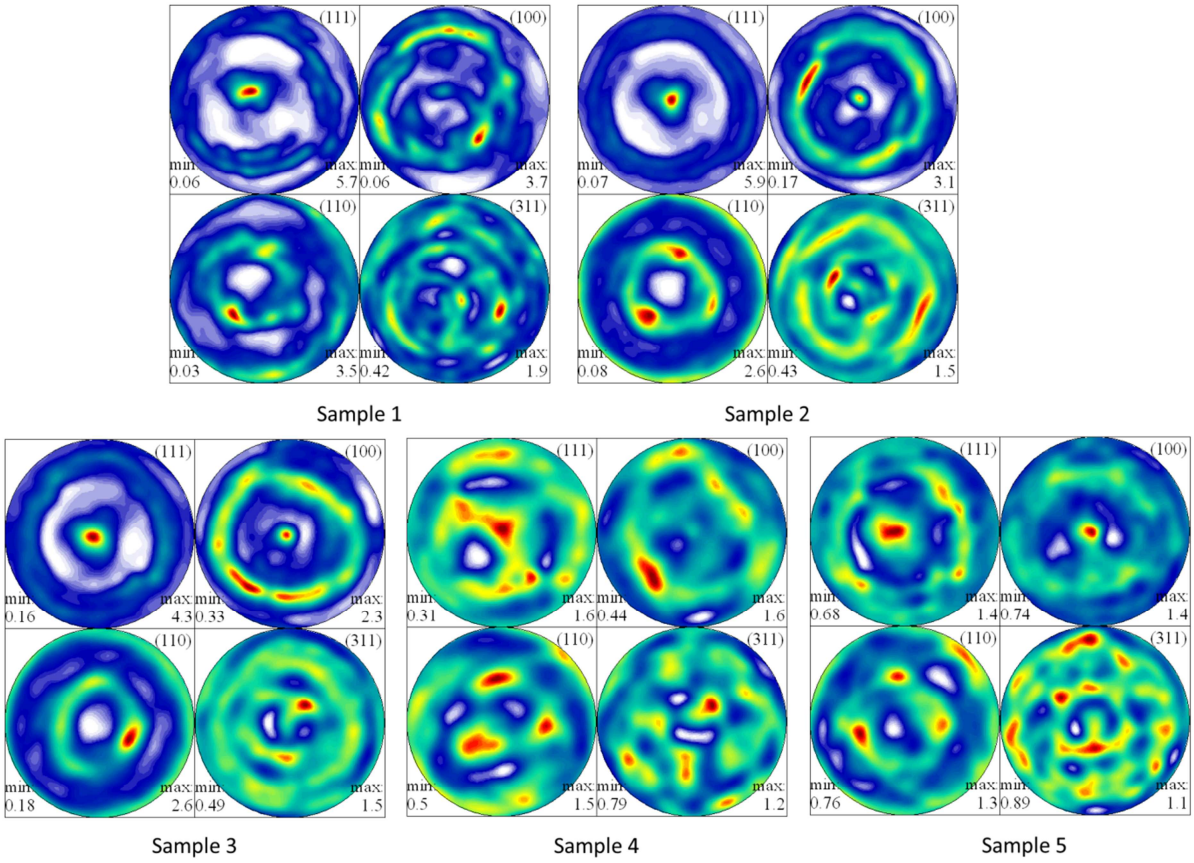

Fig. 8.5 Pole figures of five samples calculated from GEM diffraction data with two sample orientations.

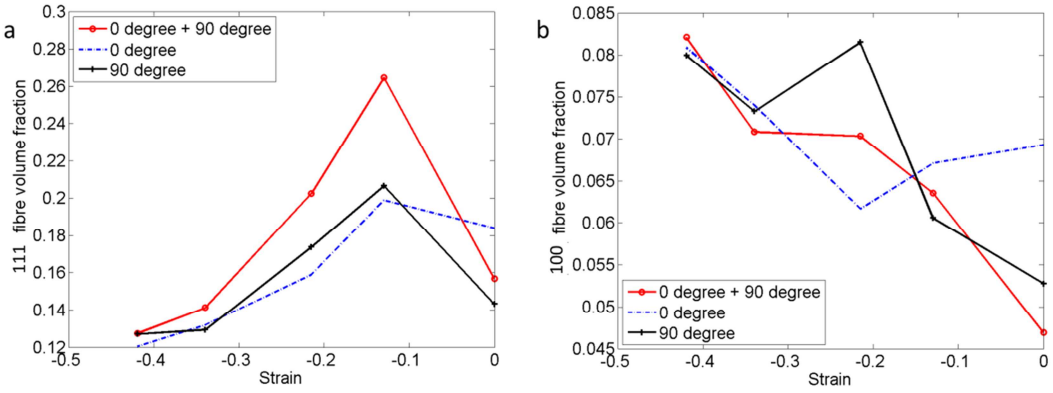

Fig. 8.6 (a) 111 and (b) 100 fibre texture volume fraction changes as a function of compression strains. Results obtained from three groups of diffraction patterns: 0° sample orientation (blue dash line), 90° sample orientation (black line) and two sample orientations (red line).

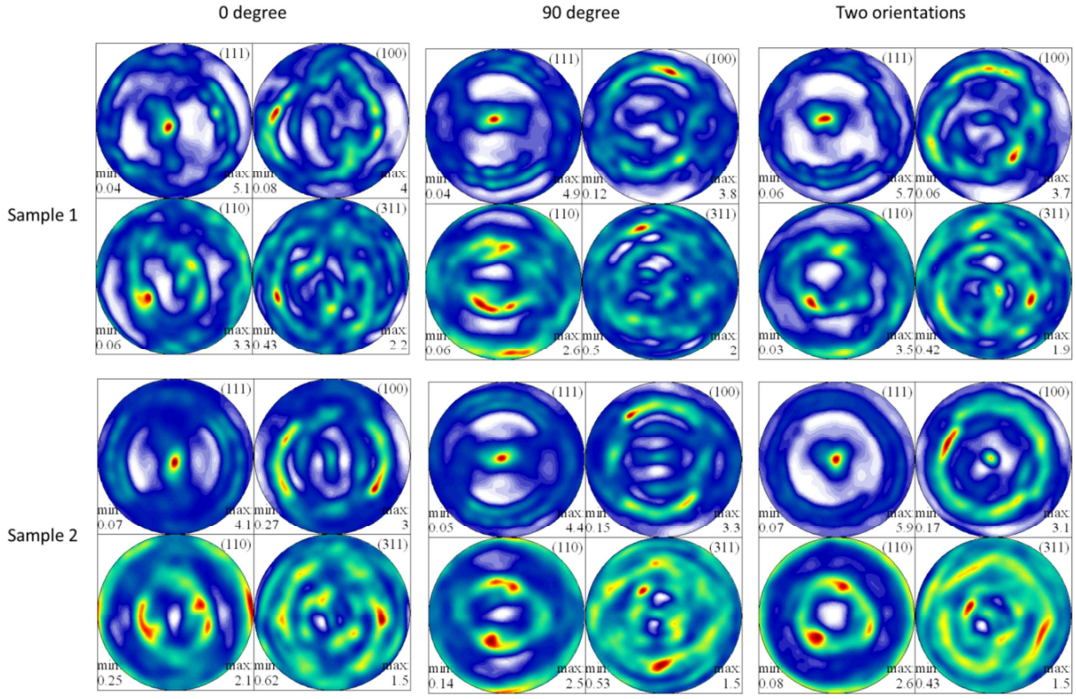

Fig. 8.7 Pole figures of samples 1 and 2.

8.2.3.2 ODF discretization and OD estimation

While implementing a CPFE model to simulate the texture evolution of the aluminium alloy cylinder under uniaxial compression, it should be noted that the starting texture of the RVE is not random (unlike in the case of tungsten wire in section 8.1, where the starting texture of the RVE was assumed random). In this case of texture evolution modelling, the initial texture of the RVE should be given by the ODF of the nominally

undeformed sample. Since the RVE consists of a finite number of elements N, the texture of the RVE is described by a discrete Orientation Distribution (OD), rather than a continuous ODF output from the experiment interpretation and analysis. Therefore, it is necessary to develop and apply a systematic way of converting (sampling) a continuous ODF to obtain a discrete OD without losing much orientation information, and vice versa. In section 8.1 the conversion from discrete OD to continuous ODF has been shown, but the reverse conversion (ODF discretization) is a more challenging problem. There are several ODF discretization techniques summarized in literature [127]. Here, a novel ODF discretization technique using MTEX is proposed and described below. The technique shares some common principles with other ODF discretization techniques.

A 3D grid is created in orientation space by MTEX to have M cubic cells of equal size. The continuous ODF is sampled by this 3D grid, so that the sampling data is obtained in four columns: three columns are Euler angles and the fourth column is the volume fraction referring to a particular orientation given by these three Euler angles. The volume fractions in the fourth column (f_i) are not integer, so that the sampling results cannot be directly assigned to RVE. In order to convert the non-integer values into integers without losing information or distorting the ODF representation, a threshold is set by choosing a small volume fraction value (f_0) that is set to be a unit orientation. Any volume fraction f_i below the threshold is ignored. Any volume fraction f_i above the threshold is divided by the volume fraction of the threshold f_0, and the rounding (floor) of the division is used to represent the original volume fraction. This process is summarized below in the form of the following equations:

(Eq. 8.3)

If $f_i < f_0$,then

$R_i = 0$

If $f_i \geq f_0$, then

$$t_i = \frac{f_i}{f_0}$$

$$R_i = floor(t_i)$$

Here, f_i is an arbitrary cell volume fraction, f_0 is the threshold volume fraction, t_i is the ratio between f_i and f_0, and R_i is the integer division of t_i.

In order to assess the goodness of this ODF discretization, a ratio (τ) between the sum of t_i and that of R_i can be defined:

$$\tau = \frac{\sum_i R_i}{\sum_i t_i} \qquad \text{(Eq. 8.4)}$$

τ value of unity corresponds to good fidelity of discretization. The more τ differs from unity, the more texture information is likely to have been lost. This ratio τ is dictated by three factors: N, M and the ratio between them. For all ODF discretizations described in this chapter, τ is set to be larger than 0.9, so that only a very small amount texture information may be lost in ODF sampling. The scatter representation of the 111 pole figure of the discrete OD consisting of 2353 individual orientations corresponding to sample 2 is shown in Fig. 8.8.a. The discrete OD is converted back to a continuous ODF in order to compare the modelling results with experimental ODFs. It is found that the orientation broadening can affect strongly the intensity of the re-calculated ODF, so that careful attention has to be paid to choosing the suitable value of the orientation broadening parameter. The rule used is to ensure that the re-estimated ODF is as similar as possible to the original ODF *i.e.* the error between the two ODFs is as small as possible. The 111 pole figure of the re-estimated ODF

from the discrete OD referring to Fig. 8.8.a is shown in Fig. 8.8.b. It is clear that this pole figure is very similar to the original one (see sample 2 in Fig. 8.8).

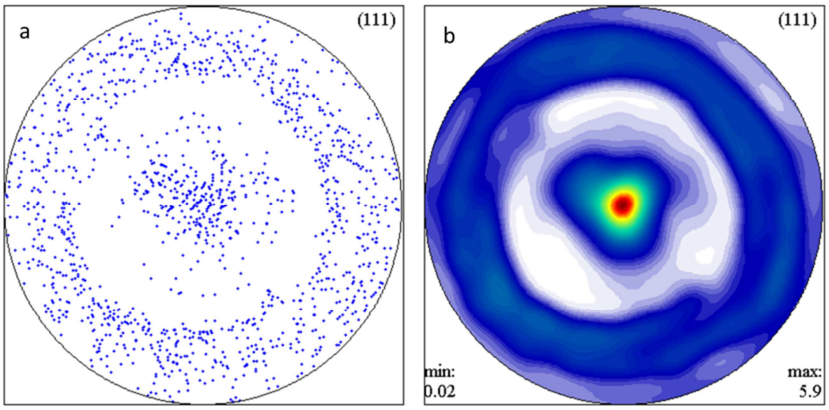

Fig. 8.8 (a) 111 scattering pole figure of discrete OD sampled from the ODF of sample No.2 (only display randomly 416 orientations rather all the 2353 orientations) and (b) the recalculated 111 pole figure of *a*.

8.2.3.3 A full scale CPFE model

A full scale model (shown in Fig. 8.9) was set to simulate the texture evolution of the aluminium alloy cylinder under uniaxial compression. The cylinder in the model consists of 2353 finite elements (grains). In order to study how the sample misalignment in the experiment can affect the simulation results, two different staring textures were assigned to the model: 1) sample No. 1 (misaligned); 2) sample No. 2 (well aligned).

Using sample No.1's measurement as the initial texture, the pole figures from modelling are shown in Fig. 8.10. It is evident that a strong intensity (preferred direction) still exists in the region next to the centre of the 111 pole figures, indicating that the uniaxial compression fails to suppress the 111 fiber texture. Thus, this simulation is in conflict with the experimental results (Fig. 8.5).

Using sample No.2's measurement as the initial texture of another simulation, the results are shown in Fig. 8.11. It clearly shows that 1) both the 111 and 100 fibre texture

remain aligned with the Z axis (the centre of the pole figure) throughout the compression process, and 2) the 111 fiber texture is suppressed during compression. Therefore, it is concluded that even a slight misalignment of compressive load with respect to the preferred orientation direction may have very significant implication of subsequent deformation.

Fig. 8.12 shows the simulated changes in the 111 and 100 fibre texture volume fraction in comparison with experiments, using sample No.2 as initial texture. The 111 fibre texture volume fraction curves of the two agree very well, and the 100 curves are a little different. Nevertheless, the intensity of 100 fibre volume fraction is very small compared to the 111 fibre texture, making it difficult to capture precisely its change during the deformation. In summary, the full scale CPFE model captured well the evolution of the main texture (111 fibre texture) in an aluminium alloy cylinder under uniaxial compression.

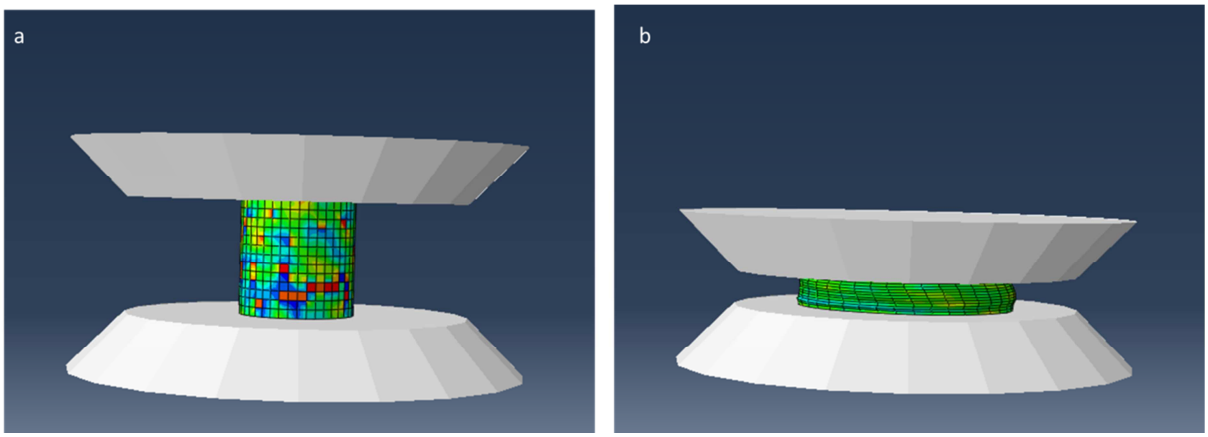

Fig. 8.9 Shape change of a cylinder due to uniaxial compression.

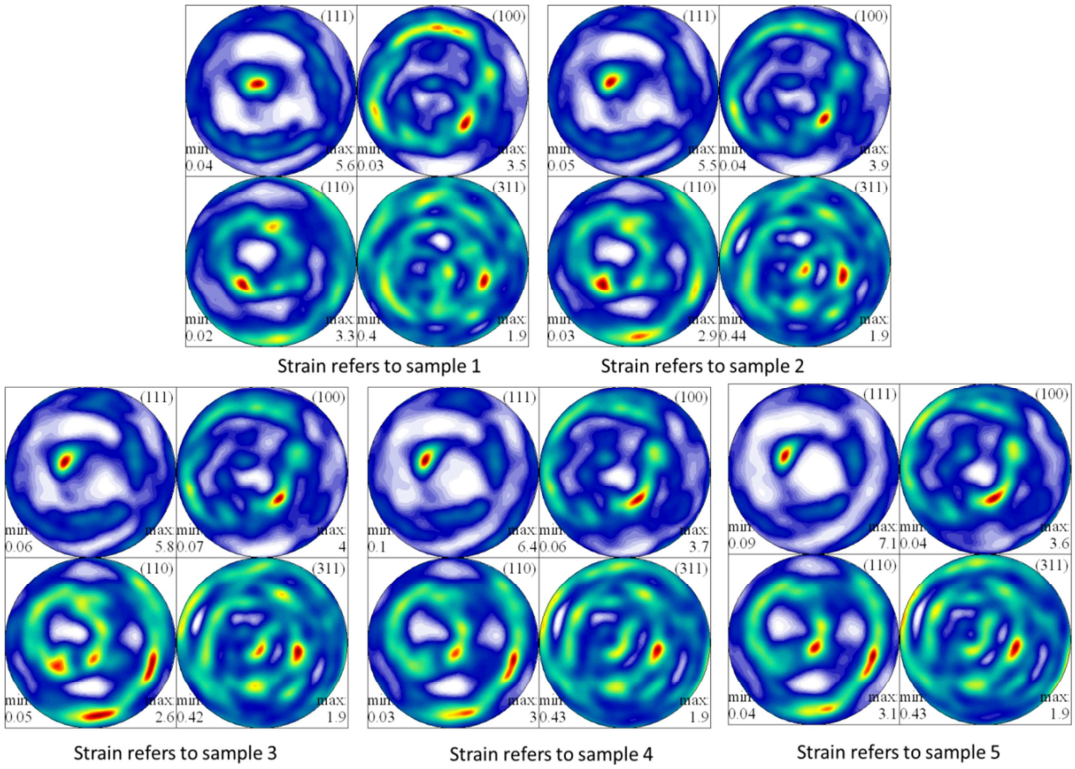

Fig. 8.10 Simulated pole figures by using sample.1 initial texture.

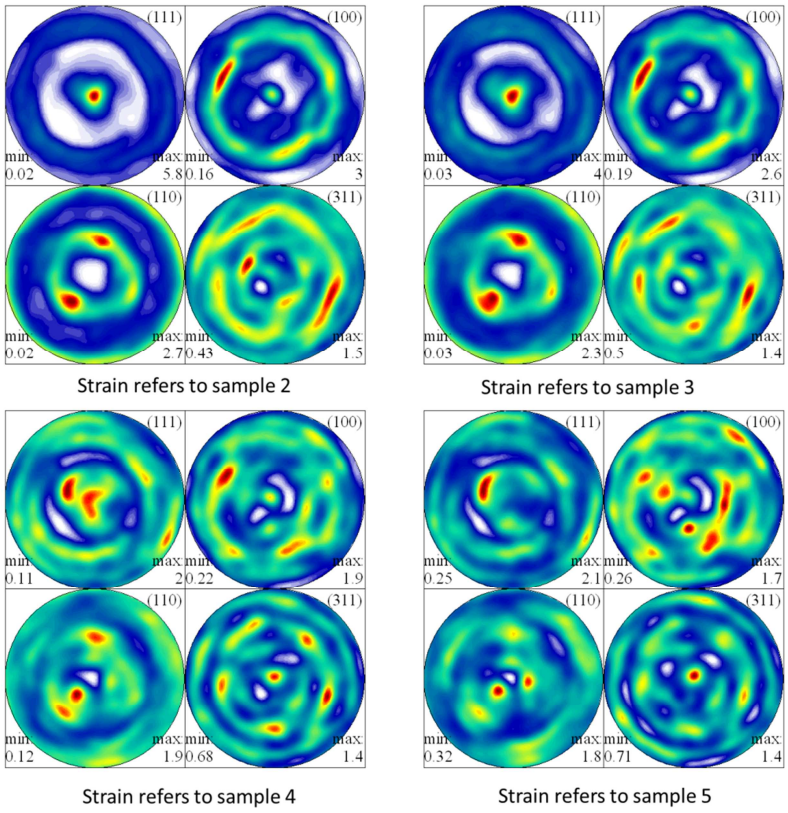

Fig. 8.11 Simulated pole figures by using sample 2 initial texture.

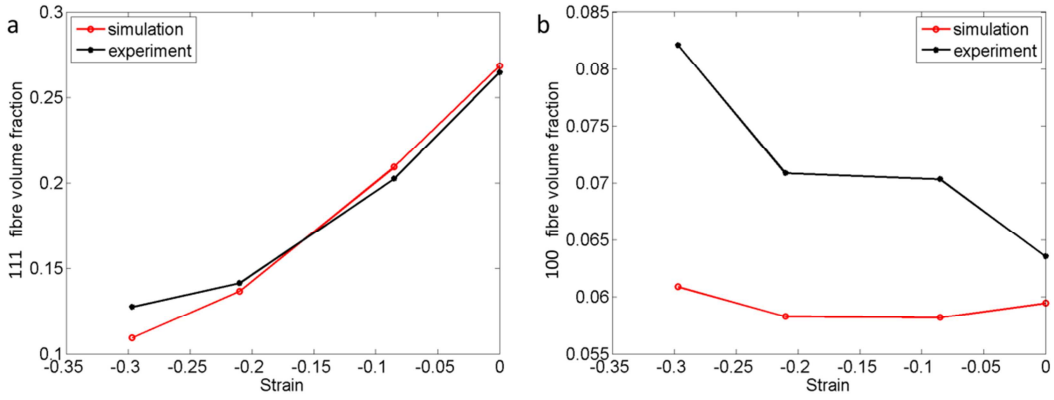

Fig. 8.12 (a) (111) and (b) (100) fibre texture volume fraction change as a function of compression strain in the simulation and experiment.

8.2.3.4 CPFE model VS Taylor model

The difference of texture evolution between CPFE and Taylor models are often compared qualitatively in literature. In this section, texture simulations between the two types of models are compared quantitatively using the volume fraction of the fibre texture as a quantitative measure.

In order to make a fair comparison between the two models, a cubic RVE (see Fig. 8.13) was created in ABAQUS (cubic RVE is often used in the literature for the purpose of comparing the two types of models). For the CPFE model, the RVE is meshed into 1000 C3D8R elements (1000 grains) and the deformation simulation was only carried out once. In contrast, for the Taylor model the RVE was meshed into a single C3D8R element (single orientation), but the deformation was simulated a 1000 times, with a different orientation assigned to the model every time). The simulation results of the CPFE and the Taylor models are shown in Fig. 8.14 and Fig. 8.15 respectively. Both results show the trend that the 111 fibre texture decreases as the compressive strain increases. Fig. 8.16 shows the 111 and 100 fibre texture volume fraction changes in the course of compression. It is clear that the CPFE model offers closer results to the experiments than the Taylor model.

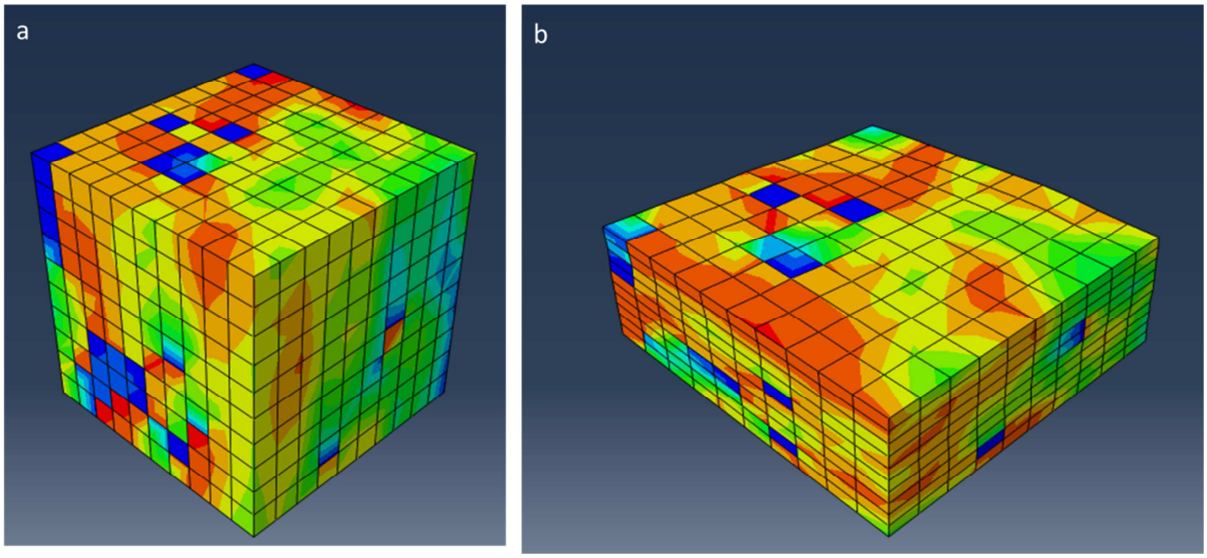

Fig. 8.13 Cubic RVE (a) before, and (b) after the uniaxial compression.

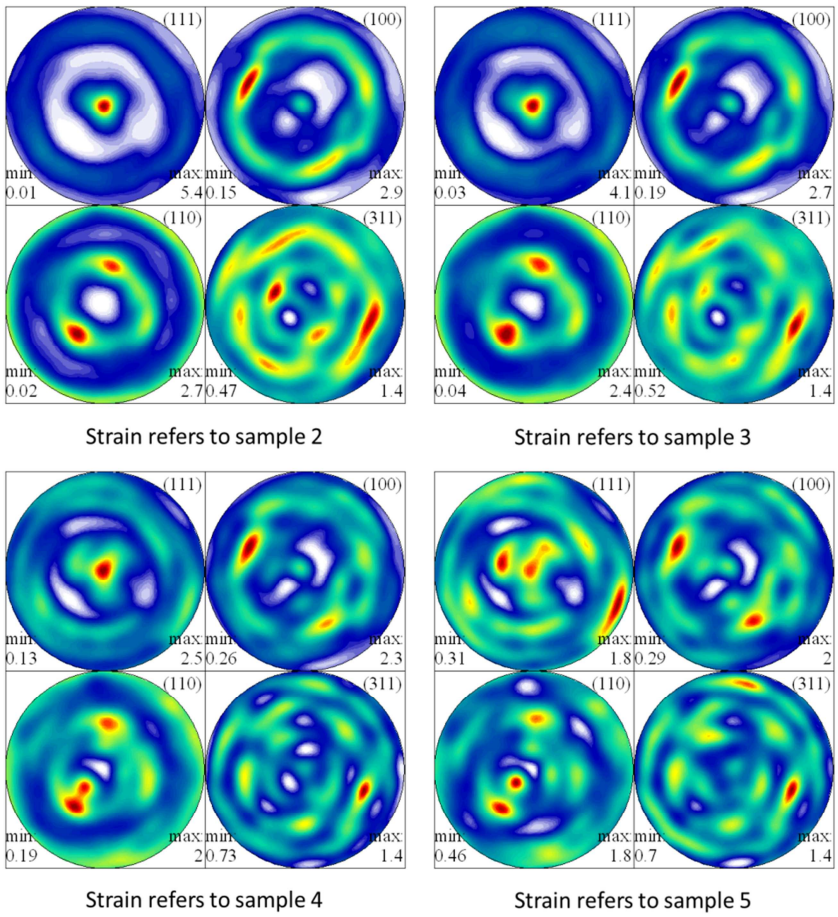

Fig. 8.14 Simulated pole figures from the CPFE model using sample No.2 texture as initial texture.

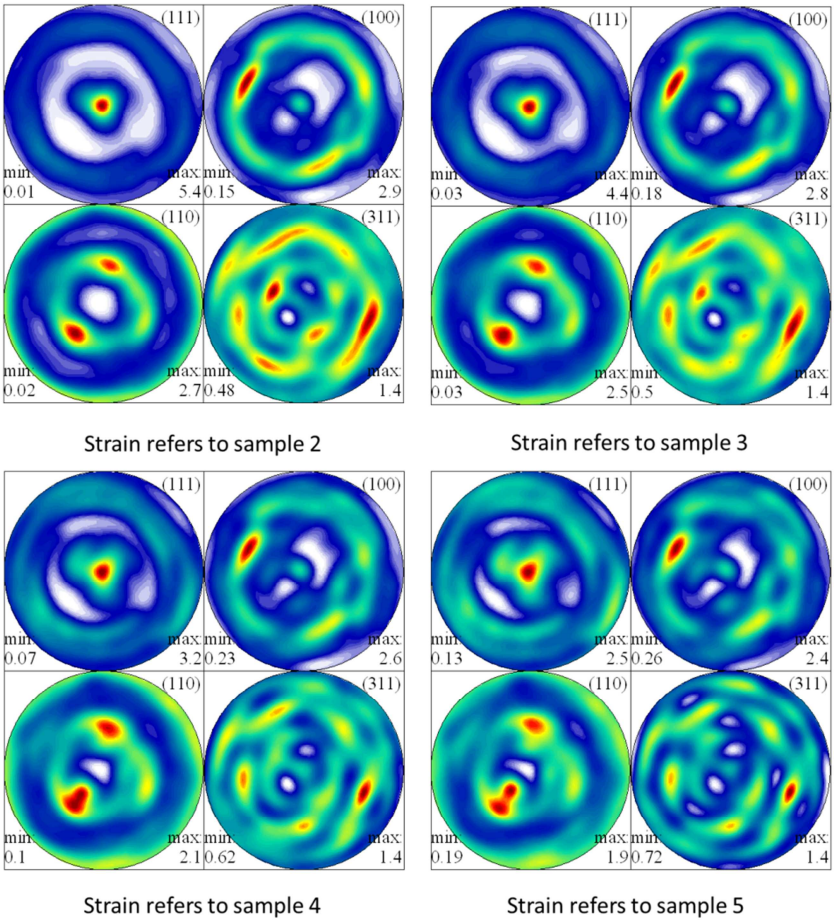

Fig. 8.15 Simulated pole figures of the Taylor model by using sample No.2's texture as initial texture.

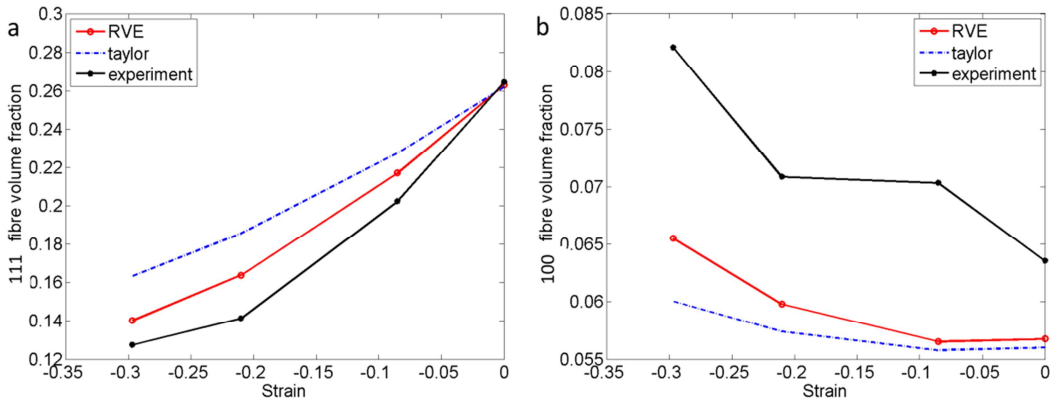

Fig. 8.16 (a) (111) and (b) (100) fibre texture volume fraction change as a function of compression strain in the simulation and experiment.

8.2.3 Conclusion

In summary, the main findings of section 8.2 are:

1) The texture evolution of an aluminium alloy cylinder under uniaxial compression is modelled successfully using the CPEM approach. The texture results between the CPFE model and the experimental measurements from an *ex situ* neutron diffraction experiment of aluminium alloy cylinder under uniaxial compression were correlated quantitatively using the volume fraction of 111 fibre texture as a measure.

2) A systematic way is presented for convert forward and backward from continuous ODF to discrete OD, in order to allow direct comparison between models and experiment.

8.3 Texture evolution modelling of a LFW joint

Texture characterization results for a few points on the central scanning line of sample W7 (section 5.2) have already been presented in section 7.1 by processing the single exposure multi-directional energy-dispersive diffraction patterns. The mechanical deformation during the linear friction welding process is more complicated than the uni-axial tension and compression cases considered in the previous two sections As revealed in the previous section, the accuracy of ODF determination in texture measurement is crucial to the texture evolution simulation. In this section the texture state in the LFW joint sample W7 is carefully characterised by Debye-Scherrer diffraction and EBSD in order to obtain further, more accurate results than those presented in section 7.1 for the modelling calibration. Then, the possibility of using the CPFE approach to model the texture evolution in the LFW process is explored.

8.3.1 Texture characterization results

8.3.1.1 Debye-Scherrer diffraction

The LFW sample W7 was measured using the Debye-Scherrer setup to scan the central line along the longitudinal direction (the same scanning line as in section 7.1). The diffraction pattern from a particular scanning point is shown in Fig. 8.17.a. The pole figure coverage for a 111 Debye-Scherrer ring is shown in Fig. 8.17.b. The changes in the total intensity of Debye-Scherrer patterns (the sum of diffraction intensity over the 2D area) act as the signs of texture change. . The total intensity at each scanning point is plotted in Fig. 8.17.c. According to the total intensity curve, the scanning line can be divided into three distinct zones in: **bond line zone** (from position No.5 to No. 7), **intermediate zone** (from position No. 3 to No. 5), and **far field zone** (from position No.1 to No. 3).

The pole figures of several representative points within the three zones are shown in Fig. 8.18. Since in FCC structure crystal the slip is primary on the {111} crystal planes, only the change in the 111 pole figures will be discussed below. Besides, it is evident that the texture distribution on the scanning line is symmetric about the bond line of the sample, so that only the texture change on the left half of the scanning line is discussed below.

Far field

The pole figures of position No.1 show a typical plate rolling texture in aluminium alloys [128, 129]. The raw pole figures directly converted from the diffraction patterns are shown in Fig. 8.18.a. It is evident that the full pole figures match well all the PFM in the raw pole figures. The far field pole figures are similar to the ones shown in section 7.1 (see Fig. 7.3). The main difference between them is that the 111 pole figure obtained using the Debye-Scherrer setup presents more detailed features than the one in section 7.1. For instance, two separate PFM spots next to RD are seen in the 111 pole figure here, but they appear to be a

single spot on RD in Fig. 7.3. This is because the “horseshoe” detector used in section 7.1 has a lower azimuthal resolution (8.2°) than the present setup (5°).

Intermediate zone

From the consideration of patterns No.4 to 12~14 it is clear that:

1) The two PFM spots next to RD in 111 the pole figures get closer and merge into a single spot as the scanning point moves closer to the bond line;

2) The two spots next to TD are moving away from each other.

In general, the 111 pole figures considered in this section are significantly different from those measured by the “horseshoe” detector (see Fig. 7.3). The difference mainly comes from two reasons:

1) The pole figure coverage of the “horseshoe” detectors is only half of the Debye-Scherrer setup, so that the ODF calculated by using the horseshoe detector is less accurate than that using the Debye-Scherrer setup.

2) The shapes of the diffraction gauge volumes in the two setups are largely different, so that the pole figures difference might be the manifestation of the strong texture gradient in the intermediate zone.

Welding zone

Inside the bond line region (No.5 & 6), the pole figures show a typical shear type texture, *i.e.* a “6-fold” symmetry present in both the 111 and 110 pole figures. It is evident that the distribution of PFM in the 110 pole figure can be rotated around ND (the Z axis) by the rotation angles that are multiples of 30 degrees to have the same distribution as in 111

pole figure. The same 6-fold symmetry and PFM distribution are also seen in the results measured by the “horseshoe” detector.

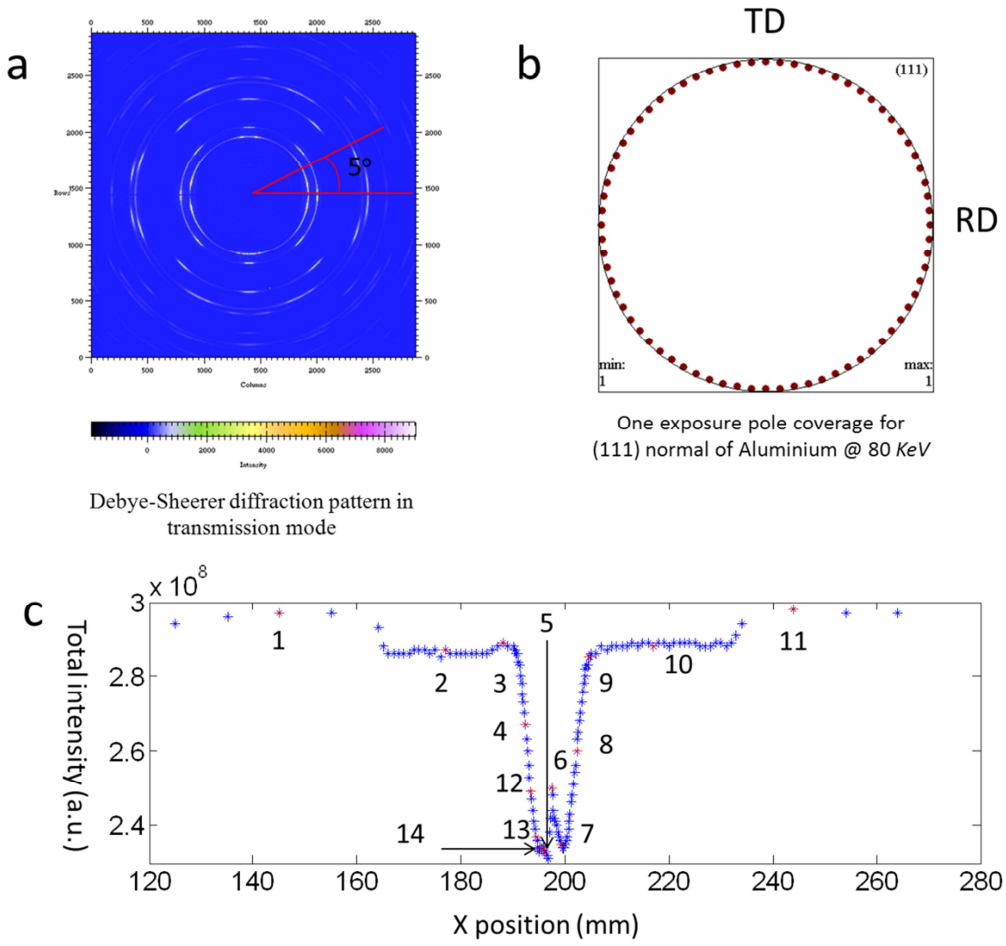

Fig. 8.17 a) Debye-Scherrer diffraction pattern of a scanning point of the LFW sample W7, (b) pole figure coverage of Debye-Scherrer setup and (c) total diffraction intensity of Debye-Scherrer diffraction patterns along the central scanning line of sample W7. The positions of several representative scanning points are highlighted in *c*.

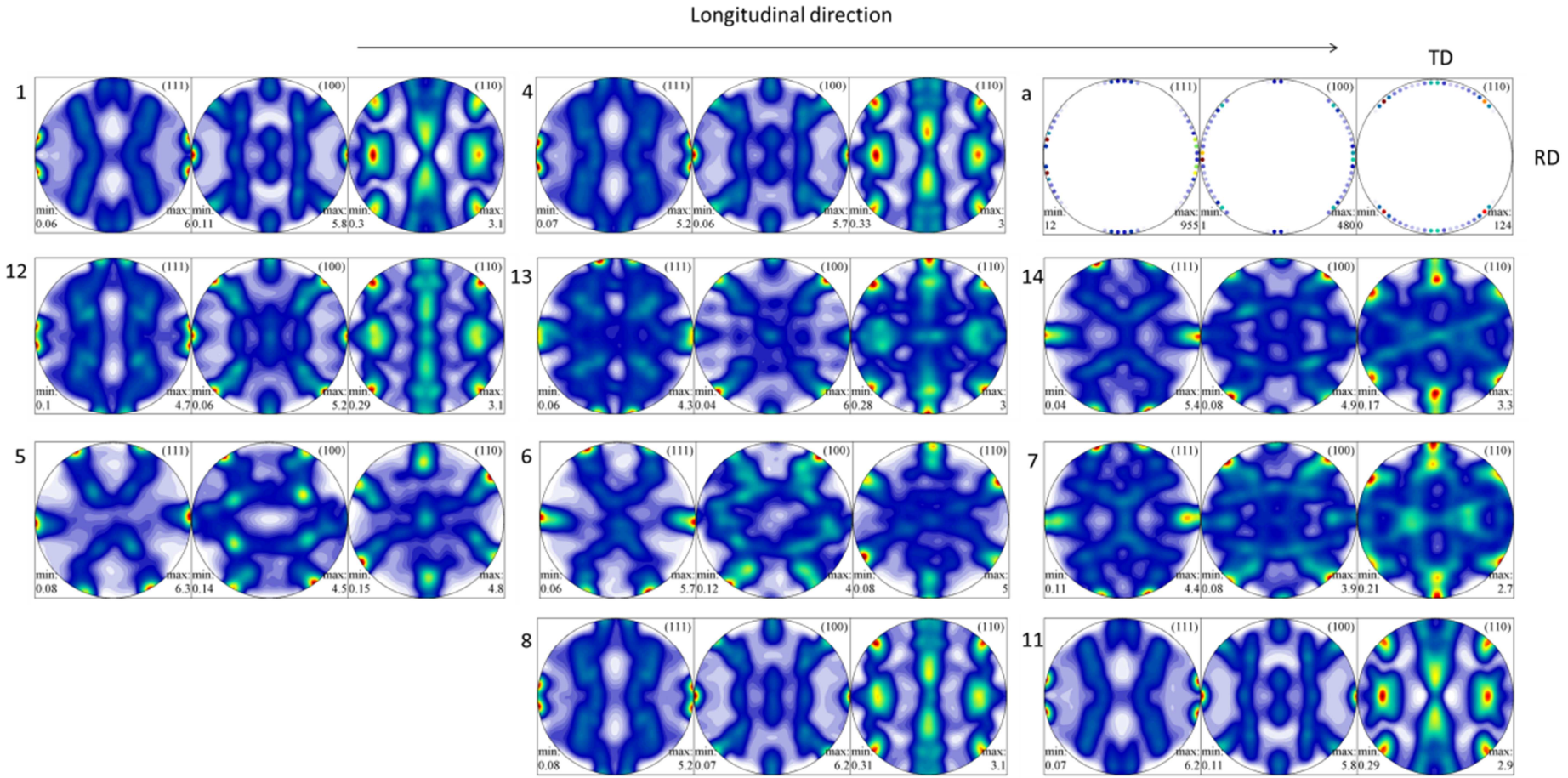

Fig. 8.18 Pole figures of the representative positions highlighted in Fig. 8.17.c. (a) the experimental pole figures of position No.1.

The Debye-Scherrer diffraction patterns of position No.1 (the far field), No.13 (the intermediate zone) and No.6 (the bond line) are also processed by MAUD and the results are shown in Fig. 8.19. It is clear that the pole figures in Fig. 8.19 and Fig. 8.18 are quite consistent, although different ODF calculation algorithms have been used.

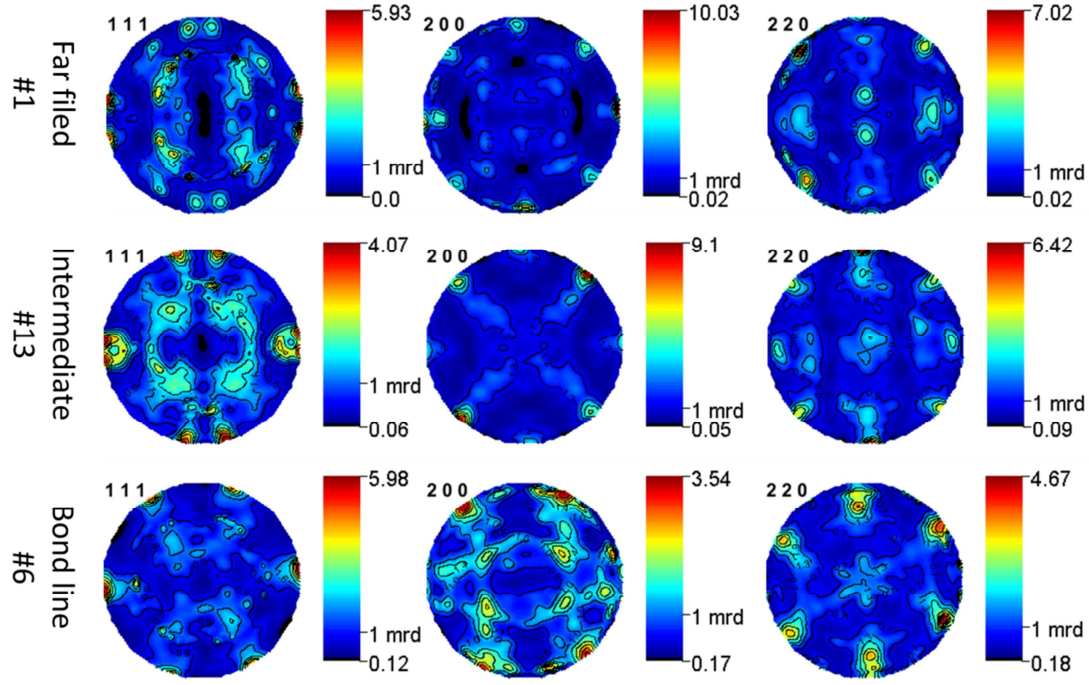

Fig. 8.19 Pole figures calculated by MAUD for three positions of sample W7.

8.3.1.2 EBSD measurement

The textures of the central scanning line of sample W7 were also measured by EBSD, and the results are shown in Fig. 8.20, in which a different position numbering is used to define several representative regions.

Far field (position No. 3-6 and 9)

The sample was polished and measured on the X-Y plane, such that the corresponding grain maps and scattering pole figures correspond only to the X-Y plane (2D). In contrast, the powder diffraction techniques (Debye-Sherrer, multi-directional energy-dispersive X-ray and TOF neutron diffractions) measure the texture in the bulk (3D).

From position No.3 to 6, the grain maps have the following common characteristics: 1) the grains are elongated along RD; 2) the scattering pole figures are similar, so that only the scattering pole figures of position No.6 are shown in Fig. 8.20 . In contrast, position No. 9 that also represents the far field, was polished and measured on the Y-Z plane. The grain map shows that grain sizes are almost uniform on the Y-Z plane. It is concluded that the grains in far field have a “needle” shape (i.e. the grains are elongated along the rolling direction).

It should be noted that the textures are different between positions No.6 and No.9. In order to a make a fair comparison between the pole figures in the two positions, the pole figures of position No.9 are re-plotted on the X-Y plane and shown in Fig. 8.21. Fig. 8.21.a and c are the original pole figures of positions No.9 and No.6, respectively. Now Fig. 8.21.b and c are plotted in the same coordinates, so that a direct comparison can be made between them. Fig. 8.21.b indicates that position No.9 has a combination of the 111 and 100 fibre textures with the extrusion directions along the RD (X direction) [130], whereas Fig. 8.21.b suggests that position No. 6 is more similar to a plate rolling texture with the rolling direction along RD (X direction). This difference seems reasonable, since during bar rolling the X-Y plane of the sample approximately experiences a uni-axial tension (fibre texture) and the Y-Z plane mainly experiences plane strain compression (plate rolling texture). However, it remains difficult to decide which texture should be used in the validation of CPFE modelling. In the end, X-ray rather than EBSD results were used for model validation.

Intermediate (position No.2)

In position No. 2 the grain sizes are clearly seen to be smaller than in the far field (position No.6), but significantly larger than on the bond line (position No.1), suggesting that it is really an “intermediate” region in terms of grain morphology. It is evident that from position No.3 to No. 2 the grain width (Y dimension) remains the same but the grain lengths

(X dimension) is reduced. This is probably because of the shear deformation between X and Y axes during welding process that shears the grains along the Y axis. The scatter pole figures show a slight deviation from the far field, but are not similar to the pole figures within intermediate zone measured by both the “horseshoe” detector (Fig. 7.3) and Debye-Scherrer setup (Fig. 8.18). The disagreement might be caused by the fact that the diffraction volumes of these diffraction techniques are very different, so that the texture measurements from nominally the same region are different when the texture gradient within the region is very strong.

Welding zone (position No.1 and 7-8)

In position No. 1 and 7-8, the grains turn to be much smaller than both the intermediate and far field regions. The collected Kikuchi patterns for this region are very noisy, making the indexing error rather high. That is the reason the grain map to appear as a mosaic. This high indexing error is also noticed in other EBSD studies of LFW samples [109], where it was concluded that the grains in welding zone were severely distorted during LFW process, making the Kikuchi patterns difficult to be indexed. The scatter pole figures are consistent with those measured by both the “horseshoe” detector and the Debye-Scherrer setup, with the shear type texture clearly seen.

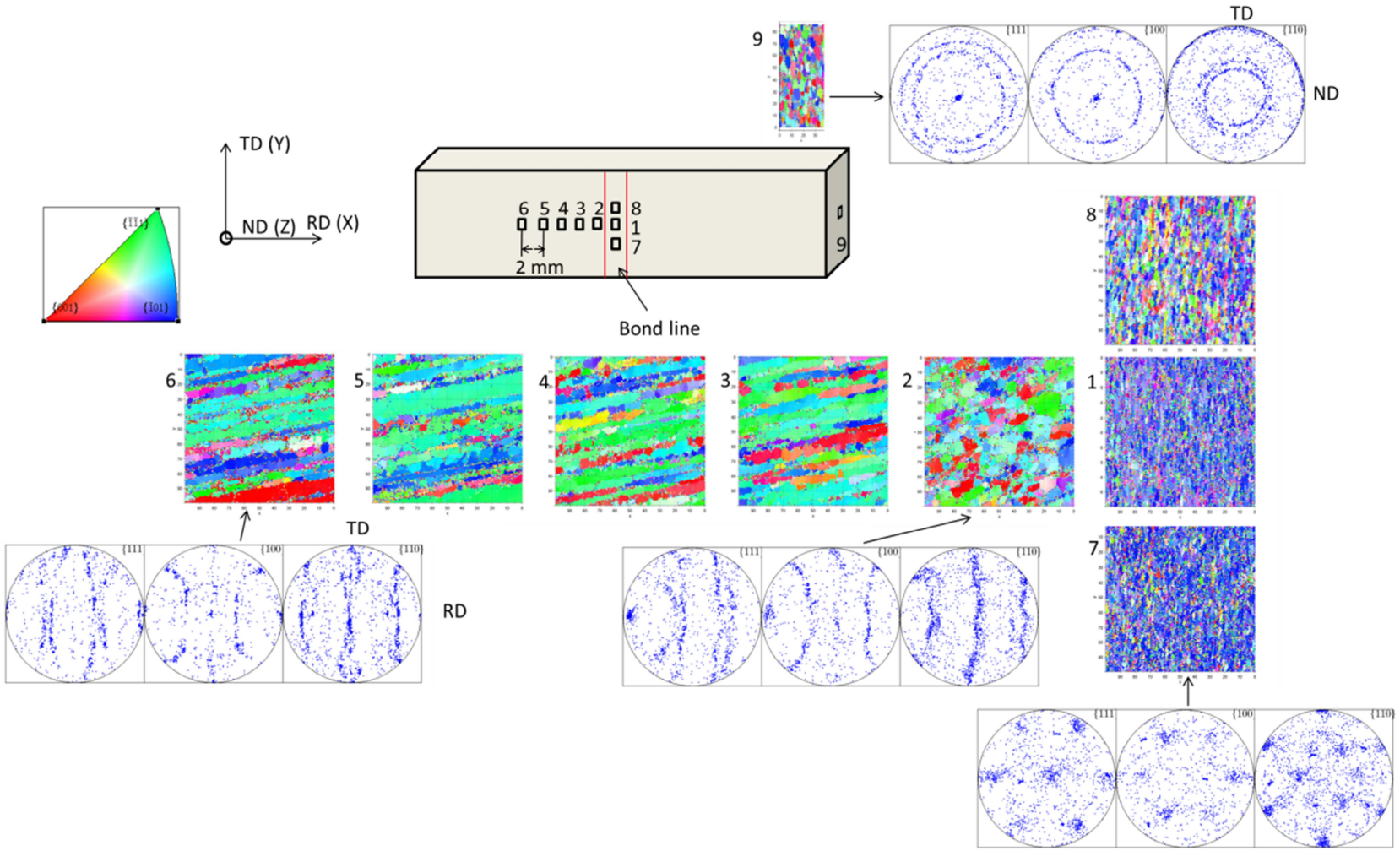

Fig. 8.20 EBSD results of sample W7 on X-Y and Y-Z cross-sections.

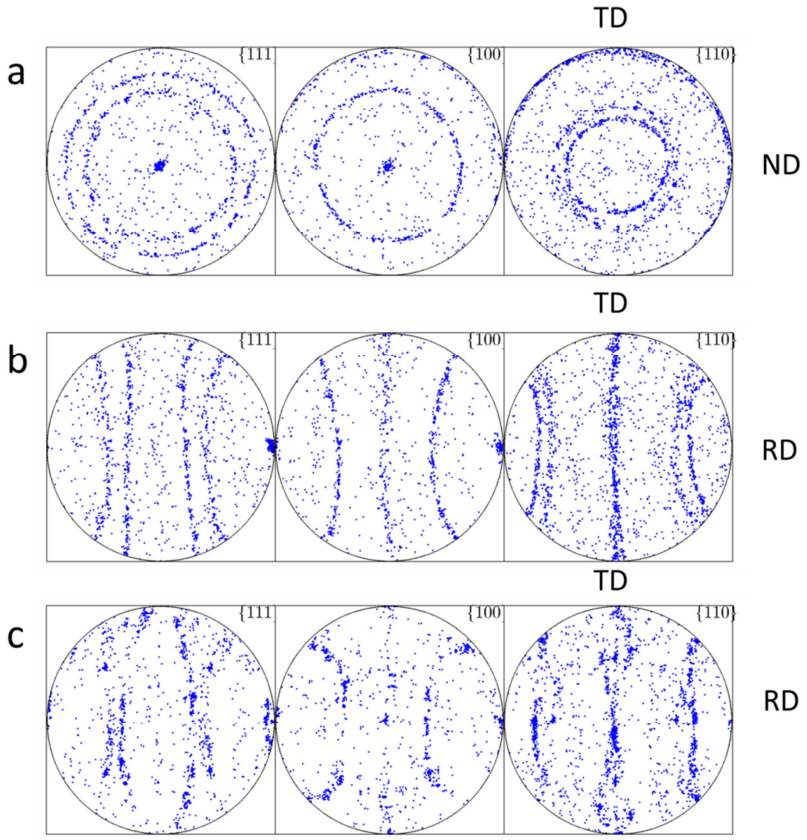

Fig. 8.21 Scattering pole figures of position No.9 on Y-Z plane (a) and X-Y plane; scattering pole figures of position No.6 on X-Y plane.

8.3.2 Grain orientation assignment in the CPFE model

The texture information measured by the Debye-Scherrer setup corresponds to the material bulk rather than the material suface measured by EBSD. Hence, the pole figures shown in Fig. 8.18 were used as the reference to validate the CPFE model using a cubic RVE. The cubic RVE consisted of 4096 C3D8R elements representing 4096 grains.

In the far field (position No.1), texture is assigned to the RVE as the initial texture setting. Two different grain assignment methods can be used here: 1) randomly assign the discrete OD to the RVE (as shown in Fig. 8.22.a); 2) assign the OD to the RVE in a way to ensure that the “needle” shape of grains observed from the EBSD characterization is preserved (shown in Fig. 8.22.b).

It is evident that the second grain assignment method would result in a RVE with a more realistic microstructure. Interestingly, simulation reveals that using the two grain assignment methods leads to very similar results, although the textures results by using the first method are slightly sharper (stronger) than when using the second one. In the discussion below only the results of the second grain assignment method are presented.

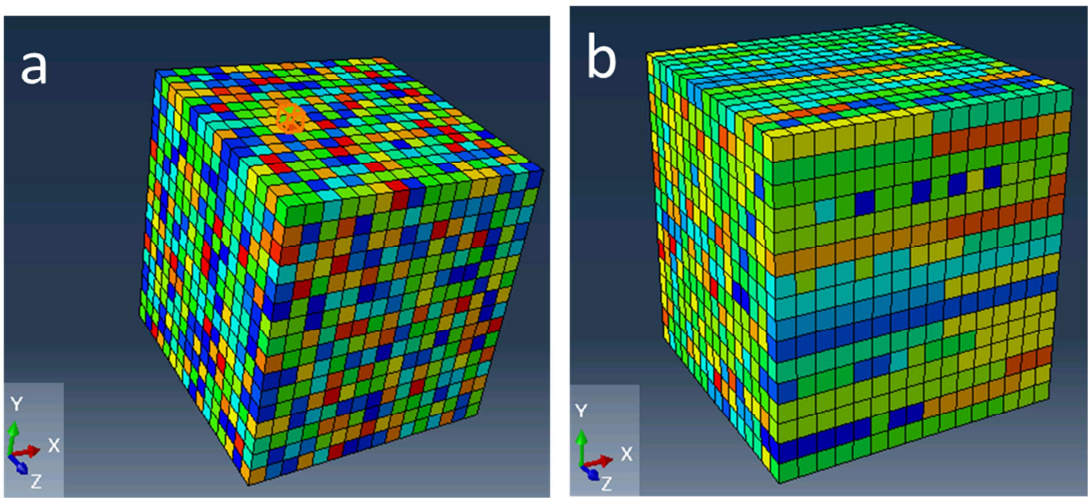

Fig. 8.22 In (a) grains are randomly assigned to the cubic RVE, and in (b) grains appear to have “needle” shape in the cubic RVE.

8.3.4 Boundary conditions and simulation results

8.3.4.1 Possible boundary conditions

LFW is a complicated thermal-mechanical coupled deformation process compared to the wire extrusion (section 8.1) or uniaxial compression (section 8.2), for which texture evolution appears better understood in the literature. The most difficult part in the texture evolution modelling for linear friction welding is to determine (idealize) the boundary conditions of the RVE. The most faithful boundary condition implementation is impractical because of the complexity of the LFW process. Some possible boundary conditions idealizations are discussed below.

The effect from the temperature on the texture evolution is ignored because: 1) the temperature in the welding process remains much lower than the melting point of the sample; 2) as discussed in chapter 4, even though in the FCC crystal slip systems other than {111}<110> may be activated owing to the high temperature, the texture evolution is captured well even considering only the slip system {111}<110>

Fig. 8.23 shows a schematic of the two mechanical deformation steps during a linear friction welding. Fig. 8.23.b states that a material point experiences cyclic shear deformation (reciprocal sliding). The magnitude of shear is a function of the distance from the bond line (the interface). Fig. 8.23.c states that for all material points, the uniaxial compression owing to the forging force. This deformation is non-uniform due to the dependence of the flow stress on temperature, and hence on the distance from the heat source (the bond interface). Since the two main deformation modes are confined to the X-Y plane, in the simulation below plane deformation in the X-Y plane is applied to the RVE.

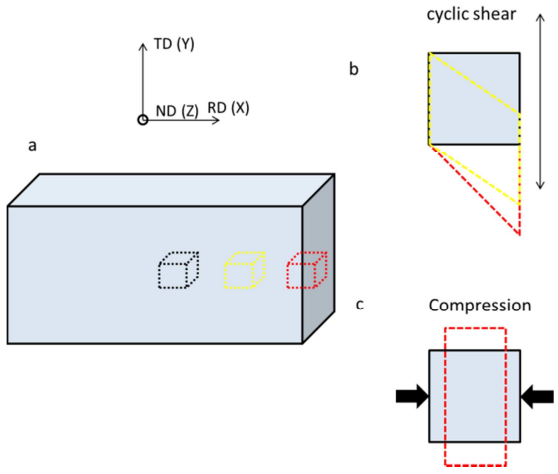

Fig. 8.23 (a) half of a LFW sample and three materials points referring to welding zone (red), intermediate zone (yellow) and far field (black), (b) illustration of cyclic shear deformation owing to the linear friction and (c) illustration of uniaxial compression owing to the forging force.

8.2.4.2 Simple shear

A typical shear texture (i.e. the 6-fold symmetry in the 111 and pole figures) is observed in the welding zone of the sample from the experimental measurements by EBSD, the “horseshoe” detector and Debye-Scherrer setup. This texture often arises in texture simulations after applying a planar simple shear deformation to an RVE starting with random texture. On the texture characterization side, this texture has also been observed in other types of friction welding, for instance Friction Stir Welding (FSW) [131, 132]. The main difference in terms of process between FSW and LFW is that the friction in the FSW can be approximated as monotonic shear (simple shear) in the same direction, whereas reciprocal shear (cyclically reversed shear) takes place in LFW.

Therefore, although simple shear is not a perfect idealization of the boundary conditions, it is still worth considering the application of shear boundary condition to the RVE to check whether simple shear may be the main cause for the formation of shear type texture in the welding zone. A simple shear deformation corresponding to a shear strain γ_{12} can be written in terms of strain increment as

$$\dot{E} = \begin{bmatrix} 0 & +\Delta & 0 \\ 0 & 0 & 0 \\ 0 & 0 & 0 \end{bmatrix} \qquad \text{(Eq. 8.5)}$$

It has been reported that while simulating texture evolution during simple shear deformation, the starting texture of the RVE can affect the simulation results significantly [133, 134]. For the simulation of the LFW case, the starting texture of the RVE is assigned by the ODF of position No. 1 in Fig. 8.18. Thus the texture evolution of the RVE obtained is different from models starting with random textures. In order to understand how the starting texture and the direction of simple shear affect the texture evolution of RVE, three simulations were carried out: 1) starting with random texture and the total shear strain of

γ_{12}=1.5; 2) starting with the texture of the far field of sample W7 and the total strain also of γ_{12}=1.5; 3) starting with the texture of the far field of sample W7 with the total strain of γ_{12}=-1.5. The simulation results of the three cases as well as the results from the experiments within far field, intermediate and welding zone are plotted in Fig. 8.24 in order to make comparisons.

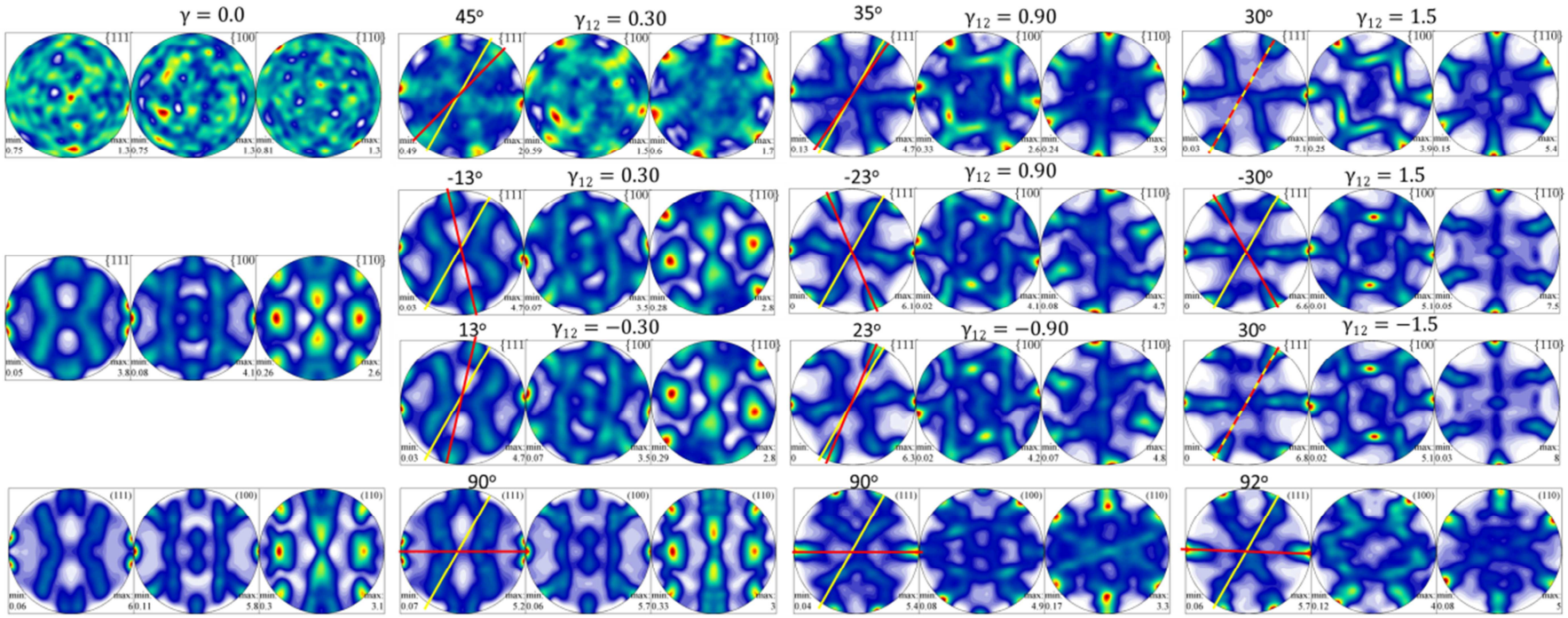

Fig. 8.24 Texture evolutions of RVE started with random texture and γ_{xy}=1.5 (first row), RVE started with the texture of the far field of sample W7 and γ_{xy}=1.5 (second row), RVE started with the texture of the far field of sample W7 and γ_{xy}=-1.5 (third row) and the corresponding experimental results by Debye-Scherrer setup (fourth row).

Some axillary lines are drawn in the pole figures to illustrate the “orientation” change of 111 pole figures. The orientation of a 111 pole figure is highlighted by the symmetric axis of the PFMs. The red line in 111 pole figure refers to the current orientation of the pole figure. The yellow line refers to the orientation of a standard simple shear texture, which corresponds to a RVE starting with random texture and subjected to a γ_{12}=1.5 simple shear deformation. The rotation angle around ND (Z direction) from TD (Y direction) to the current orientation (red line) is marked on the top of each 111 pole figure.

In the first row of Fig. 8.24 (starting with random texture), the orientations of the 111 pole figures are gradually changed from 45° to 30^o as shear strain is increased from 0.3 to 1.5. This change is in agreement with the simulation results in the literature [135].

In the second row of Fig. 8.24 (starting with the far field texture), the orientations of the 111 pole figures are changed from -13° to -30° as the shear strain increases. The orientation of the final 111 pole figure has a 60° rotation angle difference to its counterpart in the first row. The differences between these two simulations are only due to the starting textures! This confirms that the starting texture indeed affects significantly the texture evolution simulation.

In the third row of Fig. 8.24 (starting with far field texture but with the negative shear direction applied), the orientation of the 111 pole figure is changed from 13° to 30° as the shear strain is increased. The orientation of the final 111 pole figure is the same as the one in the first row, although the starting texture and shear direction between them are different.

It is easy to notice that the difference between all four rows of the 111 pole figures is only in the rotation angle around ND (Z direction). However, neither row of simulated pole figures matches fully the experimental results.

8.2.4.3 Plane strain compression (pure shear deformation)

A noticeable feature in the experimental results (i.e. the fourth row in Fig. 8.24) is that the orientations of 111 pole figures (red lines) do not change from the far field to the welding zone. It is well known that a simple shear deformation can be mathematically decomposed into a pure shear deformation and a rigid body rotation around the axis out of the plane of the object. Thus, if pure shear deformation were to be applied to the RVE, the orientation of the 111 pole figures may remain unchanged. A plane strain deformation can also be decomposed into a rigid body rotation and a pure shear deformation, such that plane strain deformation is commonly accepted as a case of pure shear deformation. Noting the compression caused by uniaxial forging during LFW, a possible idealization of plane strain compression may be taken for the boundary condition of the RVE. The corresponding compression direction and deformation plane should be X direction (RD) and X-Y plane respectively.

The mathematical relationship of the plane strain compressions along Y and X direction with the corresponding pure shear deformations are shown below,

$$\dot{\varepsilon} = \begin{bmatrix} +\Delta & 0 \\ 0 & -\Delta \end{bmatrix} = \begin{bmatrix} \cos(\frac{\pi}{4}) & \sin(\frac{\pi}{4}) \\ -\sin(\frac{\pi}{4}) & \cos(\frac{\pi}{4}) \end{bmatrix} \begin{bmatrix} 0 & +\Delta \\ +\Delta & 0 \end{bmatrix} \begin{bmatrix} \cos(\frac{\pi}{4}) & -\sin(\frac{\pi}{4}) \\ \sin(\frac{\pi}{4}) & \cos(\frac{\pi}{4}) \end{bmatrix} \quad \text{(Eq. 8.6)}$$

$$\dot{\varepsilon} = \begin{bmatrix} -\Delta & 0 \\ 0 & +\Delta \end{bmatrix} = \begin{bmatrix} \cos(\frac{\pi}{4}) & \sin(\frac{\pi}{4}) \\ -\sin(\frac{\pi}{4}) & \cos(\frac{\pi}{4}) \end{bmatrix} \begin{bmatrix} 0 & -\Delta \\ -\Delta & 0 \end{bmatrix} \begin{bmatrix} \cos(\frac{\pi}{4}) & -\sin(\frac{\pi}{4}) \\ \sin(\frac{\pi}{4}) & \cos(\frac{\pi}{4}) \end{bmatrix} \quad \text{(Eq. 8.7)}$$

Four simulations were carried out:

1) A RVE with initial random texture subjected to plane strain compression along the X direction (RD);

2) RVE with initial random texture subjected to a plane strain compression along the Y direction (TD);

3) RVE with initial texure of the far field of sample W7 subjected to plane strain compression along the X direction (RD);

4) RVE with initial texture of the far field of sample W7 subjected to a plane strain compression along the Y direction (TD).

The four rows of simulation results as well as the fifth row corresponding to the experimental results are presented in Fig. 8.25.

It is evident that the initial texture of the RVE does not affect significantly the final texture in this case, taking the first (or second) and third (or fourth) rows of pole figures at strain ε of 0.7. This is different from the simulation in the previous section in which initial texture strongly affected the final texture of RVE subjected to a simple shear deformation.

It is evident that the fourth row offers the best match to the experimental results (the fifth row) from the far field to the welding zone. However, the texture changes in the fourth row corresponds to plane strain compression along Y direction (TD), which is in conflict with the fact that the forging direction is along X direction (RD) during the LFW process. The compression direction for the third row is along the X direction. It may be expected that it ought to offer the best similarity to the experimental results. The pole figures of the third row are indeed similar to the experimental results, but they have to be rotated around the Z axis (ND) by 90^{o} to have the same orientations as the experimental results.

In summary, very similar results compared to the experiments have been obtained by applying plane strain compression to the RVE. However, the compression direction of the

best simulation is not consistent with the LFW process, so that the judgement of these simulation outcomes remains critical.

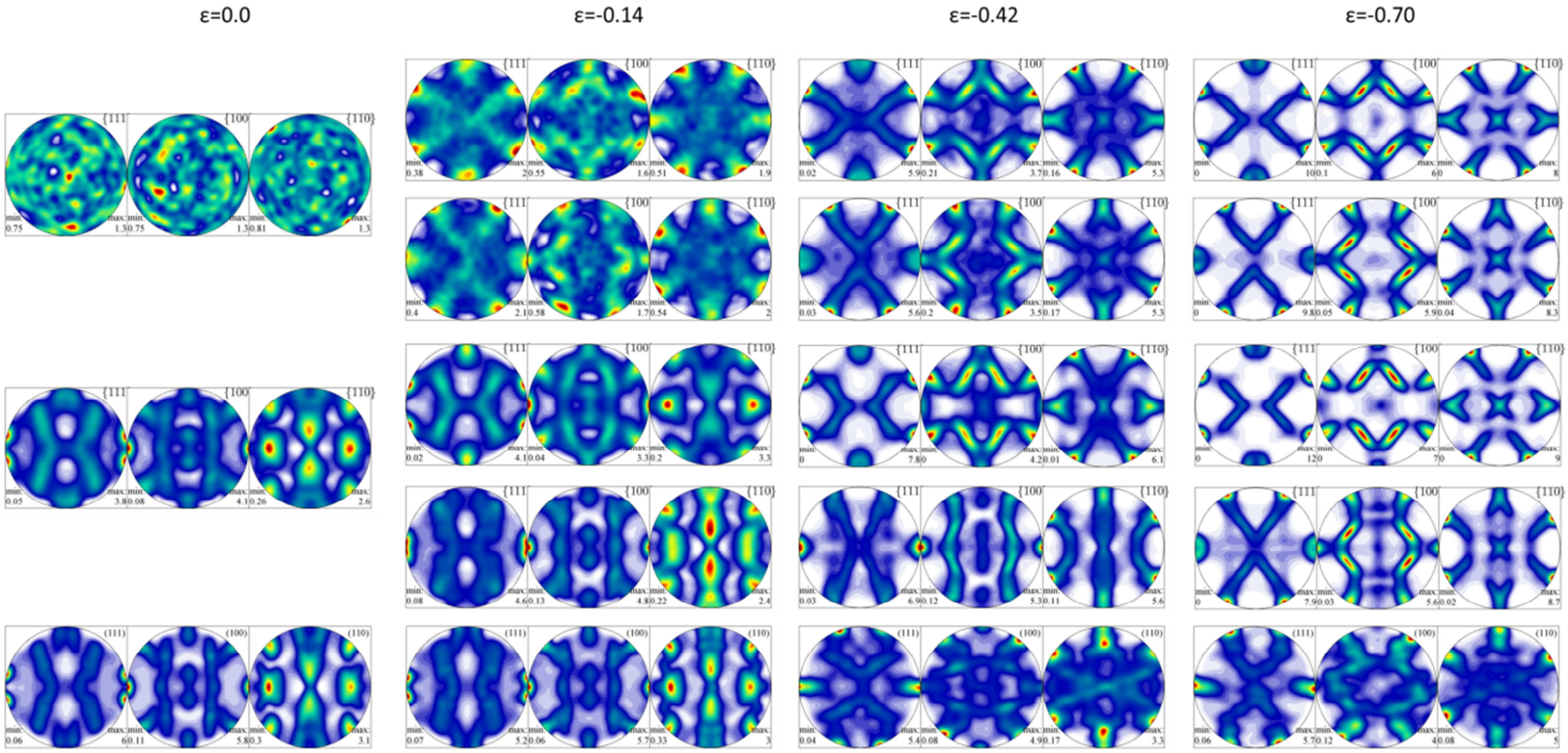

Fig. 8.25 Texture evolutions of RVE started with random texture and the compressive direction is along RD (first row), RVE started with random texture and the compressive direction is along TD (second row), RVE started with the texture of the far field of sample W7 and the compressive direction is along RD (third row), RVE started with the texture of the far field of sample W7 and the compressive direction is along TD (fourth row) and the corresponding experimental results by Debye-Scherrer setup (fifth row).

8.2.4.4 Shear deformations in sequence

In the two previous sections, two **monotonic** shear deformations have been applied to the RVE to model the texture change. None of them fully match the experimental result of the texture evolution on the central scanning line of sample W7 measured by the Debye-Scherrer setup. Therefore, in this section the possibility of applying a sequence of deformation steps to the RVE is explored in order to match the experimental results.

It is well known that in plastic flow the sequence of deformation steps (strain path) has huge impact on the final mechanical characteristics of the object, such as residual strain and texture. Thus, any proposed sequential loadings used for the CPFE modelling without the validation through *in situ* experimental results are highly likely to be wrong. For the LFW sample W7 only the texture characterization at as-received condition was available. The boundary conditions proposed below should not be regarded as reflections of what happened during linear friction welding, but should rather be used as guidance for future texture evolution studies on LFW processes or any similar shear type deformation.

Below we present the texture simulation by considering the LFW process as

1) a series of reciprocal simple shear deformation in order;

2) a three-step sequential deformation in order.

Pure cyclic shear

The reciprocal friction deformation (as shown in Fig. 8.23.b) in the welding zone can be regarded as a cyclic simple shear deformation. If the forging deformation in LFW process is ignored, the LFW process can be simplified as a pure cyclic simple shear deformation. The Route C deformation in Equal Channel Angular Extrusion (ECAE) [136, 137] is also a type of cyclic shear deformation, and the texture evolution has been well studied from both

experimental and modelling points of view. ECAE is one of the advanced techniques for ultra-fine grain materials manufacturing. The key part in an ECAE setup is a hard die with a 90^o bent channel inside. When using the die, a metal billet is pushed through the channel in many passes. Each pass can be idealized as a simple shear deformation owing to shear deformation at the 90^o corner. Thus, multi-pass deformation refers to many simple shear deformations in a certain order. A so-called Route C [138] deformation in ECAE is a process with even number of passes in which the billet is rotated around the longitudinal axis by 180^o before each subsequent pass. Therefore, the shear direction of the even-numbered passes is reversed compared with that of the odd-numbered passes. Such cyclic shear deformation is identical to the linear friction deformation in the welding zone of the LFW process. However, it is found in literature that, while applying the cyclic shear deformation to either a 2D [139] or 3D [137] RVE started with random texture, the texture becomes a typical shear type (i.e. the pole figures has 6-fold symmetry) after the odd number of passes, but is reversed back to random texture after the even shear. The findings from the simulations are in conflict with most experimental results, as a typical shear texture is *always* found in ECAE samples after Route C deformation, no matter whether odd pass or even pass was last.

The results of applying cyclic simple shear simulation to the cubic RVE using the CPFE approach are shown in Fig. 8.26. It shows the same phenomenon as in the modelling literature: after even (2 and 4) shear cycles, the shear type texture is reversed back to random texture.

In summary, the attempt by approximating the boundary conditions of the RVE as cyclic shear deformation failed.

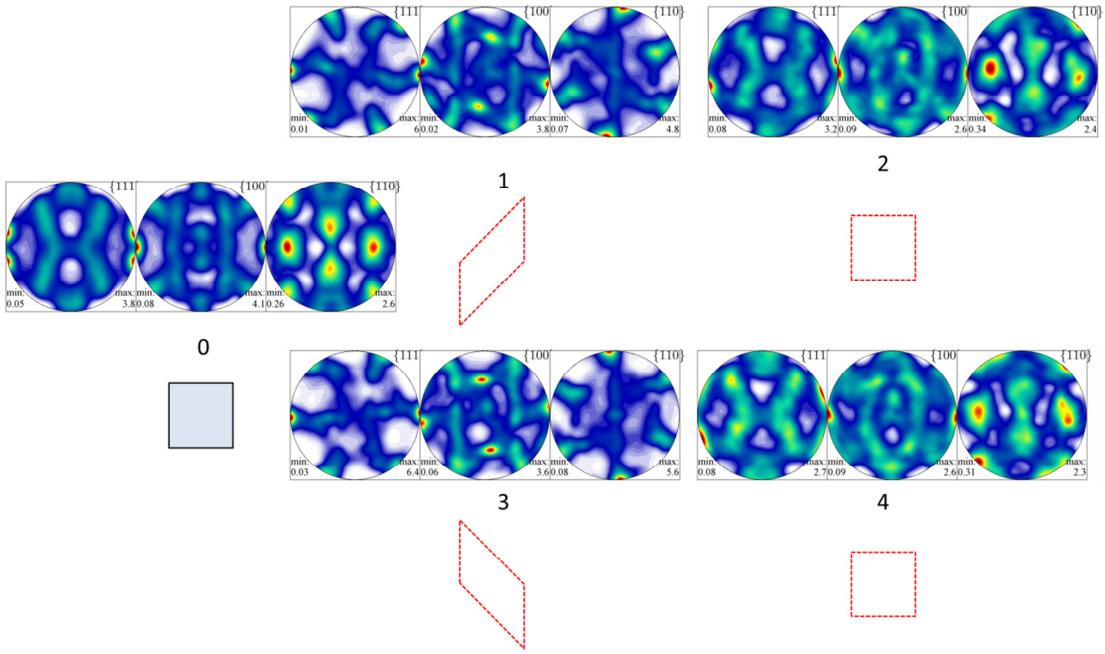

Fig. 8.26 Texture evolution of RVE during 4 steps of cyclic simple shear deformation. Cyclic number and the 2D shape of the RVE are shown below the pole figures.

Three-step sequential shear deformation

In the LFW process, apart from the cyclic shear deformation corresponding to the reciprocal friction, the contribution of the forging force should not be ignored in the texture simulation. The forging can be approximated as either a uni-axial compression, or a plane strain compression, or a simple shear deformation along the X direction (consistent with the forging direction). Thus, a three-step deformation can be used to approximate the full LFW process: the first step is to apply a simple shear deformation along positive Y direction, the second step is to apply the forging deformation, and the third step is to apply a simple shear deformation along the negative Y direction. It is evident that without the second forging step, the three-step deformation is equivalent to the cyclic shear deformation with one period.

Unfortunately, the simulation results by assuming the forging deformation in the second step as either uni-axial compression or plane strain compression give the pole figures without any regular features. It suggests that the assumptions are not valid in the simulation.

Only by assuming the forging step to correspond to simple shear deformation along the X direction, the final pole figures of the RVE show the 6-fold symmetry consistent with the experimental results.

Therefore, the LFW process can be successfully approximated as a three-step sequential shear deformation:

1) Applying the first simple shear deformation of γ_{12}=1.5 to the RVE;

2) Applying a γ_{yx} simple shear deformation (with the magnitude that is much smaller than in the first step) to the RVE (referring to the forging force);

3) Applying a γ_{xy}=-1.5 shear deformation to the RVE.

The simulation results are shown in Fig. 8.27. The first simple shear deformation rotates the 111 pole figure around ND (the Z axis) from 90^o to -30°. In the second γ_{yx} shear deformation, texture changes caused by five different strain magnitudes are modelled. It shows that, the higher the strain magnitude is applied to the RVE in the second step, the more the orientation of the 111 pole figure approach to TD. In the third step of shear deformation, two noticeable outcomes are observed: 1) the pole figures by considering a simple shear in the step clearly display the shear type texture as seen in the experimental results; 2) the higher shear strain is applied in the second step, the sharper the final shear texture is observed after the third step.

This three-step simple shear deformation simulation provides a possible explanation to the presence of the shear type texture in the bond line of a LFW sample. It mainly reveals that, by inserting a simple deformation along the different direction into a cyclic shear deformation, the final shear type texture is obtained. The simulation may also help explain the shear texture formation in the Route C deformation of the ECAE process.

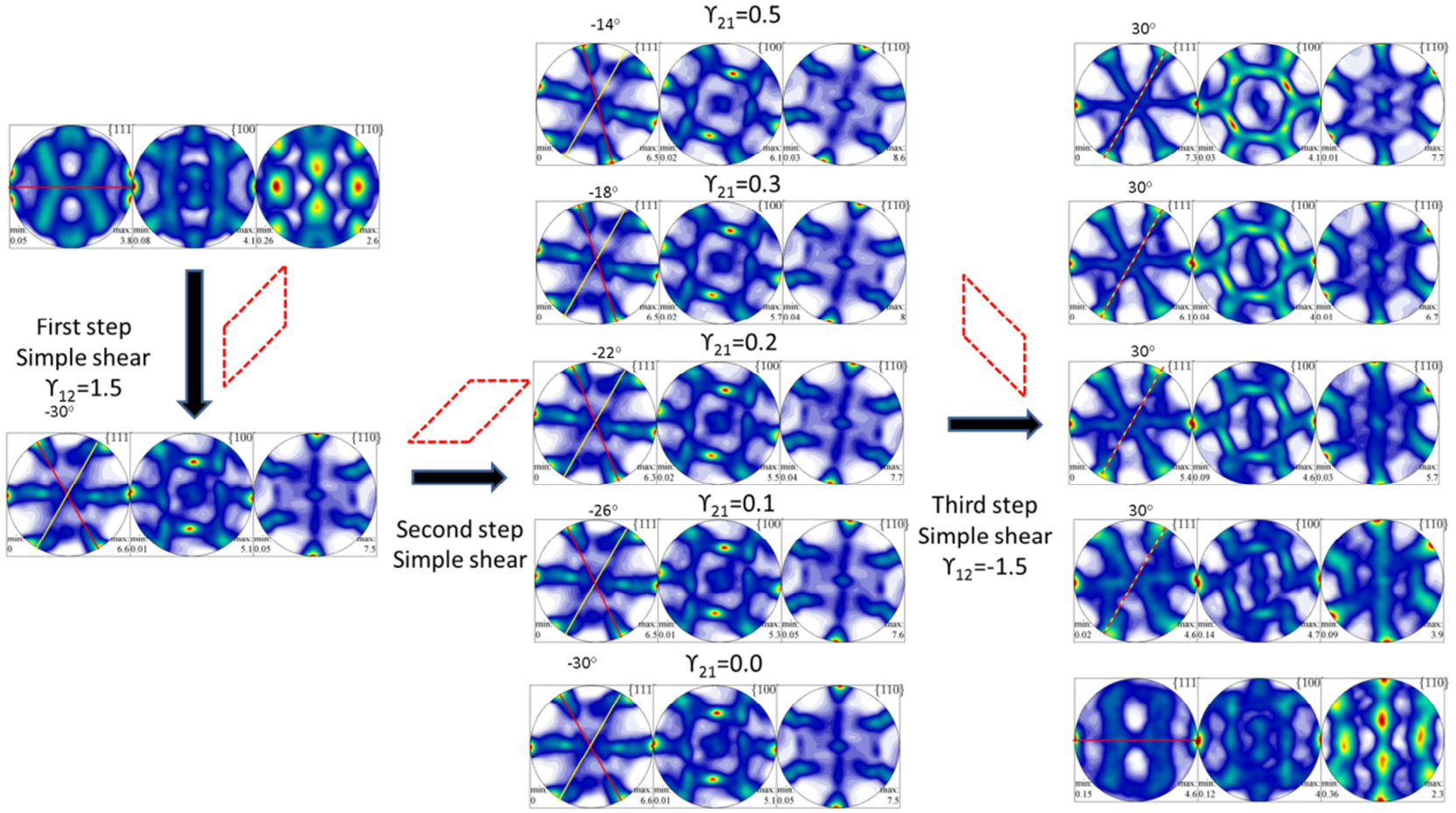

Fig. 8.27 Texture evolution of the RVE during the three-step shear deformation. The shape of the RVE is plotted in each step in order to illustrate the shear direction. Five different shear strain magnitudes are applied in the second step: 0.5 (first row), 0.3 (second row), 0.2 (third row), 0.1 (fourth row) and 0.0 (fifth row).

8.3.5 Conclusion

The main findings of this section are:

1) While modelling the texture change during a LFW process, the mechanical deformation cannot be regarded as a monotonic shear type deformation (either a simple shear or a pure shear deformation).

2) A three-step sequential shear deformation is proposed to model the texture formation at the very bond line of the LFW sample. The simulation results are consistent with the experimental results as both of the pole figures display a 6-fold symmetry (shear type texture).

Chapter 9 Conclusions and future work

9.1 Conclusions

The purpose of the present thesis was to make contributions to the advancement of knowledge and practice in three principal areas:

1) Improving the accuracy of strain measurements at the meso-scale by carrying out data analysis of the diffraction patterns obtained from multi-directional energy-dispersive synchrotron X-ray powder diffraction;

2) Developing texture characterization techniques based on the single-exposure powder diffraction with monochromatic and polychromatic beams and the correspondent detectors with large pole figure coverage;

3) Improving the understanding of texture evolution in polycrystalline samples during manufacturing processes by matching CPFE models to experimental results.

In order to address the challenges that remain outstanding in these areas, in Chapters 5 to 8 alongside fundamental technique developments, a range of original experimental studies were presented.

Based on the obtained results, the main conclusions of the thesis are summarized below.

9.1.1 Strain measurement

Section 5.1 presented a “numerical experimental” study aimed at validating the claim that the lattice parameter derived from an experimental diffraction pattern via the application of Gaussian peak fitting and Bragg’s law corresponds to the average lattice parameter within the diffraction gauge volume. In the numerical simulation, several different cases of strain distribution in the gauge volume were assumed, and the formation of the diffraction peak

from this volume was simulated. The peak centre was determined by Gaussian peak fitting and converted into lattice parameter, which was then compared with the average lattice parameter within the gauge volume. It was found that, in the presence of steep strain gradients or discontinuities of the lattice parameter in the gauge volume, e.g. step-wise and quadratic distributions, the difference between the two values of the lattice parameter was much greater than in the case of linear or constant distributions. Nevertheless, in all cases the differences remained within a range acceptable for experimental strain analysis, *i.e.* less than 10^{-4}, or 100 microstrain.

Section 5.2 presented a method for processing multi-directional energy-dispersive x-ray diffraction patterns in order to determine the full 2D strain tensor and improve the averaging of strain at the mesoscopic level. This method provides an indirect way of evaluating the shear strain in polycrystalline materials. The weighted least square fitting was implemented in order to extract robust strain tensor information from noisy diffraction data that often arises when the sample has strong texture. The method is applied to study the strain distribution in several LFW samples expected to have a high level of residual shear strains. It is found that the residual shear strains are distributed symmetrically and concentrated at the four corners of the LFW samples. The shear strain distribution is closely related to the *von Mises* residual stresses, since the region these two types of stress reach maximum values are closely correlated.

9.1.2 Texture measurement

Chapter 6 presented a thorough numerical and experimental study aimed at the validation of the single exposure Debye-Scherrer diffraction pattern analysis as a quantitative tool for extracting texture information in cubic polycrystals. The texture processing package

called MTEX is the principal tool used in both the simulation and analysis of the experimental data.

The numerical analysis was performed to support two postulates:

1) That an arbitrary single preferred orientation in cubic polycrystals can be determined using single exposure Debye-Sherrer diffraction pattern;

2) That texture given by a linear combination of a few single preferred orientations can also be determined from a single exposure Debye-Sherrer diffraction pattern.

Regarding to the first postulate, the single preferred orientations functions are assumed to have either 5° or 10° orientation broadening. It was found that:

1) the highest reconstruction error of the single preferred orientation function with 5° broadening is significantly higher than that with 10° broadening, suggesting that the single exposure method may give results with higher errors when it is used to analyse samples with sharp texture (*i.e.* with small orientation broadening);

2) the reconstruction quality is acceptable for the single preferred orientation with either 5° or 10° broadening. Regarding to the second postulate, two types of linear combination of single preferred orientations can be successfully reconstructed using the single exposure Debye-Scherrer diffraction data.

To provide experimental validation, experiments were carried out for a tungsten wire and a copper cylinder to determine their ODFs using different methods. For the tungsten wire, it was found that the ODF obtained from the single exposure diffraction method shows a typical 110 fibre texture that is in good agreement with the deformation history. For the copper cylinder, it is found that 1) the pole figures calculated by using the single exposure diffraction patterns are quite similar to that from multiple exposure analysis with sample

rotation; 2) the more sample rotations (exposures) are included in the ODF analysis, the smaller is the quantitative difference between the ODF and the reference ("correct") ODF.

Chapter 7 applies the single exposure texture analysis method to process the single exposure diffraction data collected by the "horseshoe" energy-dispersive X-ray detector at beamline I12, Diamond Light Source and the TOF neutron diffractometer at beamline GEM, ISIS Spallation Neutron Source. The texture variation along the longitudinal direction of a linear friction welded sample was characterized by using the "horseshoe" detector. It was found that the sample's far field shows texture typical of plate rolling in cubic crystals. Near the bond line, a typical shear texture was found. Section 7.2 presents the data processing routine used to determine ODF from the diffraction data collected by GEM neutron diffractometer. Several possible challenges associated with the data processing approach are discussed. It was found that: 1) sample geometry has minor influence on the accuracy of the ODF determination of the copper cylinder; 2) for the aluminium bar with pre-characterized fibre texture, the reconstructed ODF has large errors compared to the accurate ODF when the GEM diffraction data does not cover key texture information; 3) possible "ghost" problem associated with the harmonics method was examined by studying the nickel DLD blade whose texture known to be weak from pre-characterisation. The problem was found to be insignificant, as both MTEX and MAUD (Rietveld refinement based approach) gave similar results.

9.1.3 Texture evolution modelling

Chapter 8 presents the CPFE models to simulate texture evolution of polycrystalline samples during three metal forming processes: 1) wire extrusion (bi-axial compression); 2) uni-axial compression; 3) linear friction welding (sequential shear).

In section 8.1, the CPFE model was used to simulate texture evolution of tungsten wire during extrusion process by matching the ODF measured in the as-received condition. ODF error was used quantitatively to relate the ODFs obtained from the experiment and modelling. It is found that the ODF error decreased monotonically as the compressive strain was increased. The CPFE model could only achieve convergence until strain reached 49. Simulated pole figures were most similar to the experimental ones at this last step.

In section 8.2, the CPFE model was used to simulate texture evolution of an aluminium cylinder subjected to uniaxial compression. Texture analysis of cylinders after *ex situ* uniaxial compression was used to validate the model. A systematic way allowing the conversion between continuous ODF and discrete OD was developed to allow quantitative comparison of texture results. It was found that cylinders always have 111 fibre textures during uniaxial compression, so that the volume fraction of 111 fibre texture was used make comparison between the experiments and the model. The CPFE model was found to capture well the texture change in aluminium cylinders during uniaxial compression.

In section 8.3, the possibility of modelling texture evolution during linear friction welding was explored. The texture data for the LFW sample W7 was collected by many diffraction techniques in order to obtain the most accurate texture characterization for the model validation. The texture results measured by the Debye-Scherrer setup were finally chosen for model validation. Three different types of boundary conditions were applied to the RVE in order to match experimental results, and the boundary conditions were: 1) single simple shear deformation; 2) single pure shear deformation (plane strain compression); 3) sequential shear deformation. It was found that simulation results obtained by applying either single simple shear or plane strain compression were very similar to the experimental results. However, there was a mismatch in the rotation angle about the *Z* axis of pole figures between the experimental and simulated pole figures. When sequential shear deformation (three-step

shear deformation) was applied to the RVE, pole figures at the final stage of deformation appeared to acquire 6-fold symmetry (classical shear texture in cubic crystals) which was also observed in the experimental pole figures in the welding zone of the sample. This suggests a possible mechanism of deformation during LFW. However, further experimental results are required for validation, particularly collected *in situ* in the course of linear friction welding.

9.2 Directions for future work

The research presented in this thesis represents a significant advancement in the experimental and analysis methodologies for stress and texture evaluation, and in texture evolution modelling by the CPFE approach. The methods developed in the thesis can be improved further in order to solve practical engineering problems. In particular, further studies may be directed fruitfully at the following specific areas.

9.2.1. 3D strain tensor measurement

The diffraction patterns collected by the GEM diffractometer correspond to scattering vectors from different planes and in different orientations. These diffraction patterns can be used to determine the 3D strain tensor in a sample using the algorithm presented in section 5.2. The current limitation for using GEM diffractometer to study 3D strain tensors is the fact that diffraction gauge volume is not well-defined, because no effective collimation systems are installed. GEM beamline scientists are currently working on designing and manufacturing the collimation system. Once the collimation system is in service, the possibility of evaluating 3D strain tensor from the GEM diffraction pattern can be explored.

9.2.2 *In situ texture* evolution study

The single exposure texture characterisation technique presented in this thesis, especially the Debye-Scherrer setup and the “horseshoe” setup, can be readily used to study

texture evolution during *in situ* deformation experiments, such as equal channel angular extrusion (ECAE) and linear friction welding (LFW). As mentioned in section 8.3, the characterisation of texture evolution during *in situ* deformation is crucial for the validation of the texture evolution model. To the author's knowledge, the analysis of texture evolution during either *in situ* ECAE or LFW is not found in literature, mainly due to the limitations of currently available texture characterisation techniques. The results of this thesis provide several significant steps towards that goal.

Reference

[1] http://aluminium.matter.org.uk/content/html/eng/default.asp?catid=175&pageid=2144416783.
[2] Tilley RJD. Crystals and Crystal Structures. Chichester: John Wiley & Sons, 2006.
[3] Thornton STRAF. Modern physics for scientists and engineers. Boston, MA: Cengage Learning, 2013.
[4] http://en.wikipedia.org/wiki/Bremsstrahlung.
[5] http://en.wikipedia.org/wiki/X-ray_fluorescence.
[6] Wilson E. Fifty years of synchrotrons.
[7] http://www.diamond.ac.uk/Home/About/Synchrotrons/Machine.html.
[8] Fitzpatrick ME, Lodini A. Analysis of residual stress by diffraction using neutron and synchrotron radiation: CRC Press, 2003.
[9] http://www.rsc.org/Education/EiC/issues/2011November/ResearchIsis.asp.
[10] Mittemeijer EJWU. Modern diffraction methods. Weinheim: Wiley-VCH-Verl., 2013.
[11] Schwartz AJ. Electron backscatter diffraction in materials science. New York: Springer, 2009.
[12] Bollinger C, Merkel S, Raterron P. Journal of Applied Crystallography 2012;45:263.
[13] Wenk HR, Lutterotti L, Vogel S. Nuclear Instruments and Methods in Physics Research Section A: Accelerators, Spectrometers, Detectors and Associated Equipment 2003;515:575.
[14] Hammersley A, Svensson S, Hanfland M, Fitch A, Hausermann D. International Journal of High Pressure Research 1996;14:235.
[15] Rietveld H. Journal of Applied Crystallography 1969;2:65.
[16] Lutterotti L, Matthies S, Wenk H, Schultz A, Jr. R. J. Applied Physics 1997;81:594.
[17] Pawley G. Journal of Applied Crystallography 1981;14:357.
[18] Toby BH. Journal of Applied Crystallography 2001;34:210.
[19] Cheng WFI. Residual stress measurement and the slitting method. New York, NY: Springer, 2007.
[20] Lianxiang Y, Yonghong W, Rongsheng L. Advanced optical methods for whole field displacement and strain measurement. Optomechatronic Technologies (ISOT), 2010 International Symposium on, 2010. p.1.
[21] Liu L, Morgan EF. Journal of biomechanics 2007;40:3516.
[22] Kocks UFWH-RTCN. Texture and anisotropy : preferred orientations in polycrystals and their effect on materials properties. Cambridge: Cambridge University Press, 2000.
[23] Bower AF. Applied mechanics of solids: CRC press, 2011.
[24] Hosford WF. The mechanics of crystals and textured polycrystals. New York: Oxford University Press, 1993.
[25] Zener C. Elasticity and anelasticity of metals. Chicago, Illinois: University of Chicago Press, 1948.
[26] Hill R. Proceedings of the Physical Society. Section A 1952;65:349.
[27] Hutchings T, Withers PJ, Holden TM, Lorentzen T. Introduction to the Characterization of Residual Stress by Neutron Diffraction: Taylor & Francis, 2005.
[28] Korsunsky AM, Baimpas N, Song X, Belnoue J, Hofmann F, Abbey B, Xie M, Andrieux J, Buslaps T, Neo TK. Acta Materialia 2011;59:2501.
[29] Villert S, Maurice C, Wyon C, Fortunier R. Journal of Microscopy 2009;233:290.

[30] Budai JD, Yang W, Tamura N, Chung J-S, Tischler JZ, Larson BC, Ice GE, Park C, Norton DP. Nature Materials 2003;2:487.
[31] Rosenauer A, Remmele T, Gerthsen D, Tillmann K, Förster A. Optik 1997;105:99.
[32] Liu J, Kim K, Golshan M, Laundy D, Korsunsky A. Journal of Applied Crystallography 2005;38:661.
[33] Zhang SY. High Energy White Beam X-ray Diffraction Studies of Strains in Engineering Materials and Components: University of Oxford, 2008.
[34] Korsunsky AM, Wells KE, Withers PJ. Scripta materialia 1998;39:1705.
[35] James KE, University of Newcastle upon Tyne. Dept. of Mechanical M, Engineering M. The Effect of Microscopic Residual Stress on the Deformation of Polycrystals: University of Newcastle upon Tyne, 2001.
[36] Warren B, Averbach B. Journal of Applied Physics 1950;21:595.
[37] Snyder RLBHJFJIUoC. Defect and microstructure analysis by diffraction [...] [...]. Oxford [u.a.: Oxford Univ. Press, 1999.
[38] Wenk H, Van Houtte P. Reports on Progress in Physics 2004;67:1367.
[39] Heilbronner RP, Pauli C. Journal of Structural Geology 1993;15:369.
[40] http://solidmechanics.org.
[41] Liu Q. Ultramicroscopy 1995;60:81.
[42] Dingley DJ, Randle V. Journal of Materials Science 1992;27:4545.
[43] Chung J-S, Ice GE. Journal of Applied Physics 1999;86:5249.
[44] Tamura N, Celestre R, MacDowell A, Padmore H, Spolenak R, Valek B, Meier Chang N, Manceau A, Patel J. Review of scientific instruments 2002;73:1369.
[45] Chernock WP, Beck PA. Journal of Applied Physics 1952;23:341.
[46] Heidelbach F, Riekel C, Wenk H-R. Journal of Applied Crystallography 1999;32:841.
[47] Wenk H-R, Grigull S. Journal of Applied Crystallography 2003;36:1040.
[48] Margulies L, Winther G, Poulsen H. Science 2001;291:2392.
[49] Merkel S, Wenk HR, Shu J, Shen G, Gillet P, Mao H-k, Hemley RJ. Journal of geophysical research 2002;107:2271.
[50] Puig-Molina A, Wenk HR, Berberich F, Graafsma H. Zeitschrift Fur Metallkunde 2003;94:1199.
[51] Walther K, Heinitz J, Ullemeyer K, Betzl M, Wenk H-R. Journal of Applied Crystallography 1995;28:503.
[52] Wenk HR, Lonardelli I, Williams D. Acta Materialia 2004;52:1899.
[53] Matthies S, Pehl J, Wenk H-R, Lutterotti L, Vogel S. Journal of Applied Crystallography 2005;38:462.
[54] Wenk H-R, Lutterotti L, Vogel S. Powder Diffraction 2010;25:283.
[55] Kallend JS, Kocks UF, Rollett AD, Wenk HR. Materials Science and Engineering: A 1991;132:1.
[56] Kallend J, Morris P, Davies G. Acta Metallurgica 1976;24:361.
[57] Matthies S, Vinel G. physica status solidi (b) 1982;112:K111.
[58] Hielscher R, Schaeben H. J. Appl. Crystallogr. 2008;41:1024.
[59] Deans SR. The radon transform and some of its applications. Mineola, N.Y.: Dover Publications, 2007.
[60] Meredith CS, Khan AS. International Journal of Plasticity 2012;30–31:202.
[61] Carpenter JS, Vogel SC, LeDonne JE, Hammon DL, Beyerlein IJ, Mara NA. Acta Materialia 2012;60:1576.
[62] Schaeben H, Hielscher R, Bachmann F. Solid State Phenomena 2010;160:63.
[63] Voltolini M, Dalconi MC, Artioli G, Parisatto M, Valentini L, Russo V, Bonnin A, Tucoulou R. Journal of Applied Crystallography 2013;46:142.
[64] Williams R. Journal of Applied Physics 1968;39:4329.

[65] Wenk H-R, Matthies S, Donovan J, Chateigner D. J. Appl. Crystallogr. 1998;31:262.
[66] Lutterotti L, Chateigner D, Ferrari S, Ricote J. Thin Solid Films 2004;450:34.
[67] Lonardelli I, Wenk H-R, Lutterotti L, Goodwin M. Journal of Synchrotron Radiation 2005;12:354.
[68] Wenk H-R, Cont L, Xie Y, Lutterotti L, Ratschbacher L, Richardson J. Journal of Applied Crystallography 2001;34:442.
[69] Taylor GI, Elam CF. Proceedings of the Royal Society of London. Series A 1923;102:643.
[70] Schmid E, Boas W. Plasticity of crystals. London: Chapman and Hill, 1935.
[71] http://www.doitpoms.ac.uk/tlplib/superelasticity/twinning.php.
[72] Tomé C, Lebensohn R, Kocks U. Acta metallurgica et materialia 1991;39:2667.
[73] Bouaziz O, Allain S, Scott C, Cugy P, Barbier D. Current Opinion in Solid State and Materials Science 2011;15:141.
[74] Taylor G. Journal of the institute of metals 1938:307.
[75] Hill R. Journal of the Mechanics and Physics of Solids 1966;14:95.
[76] Rice JR. Journal of the Mechanics and Physics of Solids 1971;19:433.
[77] Hill R, Rice J. Journal of the Mechanics and Physics of Solids 1972;20:401.
[78] Asaro RJ, Rice J. Journal of the Mechanics and Physics of Solids 1977;25:309.
[79] Asaro RJ. Journal of Applied Mechanics 1983;50:921.
[80] Hibbitt K, Sorensen. ABAQUS/CAE : user's manual. Pawtucket, RI: Hibbitt, Karlsson & Sorensen, Inc., 2001.
[81] Bonet J. Nonlinear continuum mechanics for finite element analysis: Cambridge university press, 1997.
[82] Abdolvand H. 2012.
[83] Hutchinson J. Proceedings of the Royal Society of London. A. Mathematical and Physical Sciences 1976;348:101.
[84] Peirce D, Asaro R, Needleman A. Acta metallurgica 1982;30:1087.
[85] Asaro RJ. Advances in applied mechanics 1983;23.
[86] Chapter 6 Experimental studies of Peierls-Nabarro-type friction forces in metals and alloys. In: Caillard D, Martin JL, editors. Pergamon Materials Series, vol. Volume 8. Pergamon, 2003. p.159.
[87] LI H-w, YANG H. Transactions of Nonferrous Metals Society of China 2012;22:s222.
[88] Boogaard vdA, Kurukuri S, Ghosh M, Miroux AG. Computer methods in materials science 2009;9:5.
[89] Sachs G, Ver Z. Dent. Ing. 1928;72:734.
[90] Eshelby JD. Proceedings of the Royal Society of London. Series A. Mathematical and Physical Sciences 1957;241:376.
[91] Kröner E. Acta metallurgica 1961;9:155.
[92] Lebensohn R, Tomé C. Materials Science and Engineering: A 1994;175:71.
[93] Roters F, Eisenlohr P, Hantcherli L, Tjahjanto D, Bieler T, Raabe D. Acta Materialia 2010;58:1152.
[94] Kalidindi SR, Bronkhorst CA, Anand L. Journal of the Mechanics and Physics of Solids 1992;40:537.
[95] Bronkhorst C, Kalidindi S, Anand L. Philosophical Transactions of the Royal Society of London. Series A: Physical and Engineering Sciences 1992;341:443.
[96] Beaudoin A, Dawson P, Mathur K, Kocks U, Korzekwa D. Computer methods in applied mechanics and engineering 1994;117:49.
[97] Očenášek J, Ripoll MR, Weygand S, Riedel H. Computational materials science 2007;39:23.

[98] Duchêne L, El Houdaigui F, Habraken AM. International Journal of Plasticity 2007;23:1417.
[99] Dunne FPN. Introduction to computational plasticity. Oxford, NY [u.a.]: Oxford Univ. Press, 2006.
[100] Huang Y. A User-material Subroutine Incroporating Single Crystal Plasticity in the ABAQUS Finite Element Program: Harvard Univ., 1991.
[101] McGarry JP, O'Donnell BP, McHugh PE, McGarry JG. Computational materials science 2004;31:421.
[102] Kysar JW. Journal of the Mechanics and Physics of Solids 2001;49:1099.
[103] Abdolvand H, Daymond MR, Mareau C. International Journal of Plasticity 2011;27:1721.
[104] Peirce D, Shih CF, Needleman A. Computers & Structures 1984;18:875.
[105] Korsunsky AM, Vorster WJJ, Zhang SY, Dini D, Latham D, Golshan M, Liu J, Kyriakoglou Y, Walsh MJ. Acta Materialia 2006;54:2101.
[106] Korsunsky AM. J. Mech. Mater. Struct. 2006;1:259.
[107] Bhamji I, Preuss M, Threadgill P, Addison A. Materials Science and Technology 2011;27:2.
[108] Korsunsky AM, Song X, Hofmann F, Abbey B, Xie M, Connolley T, Reinhard C, Atwood RC, Connor L, Drakopoulos M. Materials Letters 2010;64:1724.
[109] Romero J, Attallah MM, Preuss M, Karadge M, Bray SE. Acta Materialia 2009;57:5582.
[110] Wenk HR, Grigull S. J. Appl. Crystallogr. 2003;36:1040.
[111] Ischia G, Wenk H-R, Lutterotti L, Berberich F. J. Appl. Crystallogr. 2005;38:377.
[112] Bollinger C, Merkel S, Raterron P. J. Appl. Crystallogr. 2012;45:263.
[113] Wenk HR, Lutterotti L, Vogel S. Nucl. Instrum. Methods Phys. Res. Sect. A-Accel. Spectrom. Dect. Assoc. Equip. 2003;515:575.
[114] Lutterotti L, Bortolotti M, Ischia G, Lonardelli I, Wenk HR. Zeitschrift für Kristallographie Supplements 2007;2007:125.
[115] Lutterotti L, Matthies S, Wenk H. Newsletter of the CPD 1999;21:14.
[116] Larson AC, Von Dreele RB. General Structure Analysis System. LANSCE, MS-H805, Los Alamos, New Mexico 1994.
[117] Helming K. Textures and Microstructures 1991;14:187.
[118] Helming K. Textures and Microstructures 1992;19:45.
[119] Kocks UF, Tomé CN, Wenk HR. Texture and Anisotropy: Preferred Orientations in Polycrystals and Their Effect on Materials Properties: Cambridge University Press, 2000.
[120] Hannon AC. Nuclear Instruments and Methods in Physics Research Section A: Accelerators, Spectrometers, Detectors and Associated Equipment 2005;551:88.
[121] Kockelmann W, Chapon LC, Radaelli PG. Physica B: Condensed Matter 2006;385–386, Part 1:639.
[122] Obasi GC, Moat RJ, Leo Prakash DG, Kockelmann W, Quinta da Fonseca J, Preuss M. Acta Materialia 2012;60:7169.
[123] Von Dreele RB, Jorgensen JD, Windsor CG. Journal of Applied Crystallography 1982;15:581.
[124] Ikeda S, Carpenter JM. Nuclear Instruments and Methods in Physics Research Section A: Accelerators, Spectrometers, Detectors and Associated Equipment 1985;239:536.
[125] Le Bail A, Duroy H, Fourquet JL. Materials Research Bulletin 1988;23:447.
[126] Xie M. Journal of Applied Physics 2013;sumbitted.
[127] Toth LS, Van Houtte P. Textures and Microstructures 1992;19:229.
[128] De PS, Mishra RS, Baumann JA. Acta Materialia 2011;59:5946.
[129] Rousselier G, Barlat F, Yoon JW. International Journal of Plasticity 2009;25:2383.

[130] Wang SC, Starink MJ, Gao N, Qiao XG, Xu C, Langdon TG. Acta Materialia 2008;56:3800.
[131] Mironov S, Zhang Y, Sato YS, Kokawa H. Scripta Materialia 2008;59:27.
[132] Prangnell PB, Heason CP. Acta Materialia 2005;53:3179.
[133] Li S. Scripta Materialia 2009;60:356.
[134] Li S, Beyerlein IJ, Alexander DJ, Vogel SC. Scripta Materialia 2005;52:1099.
[135] Li S, Beyerlein IJ, Bourke MAM. Materials Science and Engineering: A 2005;394:66.
[136] Kalidindi SR, Donohue BR, Li S. International Journal of Plasticity 2009;25:768.
[137] Li S, Donohue BR, Kalidindi SR. Materials Science and Engineering: A 2008;480:17.
[138] Furukawa M, Horita Z, Nemoto M, Langdon T. Journal of materials science 2001;36:2835.
[139] Wu PD, Huang Y, Lloyd DJ. Scripta Materialia 2006;54:2107.